

Femtosecond laser-induced modifications and self-organization in complex glass systems

Présentée le 5 juillet 2023

Faculté des sciences et techniques de l'ingénieur
Laboratoire Galatea
Programme doctoral en manufacturing

pour l'obtention du grade de Docteur ès Sciences

par

Gözden TORUN

Acceptée sur proposition du jury

Prof. C. Moser, président du jury
Prof. Y. Bellouard, directeur de thèse
Prof. C. Arnold, rapporteur
Prof. J. Solis, rapporteur
Prof. V. Subramanian, rapporteur

Our true mentor in life is science.
— Mustafa Kemal Atatürk

To my family and loved ones...

Acknowledgements

I would like to express my sincere gratitude to my thesis supervisor, Prof. Yves Bellouard, for his support, kindness, and encouragement. I appreciate the care, enthusiasm, and opportunities he gave and the support for future steps. He has also provided me with many exciting collaborations across the world. I am grateful to our collaborators, Prof. Tetsuo Kishi, Prof. Kathleen A. Richardson, Dr. Anupama Yadav, Dr. Diego Pugliese, Prof. Daniel Milanese, Dr. Andrea Lovera, Marco Giaccone, Simone Frisoni, Dr. Ben McMillen, Prof. Lukas Emmenegger, Prof. Christoph Bostedt, Prof. Rasmus Ischebeck, Dr. Daniel Grolimund, Prof. Jerome Faist, Dr. Mathieu Bertrand, Dr. Malgorzata Grazyna Makowska, Dr. Dario Ferreira Sanchez, Dr. Larissa Boie, Dr. Matthew Singleton, and many other great people.

Furthermore, I like to thank all the staff of the Galatea laboratory, Dr. Pieter Vlugter, Dr. Saood I. Nazir, Dr. Julien Gateau, Dr. Andrea Kraxner, Dr. Magarita Lesik, Dr. Manon Tardif, Dr. Sargis Hakobyan, Dr. Benedikt Hermann, Dr. Daniel Talán Echarri, Dr. Antoine Delgoffe, Dr. Enrico Casamenti, Dr. Arunkrishnan Radhakrishnan, Dr. Olivier Bernard, (soon to be Dr.) Ruben Ricca, David Lambelet, Ernesto Gribaudo, Sacha Pollonghini, Samuel Y. Benketaf, Samuel P. Rey, and Josiane Pachoud. I am pleased to accomplish many successful works for which I collaborated with dear Pieter and Enrico. I am indebted to Ruben, Arun, Pieter, Julien, Samuel, and Saood for their support on technical matters. My sincere gratitude goes to the students who assisted with a part of this work, Anastasia Romashkina and Loic Chautems. Thanks to dear former exchange students Dr. Kana Tomita and Dr. Daijiro Tokunaga for their friendship, the laboratory became more joyful. Furthermore, a special thanks to Benedikt, Daniel, and Antoine for proofreading some parts of the manuscript, and Ruben for the help on the French translation of the abstract.

I further wish to acknowledge the staff of other EPFL laboratories I interacted with AQUA, LMTM, PV-LAB, LMM, LAI, CMI, and CIME. This thesis would be incomplete without the help of Dr. Franz Haug and Dr. Richard Gaul for their help in Raman spectroscopy, Dr. Lucie Navratilova and Dr. Rita Theresoid for their support at CIME, Dr. Adrien Toros for wire bonding in CMI, Dr. Cyril Cayron for general discussion in crystallography, Priscille Bôle for the help in metallography laboratory, Dr. Peter van der Wal for all his assistance in the chemical laboratory. I would like to specifically thank Ezgi Genc, Ekin Kizilkan, Utku Karaca, Ming-Lo Wu, Dr. Francesco Gragmuli, Deniz Turkay, Sophie Libraro, Antognini Luca Massimiliano, Dr. Baptise Rouxel, Dr. Babak Mazinani, Dr. Paulo Germano, and many EPFL staffs for their

help. I would like to also thank all my women colleagues and friends at EPFL, Ezgi, Ece, Marian, Margaux, Rita, Claire, Andrea, Andrada, and Julie for their support and empowering meetings. A big thanks go to my mentor, Prof. Veronique Michaud, for her precious time and encouragement.

Last but not least, big applause to all the great people with who I shared my enthusiasm for science anywhere in the world. Many thanks to all my friends and family who supported me during this time and who made this period an unforgettable moment in my life. My dear family, this thesis would not be here without your support and understanding. I shall continue to work and support young generations as you did for me.

I would like to pay tribute to my great teacher, Dr. Liz Webeck, who passed away during this thesis work and left us alone, even though I still cannot accept this fact. Another commemoration goes to my dear grandmother, who passed away during this thesis work. Rest in peace, and I shall remember all the good times together.

Neuchâtel, 10 April 2023

Gözden Torun

Abstract

Ultrashort laser pulses, i.e., pulses emitted shorter than a picosecond, can tailor material properties by introducing permanent modifications locally in three dimensions. Remarkably, under a certain exposure condition, these modifications are accompanied by self-organized patterns with nanoscale periodicity. These peculiar light-induced structural and morphological modifications raise numerous intriguing material questions, in particular, related to their formation mechanisms and characteristic features that are to date largely unanswered.

In this thesis, we investigate the femtosecond laser response of selected complex glass systems. Specifically, this thesis reports laser-induced modifications and self-organization in the ultra-low expansion (ULE), tellurite, and chalcogenide glass systems based on post-mortem observations and analysis. With multiple objectives in this comparative study, we aim to outline complete modification lists for selected glass systems within the parametric window, determine laser exposure conditions to sustain/annihilate self-organization and unravel the role of key material properties on the formation of local modifications along with self-organized patterns. The final objective is to engineer smart materials and devices based on laser-induced localized transformation.

This thesis reveals numerous unprecedented laser-induced modifications. Unusual physiochemical properties of the representative glass systems lead to 1) a few common modifications, such as photo-contraction, photo-darkening, valence state change, and ion migration. The amorphous nature of the modification is preserved by rearranging the glass network, while the laser-affected zone of chalcogenide glass exhibits fluence-dependent density and refractive index variations. 2) Less common modifications, such as crystallization, require either a metastable system or extreme processing conditions. Specifically, under a given condition, glass decomposition of tellurite and ULE glass generates localized nanocrystalline precipitates in the glass. 3) Self-organization, strongly dependent on laser parameters, is typical on the surface of all selected glass systems; further dependency on the electronic and thermomechanical properties of the glass can suppress their formation in the volume. Such volume nanogratings are not present in the tellurite glass, although salient features are achieved on its surface. 4) Particularly, the etching selectivity of laser-modified material opens up the possibility to fabricate monolithic substrates in chalcogenide and ULE glass, and semiconducting nanocrystals in the laser-affected area enable UV photodetection in tellurite glass.

Overall, this thesis provides new insights toward a general understanding of how dielectrics behave under femtosecond laser irradiation and serves as a guideline for future in-situ experimentation.

Key words: Glass science, femtosecond laser processing, self-organization, laser-induced modifications, smart materials and devices

Résumé

Les impulsions laser ultra-courtes, d'une durée inférieure à la picoseconde, peuvent changer les propriétés des matériaux en introduisant localement des modifications permanentes, dans trois dimensions. Dans certaines conditions d'exposition, ces modifications sont accompagnées de motifs auto-organisés avec une périodicité nanométrique. Ces modifications structurales et morphologiques particulières, induites par la lumière, soulèvent de nombreuses questions intrinsèques au niveau des matériaux, en particulier liées à leurs mécanismes de formation et à leurs caractéristiques, qui restent largement sans réponse à ce jour.

Dans cette thèse, nous étudions les modifications induites par un laser femtoseconde dans une sélection de systèmes de verres complexes. Plus précisément, ce travail rend compte des modifications et de l'auto-organisation induites par l'exposition à des lasers femtosecondes dans les verres à coefficient de dilatation ultra-faible (ULE), les verres de tellurite et les verres de chalcogénures. Cette étude se base sur des observations et des analyses post-mortem. Dans cette étude comparative, nous visons à établir des listes de modifications complètes pour les verres sélectionnés en établissant une fenêtre paramétrique, ainsi qu'à déterminer les conditions d'exposition au laser pour maintenir ou effacer l'auto-organisation et à élucider le rôle des propriétés des matériaux qui jouent un rôle clé dans la formation de modifications locales ainsi que de motifs auto-organisés. L'objectif final est de concevoir des matériaux et des dispositifs intelligents basés sur des transformations localisées induites par un laser.

Cette thèse révèle de nombreuses modifications induites par laser, avec une variété sans précédent. Les propriétés physicochimiques inhabituelles des systèmes de verres sélectionnés conduisent à 1) des modifications communes, telles que la photo-contraction, le photonoircissement, le changement d'état de valence et la migration ionique. La nature amorphe de la modification est préservée en réorganisant le réseau de verre, tandis que les zones du verre chalcogénure affectées par le laser présentent des variations de densité et d'indice de réfraction dépendantes de l'énergie déposée. 2) Les modifications moins courantes, telles que la cristallisation, nécessitent d'un système métastable ou des conditions de traitement extrêmes. Plus précisément, dans certaines conditions, la décomposition du verre tellurite et du verre ULE génère des précipités nanocristallins localisés dans le verre. 3) L'auto-organisation, fortement dépendante des paramètres du laser, est observée à la surface de tous les systèmes de verre sélectionnés; une dépendance supplémentaire aux propriétés électroniques et thermomécaniques du verre peut supprimer leur formation dans le volume. De tels nanoréseaux volumiques ne sont pas présents dans le verre tellurite, bien que d'autres caractéristiques saillantes soient obtenues à sa surface. 4) En particulier, la sélectivité de gravure du matériau modifié

par laser ouvre la possibilité de fabriquer des substrats monolithiques en verre chalcogénure et ULE, tandis que, dans le verre tellurite, les nanocristaux semi-conducteurs observés dans la zone affectée par le laser permettent la photodétection de rayonnement UV.

D'un point de vue plus général, cette thèse fournit de nouvelles perspectives pour une compréhension générale du comportement des diélectriques sous irradiation laser femtoseconde, et sert de guide pour des futures expérimentations in situ.

Mots clefs: Science des verres, traitement laser femtoseconde, auto-organisation, modifications induites par laser, matériaux et dispositifs intelligents.



Nomenclature

Table 1: Table of abbreviations used in the thesis and their descriptions.

Descriptions	Abbreviations
Femtosecond	fs
Optical microscopy	OM
Differential interference contrast	DIC
Digital holographic microscope	DHM
Optical path differences	OPD
Secondary electron images	SE images
Scanning electron microscopy	SEM
Energy dispersive spectroscopy	EDS
Inverse Polar Figure	IPF
Transmission electron microscopy	TEM
High-resolution transmission electron microscopy	HR-TEM
Scanning transmission electron microscopy	STEM
High-angle annular dark-field	HAADF
Selective area electron diffraction	SAED
Fast Fourier transformation	FFT
X-ray diffraction	XRD
Small angle X-ray scattering	SAXS
Extended X-ray absorption fine structure	EXAFS
Neutron diffraction	ND
Nuclear magnetic resonance	NMR
X-ray absorption near edge structure	XANES
Electron paramagnetic resonance	EPR
Photoluminescence	PL
Cathodoluminescence	CL
Ultraviolet-visible-near-infrared	UV-VIS-NIR
Finite-difference time-domain	FDTD
Molecular dynamics	MD
Two-temperature model	TTM
Long-wave infrared	LWIR
Mid-infrared	MIR
Extreme-ultraviolet	EUV
Coordination number	CN
Supercooled liquids	SCL
Room temperature	RT
Glass transition temperature	T_g
Crystallization temperature	T_c
Melting temperature	T_m
Short range order	SRO
Medium range order	MRO
Non-bridging oxygen hole centers	NBOHC
Oxygen vacancies with 3-fold-coordinated silicons	E' centers
Oxygen-deficiency center	ODC
Laser-induced periodic surface structures	LIPSS
Yttrium aluminum garnet	YAG
Time-Temperature-Transformation	TTT

Contents

Acknowledgements	i
Abstract (English/Français)	iii
Nomenclature	vii
1 Introduction	1
1.1 Fundamentals of a glass and complex glass families	2
1.2 Ultrafast laser-matter interaction	3
1.3 State-of-the-art: Femtosecond laser-induced phenomena	5
1.3.1 Laser-induced modifications	5
1.3.2 Self-organization	6
1.4 Femtosecond laser-enabled multi-functional materials	13
1.5 Thesis purpose	13
1.6 General methodology	15
1.7 Thesis outline	16
2 Silicate glass system: Ultra-low expansion glass	17
2.1 Glass structure and properties	18
2.2 Femtosecond laser and ULE®Glass interaction	20
2.3 Experimental procedure	22
2.3.1 Femtosecond laser irradiation	22
2.3.2 Specimen characterization	23
2.4 Results and discussion	24
2.4.1 Regimes of femtosecond laser-induced modifications	24
2.4.2 Self-organization and laser induced-modifications in the volume	26
2.4.3 Photo-darkening phenomenon	33
2.4.4 Glass decomposition and the formation of β -TiO ₂ nanocrystals	34
2.4.5 Remarks on the surface modifications	39
2.5 Summary	39
3 Non-silicate oxide glass systems: Tellurite glass	41
3.1 Glass structure and properties	42
3.2 Femtosecond laser and tellurite glass interaction	44

3.3	Experimental procedure	46
3.3.1	Glass specimen preparation	46
3.3.2	Femtosecond laser irradiation	47
3.3.3	Specimen characterization	48
3.4	Results and discussion	49
3.4.1	Self-organized nanostructures in non-cumulative regime	49
3.4.2	Glass decomposition and the formation of Te nanocrystals	53
3.4.3	Self-organized nanostructures in thermal cumulative regime	58
3.4.4	Effect of ambient conditions on laser-induced modifications	68
3.4.5	Effect of glass composition on laser-induced modifications	70
3.4.6	Phenomenological interpretation of self-organization in cumulative regime	73
3.4.7	Morphological and structural changes in the volume	76
3.5	Summary	78
4	Non-oxide glass systems: Chalcogenide glass	81
4.1	Glass structure and properties	82
4.2	Femtosecond laser and chalcogenide glass interaction	84
4.3	Experimental procedure	86
4.3.1	Glass specimens preparation and characterization	86
4.3.2	Femtosecond laser irradiation	87
4.3.3	Specimen characterization	88
4.4	Results and discussion	89
4.4.1	Self-organization and photo-modifications in the volume	89
4.4.2	Self-organization and photo-modifications on the surface	92
4.4.3	Stability of morphological and structural modifications	97
4.4.4	Effect of the glass network on laser-induced modifications	100
4.5	Summary	104
5	Device fabrications and applications	107
5.1	ULE®Glass	108
5.1.1	3D microstructures of ULE®Glass	108
5.2	Tellurite glass	118
5.2.1	Direct-write UV photodetectors	118
5.3	Chalcogenide glass	130
5.3.1	3D microstructures of chalcogenide glass	130
5.4	Summary	140
6	Conclusions	141
6.1	Main results	142
6.2	General discussion	145
6.3	Thesis outcome and insights for future works	148

A Experimental details	151
A.1 Femtosecond laser parameters	151
A.2 Laser spot diameter measurement	151
A.3 Time-dependent temperature distribution model	153
B ULE@Glass	155
C Tellurite glass	157
D Chalcogenide glass	163
E Device fabrication and applications	167
Bibliography	171
Curriculum Vitae	209

1 Introduction

Non-ablative laser-matter interaction in the femtosecond ($\sim 10^{-15}$ seconds) regime has led to a taxonomy of numerous materials modifications, ranging from localized densification, formation of self-organized nanostructures, elemental redistribution, and crystallization in glass, or the opposite when dealing with crystalline substrates. Altogether new categories of material modifications have been discovered [1, 2], which are not possible otherwise. These modifications are created by tightly focusing an ultrashort pulsed laser beam on the surface or inside a transparent material, leading to extreme peak power densities (\sim tens of TW/cm^2).

Remarkably, self-organized patterns with nanoscale periodicity may form within the laser focus under specific exposure conditions. These peculiar laser-induced modifications raise numerous intriguing material questions, in particular, related to their formation, structure, and properties, that are largely unanswered to date. Depending on the exposure conditions and the material, further physical and chemical modifications are generated within or outside the self-organization domain.

In this context, this thesis investigates the self-organization phenomena and photo-induced modifications in three different classes of glass systems, exposed to similar laser conditions. Specifically, we explore the cases of ultra-low expansion (ULE), tellurite, and chalcogenide glass systems. They form model materials for elaborating a general understanding of how dielectrics respond to femtosecond laser pulses. Each of these representative glass systems has striking properties relevant to technological applications, for which this work also examines the relevance of self-organized patterns. With this vision, this chapter begins with a brief description of glass and complex glass systems. Self-organization and femtosecond laser-induced material modifications are discussed from numerous examples of various dielectric systems starting with fused silica glass, a model material extensively studied previously. To this end, the objectives are detailed, followed by the general approach and the outline of the manuscript.

1.1 Fundamentals of a glass and complex glass families

Naturally occurring material, glass, has formed more than 7 billion years ago [3]. It can be much earlier since the nucleosynthesis of silicon (Si) and oxygen (O), the elements of a natural glass former, and the first reactions between them are thought to date earlier than the birth of our solar system. Whether naturally made or synthetic, glass is one of the fundamental material classes, indispensable for human life since ancient times.

Throughout history, there have been various scientific definitions for glass. The most comprehensive definition has been recently unified by Zannatto and Mauro [4]: “Glass is a non-equilibrium, non-crystalline condensed state of matter that exhibits a glass transition. The structure of glasses is similar to that of their parent supercooled liquids (SCL), and they spontaneously relax toward the SCL state. Their ultimate fate, in the limit of infinite time, is to crystallize.” Here, the glass transition is a temperature that the viscosity of the supercooled liquid is at a certain value (e.g., $\eta(T_g) \sim 10^{12}$ Pa·s for a typical oxide glass [4]). At room temperature, the relaxation is expected to happen for an infinitely long time. By heat and/or pressure, the crystallization of a glass (or devitrification) decreases the free energy, making the material stable. Thermodynamically, the glass differs from an amorphous solid since they display the glass transition upon heating, and the non-crystalline atomic structure is similar to the one of a parent supercooled liquid [5]. Still, they are both classified under non-crystalline materials.

At the atomic scale, a glass network is composed of one of the glass-forming elements, oxides, compounds, or alloys, such as S, Se, P (refer to molecular glass systems), SiO_2 , B_2O_3 , GeO_2 , ZrO_2 , V_2O_5 (oxide glass systems), As_2S_3 , Sb_2S_3 (non-oxide glass systems), and $\text{Te}_x\text{Cu}_{25}\text{Au}_5$ (metallic glass systems) [6]. The classification results from the type of bonding, such as metallic, ionic, or covalent. In addition, there are other types of glass systems, such as organic glass systems and polymers. Furthermore, a special class of non-silicate oxides, such as TeO_2 , Al_2O_3 , Pb_2O_5 , Bi_2O_3 , are considered as conditional glass formers. These glass systems require a sufficient amount of other oxides, such as network modifiers or intermediates, and/or a special quenching technique to form a glass. The addition of such oxides tailors the glass network and hence, chemical, optical, thermal, and mechanical properties.

Fused silica (pure SiO_2) and silicate (SiO_2 -based) glass systems are the most common ones, both geological-formed and human-made, dominating industrial production and usage worldwide. Other non-silicate glass-forming oxides, such as tellurites, germanates, and phosphates, lead promising technological advancements with properties beyond silicates. Additionally, non-oxide glass systems, such as chalcogenides or halides, have offered further distinctive properties, although they require a specialized installation for their production. In this thesis, complex glass systems refer to multi-component silicate, non-silicate oxide, or non-oxide glass networks, consisting of more than a single compound, presented in Figure 1.1. The structure of the complex glass systems is covered in the next chapters.

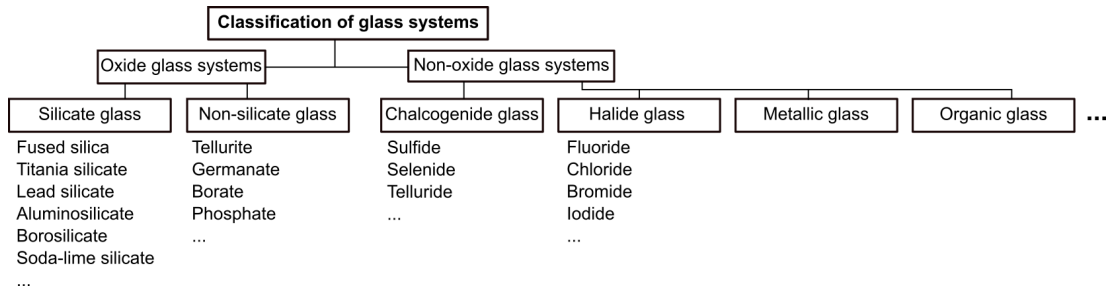


Figure 1.1: The classification of glass-forming systems based on composition and chemistry (adapted from [6]). A representative glass system from each glass family is selected to study in this thesis work, excluding the halide, metallic, and organic glass systems.

1.2 Ultrafast laser-matter interaction

Ultrashort laser pulses, i.e., pulses shorter than a picosecond (ps, 10^{-12} seconds), allow unique opportunities for tailoring material properties by introducing localized permanent structural modifications along three-dimensional (3D) trajectories. The availability of ultrashort pulses with high laser intensities opens a new realm to explore light-matter interaction dynamically, study material systems in extreme conditions, and fabricate numerous integrated monolithic devices made from transparent substrates at the micrometer scale.

The interaction between ultrafast laser pulses and the matter involves several dynamic events at various time scales that are different from classical laser-matter interaction, such as nonlinear optical absorption, electron excitation, and overcritical heating. Let us cover the principles and characteristics of this interaction in this section.

When an ultrafast laser irradiates a transparent material, a nonlinear absorption mechanism transfers optical energy to a medium by exciting electrons from the valence band to the conduction band. For optical breakdown to occur by nonlinear absorption, which in turn generates localized permanent modifications in the medium, the tightly-focused high electric field strength is required to bridge the band gap energy and produce critical free carrier density [7]. Two types of nonlinear absorption mechanisms stimulate this absorption, nonlinear photoionization and avalanche ionization [8]. Figure 1.2.I illustrate nonlinear excitation events occurring in a femtosecond timescale during laser irradiation.

Photoionization is a direct ionization of electrons by the electric field of the laser. Depending on laser exposure conditions and the material, there are different photoionization processes: multi-photon ionization (MPI), avalanche, and tunneling ionization (see Figure 1.2.I) [8]. Dielectrics with band gaps larger than the photon energy require multiple photons to ionize electrons. The sum of the simultaneously absorbed photon energy should be larger than the band gap. In tunneling ionization, the laser electric field distorts the Coulomb potential well, which describes the bound state of electrons between the parent atom and its valence electron, so that electrons can tunnel through the lower barrier and become free. MPI occurs under

a strong laser field at a high laser wavelength, whereas tunneling ionization occurs mostly under a strong laser field at a low wavelength. The transition between these two ionization states was modeled by Keldysh theory [9].

The avalanche ionization is associated with the formation and population of free carriers up to a level where a strong field, like impact ionization, can occur, typically for pulse duration > 10 fs [7, 8]. It requires some "seed" electrons, either thermally excited carriers, easily ionized impurities, or excited carriers via nonlinear photoionization in the conduction band [8]. The electrons already in the conduction band gradually gain more energy absorbing incoming photons, called free carrier absorption. The electrons energized sufficiently may collide with other electrons present in the valence band, called impact ionization, leading to the formation of extra free carriers at the bottom of the conduction band. Avalanche ionization can continue as long as the laser electric field is present in the focal volume.

Photoionization and electron-electron impact ionization can produce a free electron gas with relatively high density when about 10 percent of valence electrons are removed from bonding orbitals. The excitation of a large number of electrons from bonding to anti-bonding states results in lattice distortion by repulsive interatomic forces [10]. According to the non-thermal model, lattice distortion (around 100 fs) takes place without increasing the thermal energy of atoms since phonon emission is slower than the pulse duration [10, 11].

Once the overall electron density is increased, numerous energy dissipation mechanisms, such as carrier-carrier or carrier-phonon scattering occur. The first case (~ 10 -100 fs) is the recombination of the electrons in the matrix, whereas carrier-phonon scattering (+10 ps) is the energy transfer from free electrons to the material matrix through phonons [12]. Both dissipation mechanisms result in different electronic distributions altering the properties by introducing permanent defects in the lattice [7]. Figure 1.2.II shows the timescale of relevant events occurring during femtosecond laser irradiation. At the picosecond to the nanosecond time scale, the lattice heating starts, and a shock wave separates from the hot focal volume. Up to several microseconds, the heat dissipation process out of the focal volume is completed. Depending on the plasma density, which is proportional to the net deposited energy, quick energy transfer results in permanent structural changes in the focal volume [8]. These events occur during a single-pulse exposure, repeated by multi-pulse exposure both in static and dynamic conditions. The timescale of the energy transfer and the related events makes the final modifications dependent on exposure conditions and material properties.

Overall, nonlinear photoionization is more efficient for a short pulse, i.e., energy at the instant time should be enough to supply seed electrons, whereas avalanche ionization is more efficient for longer pulses as it needs some time to produce seed electrons in the conduction band [12]. With longer pulse durations (ps to ns), seeds are provided by thermally excited electrons, impurity, and defect states since the ionization process takes place throughout the timescale of the pulse duration [8]. The critical electron density is reached efficiently via avalanche ionization, and thus, less energy is required for the optical breakdown. Compared to longer

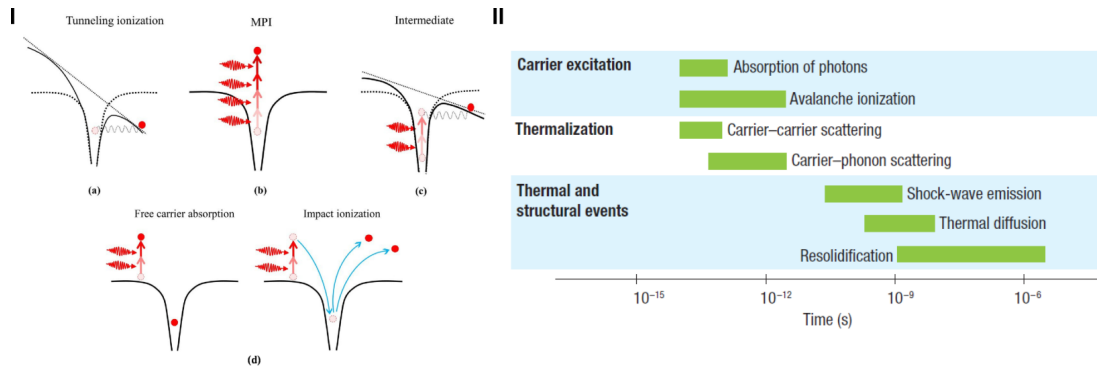


Figure 1.2: I) Schematic diagram of nonlinear electron excitations due to (a) tunneling ionization, (b) MPI, (c) intermediate (both tunneling and MPI), and (d) avalanche ionization: free carrier absorption followed by impact ionization (taken from [13]). II) Schematic representation of the characteristic timescale associated with the interaction of a fs-laser pulse with transparent materials (taken from [7]).

pulses, femtosecond lasers are an ideal tool for high-precision micromachining thanks to the self-seeded ionization process, which is less dependent on defects, and minimal heat diffusion outside the focal point due to a shorter time scale than thermal diffusion time leads to more controllable material modifications [8].

1.3 State-of-the-art: Femtosecond laser-induced phenomena

In this section, first, we present various photo-induced physical and chemical modifications in several glass and transparent dielectric systems, specifically in fused silica. Later, we cover extensively the physical properties and theories behind the femtosecond laser-induced fingerprint morphologies, specifically, self-organization.

1.3.1 Laser-induced modifications

Femtosecond laser direct writing is a powerful technique to modify the physical and chemical properties of transparent media through nonlinear absorption phenomena. Focused on the surface and/or inside transparent materials, the femtosecond laser can induce diverse and localized permanent morphological and chemical modifications. Relying on laser processing parameters and exposed materials, numerous types of modifications have been reported inside and on the surface of transparent media for more than the last two decades. Starting with the ones in fused silica, a small processing window at low intensity and shorter pulse duration (typically less than 200 fs) leads to uniform and positive refractive index change due to the densification process [14]. Densification results from an increase in the concentration of 3- and 4-membered Si-O molecular rings and a decrease in the average network bond angle in the laser-affected glass network, involving changes of electronic configuration and polarizability [2, 15]. This process is accompanied by direct volume change, creating the

stress-state in the material [16]. This type of modification is generally called Regime I [17]. This homogeneous modification based on a positive or negative change in refractive index has been reported for other types of glass systems, such as phosphate [18], germanate, and lead oxide-based glass [19].

Further rise in the laser intensity and pulse duration (as in Figure 1.3.I) results in birefringent anisotropic nanostructures, so-called self-organized nanogratings or Regime II [1], reviewed extensively in the next section. With even higher laser intensity, disruptive self-organized nanogratings accompanied by nano-cracks elongated millimeter-length (referring to Regime III) [20] can be detected optically by injecting a dye [21]. In addition, similar morphologies are observed on the surface of fused silica, such as self-organized nanogratings, ablation, etc. The results reported for fused silica up to this point are obtained in a non-thermal cumulative regime when the time between two pulses is long enough for the lattice to cool down. In contrast, in the thermal cumulative regime, glass decomposition followed by glass melting and the formation of voids filled with molecular oxygen has been reported [22], as in Figure 1.3.II. The formation of these voids has been attributed to microexplosion as a consequence of a high temperature and pressure ejection of material.

Other modifications, such as the point lattice defects leading to coloration (i.e., color centers), have been reported in various glass systems, such as fused silica, phosphate glass, and so on [2, 23]. This modification allows writing of arbitrary patterns with various colors in the transparent medium, as illustrated in Figure 1.3.III. Other ones are ion migrations and valence state change based on thermal dissipation and diffusion [24, 25] in multi-component glass systems in Figure 1.3.IV. For instance, the combination of Mn^{2+} into Mn^{3+} accompanied with the generation of purple color in Mn and Fe co-doped silicate glass [26]. Furthermore, crystal nuclei can be formed locally by the temperature above the crystallization temperature and/or by atomic diffusion with subsequent microstructural rearrangement [25]. The first example of the precipitations and crystallization induced by femtosecond laser-induced modifications combined with heat treatment has been reported in Ag and Ce doped photo-sensitive glass [27]. Similarly, through oxidation and reduction reactions, valence electron transfer as $Ag^+ + NBO \rightarrow Ag^0 + NBO^+$ leads to selective crystallization of Ag in photo-sensitive glass [28]. Phase separation and precipitation of crystals of various glass upon irradiation with high-intensity femtosecond laser have been reported, such as in lithium niobium silicate [29] (see Figure 1.3.V), barium-alumina-borate glass [30], etc. These modifications often require multi-component systems and can occur both on the surface and in the volume of transparent media.

1.3.2 Self-organization

Before we move on to the definition of self-organization, we need to clarify what "complex systems" mean, as in glass systems. A multi-component system with large variability on the greatest scale is referred to as a complex one. The large variability arises from the multiple

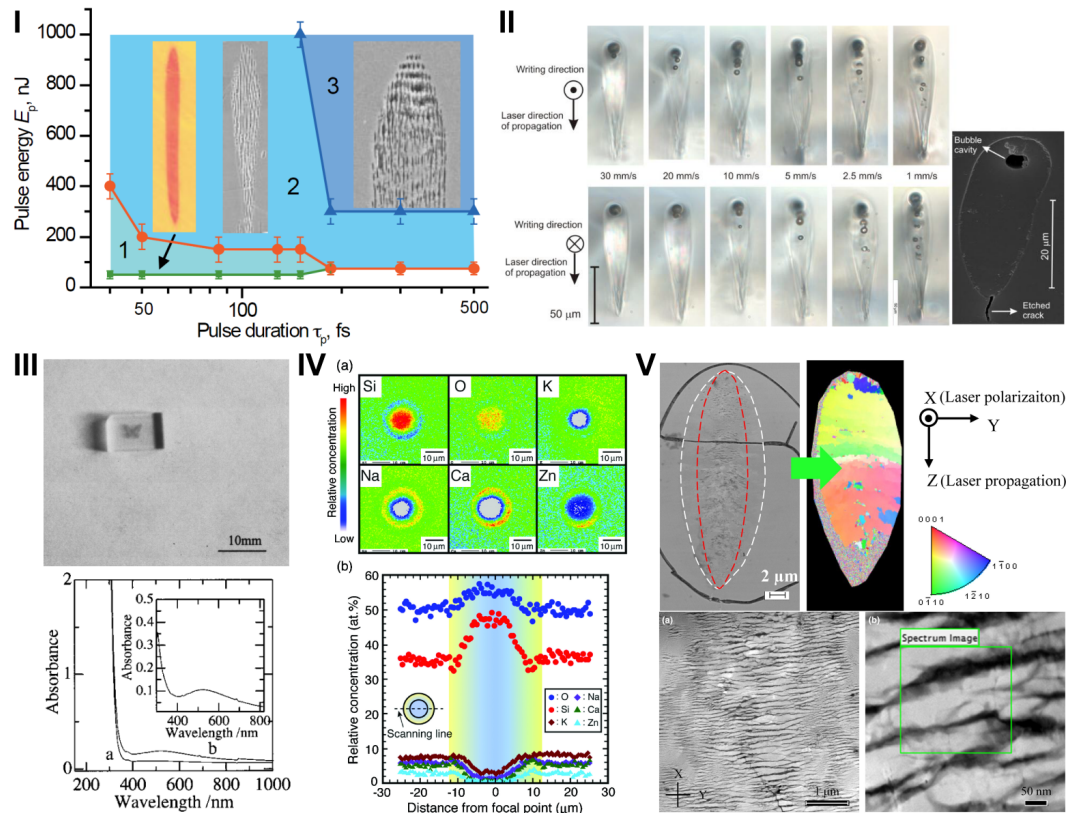


Figure 1.3: I) Parametric window and the three types of modification in fused silica (taken from [20]). II) OM and SE images of self-organized bubble structures in fused silica (taken from [22]). III) Absorption spectra and OM image of Mn and Fe co-doped silicate glass after the fs-laser irradiation. The peak at 520 nm is the absorption of Mn^{3+} ions (taken from [26]). IV) Ion distribution and relative concentration profile across the fs-laser modified area (taken from [24]). V) SE and STEM-HAADF images with the corresponding IPF map based on the LiNbO_3 crystal (taken from [29]).

dependencies, relationships, oppositions, and other interactions among components with themselves and/or their surroundings. In general, such interactions lead to collective dynamics, nonlinearity, and energy availability as a result of their non-equilibrium state. It can exhibit some feedback mechanisms. That is the reason why modeling their system-wide behavior is tremendously challenging.

The interactions among neighboring components drive an avalanche of events of all scales. The system advances into a critical state due to a minor disturbance as it is specified self-organization criticality [31]. In this critical state, a large number of simple components produce spontaneous large-scale organization only by interacting with their neighbors or surroundings within the system. Individual components are no longer autonomous but part of a big ordered structure. Since strong nonlinear dynamics and many degrees of freedom are involved, most of the transition from a disordered to an ordered state occurs through avalanches of catastrophic events rather than smooth paths [31].

Frequent from the sub-atomic to the cosmic scale, various types of self-organization exist, such as static, dynamic, templated, biological, and so on [32]. In nature, self-organization takes various forms, for instance, fundamentals of living cells, flocks of birds as well as the formation of a brain by an intricate arrangement of interacting cells [32]. In physics, laser-matter interaction is one kind of dynamic and templated self-organization: There is an energy dissipation from the system, and the interaction between the components and regular features in their environment determines the final state. In particular, it is interesting when the matter is glass, which does not show an isotropic or symmetric scheme on a molecular scale and does not possess long-range order as in crystalline materials. Other examples of templated self-organization are the crystallization of colloids under optical fields [32], surface crystallization of a glass determining the morphology of the crystal, and self-assembly of nanoparticles into various morphologies upon laser ablation.

Here, we first discuss the characteristics and several formation theories of self-organized nanostructures in volume and later on the surface. Early works have shown that upon irradiation of femtosecond laser, there are regular patterns inside fused silica, so-called self-organized nanogratings [1]. Figure 1.4 shows the characteristic features of these nanogratings. Although the final structure depends on numerous factors, nanogratings generally consist in alternating subwavelength nanoplanes with features as small as 20 nm, with an orientation perpendicular to the electric field [1, 17, 33]. Earlier results show that the composition of nanoplanes alternates between oxygen-rich and oxygen-deficient, displayed in Figure 1.4.I. Another study reported that nanogratings evolve from nanoporous planes with a periodicity of approximately 250-300 nm [33]. Later, Richter *et al.* confirmed that nanopores are the main structures of nanogratings by small-angle X-ray scattering (SAXS) measurements combined with focused ion beam (FIB) milling, and their plane-like structures give rise to the periodic arrangement, as illustrated in Figure 1.4.II [34]. The nanopores are filled with molecular oxygen in the gas form, easily detectable by Raman spectroscopy [33]. As in the self-organization phenomena, incubation and subsequent emergence of nanogratings upon accumulation of multiple laser pulses (in Figure 1.4.III) present a great example of the positive feedback mechanism. The temporal separation of pulses is required to be longer than the lifetime of the plasma and self-trapped excitons [35]. Interestingly, Figure 1.4.IV presents the evolution of erased and rewritten nanostructures by upcoming pulses, with little or no degradation [36].

Particularly in fused silica, nanogratings exhibit large birefringence [37] due to anisotropic index change in isotropic parent material [34] and chemical etching selectivity [38]. In terms of mechanical properties, nanoindentation results showed that [39] localized densification, supported by measurements of volume variation and Young's moduli with vibrating cantilevers [40, 41]. The same cantilevers have been used to determine the thermal expansion of nanogratings in fused silica [42]. Their polarization-dependent properties have been established over the last two decades, as in Figure 1.4.V [36]. Finally, the annihilation of some point and lattice defects in nanogratings starts at around 600 K, and the structures are thermally stable up to 1500 K for several hours [33, 43, 44].

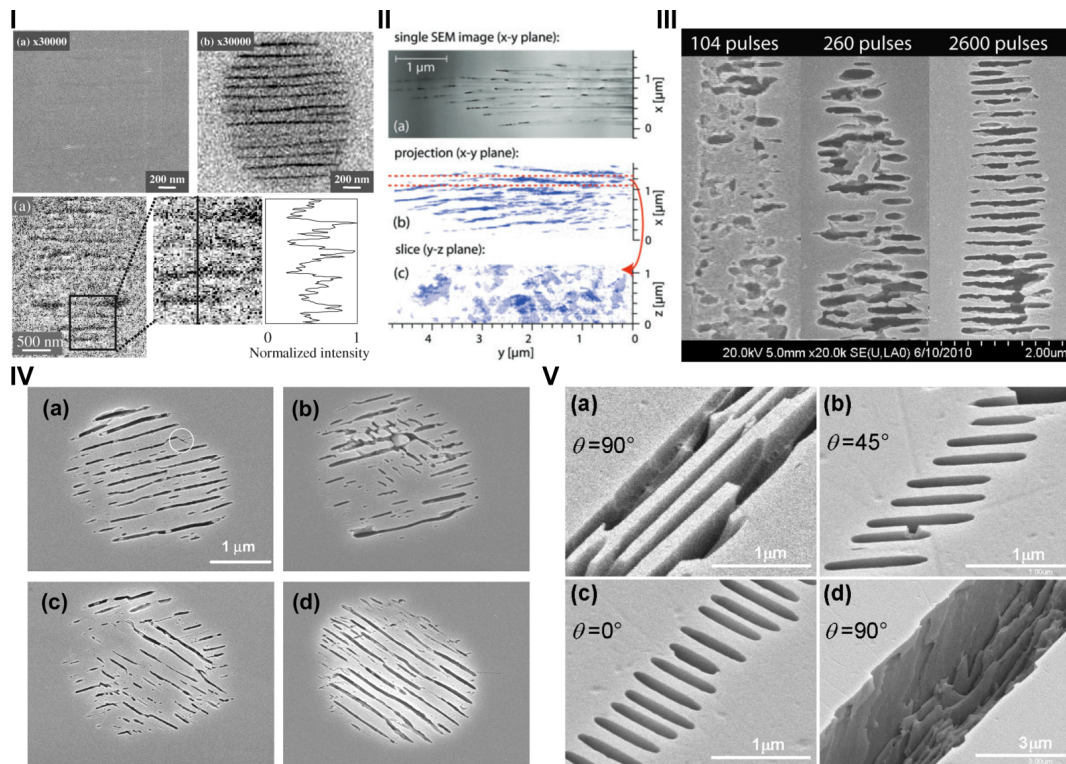


Figure 1.4: I) SE and BSE images of the polished fused silica glass surface, Auger spectra of oxygen (taken from [1]). II) 3D structure of nanogratings: a) SE image of a FIB slice in the x-y plane with projections on the b) x-y plane and c) y-z plane (taken from [34]). III) SE images of the evolution of uniform nanogratings with the number of pulses (taken from [44]). IV) SE images of the evolution nanogratings by rewriting: a) 3-pulse, b) 30-pulse, c) 300-pulse, and d) 4000-pulse irradiation to the point, initially irradiated by 4000 pulses (taken from [45]). V) SE images of nanostructures at a-c) 300 nJ and d) 900 nJ, revealed by 20 mins of 0.5% HF etching (taken from [36]).

To date, there are good agreements on the structural information of nanogratings, which is emerging from a combination of ultrafast and complex events at the nanoscale. Although the formation mechanism of nanogratings is not fully understood yet, a few theories are trying to explain the orientation, periodicity, size, shape, chemical arrangement, and dependency on laser parameters with a single model; to the best of our knowledge, none of them has been validated with other glass or dielectric systems yet.

- Shimotsuma *et al.* [1] revealed the nanogratings inside the fused silica in focal volume by secondary electron (SE) imaging. They have reported the logarithmic dependence on grating periods with the number of pulses, and the grating period increases with pulse energy. In terms of chemical compositions, modulation of the oxygen concentration has been observed between alternating structures. The formation of nanogratings has been attributed to the interference between the incident light field and the electric field of the bulk electron plasma wave, leading to a modulation in electron plasma

concentration and subsequent structural modifications. A similar theory was suggested to explain laser-induced surface ripples in 1981 [46]. However, there are some critics of this formation theory. For instance, the temperature of the plasma determines the frequency of the electric field of the plasma. It is speculated in [47] that the deposited energy is insufficient to reach the required temperatures (and so does the frequency). Also, this model fails to explain the cumulative effect. Although an interference pattern is sinusoidal, the nanograting appears as more discrete thin planes. This is one of the strong points of the model of nanoplasmonics, localized enhancement mentioned below [47].

Another investigation has shown that the periodicity is ten times smaller than a laser wavelength in porous glass [48]. Splitting in the nanogratings and the reduction in the periodicity have been observed with several pulses. The saturation of reduction in periodicity has been attributed to thermal accumulation. The model explaining the splitting behavior states that the constructive interference of the scattering light from the original nanoplanes creates a high intensity between the two adjacent nanoplanes, resulting in shortening the nanograting period by half.

- Bhardwaj *et al.* [47] proposed a nanoplasmonic model, i.e., local field enhancement (concentrated electric field) at the nanoscale, leading to light confinement, well below the wavelength. Any localized inhomogeneity, e.g., color centers, defects, etc., is ionized due to highly inhomogeneous plasma aligned with the light propagation. After multiple laser pulses, this plasma transforms into a spherical nanoplasma, expanding to an ellipsoid and finally into nanoplanes due to the asymmetric growth of the initial spherical nanoplasma. The growth of nanoplasma into nanoplanes is attributed to the pulse-to-pulse nonlinear material memory effect. It has also been suggested that periodicity follows roughly half of the incident wavelength $\lambda/2n$, suggesting the insensitivity to pulse energy. This theory also clarifies the structural modifications below critical plasma concentrations. All explanations presented above are related to the excitation of plasma and its interaction with light. It is unclear how plasmons are responsible for the formation of nanogratings in the propagation direction.
- Beresna *et al.* [49] suggested a theory based on interference and dipole-dipole attraction of exciton-polaritons (quasi-particles resulting from the coupling of a photon and an exciton) and self-trapped excitons, can exist in wide band gap amorphous materials. The once critical concentration of exciton-polaritons is achieved upon laser irradiation, the structure freezes into a form of final gratings. The molecular oxygen formation inside the nanopores is attributed to the recombination of localized high concentrations of excitons by the following decomposition reaction: $SiO_2 + excitons \rightarrow SiO_{2(1-x)} + xO_2(g)$. They also presented a mathematical model that describes the periodicity and the required energy as less than what has been shown experimentally. In agreement with this theory, Richter *et al.* [34] refers to self-trapped excitons, which can relax into permanent defects, e.g., in the case of fused silica, dangling bond type defects, such as *nonbridging oxygen hole centers* (NBOHCs) and *oxygen vacancies with 3-fold-*

coordinated silicons (E' centers). The absorption can be facilitated at the location of dangling bond-type lattice defects that have lower energy states than the band gap. Subsequently, enhanced coupling between individual laser pulses leads to a memory effect, implying that the pre-modified material causes nanogratings. In this theory, they have experimentally shown that the self-trapped excitons have a large impact on the formation of nanogratings [34].

Each of the suggested theories is supported by experimental observation. Most of the formation theories are concerned only deposition of optical energy based on laser parameters and the fundamental physics behind it, leaving the material-dependency minimum or often aside.

Let us cover a few examples of nanogratings in the volume of different transparent media. Starting with Ge- or P-doped fused silica, a larger processing window with higher birefringence is obtained as opposed to F-doped fused silica [50]. In borosilicate glass, nanogratings with much smaller periodicity and less birefringence than fused silica have been reported [51, 52]. In germanate glass systems, nanogratings obtained in pure germanium oxide glass with much smaller nanopores in the nanoplanes (less than 10 nm for GeO_2 vs. 30-50 nm for SiO_2) [53, 54]. The addition of sodium dioxide, the higher energy requirement for the formation of nanograting, which further increases with sodium content and crystallization of $\text{Na}_2\text{Ge}_4\text{O}_9$ precipitates are reported [55]. Similarly, partial crystallization accompanied by the nanogratings is observed in alumina glass [56]. Various commercial and heavy metal oxide glass systems, such as aluminoborosilicate, lithium-niobium silicate glass [29, 57–59], and crystals, such as sapphire [60] and YAG [61], have been investigated and compared with fused silica. Although there is a growing interest in other media, almost all of the theoretical work performed is based on fused silica. The thesis precisely aims to narrow down this gap of knowledge.

Now, we present the femtosecond laser-induced surface nanostructures, so-called laser-induced periodic surface structures (LIPSS), surface nanostructures, nanogratings, or ripples. Although early research on surface nanostructures dates back 1960s, our understanding of their structure and formation has advanced in the last two decades [62]. Similar to volume nanogratings, their alternating nanoplanes with a regular period, or, in this case, sort of nanocracks, range from tens of nanometers to several micrometers [63]. Since those nanogratings can be fabricated on almost all material systems by focusing the laser on the surface, more diverse morphology, periodicity, and polarization dependency have been reported compared to the ones in volume. Several studies classify these structures with respect to their periodicity expressed as a ratio of laser wavelength and the refractive index of the material [63].

Many early electromagnetic theories are based on interference of electromagnetic radiation emerging from scattered at the microscopic rough surface, or in some specific cases, near field enhancement through surface plasmon polaritons (SPPs) [62]. The surface excitation modes can lead to spatial modulation of the local energy. Still, the generation of surface roughness by multi-pulse exposure is required to excite SPPs, resulting in surface nanostructures with a

positive feedback mechanism.

According to Sipe's theory, possible excitation of SPPs is defined by wave vectors as a function of surface roughness, dielectric permittivity, and laser irradiation parameters [64]. This electromagnetic theory can predict shape, orientation, and periodicity through redistribution of the required energy and positive feedback mechanism, yet, intra-pulse feedback cannot be explained only with this theory. Later, with additional transient dielectric function adopted from the Drude model, the Sipe-Drude theory considers the changes in the dielectric permittivity during the transient metallic state in semiconductors or dielectrics due to MPI process, demonstrates the importance of intra-pulse feedback mechanism by varying interpulse delays in double fs-laser pulse experiment [65]. Relying on the Maxwell equation, the spatiotemporal electromagnetic field distribution near the surface by the finite-difference time-domain (FDTD) model has shown a successful link between a theoretical understanding of the carrier density and ablation depth-dependent with inhomogeneous energy distribution [66].

Buividas *et al.* [67] and Liang *et al.* [68] observed nanogratings on the surface, and their periodicity satisfactorily explained by the reduction with the increase of the number of overlapped pulses. The formation of nanogratings is attributed nanoplasmonic model and the incubation effect as in the volume nanogratings proposed by Bhardwaj *et al.* [47].

Similarly, by time-resolved pump-probe diffraction experiments, Rudenko *et al.* explained the surface nanogratings (with periodicity sufficiently smaller than the irradiation wavelength) by the existence of nanoscopic local defects that promote locally enhanced absorption, field-enhancement, and scattering [69]. Later, with the combination of the electromagnetic and hydrodynamic simulations, Rudenko *et al.* successfully modeled the tunable periodicity emerging from the frequency shift of quasi-cylindrical and surface plasmon waves [70, 71].

Both electromagnetic and material redistribution theories are required to explain the final structures since the former ones consider the rather immediate effects of optical absorption and scattering towards the first seed of modifications, and the latter ones can take up to ms, presented in Figure 1.2.II. The theory of the redistribution of the exposed material at the surface can explain inter-pulse feedback, and 3D modifications in volume even better than some of the electromagnetic theories; still, it is insufficient to unravel the orientation of nanostructures and intra-pulse feedback [62]. In general, formation theories of surface nanostructures are concerned with the local effects of thermodynamic and hydrodynamic, such as surface tension gradients, thermoelastic ally generated surface acoustic and thermocapillary waves, or self-organization [72, 73]. While the former is based on the thermal gradient and strain field associated with the deposited energy, the latter is based on the formation of local defects and destabilization of the surface upon femtosecond laser irradiation. The control of orientation through self-organization is correlated later by asymmetric kinetic energy distribution of excited electrons [74].

1.4 Femtosecond laser-enabled multi-functional materials

Ultrashort laser processing has evolved significantly over the last two decades and started to reveal its scientific, technological, and industrial potential not only for fabricating photonic devices but also for implementing three-dimensional and multi-functional micro-devices in bulk transparent materials towards commercialization [75]. In this section, we present numerous examples of smart materials and devices fabricated by femtosecond laser micromachining in the volume and on the surface of the glass, illustrated in Figure 1.5.I-VIII and Figure 1.6.I-III.

The first optical waveguide [76] is based on a local modification of refractive index by femtosecond laser irradiation. Later, it has been also demonstrated in fused silica [77]. A similar method is used to fabricate Bragg grating mirrors [12]. By self-organized structures, additional capabilities, including the production of Fresnel zone plates, birefringence quarter-wave plates, and beam splitters polarizers, can be achieved [12, 78, 79]. With high temperature and stability combined with birefringence, nanogratings demonstrated potential to be used as data storage [80, 81]. Furthermore, combined with an etching step, [82], these modifications have leveled up to fabricate monolithic functional glass substrates, such as hinges, cantilevers, etc., to create new tools which were not possible by other means [40, 83–86]. Combination of direct-write modifications with the etching step, numerous miniaturized systems have been fabricated, such as lab-on-a-chip, lab-in-a-fiber, and monolithic microsystems [87–89].

By focusing the femtosecond laser on the surface, maskless nanostructuring of nearly any material offers efficient means for controlling numerous properties such as optical, mechanical, wetting, chemical, and so on. Apart from glass melting, welding, or ablation, various new types of surface self-organized structures are attractive thanks to their sub-micron periodicities [91]. For instance, one can use surface periodic patterns for tailoring optical properties such as transparent antireflective glass surfaces in the visible and infrared spectral range or wetting properties from hydrophilic to hydrophobic behavior [91–93]. Designing laser patterns can even enable liquids to run vertically uphill against gravity over an extended surface area on the glass surface [94]. Other tested features are encoding local and selective coloration of metal and semiconductor surfaces [94], modifying wear-rate in tribological application [95], etc.

1.5 Thesis purpose

This thesis aims to draw a general roadmap toward understanding ultrafast laser-matter interaction in selected complex glass systems; the role of material's properties on the generation of laser-induced modifications and self-organization. It will serve as a guideline for in-situ observations.

Towards this ambitious endeavor, this thesis explores femtosecond laser interaction with complex glass systems, namely, ULE, chalcogenide, and tellurite glass systems, which possess striking similarities and differences. Altogether, they form a representative group of materials for systematic investigation of local modifications towards how dielectrics respond to fs-

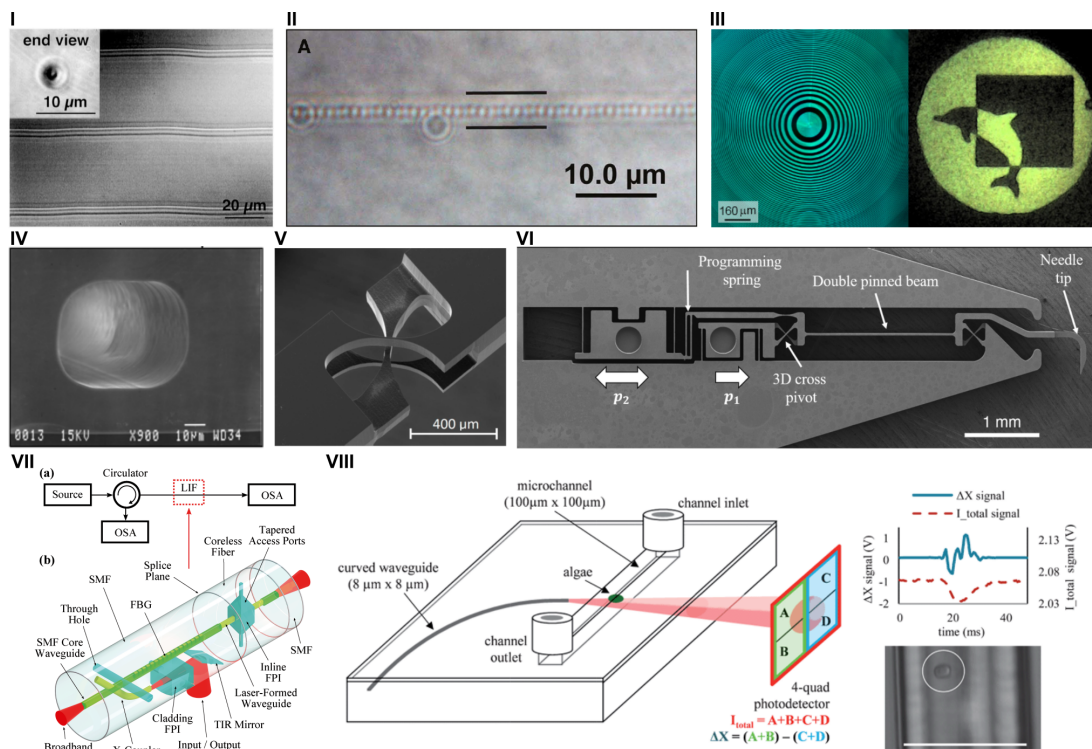


Figure 1.5: I) OM image of the top view and end face of waveguides in fused silica (taken from [77]). II) The first demonstration of a waveguide integrated with Bragg gratings (taken from [90]). III) Femtosecond laser inscribed Fresnel zone plate with the image of the logo projected onto the CCD camera with embedded Fresnel zone plate (taken from [79]). IV) SE image of micro-tunnel by selective chemical etching of femtosecond-laser modified fused silica (taken from [83]). V) SE image of a cross-spring pivot (taken from [85]). VI) The surgical tool produced by femtosecond laser combined with etching (taken from [86]). VII) A multifunctional fiber sensor design lab in a fiber (LIF) with optical waveguides and optical cavities fabricated by fs-laser (taken from [87]). VIII) The schematic representation of a glass chip with a curved waveguide directing light across a microchannel for algae detection (taken from [88]).

laser pulses. Each of the selected glass systems has intriguing properties, relevant to various technological applications. Upon laser irradiation, the flexibility of multi-component glass systems allows tuning of glass properties, including not only photosensitivity but also density, thermal and environmental stability, etc. To this end, a comparison is made with fused silica, a model material extensively studied in the field of ultrafast laser micromachining.

The objectives of this comparative study are multiple. One is to systematically investigate the influence of the field strength (by varying the pulse duration) and the energy deposited (net fluence) on the photo-induced physical and chemical modifications correlating them with numerous phenomena in complex glass matrices. A second objective is to investigate the formation of self-organized nanostructures. These observations test various hypotheses formulated to elucidate the conditions for forming nanostructures. Then, the effect of key

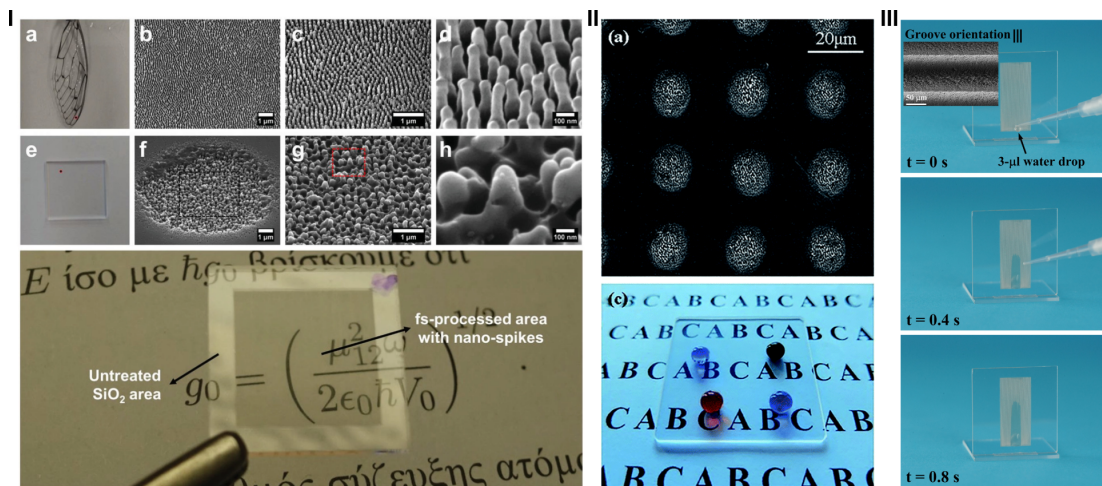


Figure 1.6: I) OM and SE images of natural Cicada Cretensis wing and the biomimetic artificial surface of the laser-processed fused silica (taken from [93]). II) SE image of the laser-processed fused silica glass surface (taken from [92]). III) Time-lapse images of water running uphill on a vertically-standing glass with SE images of microgrooves (taken from [96]).

material properties is discussed for each type of final modification. The final objective is the fabrication of novel materials and devices using optimized femtosecond laser processing parameters to tailor the material properties. This thesis work is built on existing advanced experimental methods, laser platforms, and investigation tools to focus on the detailed analysis of the post-mortem material response after laser exposure supported with a numerical simulation.

1.6 General methodology

The transfer of the optically-absorbed energy to a transparent medium is affected by several other factors, including exposure parameters, such as pulse energy, repetition rate, wavelength, polarization, writing speed, and focusing conditions, as well as material properties, such as band gap, composition, viscosity, and thermomechanical properties. Experimental details are presented in a separate section in each chapter. In brief, the experimental work in this thesis starts developing quantitative information with systematic laser processing. This allows us to optimize the parameters and draw a baseline of possible types of modifications and structures. Within the established laser systems, modulation of pulse duration, pulse energy, repetition rate, writing speed (or pulse overlapping), polarization, writing direction, and wavelength maps our possibilities and limitations. In our experiments, the beam profile (Gaussian beam) and focusing objective were kept constant.

The results are classified in morphological and chemical modifications on the surface and in the volume. While pulse energy determines the field strength, various pulse duration leads to a large range of peak power. The effect of laser pulse-to-pulse overlapping, an effective

way to determine the number of pulses per focal volume in a dynamic laser writing process, is discussed to understand the pulse-to-pulse evolution and the feedback mechanism. Additionally, the post-mortem observation is performed in two different regimes with low and high repetition rates to keep thermal accumulation separate from other ionization events. The thermal diffusion model has supported an understanding of the effect of the thermal gradient. The effect of an atmosphere and the substrate temperature is investigated in a controlled environment. The effect of glass modifiers is considered in various glass systems with an effort to generalize the modifications within their initial systems. The characterization is performed by existing techniques to correlate the laser parameters to the final optical, chemical, thermal, and structural properties. Various advanced characterization techniques are employed, such as optical microscopy, high-resolution imaging, and elemental analysis by electron microscopy, ultraviolet-visible (UV-VIS), and Raman spectroscopy. Finally, numerous post-processing methods are applied to fabricate smart materials and devices.

1.7 Thesis outline

This thesis consists of six chapters, and the rest of the thesis is subdivided as follows:

- *Chapter 2* focuses on femtosecond laser interaction with ULE glass and compares it with fused silica. Specifically, the photo-induced modifications illustrate several phenomena, such as glass decomposition, crystallization, and self-organized nanogratings in the volume and the surface.
- *Chapter 3* investigates the laser-induced modifications on the surface and in the volume of various tellurite glass, highlighting the glass decomposition and elemental crystallization phenomena. We also investigate the influence of the atmosphere and various compositions with a similar primary glass network.
- *Chapter 4* deals with laser interaction with non-oxide mid-infrared glass, which is the chalcogenide glass system with various compositions. This chapter covers photo-induced modifications, such as photo-oxidation, photo-darkening, photo-expansion, and photo-contraction, some of which are accompanied by self-organization on the surface and in the volume.
- *Chapter 5* presents the fabrication capability of smart materials and devices initially based on femtosecond laser irradiation, which is later combined with various techniques. This chapter is also a showcase of how tailoring complex glass systems by femtosecond laser method gives rise to new functionalities.
- *Chapter 6* summarizes all of the findings to draw a general understanding of the femtosecond laser interaction with complex glass systems, discuss the potential of main results, and gives a direction for further research.

2 Silicate glass system: Ultra-low expansion glass^I

^IExternal contributions: In this study, the initial laser machining parameters were chosen together with Dr. Margarita Lesik. The femtosecond laser machining for initial coarse parametric search with various pulse durations was performed by Dr. Margarita Lesik.

In this chapter, we begin with the glass structure of fused silica, the effect of the addition of TiO_2 , and the interaction of ULE glass interaction with femtosecond lasers. Specifically, we show how the fused silica is perturbed by the presence of TiO_2 , its influence on the formation of self-organized nanogratings, and various photo-induced modifications, such as photo-darkening, photo-induced glass decomposition, and crystallization.

2.1 Glass structure and properties

Silicate glass systems are one of the oldest, highly abundant, naturally occurring as well as massively produced man-made refractory glass, based on silicon dioxide, as a main glass backbone structure. A wide range of compositions are available for numerous applications in our daily life thanks to their excellent optical, thermal, and chemical properties. Their versatile technical capabilities satisfy a broad range of requirements in high technology fields, such as biocompatibility for medical, high transmission for optics and telecommunications, chemical durability and environmental stability for nanotechnology, nuclear waste disposal, and high-temperature applications [97].

Let us describe the glass network of pure silicon dioxide, commonly referred to as fused silica. SiO_2 glass consists of slightly distorted SiO_4 tetrahedra, in which Si-O has approximately 50:50 ionic and covalent bond characteristics (sigma bonds between Si sp^3 and oxygen and pi bonds between Si d orbital electrons and oxygen) [98]. Tetrahedra bridged between each other by their oxygen atoms from their corners in the glass network refer to *bridging oxygens* (BOs). Although ideally, most oxygen is connected with silicon to satisfy the charge balance, with some exceptions due to defective sites generated from impurities. These sites lead to broken bridges of oxygen, referring to *non-bridging oxygens* (NBOs). Figure 2.1.I displays the Si-O tetrahedron, local coordination sphere (within the first 2.5 Å), or short-range order of the fused silica. The inter-tetrahedral angle between silicon atoms connected with bridging oxygen (Si-O-Si) is called the bond angle, and azimuth oxygen-silicon angles within the tetrahedron are called torsion angles [99], as demonstrated in Figure 2.1.II. With the bond length, they determine their intermediate-range order (2.5-5 Å) of the glass network. Additionally, they define the medium range order (MRO), i.e., how tetrahedrons are interconnected in a 3D glass network. Finally, Figure 2.1.III illustrates the fused silica glass network projected in a 2D plane. Corner-sharing tetrahedra form polygon ring with 2- to 8-fold members [100]. The number of ring members determines the various physical properties.

On an atomic scale, there are various defects intrinsically in fused silica. For example, E' centers consist of *silicon with three oxygens* with an unpaired electron in a dangling tetrahedral (sp^3). *Non-bridging oxygen hole center* (NBOHC) represent the missing bond of one of the 2p orbital electron of the oxygen in the Si-O tetrahedron. In contrast, *the oxygen deficiency center* (ODC) refers to the missing oxygen bond in the Si-O-Si bridge. While E' center and NBOHC are paramagnetic and the latter is diamagnetic, they have been subjected to investigation by numerous methods, such as electron paramagnetic resonance (EPR), photoluminescence (PL),

and cathodoluminescence (CL) spectroscopy [101–104]. Many of these defects are generated during the glass formation from the supercooled liquid as well as by various irradiation, such as γ -ray or fs-laser [44, 104].

Considering that silicon dioxide is the basis of naturally occurring silicate glass, fused silica can form glass during the standard melting and quenching method. According to its TTT diagram, the critical cooling rate for homogeneous crystallization is around $9 \cdot 10^{-6}$ K/s, slightly faster for heterogeneous crystallization ($\sim 10^{-1}$ – 10^{-5} K/s) [99]. However, due to the high cost of manufacturing fused silica, it is often preferred in high-technology applications. For other commercial applications, silicate glasses with additives such as soda-lime silicate (SiO_2 , CaO , Na_2O and Al_2O_3), borosilicate (SiO_2 , B_2O_3 , and alkali oxides), lead silicate (SiO_2 , PbO and other oxides), and aluminosilicate (Al_2O_3 , SiO_2 , with other alkali and alkaline oxides) are preferred, thanks to easy and low-cost process [99].

The most common metal oxide additives of technical silicate glass are alumina (aluminum oxide, Al_2O_3) or titania (titanium dioxide, TiO_2). The addition of TiO_2 has been practiced since the 1960s, and around that time, the binary glass of SiO_2 with TiO_2 was developed [105]. Starting with exploring various compositions, later it has been found out that SiO_2 with around 5–10 wt% TiO_2 exhibits near zero thermal expansion coefficient (0 ± 30 ppb/K from 278 to 308 K compared to fused silica ~ 500 ppb/K [105]) at room temperature [106]. Other notable examples of glass, glass-ceramics, and ceramic exhibiting low thermal expansion coefficients are Vycor® (from Corning), Zerodur® (from Schott), and SiC, respectively [107].

The glass structure of SiO_2 with ~ 1 –10 wt% TiO_2 which has been studied by various methods such as XANES and EXAFS, XPS, Raman, NMR [108–111] consists of 4-fold coordination of Ti^{4+} ions, substituting the Si ions in the tetrahedra and Si-O-Ti bridges, which has lower bond energies compared to Si-O-Si bridges in addition to the fused silica glass network [109, 112]. The glass network changes to a higher bond angle ($\sim 159^\circ$) to accommodate Ti substitution, further causing a more open glass structure and lower density [109]. In addition to Ti ions in four-fold coordination, a small number of Ti ions in six-fold coordination increases further with the addition of TiO_2 [109], as shown in Figure 2.1.IV-V.

TiO_2 is one of the glass intermediates, acting as a glass network former and modifier. While substituting Si ions with Ti in fused silica in general results decrease in the mechanical properties of fused silica, coordination of Ti with NBO in some silicate glass systems actually increases the overall mechanical properties [114, 115]. Although TiO_2 causes more open glass structure, high crystallization temperature ($T > 1573$ K) is maintained thanks to a fully polymerized glass network (connection of NBO with Ti). Depending on the titanium dioxide content, binary TiO_2 - SiO_2 glass exhibits superior optical, electrical, thermal, and chemical properties. The addition of TiO_2 up to 10 wt%, increases the refractive index, while the density stays stable since increases in the free volume compensate for the higher density of TiO_2 ($\rho_{\text{anatase}} = 3.9$ g/cm³). Increasing the TiO_2 content more than ~ 15 wt% (production process-dependent value) results in phase separation of the glass and the formation of anatase or rutile crystals

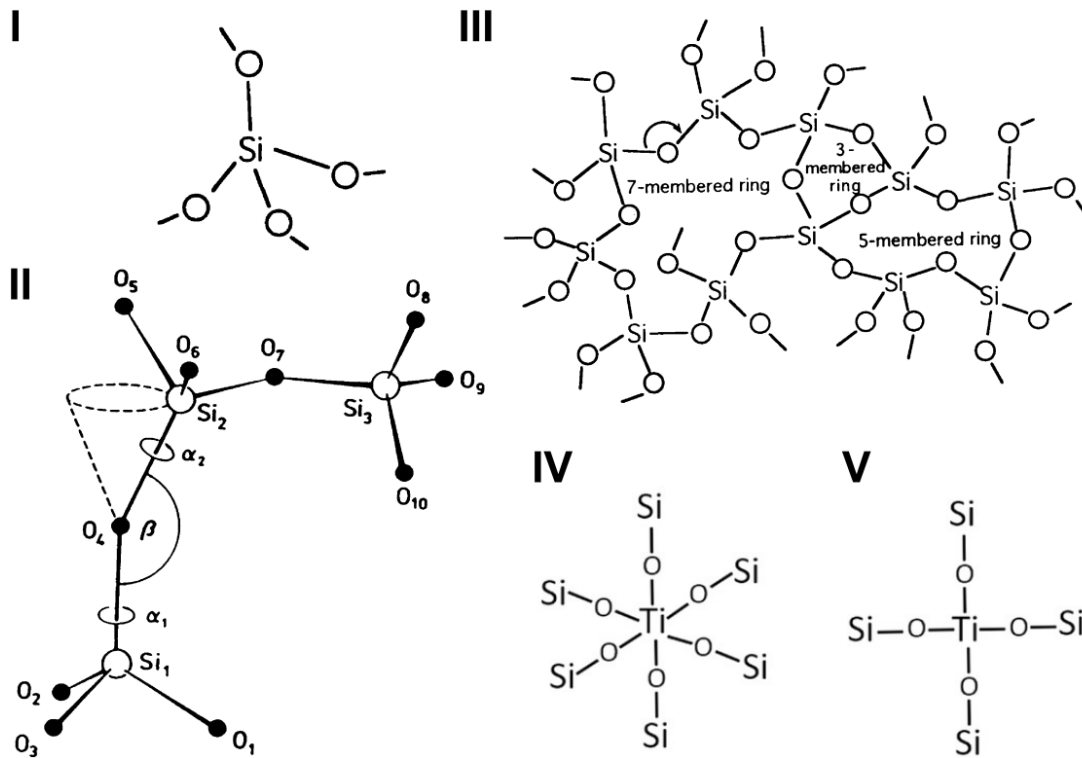


Figure 2.1: Illustrative glass network images of fused silica: I) The basic structural unit of SiO_4 tetrahedron, II) MRO with the bond angle of β ($\sim 120\text{-}180^\circ$) and torsion angles of α_{1-2} . III) Schematics of fused silica glass network (taken from [99]) projected in 2D. Structural units of TiO_2 in silica: IV) octahedral-coordinated Ti and V) tetrahedral-coordinated (taken from [113]).

with continuous Si-O-Si glass network around [109, 112].

Thanks to its near-zero thermal expansion coefficient combined with lightweight, rigidity, polishability, and excellent thermomechanical and chemical properties as fused silica, ULE® glass has been practiced as glass blanks, optics, masks, and mirrors in the ground- and space-based astronomical telescopes, space satellites, astronomical instruments, and among others [107, 116, 117].

2.2 Femtosecond laser and ULE®Glass interaction

As discussed in the first chapter, numerous femtosecond laser-induced modifications in fused silica have been documented. Here, we cover the known facts on how TiO_2 disturbs the silica-based glass network and prompts numerous permanent photo-induced structural and chemical modifications locally upon femtosecond laser irradiation.

TiO_2 , known as a photo-sensitive compound, undergoes photo-induced chemical modifications under laser irradiation. For instance, photo-darkening can lead to colorization without

damage in an elastomer containing fine TiO_2 particles [118]. Since TiO_2 has a large band gap (3-3.2 eV [119]), it acts as a photocatalyst, giving rise to the decomposition of the media and acting as a crystal nucleation site [120–122]. In addition, its high refractive index (2.5-2.7 [118]) is attractive for nonlinear optics and photonics applications.

TiO_2 containing multi-component glass systems also presents crystallization by electromagnetic irradiation [122]. Specifically, femtosecond laser irradiation can lead to the formation of crystalline phases of TiO_2 such as rutile in $\text{CaO-Al}_2\text{O}_3\text{-Bi}_2\text{O}_3\text{-TiO}_2\text{-B}_2\text{O}_3$ (aluminoborate glass) [123], but also more complex oxides, such as the formation of $\text{Ba}_2\text{TiSi}_2\text{O}_8$ in $\text{BaO-TiO}_2\text{-SiO}_2$, or $\text{Sr}_2\text{TiSi}_2\text{O}_8$ in a stoichiometric $\text{SrO-TiO}_2\text{-SiO}_2$ glass accompanied with the reduction of Ti^{4+} to Ti^{3+} [124, 125]. These direct-write crystals open up new possibilities of tailored properties and multi-functionalities.

There are only a handful of studies on the interaction of ULE glass with femtosecond laser interaction, such as the formation of self-organized nanogratings and their erasure mechanism, photodarkening, and local structural transformations [52, 54, 126–129], illustrated in Figure 2.2. Led by Richter *et al.* [52] in 2013, the nanogratings perpendicular to the laser electric field with a nanoplane periodicity of 250 nm and much smaller internanoplane periodicity are presented in Figure 2.2.I. The retardation of the birefringent nanostructures (due to the density modulation in refractive index change) is independent of pulse duration (from 40 fs to 400 fs) at fixed laser parameters, and the value is comparable with fused silica at pulse duration above 150 fs. Further study has explored the quantitative evolution of pores within the nanoplanes by SAXS (Figure 2.2.II) and its relationship with the birefringence [54, 126]. Raman spectroscopy results are indicated the presence of molecular oxygen in the nanopores (around 30 nm [126]).

The transition between modifications from nanograting to melting region upon microexplosion in thermal cumulative regime is previously reported by irradiating samples with 450 fs pulses at 515 nm [126]. At this regime, the laser-affected zone consists of a molten glass network centered by a hollow cavity containing molecular oxygen surrounded by a densified dark shell with reduced Ti^{4+} , Ti^{3+} . Well-detailed Raman spectroscopy analysis has highlighted that the molecular oxygen is surrounded by Ti^{3+} octahedral sites in the Ti_2O_3 -type cluster shell. At the same time, the shell is also surrounded by resolidified Ti^{3+} tetrahedral sites by irradiation with a femtosecond laser emitting at 515 nm in thermal cumulative regime (9.4 MHz) [127]. In addition, unlike silica, the photo-darkening of the laser-affected zone, covering almost the entire fs-laser processing windows reported previously [126], is demonstrated in Figure 2.2.III.

Furthermore, the thermal stability of nanogratings has been subjected to extensive research along with ones in ULE glass [128, 129]. The retardance measurement of the birefringence after the accelerated aging by classical heat treatment is correlated with the presence or the erasure of the nanogratings. Figure 2.2.IV highlights the retardance of the nanostructures over a temperature range [129]. The initial decay is associated with the point defects, and a further

increase in the temperature annihilates the stress-induced birefringence and nanotexture. Finally, at 1298 K, nanogratings in ULE glass are erased, leading to zero retardance. Yet to the best of our knowledge, no comprehensive and systematized study over a large parameter window has been reported on the photo-induced structural and chemical modifications of ULE glass generated by femtosecond laser exposure.

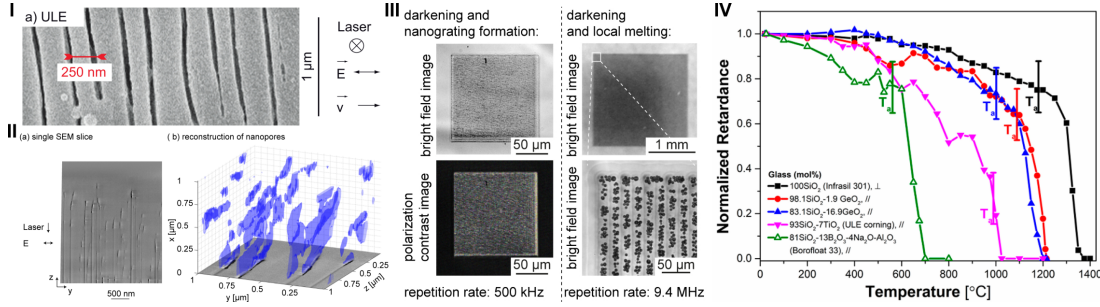


Figure 2.2: I) SE image of nanogratings in ULE with 200 nJ, 800 pulses, and at 120 fs with 800 nm, taken from [52]). II) SE image of the nanopores in ULE shown in the y - z plane, and 3D reconstruction of SE images of nanogratings (2000 pulses per spot at a pulse energy of 150 nJ) prepared by FIB milling (taken from [126]). III) OM images of different laser-induced modifications in ULE (taken from [126]). IV) Normalized retardance as a function of annealing temperature of various silicate and ULE glass systems (taken from [129]).

In this chapter, we first briefly report morphological and structural modifications in the ULE glass by various writing in non-cumulative and thermal-cumulative regimes. Further, we extend our systematic research on volume modifications, especially the formation of self-organized nanogratings and various photo-induced phenomena such as photo-darkening, photo-decomposition, and crystallization. Our methodology is exposing the glass to ultrafast laser pulses of varying intensity and peak power by altering pulse duration, pulse energy, repetition rate, and writing speed in a wide range. In addition, the non-cumulative and cumulative regimes are demonstrated both experimentally and numerically. Finally, the results are correlated and compared with well-studied fused silica with an effort to draw a general modification map for ULE glass.

2.3 Experimental procedure

Commercial Corning ULE®Glass (7972), consisting of SiO₂ with 7.4 wt% TiO₂ was used to study in this chapter. The physical properties of the glass properties are presented in Table 2.1 [106, 107].

2.3.1 Femtosecond laser irradiation

Four different femtosecond laser systems were used, emitting pulses of different durations: 50 fs pulses at 850 nm (Yb-doped fiber, Satsuma with an OPA from Amplitude), 150 fs pulses at

Table 2.1: The physical properties of ULE®Glass [106, 107]. The table displays the sample name, density, refractive index at 656 nm, the softening temperature, heat capacity, Young's modulus, thermal conductivity, and coefficient of thermal expansion (CTE).

Sample	ρ (g/cm ³)	n	T _s (K)	C _p (J/kg·K)	E (GPa)	K (W/m·K)	α (ppb/K)
ULE 7972	2.21	1.4801	1763	767	67.6	1.31	0 ± 30

1030 nm (Regen amplifier, S-pulse from Amplitude), 270 fs pulses also at 1030 nm (Yb-doped femtosecond fiber laser, Yuzu from Amplitude), and finally, 500 fs pulses at 1030 nm (Yuja from Amplitude). 100 fs pulses were obtained by negatively chirping the pulse in the compressor, which is the maximum pulse duration in the OPA laser configuration.

Laser patterns were inscribed on the surface and in the volume (with a depth of 100 μm) of the ULE glass as parallel lines with a length of 10 mm. Square patterns (1x1 mm²) consisting of several lines with a spacing of 2 μm were written inside the glass to study optical properties. The specimen was translated under the laser focus with the help of a high-precision motorized stage (Ultra-HR from PI Micos). The laser beam was focused on the surface of the specimen with a 0.4 numerical aperture (NA) objective (OFR-20x-1064 nm from Thorlabs), resulting in a spot-size (defined at $1/e^2$) of 1.94 μm (see Appendix A for the laser spot size measurement). The transition from a non-cumulative to a cumulative thermal regime exposure regime was determined by observing the evolution of the width of the laser-affected zone with the pulse repetition frequencies for the same net fluence at static exposure conditions. A wide range of pulse repetition rates (1 kHz-1 MHz) was employed at 270 fs. The transition from a non-cumulative to a thermal-cumulative regime was found at around 500 kHz. The repetition rate of 1 MHz is within the cumulative regime for the glass. For comparative experiments, repetition rates of 100, 250, 333, 500 kHz, and 1 MHz were used. Here, pulse-to-pulse overlapping ratios were varying from 0 to 99.9%, and the pulse energy was ranging from 50 nJ to 1700 nJ, as measured after focusing with the objective lens (see Appendix A for details of the calculation of net fluence). Furthermore, tracks were inscribed using opposite directions of laser beam movement along a single writing axis and under three different linear polarization states (and therefore, the orientation of the electrical field E) defined as parallel, at 45°, and perpendicular to the writing direction, respectively.

2.3.2 Specimen characterization

After laser exposure, specimens were observed using an optical microscope (BX51 from Olympus) and a digital optical microscope (KH-8700 from Hirox), and subsequently, the cross-polarizer optical images were obtained using a polarized light microscope (Olympus BX51). A Raman spectrometer (LabRam HR from Horiba), equipped with a 532 nm laser excitation source attenuated down to 4 mW was used to record Raman spectra. A series of line scans were performed from 10 μm outside the laser-affected zone towards the center of the modification with a period of 1 μm , and with acquisition times of 30 s for an individual spot. The transmission and absorption spectra were measured for wavelengths ranging from 250 to

2500 nm using an ultraviolet-visible-near-infrared spectrometer (UV-VIS-NIR, Lambda 950 from Perkin Elmer). A mask with a hole of around $2 \times 2 \text{ mm}^2$ is prepared from black paper for broadband absorbance. For the measurement, the reference beam power was attenuated to 10%, to compensate for the presence of the mask and the ensuing effective drastic reduction of the beam size from the original 2 cm in diameter. The thickness of the sample used for this transmission measurement was 1 mm.

Specimens having volume modifications were polished to reveal the structures and etched with HF (2.5 %) for less than 300 seconds at room temperature. For high-resolution imaging and elemental analysis, a thin film of carbon was sputtered (C-sputtering from JEOL) on specimens using a field-emission scanning electron microscope equipped with energy-dispersive X-ray spectroscopy (EDS in FE-SEM, Gemini 2 from Zeiss, operated at 5 kV for imaging and 20 kV for elemental analysis). Transmission electron microscope (TEM, Talos F200S from ThermoFisher) images were obtained operating at 200 kV. TEM lamellae (thickness of about 100 nm) were prepared by a focus ion beam (FIB, NVision 40 dual-beam from Zeiss) at 5kV and 30 kV. Fast-Fourier transform (FFT) and selective area diffraction (SAED) patterns were fitted with electron diffraction simulation of GenOVa [130].

2.4 Results and discussion

2.4.1 Regimes of femtosecond laser-induced modifications

First, we provide a general purview of the selected parametric window and the observed photo-induced modifications in ULE glass. Specifically, we discuss the effect of various laser processing parameters on the laser-induced modifications step-by-step, such as pulse duration, fluence, polarization, and repetition rate.

In Figure 2.3, we examine the morphological modifications in the volume using different pulse durations in a non-cumulative regime. A lower repetition rate is beneficial not only for investigating a non-cumulative regime but also for having a high level of control pulse overlapping in dynamic writing conditions. Figure 2.3.a displays the studied laser parameter window for pulse durations ranging from 50 to 500 fs. Transmission OM images of laser-affected cross-sections are presented in Figure 2.3.b. Over an extremely large studied parametric window, four different modifications are determined in ULE glass. With low pulse energy (90 nJ) at 50 fs, homogeneous modifications associated with densification in fused silica are observed. Although this type of modification in fused silica is relatively easy to visualize [15, 131], it is challenging to point out in ULE glass. Thanks to high peak power at 50 fs, the threshold for this modification is obtained at low fluence ($\sim 14 \text{ J/mm}^2$). Once the pulse duration is around 150 fs and above, the threshold of homogeneous modifications rises gradually. However, further increments in the pulse duration cause a drop in their parametric range. The structural changes based on the homogeneous modification are given in the next section.

Additional laser fluence opens up other possibilities, such as the formation of self-organized

nanogratings, as in Figure 2.3.c. The nanograting regime is found between 150 and 500 fs pulse durations and over a larger exposure dose window. These morphologies consist of periodic nanoplanes perpendicular to the laser polarization. The determination and visualization are easier thanks to their birefringences, as in fused silica, due to anisotropic refractive index change [34, 37]. Here, self-organized nanogratings are visualized by relying on their etching selectivity. After flash etching (less than 300 seconds), each nanoplanes are revealed by electron microscopy. Other methods, such as optical microscopy with a cross-polarizer, can help to identify these anisotropic birefringent structures. In Figure 2.3.b, these structures appear much darker than homogeneous modifications. In addition to the light scattering, there is also known phenomena of photo-induced darkening, observed previously in ULE glass [126]. This phenomenon, associated with the valence state change of Ti ions, is covered in a separate section, and the influence of the laser processing parameters on the degree of darkening is quantitatively defined.

The threshold for nanogratings is inversely proportional to the pulse duration. For 150 fs, the threshold is 37 J/mm^2 , while the threshold of nanogratings for 500 fs pulses is 31 J/mm^2 for 500 pulses at 100 kHz. Although nanogratings are present at a certain parametric range, increasing pulse fluence, specifically by pulse energy, causes disrupted nanogratings. While in fused silica [17], the threshold for disrupted nanogratings depends on pulse duration, there is little or no dependence on pulse duration for ULE glass. This type of modifications have not been explored yet because self-focusing phenomenon, leading to unhomogeneous modification in the laser-affected zone. It starts to predominate the irradiation process with increase in pulse energy [126]. Characteristic features and associated chemical modifications of the nanogratings are reported in the next section.

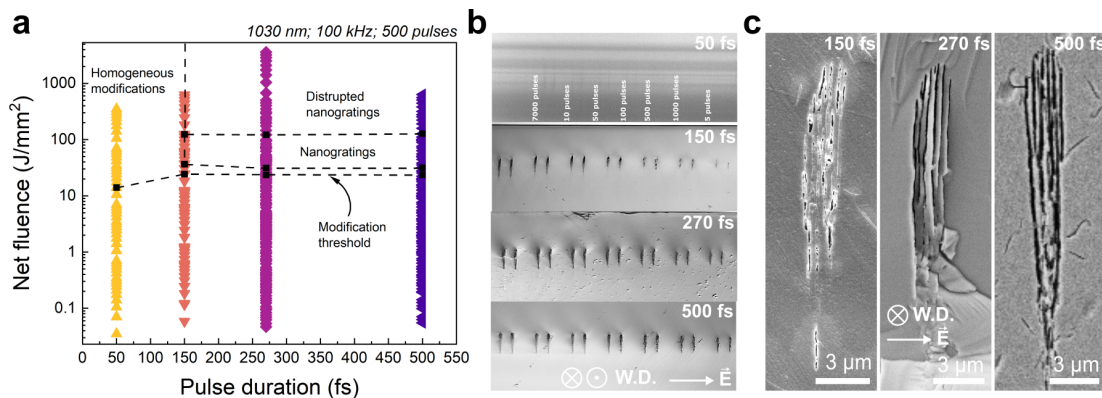


Figure 2.3: a) Laser processing map of ULE glass: Net fluence versus pulse duration. The observed photo-induced modifications are indicated in the graph. b) Transmission OM images of the cross-section prior to the flash etching. The laser parameters are 445, 469, 444, and 484 nJ at 50, 150, 270, and 500 fs, respectively. c) SE images of the laser-affected zone after inscribing with a pulse energy of 231, 288, and 320 nJ at 150, 270, and 500 fs, respectively. The repetition rate is fixed at 100 kHz.

For the fixed pulse duration of 270 fs, Figure 2.4.a displays the effect of repetition rate varied

from 100 kHz to 1 MHz range for a pulse energy range of 50 nJ to 1.5 μJ . In addition to three different modifications reported in Figure 2.3, higher repetition rate causes the transition of nanogratings into more disorganized, or chaotic, structures made of an air-bubble network trapped in the molten glass volume in a thermal-cumulative regime. SE images of the laser-affected cross-section at 500 kHz are displayed in Figure 2.4.b since all of the modifications in the selected parametric window can be observed at this rate by simply varying the pulse energy. At the onset of the cumulative regime, i.e., pulses arriving shorter than the lattice cooling time, micro-voids at the center of the modifications are achieved at 500 kHz. Above this rate, the threshold for bubble patterns decreases up to 47 J/mm^2 for 500 pulses at 1 MHz.

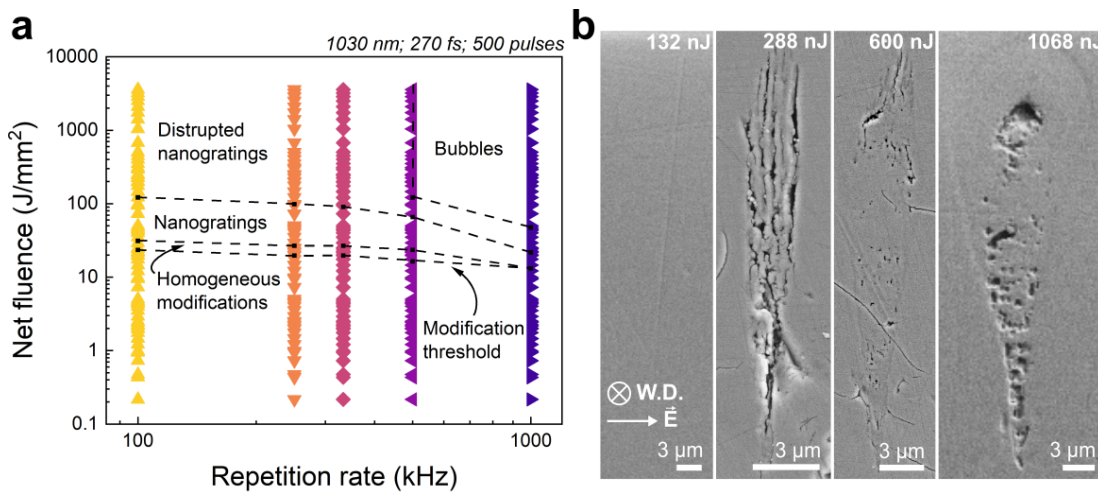


Figure 2.4: a) Laser processing map of ULE glass: Net fluence versus pulse duration. The observed photo-induced modifications are indicated in the graph. b) SE images of the laser-affected zone after inscribing with 270 fs-laser pulses at 500 kHz, displaying the cross-section of all four modifications after inscribing with 132, 288, 600, and 1068 nJ, respectively.

2.4.2 Self-organization and laser induced-modifications in the volume

Homogeneous modifications

The homogeneous regime is typically associated with low pulse duration (<150 fs). Figure 2.5 display the Raman spectra and the relative change of bands related to TiO_2 in the laser-induced modification of ULE glass. As the glass is composed of ~ 92.6 wt% of SiO_2 , there are characteristic bands of fused silica [108, 126, 132]. The bands located at 400, 484, 600, and 800 cm^{-1} are assigned to symmetric stretching of 5- to 8-membered rings of SiO_4 tetrahedra, 4-membered silicate rings, 3-membered silicate rings, bending modes of Si-O-Si bridges, and 1060 and 1200 cm^{-1} are assigned to asymmetric bond stretching of Si-O-Si bridges, respectively. With the addition of 7.4 wt% TiO_2 , peaks located at 685, 937, and 1107 cm^{-1} appear in the Raman spectra. These bands are assigned to the symmetric stretching of TiO_6 octahedra, and asymmetric and symmetric stretching of TiO_4 tetrahedra, respectively. The Raman spectra of the pristine glass and the peak deconvolution are presented in Appendix B.

Starting with short pulse irradiation (50 fs), systematic structural analysis is performed via Raman spectroscopy. Figure 2.5.a presents the Raman spectra across the laser-affected zone. Figure 2.5.b compares Raman spectra of the pristine glass and the center of the laser-affected zone indicated in Figure 2.5.a. Bands related to SiO₂, such as D₂ peak at around 600 cm⁻¹, shows a slight increase in the intensity which is related to densification in fused silica [15]. The densification by the increase in the number of 3- and 4-membered rings is due to a decrease in Si-O bond angle, thus a more compact glass network and a higher density. There is no shift in the main band at around 430 cm⁻¹, pointing out little or no significant rearrangement in the silicate network. However, upon laser irradiation, the primary modification is observed in TiO₂-related bands. The relative change in the Ti-sites is shown in Figure 2.5.c, based on the difference in the ratio of $I_{685}/I_{937+I_{1107}}$. Bond cleavage results in the valence state change from Ti⁴⁺ to Ti³⁺. In this case, the laser dose is proportionally changing Ti-sites and Si-sites, resulting in a densely-packed glass network. Longer pulse durations (>100 fs), however, cause significant structural disruption in the glass backbone structure.

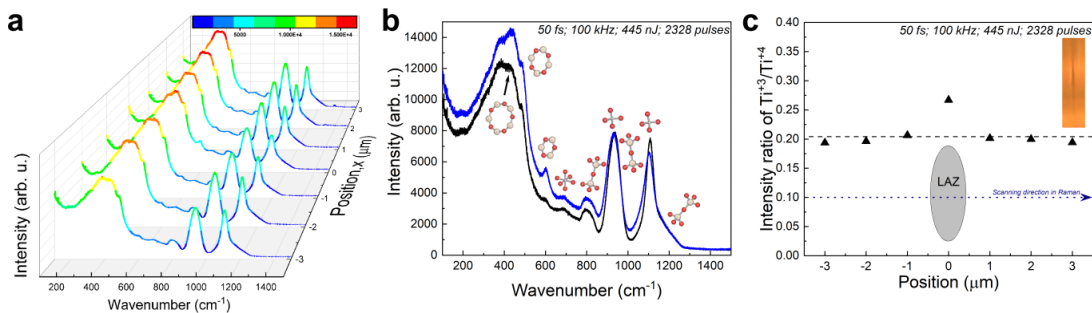


Figure 2.5: a) Raman spectra of the laser-affected zone in ULE glass. The laser irradiation parameters are 50 fs at 100 kHz with 445 nJ and 2328 pulses. b) The Raman spectra of pristine (black) versus the center of the modifications in (blue). c) The graph presenting relative $I_{685}/I_{937+I_{1107}}$ ratio along the laser-affected zone from $-3 \mu\text{m}$ to $+3 \mu\text{m}$.

Self-organized nanogratings

Above a certain threshold indicated in Figure 2.3 and Figure 2.4, self-organized nanostructures, so-called nanogratings, consisting of nanoplanes perpendicular to the laser polarization are generated in ULE glass volume. We reveal the nanograting regime between 150 and 500 fs and over a large exposure dose window.

Figure 2.6.a shows the periodicity of the nanoplanes as a function of pulses and pulse duration. Interestingly, higher pulse duration exhibits higher periodicity, and the same trend persists with an increase in the number of pulses. Likewise, periodicity with 150 fs-laser pulses has the lowest value among all pulse durations, indicating a certain relationship between the pulse duration and the initiation of nanogratings. As an example, we present SE images of structural evolution for 150 fs pulses in Figure 2.6.b. The characteristic features of the nanogratings are their periodic nanoplanes, whose periodicity decreases with the number

of pulses for each pulse duration. The formation of initial nanoplanes with a distinguishable periodicity requires multi-pulse exposure (at least 23 pulses per spot for 150 fs). Almost an order of magnitude more pulses are required to obtain uniform periodic nanoplanes. The average periodicity of initial nanoplanes is 277 nm for 150 fs, diminishing up to 196 nm with 2328 pulses. A similar observation of uniform nanogratings upon multi-pulse fs-laser exposure is also reported in fused silica [44].

Another characteristic feature of nanogratings is the polarization-dependent orientation, highlighted in Figure 2.6.b. In ULE glass, the nanogratings are oriented perpendicular to the laser polarization. While polarization is parallel to the writing direction, the cross-section of nanoplanes appears, as in the last SE image. This angle of view allows us to distinguish the nanoporous nature of nanoplanes.

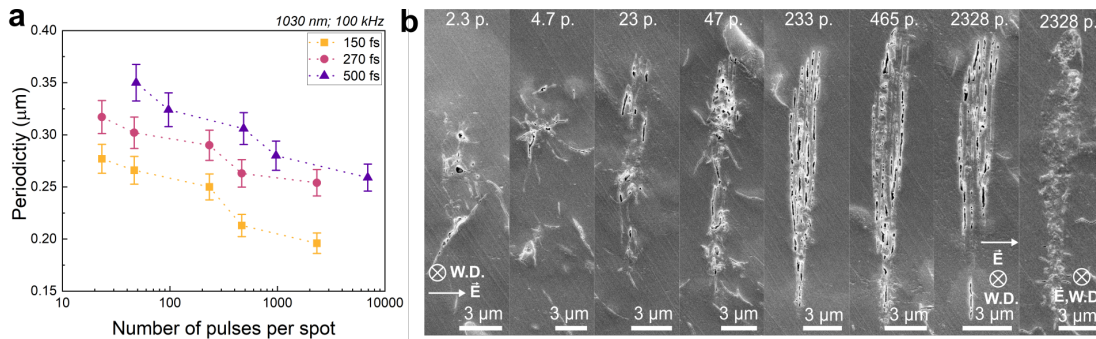


Figure 2.6: a) The periodicity versus the number of pulses per spot for three different pulse durations at 100 kHz. b) SE images of the laser-affected cross-section at 231 nJ for 150 fs pulses with 100 kHz.

Let us explore the photo-induced chemical modification associated with the nanogratings with the disrupted region in ULE glass. Figure 2.7 displays SE images of nanogratings, disrupted nanogratings at high pulse energy, and their elemental analysis. Typical nanogratings at 250 kHz with 270 fs-laser pulses are shown in Figure 2.7.a.

Once a certain pulse energy is surpassed, the degradation of nanogratings with the formation of nanopores is observed. An additional pulse energy results in elongated structures with a disruption in their periodicity. The final structures as a function of number pulses are presented in Figure 2.7.b. Although these modifications are obtained in a non-cumulative regime, each subsequent pulse rises the local temperature and pressure to extreme limits so that nanogratings can no longer be sustained at 1528 nJ. Likewise, the threshold for this regime decreases with the repetition rate.

The field strength has a direct influence on the ion migration process in the focal volume. The results in Figure 2.7.c is obtained on the nanoplanes while elemental results in Figure 2.7.d is collected from the top part of the modification at 1528 nJ. In the nanograting regime, Si and O exhibit strong dependency on the number of pulses, however, the composition of Ti ions fluctuates within ± 2 wt%. These results are predictable since nanoplanes in fused silica are

rich in oxygen, and periodic structures alternate between oxygen-deficient and oxygen-rich regions [33]. Here, we observe that the oxygen content of the nanoplanes is promoted by the number of pulses. In the disrupted region, in contrast, the oxygen content decays, and only after 500 pulses, the oxygen content at the center of the modification starts to increase. While Si also presents the opposite trend of O, Ti is proportional to the number of pulses, increasing rather exponentially with the number of pulses. In titania-silicate glass systems, TiO_2 content more than ~ 15 wt% leads to phase separation of the glass and the formation of TiO_2 crystal precipitates within the continuous Si-O-Si glass network [109, 112]. Further investigation on glass structure is performed by Raman spectroscopy, and the results are highlighted for both nanogratings and disrupted regimes in Figure 2.8.

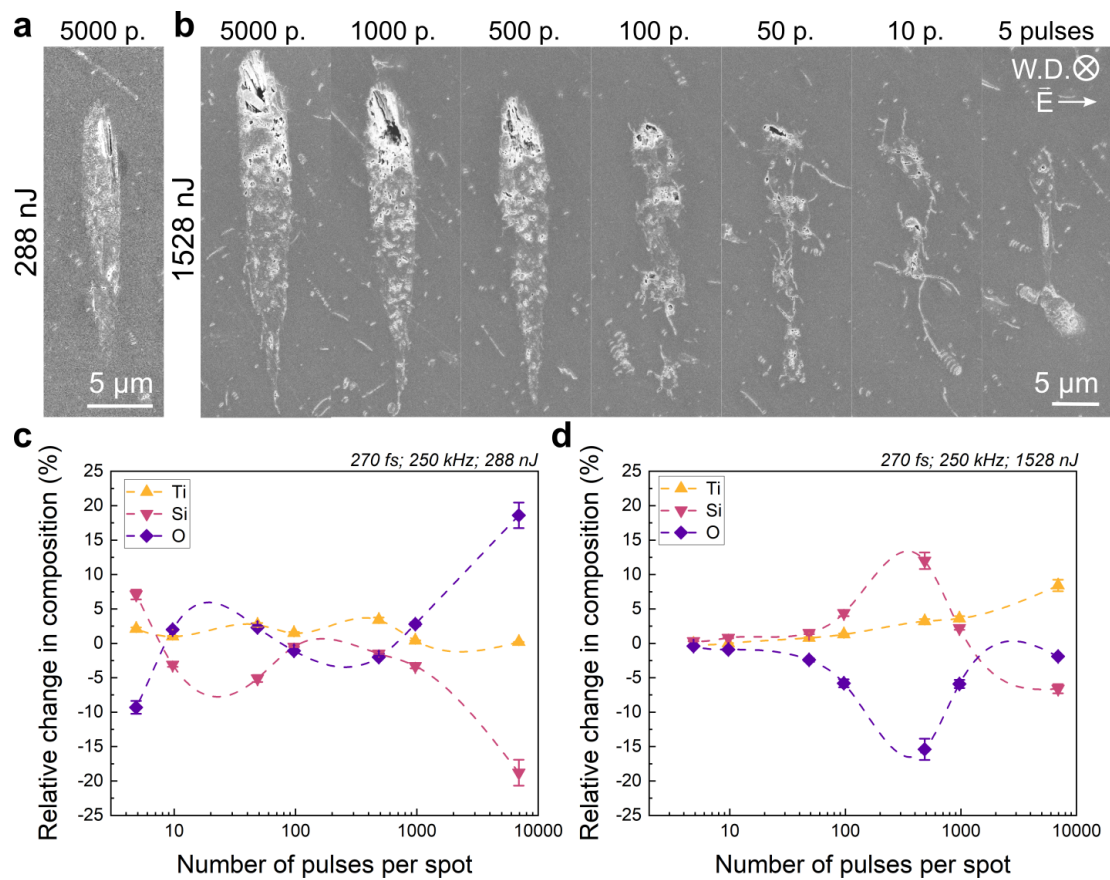


Figure 2.7: SE image of a) nanogratings inscribed at 288 nJ and b) disrupted nanogratings at 1528 nJ with 270 fs-laser pulses at a repetition rate of 250 kHz. The elemental analysis of c) nanoplanes in nanogratings at 288 nJ and d) the top region of the disrupted nanogratings at 1528 nJ as a function of the number of pulses.

Figure 2.8 displays OM images and corresponding Raman spectra with the relative intensity ratio of the main bands at the laser-affected zone both in nanograting and disrupted regimes. Figure 2.8.b-c presents the Raman spectra and the relative intensity of the main bands collected along the dashed line indicated in Figure 2.8.a. At the nanograting regime, a transformation of

the D_2 peak at 600 cm^{-1} is observed towards the center. As in homogeneous modifications, this peak is related to the Si-O bond angle, which determines the compactness of the glass network. The intensity of D_1 and D_2 peaks alternates along the cross-section of the laser-affected zone at 288 nJ. At the center of the modification ($x = 4\text{ }\mu\text{m}$), their intensities rise simultaneously along with a blue shift of the main band from 400 to 430 cm^{-1} . The blue shift indicates the tendency towards glass crystallization. These modifications are followed by the progressive transformation of Ti^{4+} to Ti^{3+} and the generation of molecular oxygen at 1554 cm^{-1} at 288 nJ.

In the disrupted regime displayed in Figure 2.8, numerous new features are detected. First, the laser-affected zone at 1528 nJ is much larger than the one inscribed at 288 nJ, possessing a shell-like region at the center surrounded with some light scattering features, as in Figure 2.8.d. In Figure 2.8.e, Raman spectra scanned across the laser-affected zone display new low wavenumber bands. Starting with the formation of new peaks at 153 and 253 cm^{-1} , the shift of the main band, and the formation of molecular oxygen appear in the laser-affected zone. The new peaks are associated with $\beta\text{-TiO}_2$, commonly known as anatase, one of the metastable polymorph of TiO_2 [112, 133, 134]. The detailed analysis in Figure 2.8.e emphasizes the progressive transformation of Ti^{4+} to Ti^{3+} and sharp decay of the Ti-related bands in the glass network as a result of crystallization.

The Raman spectra agree with the elemental analysis. Note that while EDS results accurately display the composition of nanoplanes, Raman spectra present the entire structure within the focal area of the Raman laser ($\sim 1\text{ }\mu\text{m}^2$). In the nanograting regime, a decrease in Ti-related bands and the formation of molecular oxygen indicate the onset of the decomposition process at the center of the modifications although the pulse energy is not high enough to promote Ti ion migration. While Si-O-Ti bonds are progressively broken leading to disassociated Ti and O, an increase of 3- and 4-membered silica rings points out the rearrangement of the glass network and the presence of a possible densified zone.

At low pulse energy, the photo-induced reduction upon fs-laser irradiation leads to the transformation of Ti^{4+} tetrahedral sites to Ti^{3+} octahedral sites and the formation of Ti_2O_3 -type clusters, similar to the previous observation [127]. Once high temperature and pressure are generated by high field strength, the creation of Ti^{3+} octahedral sites through glass decomposition promotes the long-range order as in TiO_2 crystals [135]. The ratio of octahedral Ti-sites and tetrahedral Ti-sites, $I_{685}/I_{937+I_{1107}}$, at the center of modifications are 0.087 and 0.47 for 288 nJ and 1528 nJ, respectively. In addition, elemental analysis at 1528 nJ indicates that the composition of Ti can increase up to 10 wt% at the center of the laser-affected zone. These results indicate the support of high field strength on the Ti ion migration towards the center. In glass melting of ULE, more than 15 wt% of TiO_2 results in crystalline segregation as a secondary phase [109, 112]. In short, the crystallization of the TiO_2 phase locally is promoted by the dissociation of Ti-sites tetrahedral sites into octahedral sites and Ti ion migration towards the laser-affected zone simultaneously.

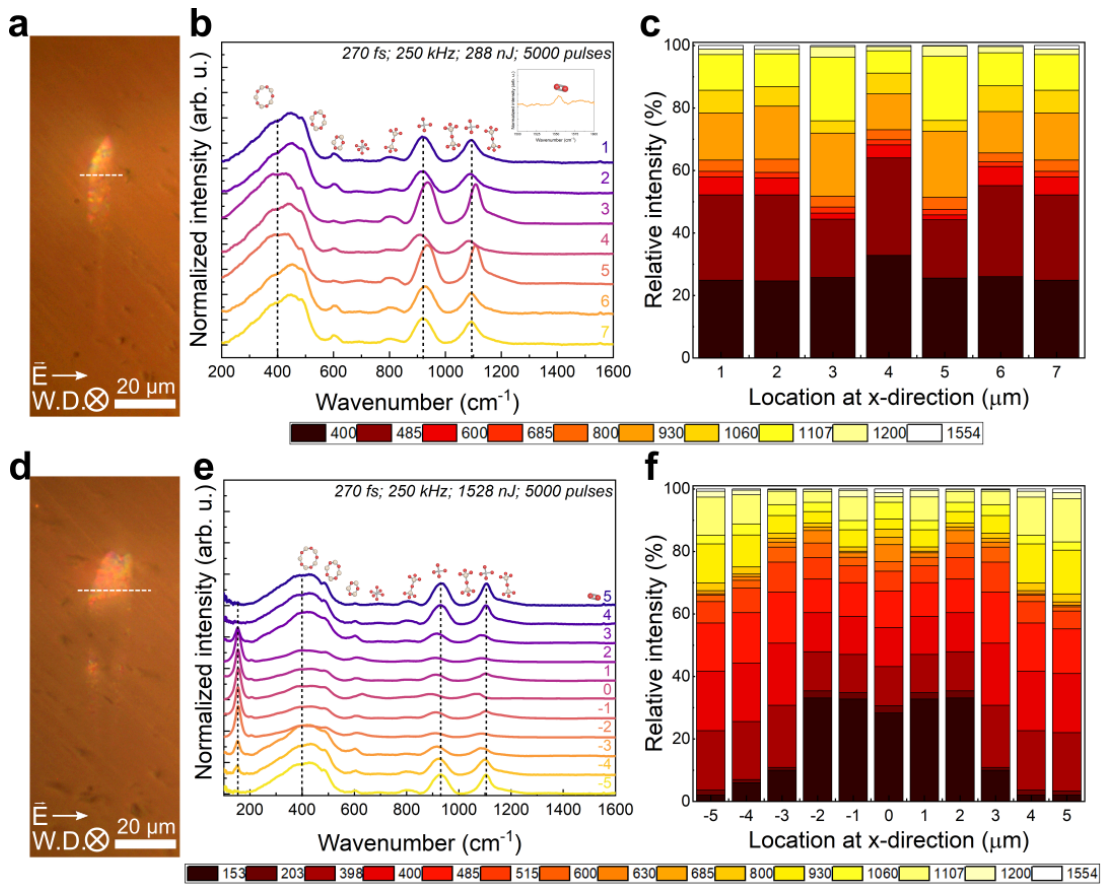


Figure 2.8: a) OM images of the laser-affected cross-section and b) corresponding Raman spectra scanned across the laser-affected zone at 288 nJ with 270 fs-laser pulses emitted at a rate of 250 kHz. c) The relative intensity ratio of main peaks indicated in (b). d) OM images of the laser-affected cross-section and e) corresponding Raman spectra scanned across the laser-affected zone at 1528 nJ. f) The relative intensity ratio of the main peaks indicated in (e).

The effect of thermal cumulative regime

So far, we unveil the laser-induced modifications in a non-cumulative regime. Now, we consider the case when the time between pulses is shorter than the lattice cooling time constant, typically in a few μs [7]. For ULE glass, the glass melting occurs in multi-pulse irradiation at 500 kHz. Compared to fused silica (~ 1 MHz), ULE glass possesses a lower transition threshold from non-cumulative to the cumulative regime, inherited from its glass network. The evolution of laser-affected cross-section as a function of repetition rate in Figure 2.9.a indicates that nanogratings are absent at 1 MHz, despite low pulse energy (288 nJ). The structure at 1 MHz displays disrupted structures located at the top of the laser-affected zone and a well-defined border of opposite teardrop shapes. At higher pulse energy with multi-pulse irradiation at 1 MHz, the laser-affected zone exhibit two different zones, i.e., a micro-void at the center, consisting of molecular oxygen and densified material surrounding the micro-void in Figure 2.9.b. These structures commonly referred to as periodic bubble

patterns, studied extensively in fused silica [22]. The well-defined border of the modifications grows as a function of the number of pulses due to cumulative energy deposition. Another characteristic feature of this type of modification is the formation of trapped gas pockets at the center of the modifications. We observe molecular oxygen formation at the center of the modifications indicated by Raman spectra in Figure 2.9.c. The crystalline phase is located at the border of the bubble pattern, shown with a black dashed line in Figure 2.9.b. Within the melted and resolidified region, Raman spectra show an increase in peaks at 600 and 1554 cm^{-1} and a decrease in 1107 cm^{-1} . These modifications in the bands correspond to the densification of the glass network due to melting and fast resolidification, the transformation of Ti ions, and molecular oxygen due to glass decomposition. Similar modifications are obtained at 288 nJ at 1 MHz despite having low optical field strength.

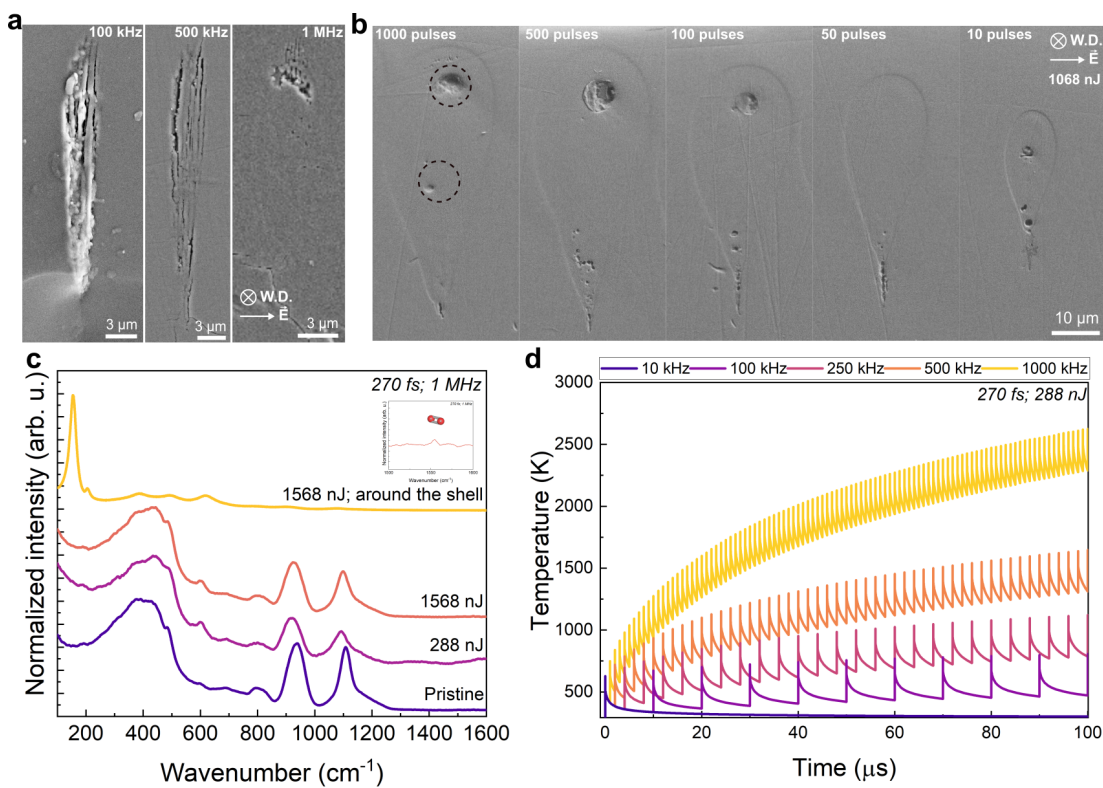


Figure 2.9: a) SE images of the laser-affected cross-section at 100, 500, and 1000 kHz with 270 fs-laser pulses. The laser processing parameters are 288 nJ with 7000 pulses. b) SE images of the laser-affected cross-section at 1 MHz as a function of the number of pulses per focal volume. c) Raman spectra of the laser-affected zone at 1 MHz with 1000 pulses, compared to the pristine glass. d) Temporal temperature evolution during the first 100 μs within the focal volume at 288 nJ with various repetition rates, ranging from 10 kHz to 1 MHz.

Finally, Figure 2.9.d displays the time-dependent temperature distribution of the focal volume calculated using the thermal diffusion model [136] for the case of multi-pulse irradiation at various repetition rates, ranging from 10 kHz to 1 MHz. The temperature rises quickly in the focal volume, and the lattice cools down with a typical quenching rate of $\sim 10^{14} \text{ K}\cdot\text{s}^{-1}$ eventually

leads to supercooling of new dense phases and/or metastable phases recovered under extreme conditions [137]. The softening temperature of ULE glass is around ~ 1763 K, which can be achieved within tens of microseconds. Once the pulses are emitted shorter than the lattice cooling time, cumulative effects dominate the laser-affected zone. Numerical simulation and experimental results agree that laser irradiation at 1 MHz with a pulse energy of 288 nJ leads to glass melting, as presented in Figure 2.9.a.

2.4.3 Photo-darkening phenomenon

Femtosecond laser-induced modifications above 100 fs are associated with the photo-darkening phenomenon. Regardless of being in the nanograting regime or not, this type of modification is related to the valence state change of Ti ions [118]. Here, we present the influence of laser parameters, particularly in the non-cumulative and thermal cumulative regimes, and quantify the relative darkening and optical absorption through optical observations and UV-VIS spectroscopy.

OM images of fs-laser scanned square patterns ($1 \times 1 \text{ mm}^2$) inside ULE glass are displayed in Figure 2.10.a. A gradual increase of the contrast compared to the pristine material is observed as a function of pulse energy, pulse durations, and repetition rate. To compare the degree of darkening qualitatively for each laser parameter, the OM images are converted to grayscale, setting the maximum pixel value as 255 after subtracting the background of the pristine glass. Although the maximum pixel value, 255, results in white and the minimum value, 0, results in black, we inverted the scale so that the maximum value corresponds to the degree of darkening. After the image processing, the pixel value assigned to each laser processing parameter is demonstrated in Figure 2.10.b-c. At 100 kHz, regardless of pulse energy, there is little or no photo-darkening in a few pulse regimes (number of pulses < 10). This regime is similar to the one in the homogeneous modification regime, in which there is little change in Ti-sites. Above this regime, the degree of darkening changes linearly as a function of pulse energy and the number of pulses per spot. Nanogratings and associated transformation of the Ti^{4+} lead to a higher level of darkening. At 1 MHz, in contrast, the degree of photo-darkening largely depends on the laser parameters, a complete darkening is achieved above 1100 nJ. Here, the formation of $\beta\text{-TiO}_2$ crystalline phase along with periodic bubble pattern leads to complete absorption. To quantify the observed photo-darkening, the absorbance spectra, and the corresponding Tauc plots are shown in Figure 2.11 for selected parameters, i.e., a few pulse regimes, the nanograting regime, and the disrupted region at 100 kHz.

The absorbance spectra at 288 nJ with 40 mm/s, corresponds to a few pulse regime and shows 10% of additional absorbance in Figure 2.11.a. Decreasing writing speed results in a nanograting regime, possessing higher absorbance. Still, the change of absorbance remains less than 25% compared to the pristine glass. However, not only the contribution of valence state change of Ti-sites but also crystallization contributes a high level of absorbance with a pulse energy of 1528 nJ in Figure 2.11.b. With 100 pulses (writing speed of 2 mm/s), 60%

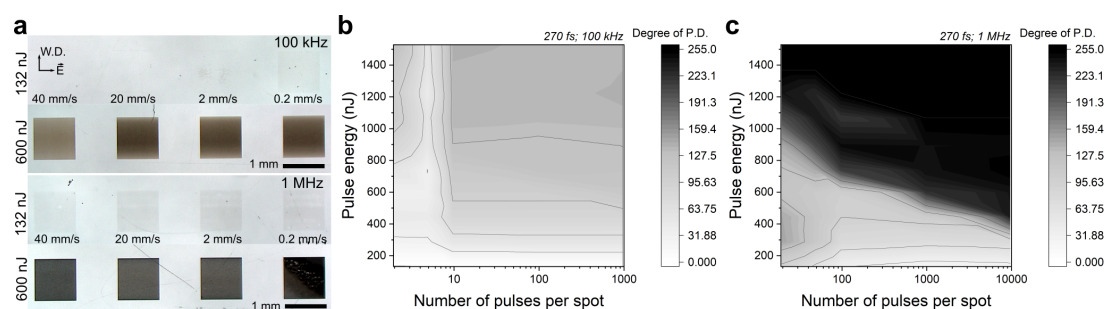


Figure 2.10: a) OM images of laser-written square patterns at 270 fs with two different repetition rates: 100 kHz and 1 MHz. b) The degree of photo-darkening (P.D.) at b) 100 kHz and c) 1 MHz for laser-inscribed square patterns in the ULE glass.

of relative absorbance is achieved for 1528 nJ. While the increment of absorbance between each writing speed is smaller for 288 nJ, a large step for each writing speed for 1528 nJ displays the strong absorbing nature of the crystalline phase. For 288 nJ, the only contributing factors to absorbance are valence state change and morphological modifications but for 1528 nJ, the formation of anatase (band gap of 3.2 eV) leads to strong absorbance in the UV-VIS-NIR spectrum. Figure 2.11 displays the corresponding SE images of the laser-affected cross-sections for 288 nJ and 1528 nJ at 100 kHz. Furthermore, Figure 2.11.d shows Tauc plot [138] for only direct band gap model behavior. While a linear region (and hence, a band gap value) is identifiable for the non-exposed case, the laser-exposed regions exhibit less pronounced linear zones that may account for their disorganized structures, interfacial effects, and crystalline phase.

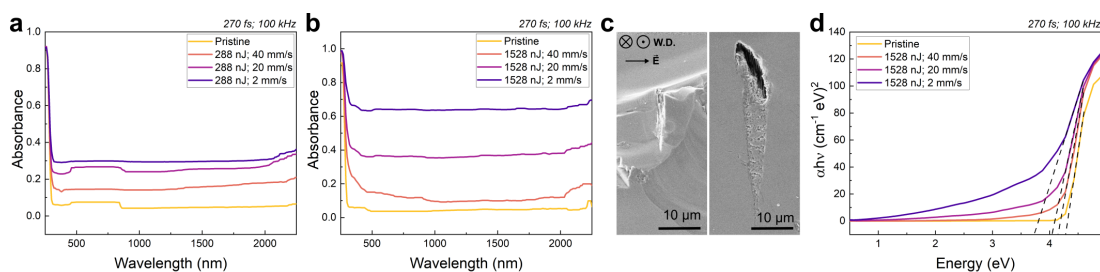


Figure 2.11: Absorbance spectra of laser-inscribed square patterns with a pulse energy of a) 288 nJ and b) 1528 nJ at 100 kHz with 270 fs-laser pulses. c) Typical SE image of microstructures at 100 kHz. The laser parameters are 288 nJ and 1528 nJ with 2 mm/s writing speed. d) The direct band gap (Tauc) plot of the square patterns inscribed with 1528 nJ pulses.

2.4.4 Glass decomposition and the formation of β -TiO₂ nanocrystals

Here, we present first the effect of laser parameters on the crystallized volume, i.e., under which conditions the crystalline phase can form, supporting the thermal diffusion model. We extend our understanding by observing structural evolution by Raman spectroscopy. The remaining open question is the size, shape, and preferred orientation of the crystals.

Titanium dioxide (TiO_2) possesses a few polymorphs, such as anatase (tetragonal), rutile (tetragonal) and brookite (orthorhombic) [134]. Among all, β - TiO_2 crystals, anatase, exhibits a tetragonal crystal structure (space group of $I4_1/amd$) with lattice parameters of $a = 0.378$ nm and $c = 0.951$ nm. Well-studied β - TiO_2 crystals transform to a rather stable phase of rutile when heated at about 733-1123 K [135]. In an interesting study, phase transformation of rutile into anatase was reported by femtosecond laser exposure [120]. In general, TiO_2 has been demonstrated as an important material for energy, environment, chemical, and biomedicine-related applications, such as photocatalysis, solar cells, sensors, and so on [135, 139]. Information on their shape, size, and orientation is particularly crucial for future applications, since each orientation possesses different surface energies resulting in variations in physical properties, for instance, differences in the photocatalytic activities of anatase due to its orientations along (101) and (001) [140].

Figure 2.12 presents OM and SE images of the laser-affected cross-section, the corresponding Raman spectra, and the time-dependent temperature distribution of the focal volume at 240 kHz for 500 fs laser pulses. The crystallization is observed above a certain fluence for all pulse durations above 150 fs. In this section, we present extensive high-resolution imaging and analysis of the laser-affected zone at 500 fs. The light scattering at the laser-affected zone allows us to distinguish the crystallized volume even under the optical microscope in Figure 2.12.a. The corresponding SE images with two different polarization states reveal the absence of clear nanogratings in this disrupted regime. The circular center of the opposite teardrop shape is somewhat well-defined and surrounded by nanopores in both polarization states. The corresponding Raman spectra are displayed in Figure 2.12.b. Locations at number 1 and 2 indicated in the SE image contain β - TiO_2 crystalline phase, whereas only densification and molecular oxygens are present at the center of the modification (at location number 3). Elongation of the laser-affected zone from the high field strength and self-focusing results in an extended tail part of the structure pointed out at number 4. Due to non-uniform field distribution, β - TiO_2 crystals. Finally, the time-dependent temperature distribution of the focal volume during the first 100 pulses shows the importance of the effect of field strength. Around 645 nJ and below corresponds to the nanograting regime at this repetition rate for 500 fs-laser pulses. In the nanograting range, the focal temperature rises to 1000 K with a single pulse but remains below the melting or glass-transition temperature. The thermal gradient decays a little above room temperature quickly within the first microsecond and therefore, the subsequent pulse does not incrementally increase the temperature. Above 1000 nJ, in contrast, a single pulse is enough to raise the local temperature twice high as the nanograting regime. This disrupted regime featured a densified shell containing molecular oxygen and surrounded with a crystalline phase as a result of glass decomposition accompanied by extremely high temperature and pressure.

Similarly, clustering of TiO_2 and increasing MRO due to gradual ordering of crystalline TiO_2 phase were reported previously upon annealing of ULE glass having different TiO_2 [141]. While below 10 wt% no crystalline phase is detected by high-resolution microscopy, nanocrystalline phases or rutile is detected in ULE glass with 11 wt% TiO_2 . Interestingly, anatase and rutile

nanocrystals are obtained above ULE glass with 13 wt% TiO_2 upon annealing TiO_2 . With the TiO_2 content above 15 wt%, the nanocrystals exist as a secondary phase [109, 112]. Here, the benefit of femtosecond laser irradiation lies within the precise control of Ti composition at the laser-affected zone and the generation of selective modifications in an arbitrary location and space in micrometer resolution.

Our observations show that the crystalline phase is observed for pulse durations of 150, 270, and 500 fs above 1000 nJ in a non-cumulative regime. In addition, we did not observe crystallization with a single femtosecond laser pulse above 1000 nJ. Once the Ti-related defects are present [123], multi-pulse exposure is needed for the decomposition. The crystallization occurs only in the disrupted nanograting regime (> 100 pulses) because high field strength is required to promote bond cleavage and ion migration associated with thermal and pressure gradients. Although the crystalline phase is present also in a thermal cumulative regime, however, the control of the location becomes very limited.

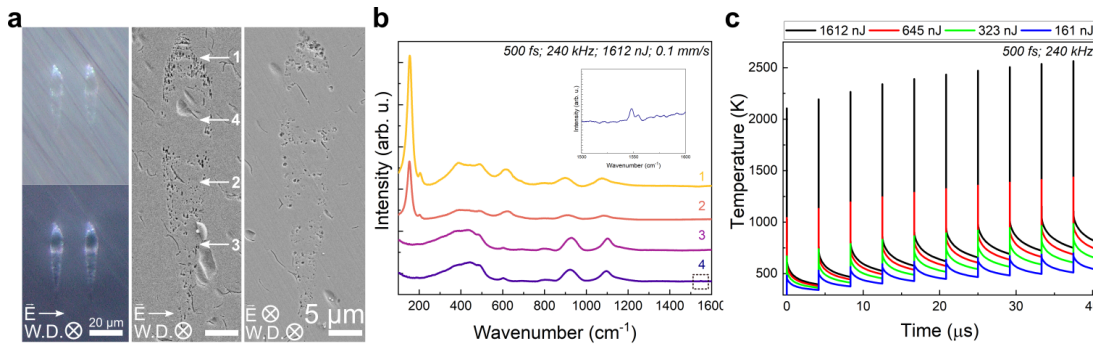


Figure 2.12: a) Reflected bright-field and dark-field OM and SE images of the laser-affected zone inscribed with 500 fs-laser pulses with 240 kHz. b) The corresponding Raman spectra along the vertical axis of the laser-affected zone indicated in (a). c) The time-dependent temperature distribution of the focal volume during the first 100 pulses at 240 kHz with various pulse energies, i.e. from 161 to 1612 nJ.

Furthermore, we investigate β - TiO_2 nanocrystals via high-resolution imaging and analysis. In Figure 2.13, we focus on the top part of the modifications, where we detected crystalline signals via Raman spectroscopy. Later in Figure 2.14, we cover the tail part of the laser-affected zone presented in Figure 2.13.a.

Figure 2.13. a displays the SE image of the laser-affected zone and the location where we obtained the TEM lamella at 1612 nJ. Figure 2.13.b presents the overall nanopores region with nanocrystals at the top part of the modifications. Although the SAED pattern consists of multiple crystallographic orientations, some of the spot diffractions are identified as anatase TiO_2 with a zone axis of [101]. The magnified image in Figure 2.13.c shows the amorphous precipitates with an average size of 4.97 ± 1.23 nm. The well-defined border between the amorphous phase around the nanopore and the crystallized area is displayed in Figure 2.13.d. We observe some Moiré fringes associated with a characteristic double diffraction pattern (not shown here) in a spatially confined area. Moiré fringes, typically with spacing an order of

magnitude higher than the original ones, may originate from the superposition of repetitive nanocrystals of TiO_2 with very small or equal spacing with suitable mutual orientation. Their thickness depends on the spacing of the interacting lattices, the misfit, and the angle formed [142]. The high lattice mismatch is related to laser-induced stress.

There are some single crystals, which can be distinguished in Figure 2.13.e. The HR-TEM image with the SAED pattern with a zone axis of $[101]$. The interplanar spacing in the oval area is measured as 0.351 nm corresponding to the (101) plane. Finally, Figure 2.13.f display HR-TEM image of the nanocrystals between two interfaces, i.e., one with the amorphous laser-affected zone and the C-coating. The average size of the nanocrystals is 4.78 ± 1.63 nm. The ring patterns in the FFT image represent the polycrystalline nature of the region of interest.

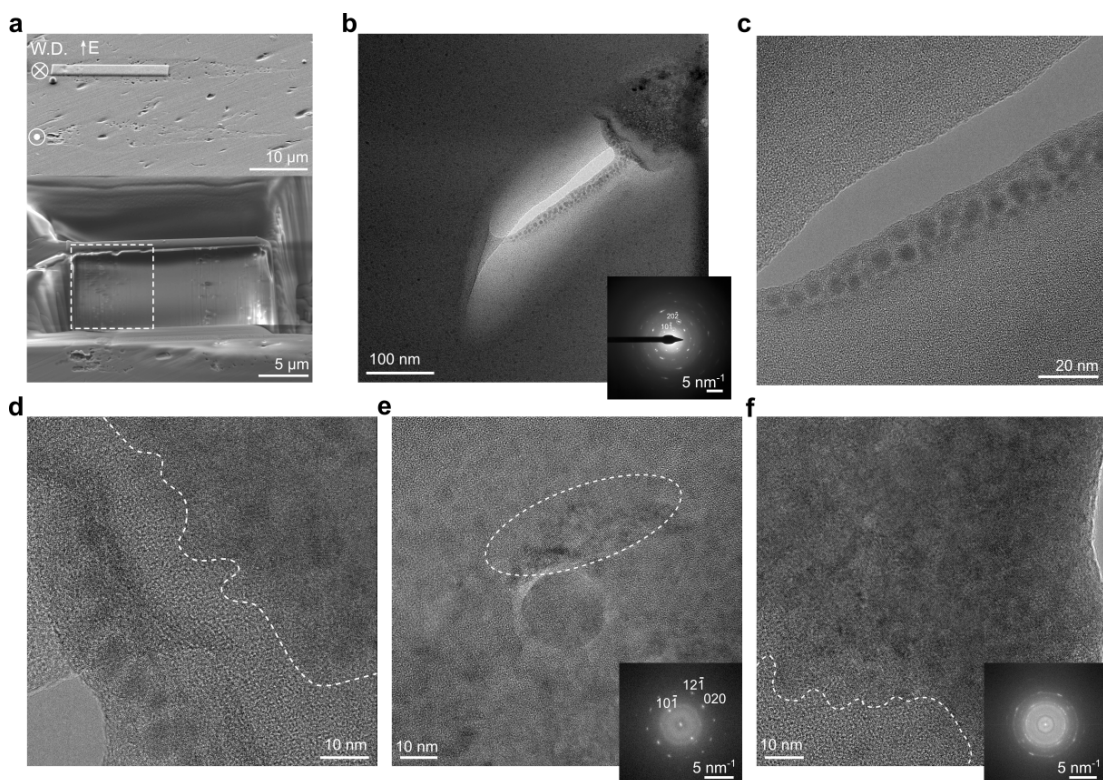


Figure 2.13: a) SE images of the laser-affected zone before and after FIB milling. The TEM lamella was coated with amorphous-C to protect the laser-affected zone during the milling and thinning process in FIB. The laser processing parameters are 500 fs-laser pulses at 240 kHz with 1612 nJ and 1 mm/s (500 pulses, corresponding to incoming pulse fluence of 254 J/mm^2). b) TEM images of the overall laser-affected zone within the focal volume with an inset image of the SAED pattern. c) HR-TEM image of the nanopore at the top part of the laser-affected zone in a) and d) HR-TEM image of the top part of the nanopores, showing the border between the amorphous and crystalline phase. e) HR-TEM images of the overall crystallized area with inset images of Fast Fourier transformation (FFT) patterns oriented along the crystallographic $[101]$ axis. f) HR-TEM image of the polycrystalline area with inset images of FFT patterns.

Figure 2.14.a presents the tail part of the laser-affected zone. The overall SAED diffraction

pattern and FFT patterns agree that the matrix and precipitates have an amorphous nature. Further in Figure 2.14.b-h, we demonstrate the characteristic features in this part of the laser-affected zone, which are also representative images of the nanocavities formed upon femtosecond laser irradiation. Figures 2.14.c-d are the magnified images of Figure 2.14.b. Although the features are not a cavity, the boundary of the features appears to be darker due to thicker material. While the precipitates are located throughout the area in Figure 2.14.e-f, they are heterogeneously distributed along the laser-affected zone. For example, the precipitates are located only at the boundary of the features in Figure 2.14.g-h. Overall, the average precipitate size is found as 3.84 ± 0.78 nm.

The formation of features can be considered as an onset of glass decomposition in which material is highly deformed and surrounded with amorphous precipitates of TiO_2 . These precipitates are most likely Ti_2O_3 -clusters [127] due to the promotion of Ti^{3+} octahedral sites in the laser-affected zone. Once the field strength is high enough, nuclei form and the growth stage begins, during which the nuclei continue to grow in size and transform into TiO_2 crystals. The growth process is typically driven by the diffusion of Ti and O species, which deposit on the surface of the nuclei and form new layers. The formation of anatase from Ti_2O_3 -clusters are affected by many factors such as temperature, pressure, composition, and the presence of other chemical species.

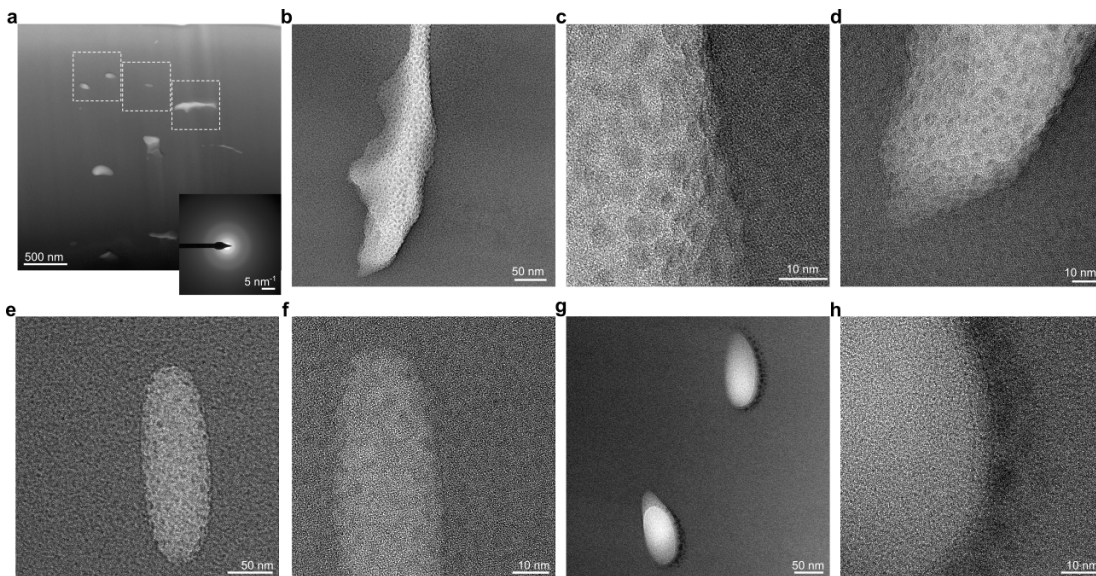


Figure 2.14: a) TEM images of the center and the tail part of the laser-affected zone within the focal volume with an inset image of the SAED pattern. The laser processing parameters are 500 fs-laser pulses at 240 kHz with 1612 nJ and 1 mm/s (500 pulses, corresponding to incoming pulse fluence of 254 J/mm^2). b,e,g) HR-TEM image of the features highlighted with white squares in a). c,d,f,h) HR-TEM image of the laser-affected zone indicated in b,e,g).

2.4.5 Remarks on the surface modifications

So far, we studied the formation of nanogratings and the related laser-induced chemical modifications. In this last section, we extend our understanding of self-organization on the surface. Figure 2.15.a presents the processing map of surface modifications. The processing window spans pulse energy from 50 to 1300 nJ and the number of pulses from 1 to 1000 at 100 kHz. The modification threshold of the ULE glass is found around 100 nJ at 100 kHz (an incoming pulse of 0.15 J/mm^2 for two pulses with a writing speed of 100 mm/s), showing relatively similar results as fused silica [68]. Nanogratings are observed in an extremely large processing parameter range. Thanks to the strong chemical bonds in the glass network, ULE glass exhibits a high ablation threshold (almost above 1000 nJ). Finally, Figure 2.15.b shows the self-organized nanostructures on the ULE glass surface. The surface nanograting consists of nanoplanes, perpendicular to the laser polarization. They are accompanied by photo-darkening on the surface, like nanogratings in volume.

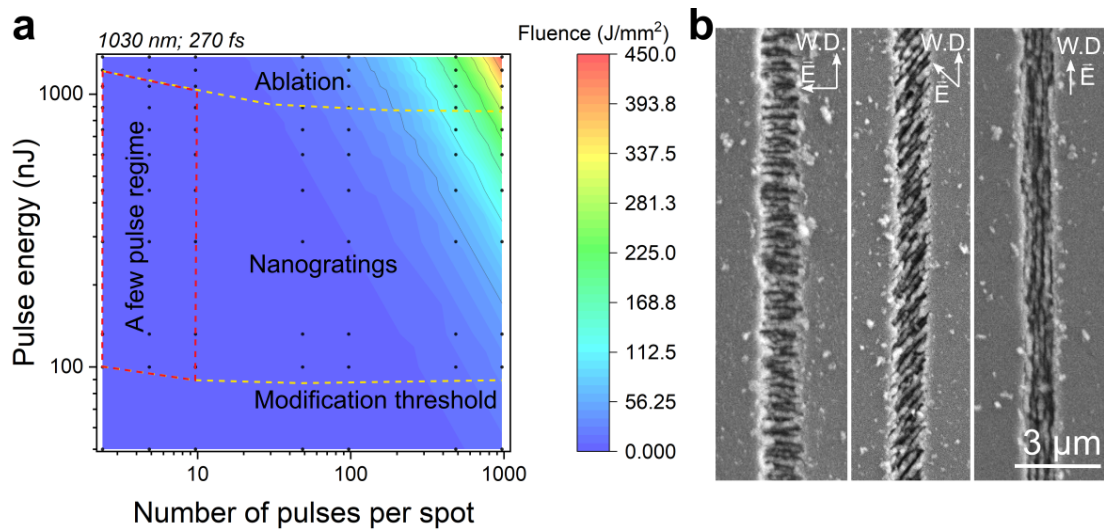


Figure 2.15: a) The laser parametric window of surface inscription of ULE glass with 270 fs-laser pulses at 100kHz. b) SE images of surface nanostructures with three different polarizations at 288 nJ with 500 pulses at 100 kHz (incoming pulse fluence of 47 J/mm^2).

2.5 Summary

In this chapter, we investigated various photo-induced modifications on the surface, especially, in the volume of ULE glass for both thermally cumulative and non-cumulative regimes. Our findings triggered the following observations:

- Numerous femtosecond laser-induced modifications, in particular, densification, volume nanogratings, photo-darkening, glass decomposition, and crystallization, are observed in ULE glass. Starting homogeneous modifications associated with densification are observed with a pulse duration below 100 fs in a non-cumulative regime with a low

fluence threshold of about $\sim 14 \text{ J/mm}^2$. Here, the increase of 3-membered silica rings leads to a more compact glass network.

- Self-organized nanogratings are formed with pulses above 150 fs with a relatively high fluence ($\sim 31\text{-}37 \text{ J/mm}^2$) in the glass volume. They are composed of nanoplanes perpendicular to the laser polarization and displays anisotropic birefringence. Above certain pulse energy in the non-cumulative regime, they are replaced by a disrupted regime in which we observe glass decomposition, formation of molecular oxygen, and crystallization in the non-cumulative regime. In the thermal cumulative regime, the periodic bubble patterns filled with molecular oxygen and surrounded by densified glass matrix are obtained.
- With the formation of self-organized nanogratings, the photo-induced chemical modifications, photo-darkening, results from the valence state change of TiO_2 in silica network from Ti^{4+} to Ti^{3+} . This phenomenon accompanies all modifications generated with 150 fs-laser pulses and above.
- Further increase in the pulse energy lead to glass decomposition and subsequent crystallization of metastable phase of TiO_2 , $\beta\text{-TiO}_2$ (anatase). The formation of amorphous precipitates, most likely composed of Ti_2O_3 -clusters, is demonstrated with low laser fluence while higher laser fluence presents the polycrystalline TiO_2 in the range of 5-10 nm in size. The formation of crystals further decreases the optical band gap, resulting in high absorption in the laser-affected zone.
- Finally, the observable laser damage threshold on the surface and in the volume is slightly lower than fused silica, possibly resulting from TiO_2 content. In addition, nanogratings and photo-induced darkening have been observed on the surface, similar to the volume.

In summary, understanding the relationship between the optical properties and physical modifications upon ultrafast laser exposure is crucial for successful photonic devices by femtosecond laser direct writing. From the application point of view, these results enable the direct-write of functional 2.5-dimensional or 3D structures with physical properties tailored to the laser inscription parameters.

3 Non-silicate oxide glass systems: Tellurite glass¹

¹This work has been partially published as G. Torun, T. Kishi, and Y. Bellouard, *Direct-write laser-induced self-organization and metallization beyond the focal volume in tellurite glass*, *Physical Review Materials* 5 (5), 055201 (2021), which can be found in the text as [143], and G. Torun, T. Kishi, D. Pugliese, D. Milanese, and Y. Bellouard, *Formation mechanism of elemental Te produced in tellurite glass Systems by femtosecond laser irradiation*, *Advanced Materials*, 2210446, (2023) cited as [144].

External contributions: In this study, potassium-tungsten-tellurite (TWK) and tungsten-silver-tellurite (TWA) were fabricated by Prof. Tetsuo Kishi at Tokyo Institute of Technology; barium-sodium-zinc-tellurite (TZNBa) and germanium-niobium-phosphor-zinc fluorotellurite (TGNPZ) were fabricated by Prof. Daniel Milanese and Dr. Diego Pugliese at Polytechnic University of Turin. The preliminary SE images on the femtosecond laser-irradiated TWK surface were observed by Prof. Tetsuo Kishi. CO₂ laser exposure was conducted with Mr. Samuel Benketaf, and UV femtosecond laser irradiation was performed with Dr. Benedikt Hermann in Galatea Laboratory at EPFL. PL spectra were performed by Ms. Ezgi Genc from PV-LAB at EPFL. Finally, the XRR data presented in Appendix C was resolved by Dr. Benedikt Hermann in Galatea Laboratory at EPFL.

In the previous chapter, we discussed the femtosecond laser interaction with a SiO₂-based glass system. Specifically, we showed how the response of fused silica to femtosecond laser exposure is perturbed by the presence of TiO₂. In this chapter, we focus on a non-silicate oxide glass system, namely tellurium dioxide (TeO₂)-based glass. First, we cover why these glass systems are unique, the current status of their research, and their use. Then, we present the femtosecond laser interaction with the tellurite glass family as currently known in the literature. Finally, morphological and structural photo-induced modifications both on the surface and in the glass volume are introduced by altering laser parameters in common tellurite glass compositions under various ambient conditions.

3.1 Glass structure and properties

Glass systems are divided into oxide and non-oxide glasses, which oxide glasses also can be divided further into silicate and non-silicate glasses. In non-silicate oxide glass systems, the intermediate oxides, such as TeO₂, Al₂O₃, Pb₂O₅, Bi₂O₃, Sb₂O₃, require a sufficient amount of modifier oxides and/or special quenching techniques to be stable against devitrification. TeO₂ has been considered as a conditional glass former, and the observation of the glass formation with other oxides is as early as 1834 [145]. The systematic investigation on various compositions of TeO₂-based or tellurite glass started after the 1950s [146]. It can form a glass under a traditional glass melting-quenching process, with glass formers (such as SiO₂, etc.), or with glass modifier oxides of alkali metal, alkaline-earth metal or transition metals (like K₂O, BaO, etc.) [147]. Later, with a tremendous effort of scientists, pure TeO₂ glass has been reported in the 1960s, and since then, various quenching techniques have been developed [148–150].

The unique glass structure of TeO₂ has been under a long debate. Having several crystalline polymorphs (α , β , γ , and δ), the structures are characterized by the active lone pair electrons (5s²) of tellurium atoms, causing a strong asymmetry around oxygen atoms [151]. It was initially considered that the glass structure resembles α -TeO₂, known as paratellurite [152]. α -TeO₂ constitutes corner-shared TeO₄ bipyramids with the lone-pair electrons on Te occupying one of the corners of the bipyramid and four neighboring oxygen atoms, located at two short equatorial and two long axial positions. Each Te in the 3D crystalline network is connected via single Te-O-Te bridges, i.e., through the Te_{eq}O_{ax}-Te bridges. After several observations conducted by X-ray diffraction, nuclear magnetic resonance (NMR), Raman and infrared spectroscopy, γ -TeO₂ consisting of two different kinds of Te-O-Te bridges, namely nearly symmetric and highly asymmetric, is proposed as the closest to TeO₂-glass [153–155]. Recent investigations with high-resolution X-ray pair distribution function, ab-initio molecular dynamics simulations, and Raman spectroscopy show the close relationship between metastable δ -TeO₂ and TeO₂-glass due to the presence of positional disorder in the short-range [151, 156–158], shown in Figure 3.1.I. Because as a lone-pair oxide glass, highly asymmetric Te-O-Te bridges do not indicate well-defined Te-O distance distribution and coordination number (n , 3.6 < n ≤ 4.0, from the glass to the melt) [156]. The long and weak Te-O bonds become more

asymmetric with temperature by the contraction of the short bonds in the asymmetric bridges, strengthening the short-range disorder. Subsequently, the coordination number in the glass, ~ 4 , decreases in molten pure TeO_2 . This increase in the asymmetry corroborates the transformation of the TeO_4 units into highly asymmetric TeO_3 units by temperature in pure TeO_2 [151]. Additionally, an increase in the asymmetry comes from the nonequivalent electron charge distribution on the oxygen atom, i.e., the short bond exhibits a higher charge localization than the long bond in the Te-O connection [151]. Another debate ongoing currently on the glass structure is the absence of double bonds [151, 156, 159] since they might have been confused with highly asymmetrical Te-O-Te bridges, or their presence due to unequal charge localization in short and long bonds of Te-O in pure TeO_2 -glass.

Let us look at the atomic-scale structure of glassy TeO_2 . The complex structure of pure TeO_2 -based glass consists of TeO_n structural units with *bridging oxygens* (BOs) and *non-bridging oxygens* (NBOs) atoms [151]. Either by temperature or by the addition of glass modifier oxides (such as Na, K, etc.), the rise in the number of NBOs with a decline in the coordination number of Te leads to the transformation of continuous glass network from corner-shared TeO_4 trigonal bipyramid (tbp) to TeO_{3+1} polyhedra (distorted tbp, or d-tbp) and TeO_3 trigonal pyramids (tp) having non-bridging oxygen [160], as shown in Figure 3.1.II. In addition, depending on the cation valence of the modifier oxide, Te-O-M (M=W, Nb, etc.) bridges can form, substituting Te-O-Te. This is contrary to classical glass formers, such as SiO_2 , P_2O_5 and B_2O_3 , in which the modifiers usually break the glass network. Although pure TeO_2 glass exhibits a higher optical nonlinearity over tellurite glass with modifier oxides [161], it remains difficult to obtain bulk pieces at room temperature and ambient pressure, limiting the further usage in practice as well as study in this thesis.

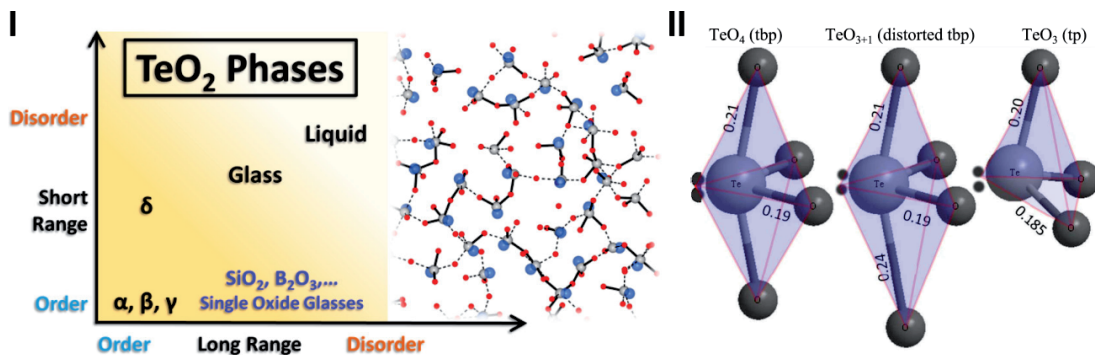


Figure 3.1: a) A schematic representation of TeO_2 phases (taken from [156]). b) A schematic representation of the TeO_2 -based glass structural units: TeO_4 trigonal bipyramid (tbp), TeO_{3+1} polyhedra (distorted tbp, d-tbp) and TeO_3 trigonal pyramid (tp). Dots near the Te atom represent the lone pair (LP) electrons (taken from [162]).

Among all the compositions, we focus on various ternary to quinary tellurite glass systems, namely TeO_2 - WO_3 - K_2O (TWK), TeO_2 - WO_3 - Ag_2O (TWA), TeO_2 - Nb_2O_5 - GeO_2 - PbO - ZnF_2 (TNGPZ) and TeO_2 - ZnO - Na_2O - BaO (TZNB). Most of the study in this chapter is conducted on the following composition: 80 TeO_2 -10 WO_3 -10 K_2O (mol%) (TWK). TWK has a wide glass-forming

region, and its properties have been studied well [147, 163–165]. The glass network of TWK is composed of TeO_4 tbp, TeO_3 tp (ratio of tp to tbp is 0.3 [160]) and WO_4 tetrahedra, WO_6 octahedra units, and the reduction in the number of Te–O–Te bonds occurs due to the addition of K_2O . Also, the presence of W–O–W and Te–O–W bonds come from the substitution of W^{6+} for Te^{4+} . The addition of WO_3 contributes significantly to the thermal stability against devitrification [163]. Therefore, it can be stated that WO_3 acts as a network former, while K_2O acts as a network modifier since an increase in K_2O decreases the network connectivity due to the formation of NBOs. In addition, the TWK glass system has an extremely wide glass-forming region thanks to weak Te–O–Te bonds [160].

TeO_2 -based glass systems have drawn significant interest due to their unusual properties compared to other oxide glass systems. Their high refractive index, low phonon energy, high third-order nonlinear susceptibility, large transmission window (up to 5 μm), high dielectric constant, low glass transition temperatures, the high solubility of rare-earth ions, and thermochromism are attractive for numerous applications in optics, photonics, and optoelectronics [150, 163, 166, 167]. Several examples for practical applications have been demonstrated as optical switching devices by second- and third-harmonic generations [168, 169], laser hosts [170], supercontinuum source [171], low-loss waveguide [172], integrated optics [173], optical recording media [174], optical fibers and amplifiers [175], fiber Raman amplifiers [176], and anodes for lithium-ion batteries (LiBs) [177].

3.2 Femtosecond laser and tellurite glass interaction

TeO_2 -based glass systems are well-known from the literature to be particularly suitable for photonic applications. The available studies regarding their interaction with fs-laser pulses include measurements of nonlinear properties, refractive index modulation, ion migration, ablation, and patterning. Here, we present some selected studies in Figure 3.2.

To the best of our knowledge, the first study on the fs-laser irradiation of tellurite glass has been reported on the positive refractive index change [178], as shown in Figure 3.2.I. The change of refractive index can be tunable with the number of laser pulses and the peak power. Later, various studies reported positive refractive index change in both non-cumulative and thermal cumulative regimes [179–189], demonstrating a waveguide at 1310 nm in Figure 3.2.II. Besides, negative refractive index change has been observed under a few conditions [185, 188, 190, 191]. For instance, in Figure 3.2.III, while waveguide A, written with a lower writing speed (2 mm/s), exhibit two different refractive index depending on the location of the laser-modified zone, the positive index change region in waveguide B is sandwiched between two negative index contrast zones, written with 4 mm/s of scanning speed [188]. There are a few reasons behind the change in refractive index. The first one is attributed to densification by the transformation of TeO_4 tbp to TeO_3 tp units, resulting in a highly packed glass network. In addition, the local ion migration of Te is accompanied by the migration of glass modifier ions to the opposite location. In this example, the ionic radius of Na (227 pm) or K (280 pm) is greater than the

ionic radius of Te (210 pm), generating a space for the migration of Te ions.

In terms of morphological changes, micro-explosion near the surface of the tellurite glass was reported [192]. Ablation threshold and the subsequent crater morphology [193] have been also addressed elsewhere. Furthermore, Shimotsuma *et al.* has demonstrated the formation of a periodic structure of voids with ~30 nm width in Figure 3.2.IV. Unlike alternating nanoplanes in terms of oxygen content in fused silica, periodic voids perpendicular to the laser polarization in a TeO₂ single crystal are generated in the material without removing any material by chemical etching [194]. Compared to TeO₂ single crystal, the dissimilar thermal dependency of the laser-affected zone in zinc tellurite glass comes from the difference in thermal diffusivity and viscosity in Figure 3.2.V [195]. Furthermore, the elemental redistribution [196] and ion migration of Te accompanied by a crack in the center of a focal spot [195] have been reported, as shown in Figure 3.2.VI.

As the characteristic timescale of fs-laser irradiation shown in Figure 1.1, the process involves the generation of high pressure and, depending on the repetition rate, heat accumulation in the lattice. Upon annealing and/or phase decomposition under pressure, some tellurite glass compositions or telluride compounds show crystallization [197, 198]. Likewise, upon fs-laser irradiation in the thermal cumulative regime, the glass decomposition and the formation of Te nanocrystals have been presented in the oxyfluoro-tellurite glass volume [199]. Later on, the same group also studied the effect of the non-cumulative and cumulative regime inside the phospho-tellurite glass [200]. After our observation of Te nanocrystals near the surface of TWK, TWA, TNGPZ, and TZNB glass systems [143, 144], another study has also demonstrated Te nanocrystals formation on tellurite glass doped with PbS, PbO, and PbO/ZnS upon pouring molten glass into a pre-heated mold and upon fs-laser irradiation in cumulative regime [201]. The details are discussed further in the chapter.

In this chapter, we first report morphological and structural modifications on the surface of the carefully selected tellurite glass compositions to ultrafast laser pulses in non-cumulative and thermal-cumulative regimes. Our methodology is exposing the glass to ultrafast laser pulses of varying intensity to highlight the photo-induced modifications and formation mechanisms of self-organized nanostructures. Further, the effect of an open-air atmosphere (nitrogen, oxygen, and humidity) is investigated by comparing it with a controlled dry-air atmosphere, a dry nitrogen atmosphere, and a vacuum. Likewise, the effect of substrate temperature is explained briefly. In addition, the influence of glass modifiers on photo-induced modifications is considered with an effort to draw a general modification map for the tellurite glass family. Finally, systematic research on morphological and structural photo-induced modifications in the tellurite glass volume is summarized.

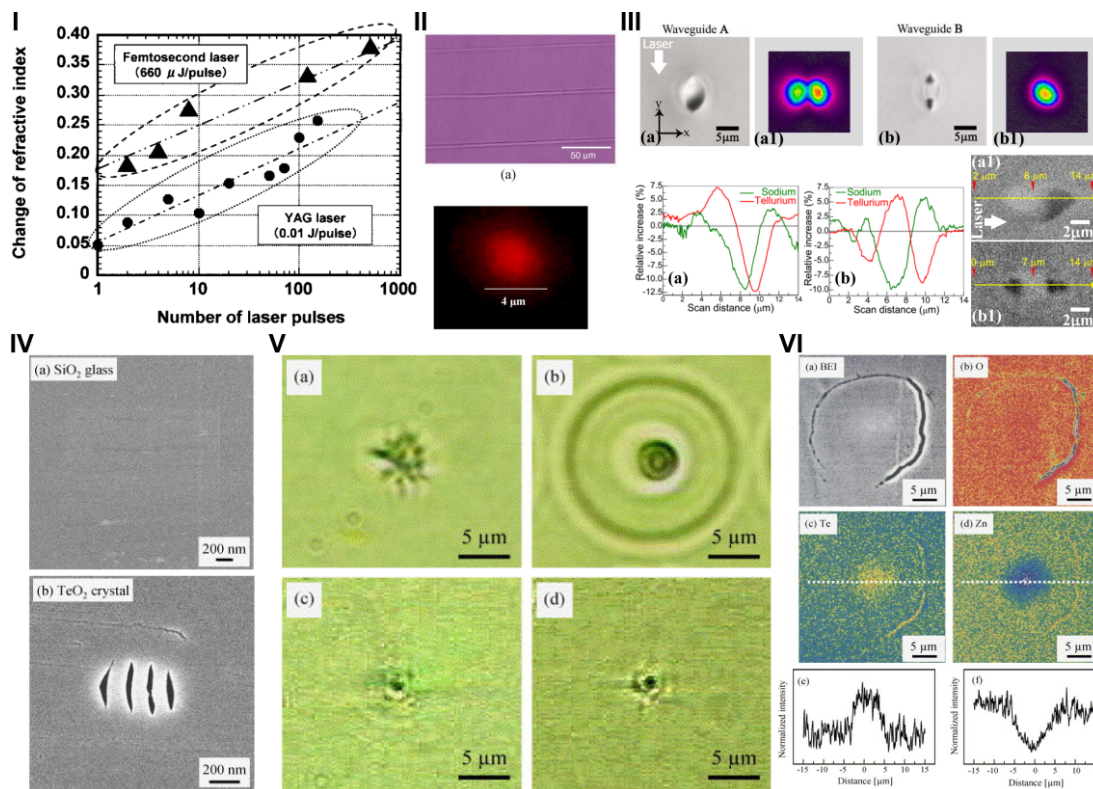


Figure 3.2: Top: I) The change of refractive index with the number of ps- and fs-laser pulses (taken from [178]). II) fs-laser-written waveguides and the mode-profile image of channel-transmitted 1310 nm laser light (taken from [182]). III) DIC microscope images of waveguides and propagation modes at 980 nm. EDS line scans along waveguides with SE images. The laser parameters are 400 fs-laser pulses emitting 1040 nm at 1 MHz with pulse fluence is 2.9 J/cm^2 . The waveguide A and B were written with 2 and 4 mm/s, respectively (taken from [188]). Bottom: IV) OM images of the modification in a,b) zinc-tellurite glass and c,d) TeO_2 single crystal. The laser parameters in a,c) are 1000 pulses at 1 kHz; 1600 pulses at 200 kHz in b,d) (taken from [194]). V) SE images of the modification in fused silica and TeO_2 single crystal (taken from [194]). VI) BSE and EDS mapping images of the volume modifications in zinc-tellurite glass (taken from [195]).

3.3 Experimental procedure

3.3.1 Glass specimen preparation

Four different compositions of tellurite glass were investigated, each chosen for their relevance in various applications. All specimens were synthesized by a conventional melt-quenching technique using high-purity chemicals (99+%). After weighing and mixing, the batched chemicals were transferred into a platinum crucible and melted at 1103 K for 2 hrs within a muffle furnace to produce TNGPZ and TZNBa. The melts were cast into a preheated cylindrical brass mold, annealed at a temperature around the glass transition temperature for 5 hrs to relieve the residual internal stresses, and cooled down slowly to room temperature. TWA and

TWK were produced by mixing commercial powders with high-purity and melting them in the Au crucible at around 973 K for 30 min in an electric furnace. The melts were quenched onto a brass plate. After quenching, the glass specimens were crushed and remelted at 973 K for 30 min, followed by subsequent annealing at 598 K for 1 hr. The specimen was cut and polished prior to fs-laser exposure.

The effect of surface chemistry, and the thermal history of the substrate, which determines the level of instability/stability of the glass against crystallization are important points for glass processing [202, 203]. For this work, all the glasses are stress relief treatments at a temperature chosen carefully according to the composition, thus, the thermomechanical effects on the crystallization due to cooling are minimized. In addition, after stress relief treatment, all glass rods were cut and optically polished into 1 to 2 mm-thick specimens. Finally, the substrates were heated to 423 K for a few hours in the furnace to remove any chemically bonded water and -OH groups from the surface and kept in a dry-air atmosphere until the fs-laser exposure. Table 3.1 and Table 3.2 show the physical properties of tellurite glass specimens used in this work.

Table 3.1: Sample, density (ρ), refractive index (n) at 1061 nm, band-gap energy (E_g), laser modification threshold (E_{th}), and laser ablation threshold ($E_{ablation}$) in terms of pulse energy and fluence of tellurite glass systems studied in this work at 1 MHz.

Sample	ρ (g/cm ³)	n	E_g (eV)	E_{th} (nJ)	$E_{ablation}$ (nJ)	$E_{ablation}$ (J/mm ²)
TWA	6.3	-	-	15	75	98
TZNBa	5.33	1.997	3.01	10	150	197
TNGPZ	5.44	2.097	2.86	5	150	197
TWK	5.31	2.025	3.04	10	250	328

Table 3.2: Sample, transmission window, dielectric constant, polarizability, the glass transition temperature, the crystallization temperature, the melting temperature, and Young's modulus of 80TeO₂-10WO₃-10K₂O (mol%) (TWK) glass [163, 165]

Sample	T (μ m)	ϵ_r	Polarizability	T_g (K)	T_x (K)	T_m (K)	E (GPa)
TWK	0.4-5	30	6.18×10^{-24}	584	729	892	41.95

3.3.2 Femtosecond laser irradiation

An Yb fiber-amplifier femtosecond laser (Yuzu from Amplitude Laser) emitting 270 fs pulses at 1030 nm was used in this experiment. Laser patterns were inscribed on the surface and in the volume (with a depth of 100 μ m) of the different tellurite glasses as parallel lines with varying lengths of 1-10 mm. To observe morphological evolution over the depth, a tilted inscription with a small angle of 15° was performed (see Appendix C). The specimen was translated under the laser focus with the help of a high-precision motorized stage (Ultra-HR from PI Micos). The laser beam was focused on the surface of the specimen with a 0.4 numerical aperture (NA) objective (OFR-20x-1064 nm from Thorlabs), resulting in a spot-size (defined at $1/e^2$)

of 1.94 μm (see Appendix A for the laser spot size measurement). The transition from a non-cumulative to a cumulative thermal regime exposure regime was determined by observing the evolution of the width of the laser-affected zone with the pulse repetition frequencies for the same net fluence at static exposure conditions. A wide range of pulse repetition rates (1 kHz-1 MHz) was employed. The transition from a non-cumulative to a thermal-cumulative regime was found at around 200-400 kHz. The repetition rate of 1 MHz lies well within the cumulative regime for the glass. The evolution of the width of the laser-affected zone upon static exposure conditions was demonstrated in Appendix C. For comparative experiments between the two exposure regimes, 1, 10, and 100 kHz-pulse repetition rates were used for representing the non-cumulative thermal exposure regime. Pulse energy and translation velocity were selected as variables to obtain different deposited energies. Here, pulse-to-pulse overlapping ratios were varying from 0 to 99.9%, and the pulse energy was ranging from 1 nJ to 500 nJ, as measured after focusing with the objective lens (see Appendix A for details of the calculation of net fluence). Furthermore, the patterns were inscribed using opposite directions of laser beam movement along a single writing axis and under three different linear polarization states (and therefore, the orientation of the electrical field E) defined as parallel, at 45°, and perpendicular to the writing direction, respectively.

Furthermore, the importance of the non-linear ionization process is highlighted by exposing the same glass with the fs-laser emitting UV wavelength (343 nm; 450 fs-laser Tangor from Amplitude Laser), compared with the fs-laser emitting near-IR with similar pulse duration (500 fs-laser Yuja from Amplitude Laser), and pulsed CO₂ laser irradiation (10.6 μm ; 1 μs - 1 ms Synrad Firestar ti60).

Finally, to understand the effect of the atmosphere, the laser inscription was also performed in the sealed chamber with various atmospheres. The inlet and outlet of the chamber were kept as shown in Figure 3.14 for constant dry air flow [O_{2(g)}+N_{2(g)}], relative humidity level < 2% (industrial grade, to eliminate the condensation)] and dry nitrogen flow [N_{2(g)}, purity > 99.9%], whereas, only inlet was kept under a vacuum (<10⁻³ Pa) in the dry chamber connected to pump. The results are compared with the open-air atmosphere [O_{2(g)}+N_{2(g)}, relative humidity level is 40% - measured constantly]. To eliminate the possible moisture on the surface of the chamber (refer to crystal water), the chamber was heated to 400 K for 2 hours in a furnace. In addition, desiccant salts were added to the chamber. Then, the dry chamber was flushed with constant dry nitrogen flow for 24 hours before the experiment. The same laser parameters were employed as mentioned above.

3.3.3 Specimen characterization

After laser exposure, specimens were observed using an optical microscope (BX51 from Olympus) and a digital optical microscope (KH-8700 from Hirox). Subsequently, the surface profile and roughness were obtained by atomic force microscopy (AFM from Nanosurf). A Raman spectrometer (LabRam HR from Horiba), equipped with a 532 nm laser excitation source

attenuated down to 4 mW was used to record Raman spectra of TWK, TZN, and TGNP. For TWA glass, a Raman spectrometer (from Renishaw), equipped with a 732 nm laser excitation source attenuated down to 4 mW was used. The linearly-polarized Raman laser beam was focused at the surface of the specimen using a 0.9 NA objective (100x-532 nm and 100x-732 nm from Thorlabs). A series of line scans were performed from 10 μm outside the laser-affected zone towards the center of the modification with a period of 1 μm , and with acquisition times of 30 s for an individual spot. The transmission and absorption spectra were measured for wavelengths ranging from 250 to 2500 nm using an ultraviolet-visible-near-infrared spectrometer (UV-VIS-NIR, Lambda 950 from Perkin Elmer). A mask with a hole of around 2x2 mm² was prepared from black paper for broadband absorbance. For the measurement, the reference beam power was attenuated to 10%, to compensate for the presence of the mask and the ensuing effective drastic reduction of the beam size from the original 2 cm in diameter. The thickness of the sample used for this transmission measurement was 2 mm. Photoluminescence (PL) imaging was performed by an in-house built setup [204]. The samples were excited using a laser (from Ostech) with a wavelength of 808 nm, operated with a power of 1.2 suns, and the images were recorded with a camera (Si-based from PIXIS Princeton instrument). In addition, DC electrical resistivity was measured by a 4-probe analyzer connected to a source measurement unit (SMU B2902A from Keysight) applying a forward bias of 40 V.

For high-resolution imaging and elemental analysis, a thin film of carbon was sputtered (from JEOL) on specimens using a field-emission scanning electron microscope equipped with energy-dispersive X-ray spectroscopy (EDS) (FE-SEM, Gemini 2 from Zeiss, operated at 5 kV for imaging and 20 kV for elemental analysis). Transmission electron microscope (TEM, Talos F200S from ThermoFisher) images were obtained operating at 200 kV. TEM lamellae (thickness of about 100 nm) were prepared by a focus ion beam (FIB, NVision 40 dual-beam from Zeiss) at 5kV and 30 kV. FFT and SAED patterns were fitted with electron diffraction simulation of GenOVa [130]. Finally, cross-sectional milling was performed in another scanning electron microscope combined with a focused ion beam (SEM-FIB from FEI Nova 600 NanoLab). The milling was performed using a Ga-ion source operated at 30 kV acceleration voltage and 7 nA emission current.

3.4 Results and discussion

3.4.1 Self-organized nanostructures in non-cumulative regime

Self-organized surface structures have generated enormous interest since it has been shown an enhancement in various properties and/or the addition of new functionalities to the surface of many materials. In this section, we investigate self-organized surface structures on the tellurite glass surface exposed to ultrafast laser under certain conditions in terms of laser parameters.

Let us first examine the morphological modifications on the surface in the case of single to a

few pulses exposure, i.e., from no to gradual accumulation of pulses. A lower repetition rate is beneficial not only for an observation in a non-cumulative regime but also for a high level of control pulse overlapping in dynamic writing conditions. At 1 kHz, the effective number of pulses at the focal volume rises from a single pulse to ten pulses forming continuous tracks. Figure 3.3.a-j displays SE images of the pulse-to-pulse laser-affected zone on the TWK surface at 1 kHz and pulse energy ranging from 50-500 nJ. The formation of the cavity and hole in a single shot continues further with the number of pulses. Interestingly, up to 10 pulses, instead of self-organization nanostructures, irregular patterns continuously along the track are present. With the 10th pulse, nanostructures, oriented perpendicular to the laser polarization, become distinguishable in all pulse energies. The periodicity is proportional to pulse energy, increasing from 161 nm to 273 nm between 50 nJ to 500 nJ, presented in Figure 3.3.k. The minimum required laser fluence to obtain nanostructures is 3.3 J/mm², although the first observable modification requires only 0.0033 J/mm² at 1 kHz.

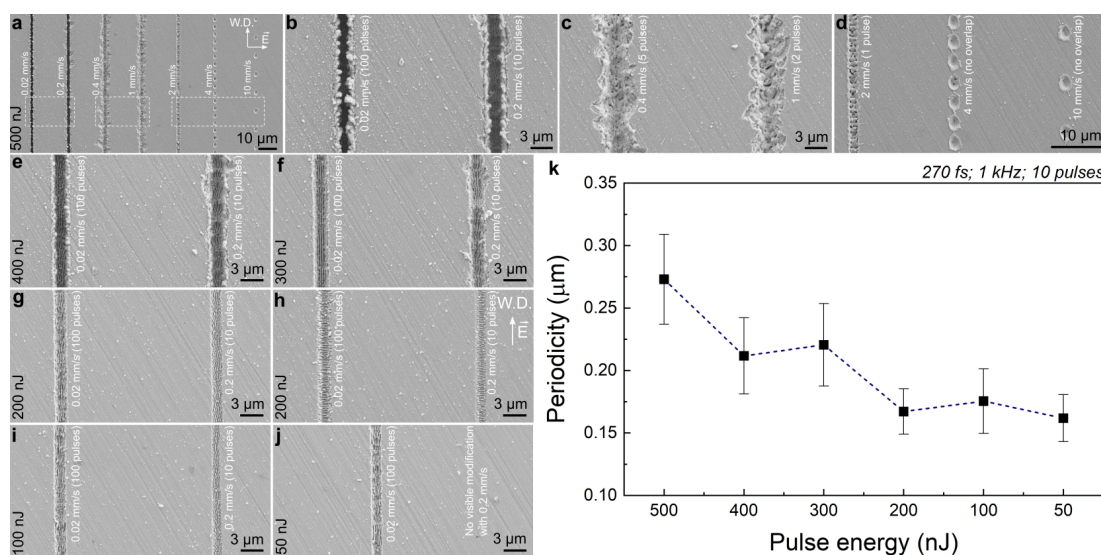


Figure 3.3: SE images of self-organized nanostructures on TWK glass at 1 kHz. a-d) Laser-written tracks at 500 nJ; e) 400 nJ, f) 300 nJ, g-h) 200 nJ, i) 100 nJ, j) 50 nJ. k) The average periodicity of the nanostructures after 10 pulses.

Here, we examine the structural evolution in the case of a single to a few pulses exposure. The rationale of these investigations is to unravel step-wise mechanisms leading to the photo-induced modifications on tellurite glass. Figure 3.4.a-b presents a schematic illustration of the typical laser processing and the structural evolution of the tellurite glass surface after the inscription. Figure 3.4.c-e demonstrates characteristic features and spectroscopy results after single to few laser pulse exposure. Figure 3.4.c shows the OM images and the Raman spectra of the laser-modified zones on the surface of tellurite glass.

The glass network of TWK is composed of TeO₄ tbp, TeO₃₊₁ distorted trigonal bipyramids (d-tbp), and TeO₃ tp units. It results in the presence of Raman peaks located at around 490, 610, 670, 720, and 790 cm⁻¹, and assigned to a symmetrical stretching of Te-O-Te linkages,

continuous network of TeO_4 , antisymmetric stretching of Te-O-Te linkages consisting two unequivalent Te-O bonds, Te and NBO of TeO_{3+1} and TeO_3 , stretching of Te-O⁻ in TeO_{3+1} and TeO_3 , respectively [163]. Depending on the glass composition, additional peaks can originate from glass modifier oxides. For instance, in TWK, Raman peaks at around 355, 860, and 920 cm^{-1} are related to tungsten-oxygen vibration, i.e., the stretching vibrations of W-O-W in the WO_6 units, the stretching of W-O, W-O⁻ and W=O bonds associated with WO_4 and WO_6 polyhedra [163, 164]. All these units are considered the backbone of the glass structure, whose intensity reduces by the presence of the peaks at lower wavenumber after fs-laser irradiation. The tabulated assignment of Raman bands are presented in Appendix C.

We note the presence of vibration peaks corresponding to trigonal tellurium (t-Te) after two effective pulses per focal volume in Figure 3.4.c-d. The characteristic vibration peaks of the laser-affected zone are located at 118, 139, and 260 cm^{-1} , corresponding to A_1 and E_2 modes, and second-order spectra, respectively [205, 206]. Another broad peak at around 170 cm^{-1} is attributed to Te-Te homopolar bonds in amorphous Te (a-Te). The a-Te observed in Raman spectra could survive even though a-Te is unstable above 285 K [207] due to higher stress around the interface, yet, it can be found up to 473 K [208] in some compounds of Te. In a different set of experiments, Vasileiadis et al. [209] reported the short-live presence of a-Te (similar peak $\sim 170 \text{ cm}^{-1}$) during the first exposure of a tellurite glass to continuous wave lasers (at visible wavelengths) at low power density. In addition, a peak at $\sim 238 \text{ cm}^{-1}$ that may originate from ionized Te dimers (Te_2^- color center) or Te_2 or Te_n clusters [210–212]. Another possible identification of this peak is TeO_3^{2-} (specifically the -OH units in the hydrogen bonding of $(\text{TeO}_3)^{2-}$ units [213] in the glass network) at the expense of those with higher wavenumbers, may indicate that the glass network is progressively cleaved. A few other studies state that this peak may also be related to the formation of WO_3 crystals [214, 215], rhombohedral- TeO_3 [216], or β - TeO_2 crystals [217]. Interestingly, this peak appears at every even pulse up to ten pulses and eventually disappears from Raman spectra when the fs-laser process is performed in an open-air atmosphere. Figure 3.4.d shows the changes in relative peak intensities extracted from Raman spectra in Figure 3.4.c. The evolution of the peak to the effective number of pulses highlights a dramatic increase in the t-Te at the expense of the glass network. The decomposition of this peak is discussed further in detail.

The UV-VIS transmission spectra of a laser-inscribed area of $2 \times 2 \text{ mm}^2$ on the TeO_2 -based glass surface in Figure 3.4.e indicate that the UV cut-off wavelength was approximately 460 nm (corresponding to 2.7 eV). The transmission spectra are progressively decreasing due to the formation of t-Te after each pulse. Compared to Raman spectra results, UV-VIS spectra results represent the gradual change in the glass structure upon single-pulse to two-pulse irradiation.

The time-dependent temperature distribution of focal volume calculated by thermal diffusion [136] of multi-pulse irradiation at 1 kHz is shown in Figure 3.4.f. The temperature rises quickly in the focal volume, and the lattice cools down with a typical quenching rate of $\sim 10^{14} \text{ K}\cdot\text{s}^{-1}$ eventually leads to supercooling of new dense phases and/or metastable phases recovered under extreme conditions [137]. As the pulse interval (1 μs) is longer than the lattice cooling

time, the temperature rise is not affected by the second pulse. We note that the modification created upon the first pulse changes the overall material properties within the focal volume, resulting in different thresholds, ionization rates, etc., for upcoming pulses.

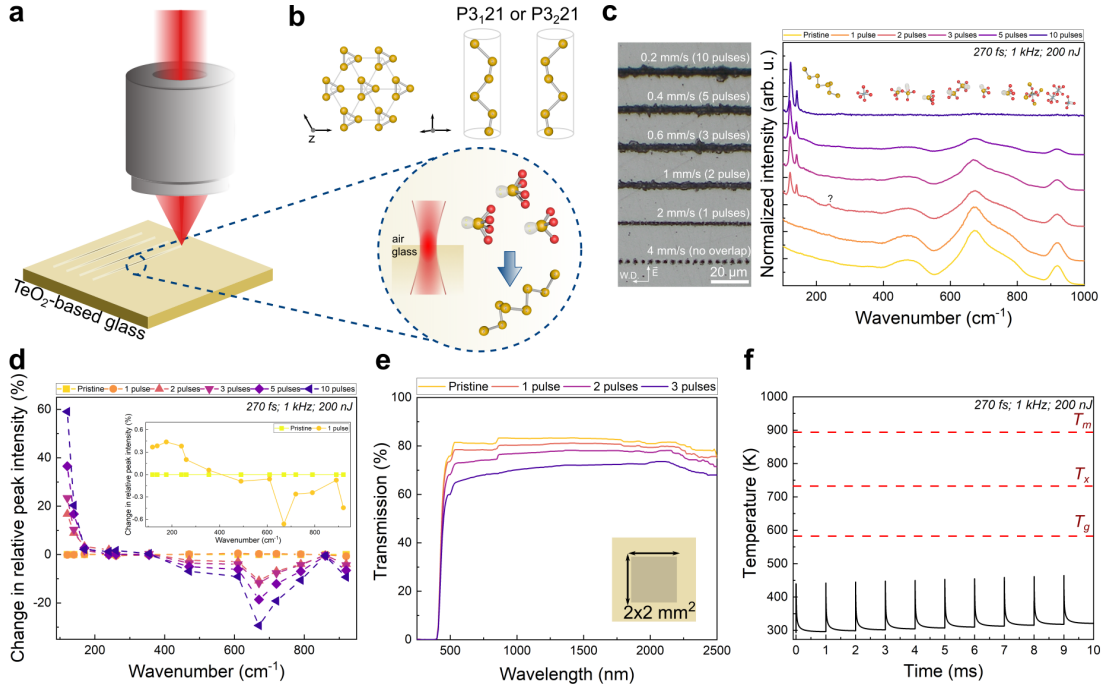


Figure 3.4: Schematic illustration of elemental Te production by fs-laser inscription on TeO_2 -based glass and its characterization at 1 kHz. a) fs-laser direct-writing process. b) The crystal structure of t-Te and the formation process of t-Te. c) Optical microscope image and Raman spectra on the surface of TeO_2 - WO_3 - K_2O glass upon fs-laser inscription at 1 kHz with 200 nJ, and from no overlap to 10 pulses (incoming pulse fluence: 0.03-0.66 J/mm^2). d) The relative intensity change of the main glass network peaks of the center of the laser-affected zone for each inscription indicated in a. Inset image shows the change in relative peak intensity upon single laser exposure. e) The transmission spectra of the scanned area of $2 \times 2 \text{ mm}^2$ with a different number of pulses per focal volume, f) simulated temporal evolution of the temperature at 1 kHz.

A similar laser exposure at 1 kHz was performed on the glass with a temperature ranging from 77 to 293 K. The sample is cooled with liquid nitrogen in a designated chamber to avoid possible thermal effects. The Raman spectra of pristine glass and three-pulse exposure are presented in Appendix C. No particular difference in Raman spectra of the laser-affected zone at room temperature or below is observed, showing the sort of athermal nature of the elemental crystallization or “phase separation” process.

Figure 3.5.a-c shows the TEM images (including HR-TEM) after a single fs-laser pulse. The overall SAED pattern in Figure 3.5.a presents a bright amorphous ring with several polycrystalline diffraction spots. The crystallized width is $\sim 1 \mu\text{m}$, and the overall depth is $\sim 350 \text{ nm}$. The laser-affected zone shows three different crystallization morphology over its depth, namely,

ejected and subsequently resolidified nanoparticles, densely packed nanocrystals, and scattered spherical nanocrystals, respectively. The different morphology of nanocrystals along the depth is related to the laser processing itself, similar to a recent study of Cu ablation by fs-laser irradiation [218]. The temperature decreases exponentially along the z-direction, resulting in a different cooling rate. The average size of the densely packed nanocrystals is 5.3 ± 1.4 nm, located at the first 143 nm below the surface. Below these nanocrystals, the scattered spherical nanocrystals are present without overlapping each other.

Figure 3.5.b shows an ejected particle, whose appearance is rare in single laser pulse irradiation. The FFT of the image indicates the presence of a nanocrystalline phase of t-Te along [100] direction, even though most of the particle remains in a glassy state, possibly due to the presence of glass structures. Figure 3.5.c shows an HR-TEM image of the center of the laser-affected zone with densely packed nanocrystals of polycrystalline t-Te along [100] direction, showing characteristic double diffraction patterns (Moiré fringes) in a spatially confined area. Moiré fringes, typically with spacing an order of magnitude higher than the original ones, may originate from the superposition of repetitive nanocrystals of t-Te with very small or equal spacing with suitable mutual orientation. Their thickness depends on the spacing of the interacting lattices, the misfit, and the angle formed [142]. The high lattice mismatch is related to laser-induced stress. A prominent example is twisted bi-layer graphene, which forms Moiré fringes at a particular angle and exhibits superconductivity and other electronic properties [219].

Figure 3.5.d-f shows the TEM and HR-TEM images upon two pulses per focal spot. With the second pulse, the surface roughness increases, and the formation of a cavity becomes prominent, filled with redeposited material. Similar to a single pulse exposure, three different characteristic morphologies along its depth are observed. The average size of the densely packed nanocrystals is 6.5 ± 2.78 nm. Several crystal orientations coexist in the FFT image of Figure 3.5.f. The interplanar distances of the nanocrystal are 0.385, 0.323, and 0.222 nm, which are in good agreement with the value of (100), (101), and (110) of the t-Te crystal structure. The lattice parameters from the SAED correspond to $a=0.4447$ nm and $c=0.5915$ nm. Details of interplanar distances and TEM analysis for a few pulses exposure are covered in Appendix C. There is no other crystalline phase detected in the laser-affected zone rather than t-Te, corroborating the Te-related nature of the extra vibration peak at ~ 238 cm^{-1} in the Raman spectra. In addition, the three-pulse exposure displayed in Figure 3.5.g-i highlights the growth of the laser-affected zone proportional to the number of pulses. Similar to the two-pulse exposure case, the irregular surface accompanied by the cavitation is still present along with t-Te nanocrystals near the surface.

3.4.2 Glass decomposition and the formation of Te nanocrystals

Glass compositions are generally designed to stay in a glassy state for their particular applications. It is more common for complex glass systems to crystallize than to decompose under

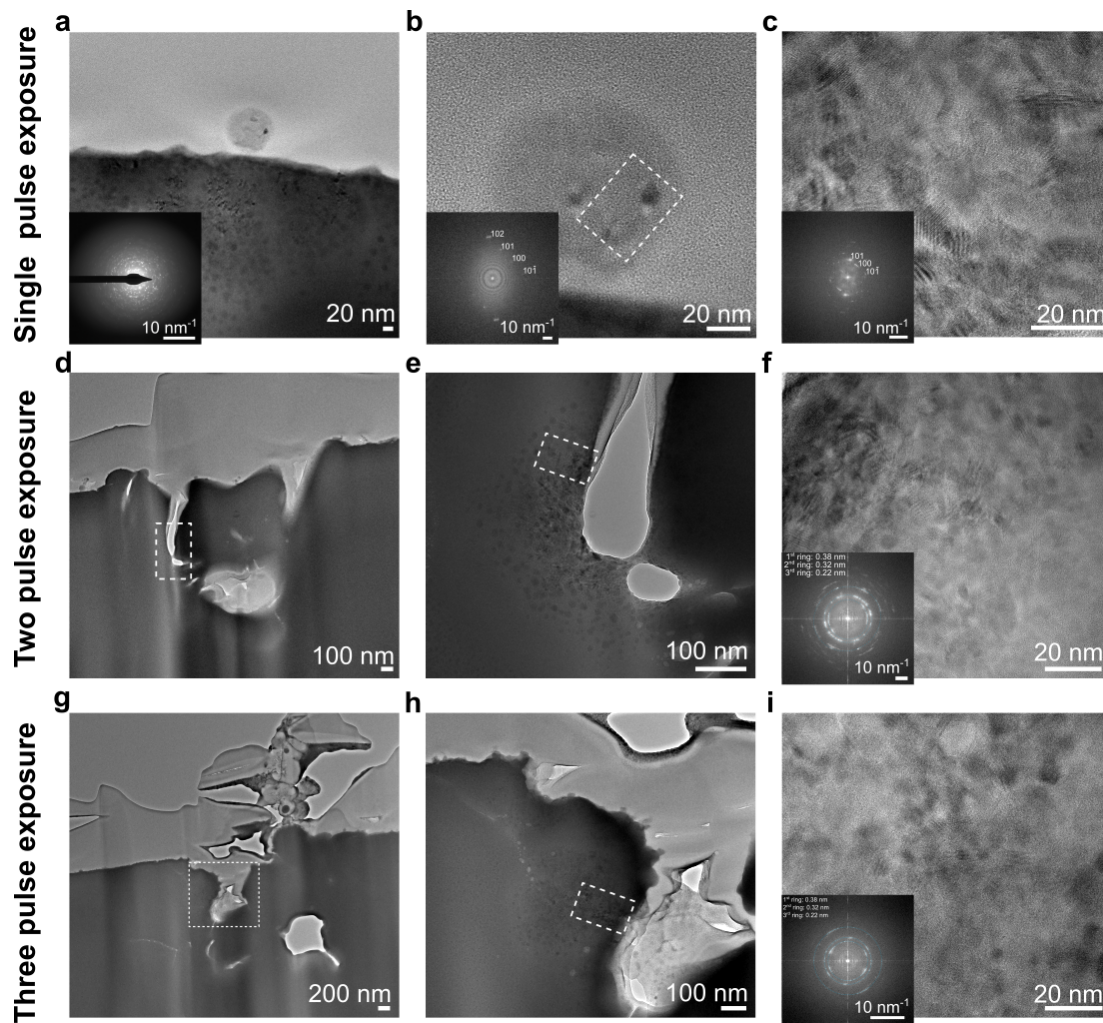


Figure 3.5: a-c) Single pulse exposure case at 1 kHz with 200 nJ (incoming pulse fluence: 0.065 J/mm^2): a) TEM images of the overall laser-affected zone within the focal volume with an inset image of SAED pattern. b) HR-TEM image of a nanoparticle in a) with inset images of Fast Fourier transformation (FFT) patterns oriented along the crystallographic [010] axis and c) HR-TEM image of the subsurface. Inset images show FFT patterns along the [010] crystallographic axis. d-e) Two-pulse exposure case at 1 kHz with 200 nJ (incoming pulse fluence: 0.13 J/mm^2): d) TEM images of the overall focal volume and e) details of the laser-affected zone. f) HR-TEM image of the subsurface zone with inset images of FFT patterns. g-i) Three-pulse exposure: g) TEM images of the overall focal volume and h) details of the laser-affected zone upon three laser pulses. i) HR-TEM image of the subsurface zone with inset images of FFT patterns.

traditional heat-treatment processes. For instance, the formation of $\alpha\text{-TeO}_2$, $\gamma\text{-TeO}_2$, and $\delta\text{-TeO}_2$ crystals, glass modifier crystals of WO_3 , or complex oxide crystals of $\text{K}_2\text{Te}_4\text{O}_9$ (potassium tetratellurite) were observed upon heat treatments [197, 202, 220, 221]. Depending on the type and the amount of glass modifier oxides, however, Te^{4+} ions in TeO_2 -based glass units can reduce partially to Te^0 by the presence of reducing glass modifiers, such as Sb_2O_3 upon glass

melting and annealing [222, 223]. In this specific case, the reduction of Te and oxidation of Sb occur homogeneously in the glass volume without any control over their precise locations.

So far, the formation of Te from tellurite glass has been observed in a handful of studies where researchers employed the addition of reducing oxides [222, 223], electro-chemical charging-discharging [177, 224] and ultrafast laser processing, the approach discussed in this thesis. In this section, we first revise what tellurium is, its properties, and common fabrication routes for micro/nano-scale devices. Further in the section, we unravel the in-depth tellurite glass decomposition and the formation mechanism of laser-induced elemental t-Te by pulse-to-pulse evolution in a non-cumulative regime.

Tellurium (Te) is a naturally occurring elemental van der Waals material that has a p-type narrow band gap semiconductor behavior, featuring a chiral atomic structure [225]. It has a trigonal crystal structure with three atoms in the unit cells, which are covalently bonded. Te atoms form elongated helical chains, side-linked one to another by weak van der Waals forces. The typical helical chain structure spirals around the z-direction, with three-fold rotational and translational symmetry, as shown in Figure 3.4.a. Depending on the helicity of the chains, either left- or right-handed (i.e., space groups $P3_221$ and $P3_121$, respectively), the material exhibits a chirality-dependent behavior [226–229]. Te has gained considerable interest because of its unique structure originating mainly from its electronic structure with four 5p-orbital valence electrons in the outer shell, with two 5s-lone-pair electrons [230] that lead to particularly attractive piezoelectric [231], thermoelectric [232], photoconductive [233], strain-sensitive [229], and nonlinear optical responses [10]. Promising devices have been reported recently, such as low-dimensional field-effect transistors [234–236], energy harvesters, and photothermal converters [237, 238].

To unleash the technological potential of Te, one has to master the production at the nanoscale. However, producing thin films, nanosheets, nanorods, nanowires, and nanoparticles remains challenging [239]. Numerous processes have been proposed, including chemical vapor deposition (CVD) [240], hydrothermal method [234], molecular beam epitaxy [241, 242], solution-based growth [243], vapor phase synthesis, growth vapor trapping [236], with many recent efforts on pulsed laser deposition [244], magnetron sputtering [245], and liquid exfoliation [246]. Here, we discuss the fabrication of t-Te nanoparticles and nanocrystals, starting from their glass oxide counterparts (TeO₂-based glass). Specifically, here, we are concerned with tellurite glass compositions that do not display any crystallization upon cooling and do not contain any dopants as a reducing agent.

With ultrafast laser processing of tellurite glass, one of the first requirements to obtain t-Te locally from TeO₂-based glass from the laser parameters are fs-laser pulse ($270 \cdot 10^{-15}$ s), high peak intensity with near-IR wavelength to satisfy the non-linear absorption, which subsequently leads to ionization and breakage of the bonds. The importance of the non-linear ionization process is highlighted by exposing the same glass with the fs-laser emitting UV wavelength (343 nm; 450 fs), compared with the fs-laser emitting near-IR with similar pulse

duration, and pulsed CO₂ laser irradiation (10.6 μm; 1 μs - 1 ms). The Raman spectra in Figure 3.6 show the signature peaks of TeO₂ crystals, similar to the results obtained from the annealing process [202]. The results highlight the importance of the interaction time and the non-linear absorption mechanism.

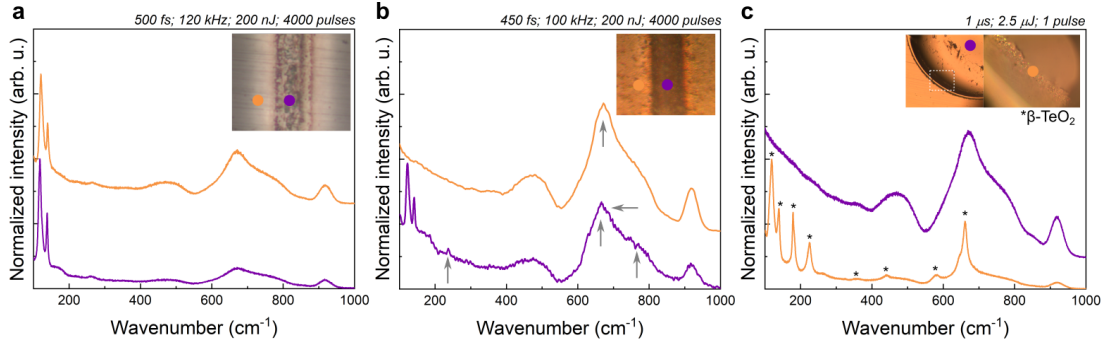


Figure 3.6: Raman spectra of the laser-affected zone in various exposure with OM images. a) After exposure with fs-laser emitting 500 fs pulse at 1030 nm, b) After exposure with fs-laser emitting 450 fs at 343 nm, and c) CO₂ pulsed laser emitting at 10.6 μm. CO₂ pulsed laser combines a relatively short pulse duration and high laser peak power at small average laser power (a few Watts).

The proposed formation mechanism of t-Te from TeO₂-based glass under a few pulses is as follows:

1. During fs-laser irradiation, the plasma is seeded by the multiphoton absorption process (~three photons) and fed through avalanche ionization of the electrons excited to the conduction band. In the present case, the plasma consists of a high concentration of Te ions upon bond cleavage. Upon the first pulse, the self-seeding reduction reaction of Te⁴⁺ to Te⁰ occurs. It has been reported that once the smallest cooperative group of molecules (Te_n clusters) consisting of two or more Te atoms together, it leads to the formation of crystalline structures or phase separation of Te. Interestingly, a similar mechanism has been reported for Te-compounds and alloys, such as Te-Se or Cd-Te-Se alloys [247, 248]. Upon the formation of multiple Te clusters, strong interchain bonding results in a decreased energetic requirement, and thus a higher Te content is more prone to crystallization. The unlocalized electrons in Te rises chain-to-chain bonding strength so that the interchain contributions increase as the glass contains more Te content [249]. According to the configurational entropy model, Te-O-Te network bonds are weak in TeO₂-based glass and bond breaking can occur upon annealing around T_g [163]. While Te makes Te-Te bonds, oxygen ions can form molecular oxygen (O_{2(g)}) as observed in other glass systems [33], and also can make a bond with the glass modifiers. The charge neutrality is satisfied by the selective oxidation of the other species, such as the conversion of WO₄ units to WO₅ or WO₆ units. In addition, W-O bonds are much stronger than Te-O bonds, therefore, higher energy is required to break the bond. The Gibbs free energy change, ΔG, of tungsten oxide, is much lower than tellurium oxide, making WO₃ formation more favorable and promoting the reduction of TeO₂ into Te [250, 251].

2. As the material is modified gradually in the focal volume, the subsequent laser pulse encounters with transformed material each time. The following pulse will be less efficiently captured by the material due to scattering by the surface roughness introduced previously [252]. Hence, the absorption efficiency will be lower for the second pulse. In addition, the absorption mechanism is altered by the presence of t-Te nanocrystals in the focal volume, whose band gap is 0.34 eV (the bandgap of the glass is ~ 3 eV). Upon the second pulse, the peak of the ~ 238 cm^{-1} in Raman spectra in Figure 3.4 can be due to Te_2 or/and Te_n clusters or interaction between species of Te-O with relative humidity, resulting in -OH groups in $(\text{TeO}_3)^{2-}$ unit. As mentioned in the first step, the self-reduction reaction of Te accompanied by the formation of Te_n clusters consisting of two or more Te atoms leads to the formation of crystalline structures of Te. In addition, upon the second pulse, a large cavity is generated, promoting the interaction between a larger surface area and the open-air atmosphere. The large surface area interacts with the open-air atmosphere, which is also the crucial step for the deoxygenation of TeO_2 -based glass units. The following chemical reactions can occur in the plasma:



The other potential assignment of the peak at ~ 238 cm^{-1} is -OH groups in $(\text{TeO}_3)^{2-}$ unit, which can be formed during the bond cleaving of the glass network such as TeO_4 , TeO_{3+1} , and TeO_3 . The origin of -OH groups can be from the inherent dangling bonds on the surface or the relative humidity in the open-air atmosphere during the fs-laser process. In our case, the glass substrates were produced in a protected atmosphere with raw materials with high purity. After glass production and stress relief treatment, the substrates were heated to 423 K for a few hours in the furnace to remove any chemically bonded water and -OH groups from the surface. Later, the substrates were kept in a dry-air atmosphere until the fs-laser exposure. In addition, it has previously been shown that tellurite glass exhibits strong resistance against relative humidity [253]. However, the interaction with the species in an open-air atmosphere in the plasma cannot be excluded completely. Therefore, the following reactions may be occurred in the plasma and facilitate Te formation in the open-air atmosphere [254]:





3. In theory, this reaction can go as long as there is a source for Te in the focal volume, such as TeO_4 , TeO_{3+1} , and TeO_3 units. Let us now examine the stopping mechanism of the t-Te formation. Figure 3.7.a shows the t-Te content at the focal volume and modified depth depending on the number of effective pulses. After forming t-Te, the concentration of t-Te rises exponentially up to ten pulses, and the concentration of Te in the glass network decays, which, in turn, affects the formation of t-Te nanocrystals and the degree of supersaturation. After the tenth pulse, the saturation indicates the completion of the conversion of the glass network to t-Te at the focal volume. The saturation mechanism is due to nucleation-induced concentration depletion in the focal volume. When the degree of supersaturation of Te is relatively low, several seeds can accumulate together to form t-Te nanocrystals. Yet, the higher degree of supersaturation causes slower nucleation kinetics of t-Te nanocrystals. Another reason is the formation of an anisotropic surface nanostructure, which makes electric field distribution non-uniform. The proposed scenarios of tellurite glass decomposition and the formation of t-Te under a few pulses are schematically illustrated in Figure 3.7.b.

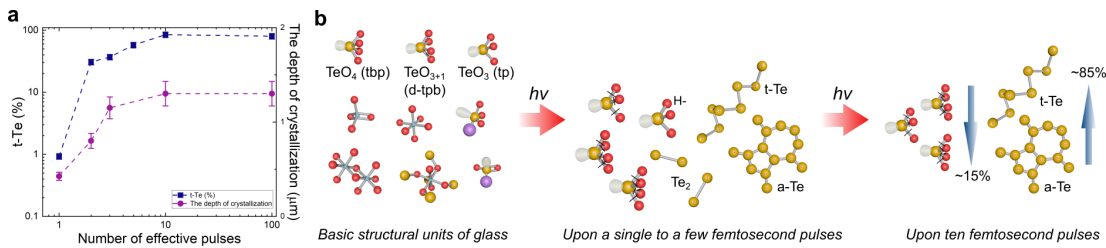


Figure 3.7: a) The percentage of t-Te Raman peaks ($I_{118, 139, 260}$) at the laser-affected zone and the maximum depth of t-Te to the number of effective pulses (measured from TEM images). b) The schematic representation of the possible scenarios of polyatomic-ions migration processes and the formation of t-Te an under few pulses.

3.4.3 Self-organized nanostructures in thermal cumulative regime

We now consider the case where the time between pulses is shorter than the lattice cooling time constant, which typically occurs in a few μs [7]. In this section, we investigate the formation of self-organized nanostructures on the surface of the tellurite glass resulting from multi-pulse irradiation coming from a scanning fs-laser beam in a thermal-cumulative regime. In particular, we report on new observations that challenge our current understanding of laser-induced nanostructure formations, highlighting the complexity and diversity of phenomena underlying this self-organization process. In addition, we observe the effect of temperature on the formation of t-Te nanocrystals and their growth.

Figure 3.8.a-i shows the laser-affected zones after irradiation with a pulse energy of 200 nJ

and a pulse overlapping ratio of 99.5% at a pulse repetition rate of 1 MHz. At 1 MHz, in the thermal-cumulative regime, self-organized nanostructures, consisting of parallel planes, oriented perpendicular to the laser electric field orientation, significantly wider than the focal area of the laser beam formed at the tellurite glass surface are observed. This fact raises interesting questions concerning the underlying mechanism driving self-organization in this particular case. To date, the formation of nanogratings has been interpreted as a subtle interplay between the incoming intense laser field and the material under direct exposure. While such a mechanism may also be present here, it is not sufficient in itself to explain the full extent of the modification. In addition, laser inscription was performed along an artificially tilted sample to observe the change of the modifications with respect to depth, as illustrated in Appendix C.

The modification exhibits two distinctive periodic arrangements: one, in the center, characterized by 800 nm-spaced nanoplanes, and a second one, near the edges of the laser-modified zone, consisting of periodic structures with a periodicity of 250 nm with a much smaller span than the one found in the center. It is worth noticing that the secondary nanostructures found at the edges of laser-affected zones are best visible for a polarization perpendicular to the writing direction and absent for a polarization aligned with the writing axis.

The electric field strength appears to be an essential parameter for triggering or suppressing self-organized nanostructures at the focal area as evidenced by varying the pulse energies in Figure 3.8.h-i. When multiple pulses accumulate at a fast enough rate, the temperature rise causes the material under exposure to melt locally (Figure 3.8.h). The nanoplanes and the secondary nanostructures are generated at higher pulse energies, consequently, at higher temperatures. They are not present at lower pulse energies (Figure 3.8.i). This sharp transition suggests the existence of a field-intensity threshold for triggering the self-organization process. In another research field exploring 'electro-crystallization', Luedtke *et al.* showed field-induced shape deformations in dielectric liquid nano-droplets [255]. Similar to Figure 3.8.j, at a low electric field, field-induced shape change was observed. Further increase in the electric field resulted in a gradual enhancement of the molecular dipole reorientation. Although in Luedtke *et al.*, the electrical field is not produced by a laser, we note intriguing similarities.

In practice, the observable surface modification threshold is found for pulse energies of 10 nJ, while the nanostructure formation starts at around 20 nJ and extends beyond 200 nJ up to the point where ablation occurs. As a characteristic signature of a temperature-cumulative process, decreasing the translation velocity (i.e., increasing the pulse-to-pulse overlapping ratio) at fixed pulse energy enlarges the modified width. Likewise, at fixed translation velocity, increasing pulse energy causes a widening of the modified area up to 10 μm . The span of self-organized nanostructures changes accordingly with an exposure time and space, and remarkably, beyond the region under direct laser exposure.

FIB milling was performed to observe the profile of these nanostructures and their extent within the material itself (Figure 3.9.a-b). Unlike surface structures reported before that are

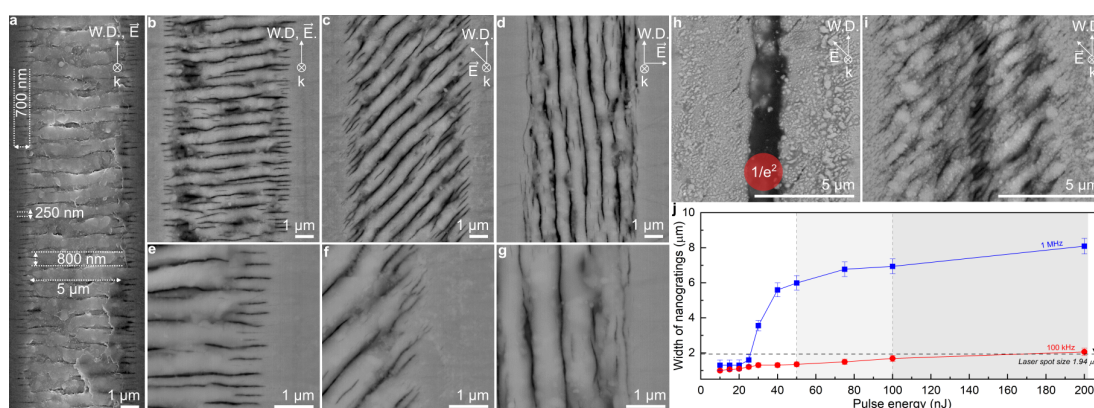


Figure 3.8: SE and BSE images of TWK surface after fs-laser irradiation at 1 MHz with different linear polarization orientations to writing direction (as indicated with the electric field orientation): a) SE and b) BSE images with longitudinal, c) 45°, and d) transverse polarization. e-g) Magnified BSE images of a boundary between the modified region and the pristine glass. The incoming pulse energy and writing speed were 200 nJ and 10 mm/s (incoming pulse fluence: 13 J/mm²), respectively. h) BSE images of 10 nJ, 0.5 mm/s (13 J/mm²); i) 200 nJ, 0.5 mm/s (262 J/mm²). j) Plot of the width of the microstructures versus pulse energy at constant writing speed (0.5 mm/s). The red and blue curves represent the width of the modified microstructures at 100 kHz and 1 MHz, respectively. In the non-thermal process, the width remains within the range defined by the beam waist at the surface. The red circle indicates the diameter of the laser spot.

in the scale of a few tens of nanometers, the depth of the nanostructures is around 1 μm in our case and increases with the pulse energy [256]. These observations show that higher fluence increase *both* lateral and depth extensions of modified volumes. Similarly, a fluence-dependent growth of the melt depth has been observed in photo-excited tellurium films [207, 257].

EDS observations of laser-modified zones in TWK glass are shown in Figure 3.9. Overall, little variations in the chemical composition have been observed as a consequence of laser irradiation. The first nanostructures observed for laser-pulse energy around 20 nJ is shown in Figure 3.9.c. Nanoplanes show alternating Te and O contents, whereas the overall W content remains slightly higher. Figure 3.9.d shows the elemental distribution across a laser-modified zone obtained with a pulse energy of 100 nJ. Alternating Te and O contents along nanoplanes are observed. Compared to the pristine material (dashed lines in Figure 3.9), both modifications show approximately 3 wt% higher Te, 4 wt% lower O, and 1 wt% higher W contents. Changes in the chemical composition of tungsten, tellurium, and oxygen elements are also found beyond the nanoplanes. On the other hand, the content of K atoms remains constant since it is the key modifier of the backbone tellurite glass structure. Experiments have shown that potassium is not sensitive to variations in the local structure of the glass, and the structure of potassium-tellurite (K₂O-TeO₂) glass has been preserved without any decomposition during heating and cooling cycles [197].

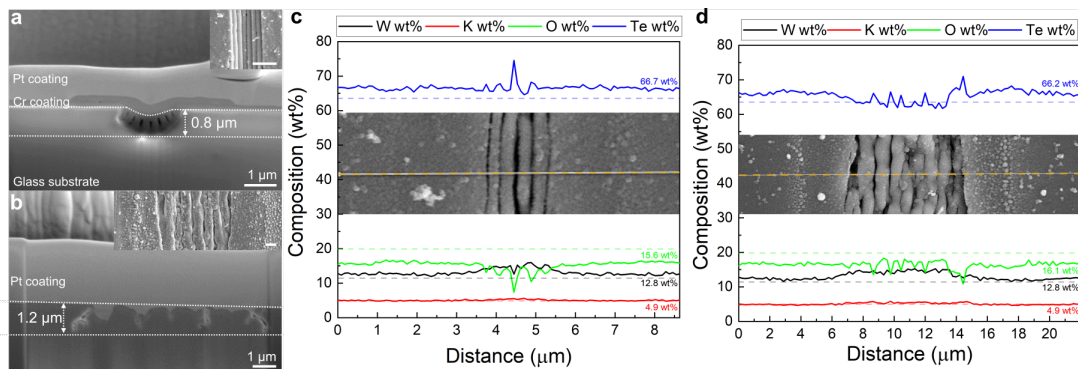


Figure 3.9: SE images of FIB-cut in TWK glass: a) 30 nJ, 100 mm/s (0.2 J/mm^2) and b) 100 nJ, 0.5 mm/s (131 J/mm^2 at 1 MHz), respectively. Inset images show the modified zone before FIB milling. The scale bars in both inset images are $1 \mu\text{m}$. Elemental distribution across a modified zone accompanied with SE images at 1 MHz: c) 20 nJ, 0.5 mm/s (26 J/mm^2); c) 100 nJ, 0.5 mm/s (131 J/mm^2). Colored values indicate the average composition along the scanned line. Dashed lines indicate the composition of pristine glass. All images correspond to a transverse polarization (to the writing direction) and a 1 MHz pulse repetition rate.

To investigate further the laser-induced modifications, we performed Raman spectroscopy measurements on various specimens. Figure 3.10 shows the optical microscopy images of TWK surfaces after fs-laser irradiation and the corresponding Raman spectra collected at points distributed across the laser-modified zone with a spatial sampling period of $1 \mu\text{m}$. The morphology of the line in Figure 3.10.a is similar to the one in Figure 3.8.h. Gradual modifications of the glass network are observed along the scanned line as shown in Figure 3.10.b. The spectrum at the beginning of the Raman scan (at $x = -10 \mu\text{m}$) is similar to the one of the pristine glass. The peak assignment, presented in Table Appendix C, was performed based on the work from Kosuge *et al.* [163, 164]. The main peaks are found around $355, 490, 610, 670, 720, 790, 860,$ and 920 cm^{-1} .

Along the scanned line in Figure 3.10.b, a few peaks with lower wavenumbers start to appear three micrometers away from the center ($x = 0 \mu\text{m}$). As their intensity gradually increases towards the center, the main peaks assigned to structures in the glass vanish in Figure 3.10.c. Raman spectra are deconvoluted into Gaussian bands, and accordingly, the peaks at $119, 139, 170, 220,$ and 260 cm^{-1} are observed at the center of the modified region. Peaks at $119, 139, 220,$ and 260 cm^{-1} belong to a crystallized t-Te phase. 170 cm^{-1} is attributed to Te-Te homopolar bonds in a-Te. This result indicates the existence of a chain-like structure within the glassy matrix after fs-laser irradiation. Detailed information on the deconvolution of Raman spectra is presented in Appendix C.

Figure 3.10.g-i shows the relative intensities of the main peaks at various fluences. From outside of the modification to its boundary, the concentration of Te-O bonds decays in quantity. At the boundary of nanostructures, there is a sharp increase in t-Te/glassy- TeO_2 ratio, followed by a decrease towards the center. There, the t-Te content decreases with laser fluence and

transforms to glassy- TeO_2 , the intensity of peaks related to $\text{TeO}_3+\text{TeO}_{3+1}$ increases, and finally, TeO_4 tbp decreases as reported for the tellurite glass with higher glass-modifier content.

Furthermore, the crystallization event expands beyond the focal volume and nanostructures, as in Figure 3.10.d-f. At a fixed number of pulses, an increase in pulse energy significantly affects the crystallization width. Above the non-linear absorption threshold, the crystallized width increases approximately by $2\ \mu\text{m}$ for every 10 nJ when the translation velocity is fixed to 0.5 mm/s. Likewise, at a fixed pulse energy, the translation velocity has a dominant effect on the crystallized region. In Figure 3.10.f, self-organization is localized within $10\ \mu\text{m}$, whereas the crystallized zone is found in a wider region (up to $40\ \mu\text{m}$). These observations are similar to a heat-driven process.

Both, Raman spectroscopy and EDS results of the self-organized nanostructures are consistent with one another. In brief, after the fs-laser irradiation, a cohort of tungsten atoms migrate to the vicinity of the nanostructures, whereas oxygen is removed along modified zones. TeO_3 tp and TeO_{3+1} d-tbp proportions are greatly reduced and change appreciably in the spatially confined medium, as Te becomes depleted by deoxygenation. In the meantime, the coordination number of tungsten atoms might be altered, inducing a change in the Raman peak-intensity ratio I_{355}/I_{920} . At lower pulse energy, the modified zone consists of a-Te and t-Te. At higher pulse energy, the final microstructure depends on the exposure dose (i.e., the number of cumulative pulses). For low-pulse overlapping ratios, only t-Te and a-Te are found via Raman spectroscopy analysis after a few pulses of exposure. As pulses accumulate, the temperature becomes high enough over a longer time to promote further glass decomposition. However, during this process, defects and dangling bonds of Te may react with neighboring oxygen molecules. This oxidation process in the nanostructured zone supports the following transformation sequence: $t\text{-Te} + a\text{-Te} \rightarrow \text{glassy-TeO}_2$ [209]. Localized ionization of the ambient air due to the high irradiance ($\sim 10\text{-}30\ \text{TW}/\text{cm}^2$) [258] in the vicinity of the material surface is likely to further enhance this effect by feeding ionized oxygen atoms to the oxidation process. In parallel, the migration of tungsten elements contributes to preserving the glassy- TeO_2 along the nanoplanes.

Self-organized nanoplanes in the center of laser-affected zones and secondary nanogratings at the boundaries have notable differences in terms of structures highlighted in Figure 3.10. Similar to Raman results, EDS shows slight differences in elemental content (Figure 3.9). We attribute the formation of these secondary gratings to mechanical rupture and cracks formation during solidification caused by a difference in thermal expansion coefficient at the boundary between modified and unmodified materials. To support this observation, we note that since W^{6+} is a heavy metal ion, the depletion of W from the matrix in the nanogratings distorts the glass network and contributes to high-stress levels at the phase boundaries, eventually leading to cracks formation. The periodicity of these boundary nanocracks originates from the periodicity of the nanogratings phase itself. The fact that the periodicity of the secondary nanogratings does not change with laser fluence, further supports that this process is of thermo-mechanical origin, and not an immediate outcome of laser exposure. Note that

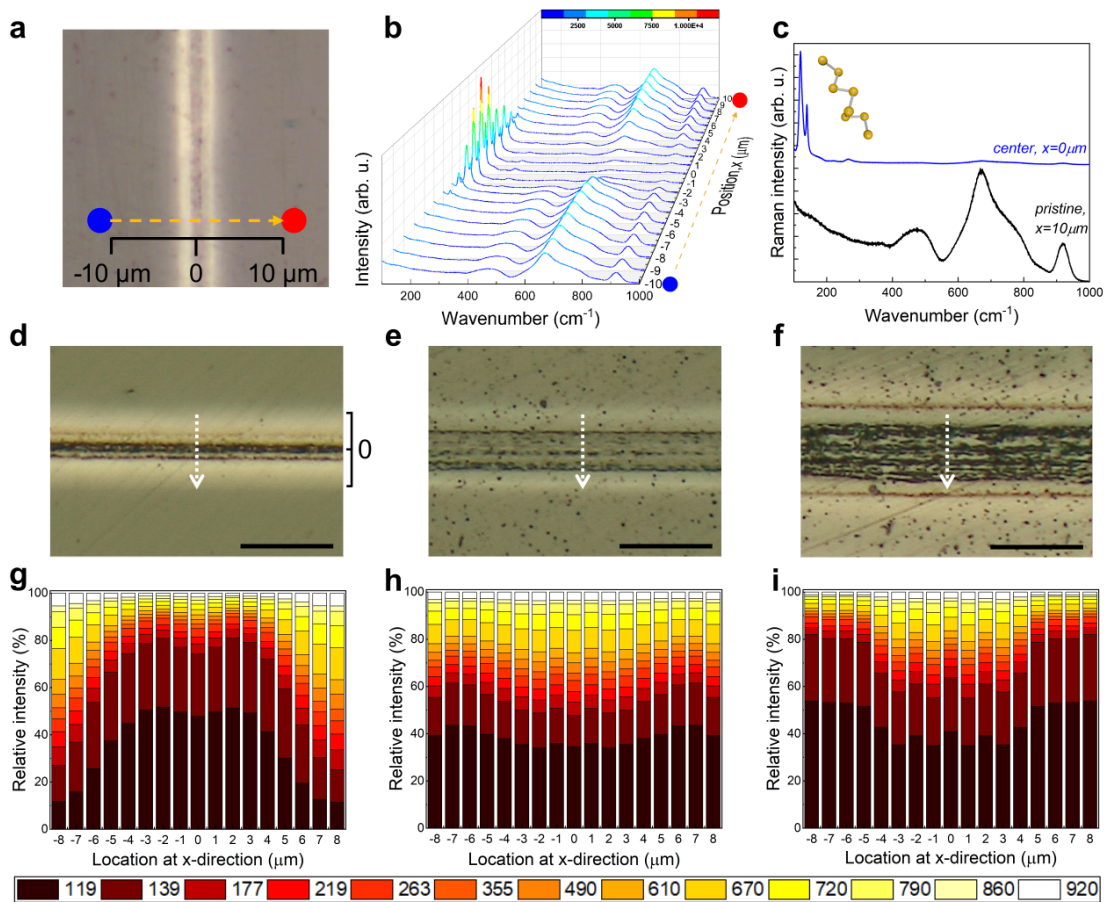


Figure 3.10: a) OM images of potassium-tungsten tellurite surface after fs-laser irradiation with laser parameters of 10 nJ, 0.5 mm/s (13 J/mm^2) at 1 MHz. b) Raman spectra collected by scanning the laser across the modified zone and spectra collected at each $1 \mu\text{m}$. The yellow dash line indicates the scanned line with the Raman laser. c) Raman spectra were taken at the center of modification at $x=0 \mu\text{m}$ and in an unmodified region at a position of $x=10 \mu\text{m}$ away from the center. OM images of TWK surface after fs-laser irradiation at 1 MHz: d) 20 nJ, 0.5 mm/s (26 J/mm^2); e) 200 nJ, 10 mm/s (13 J/mm^2) and f) 200 nJ, 0.5 mm/s (262 J/mm^2). g-i) Relative intensities of the main Raman spectra peaks found in modified zones (by scanning across the modified zone with $1 \mu\text{m}$ of step size). White dash lines indicate the Raman scanned lines and directions. The color-coded legend shows the main peaks and their assigned colors. The black scale bar is $20 \mu\text{m}$.

some of these nanocracks are also seldom present in the middle of the laser-affected zones, in between nanoplanes (see Figure 3.8 for a few examples), which is consequent with a fracture during the solidification model, as proposed above. It also explains why fewer to none is found in the case of a polarization perpendicular to the writing direction, as the vertical morphology of nanoplanes leads to fewer stress-concentration points, prone to crack-nucleation.

The fabrication of localized crystalline t-Te provides also a means for exploring how laser-

induced geometric confinement around the focal volume. Thus far, we described how the TeO_2 -based glass network undergoes a dramatic modification. For further analysis with advanced techniques, we select a representative laser parameter, the same as in Figure 3.10.i. The extended self-organized nanostructures, perpendicular to the laser polarization, and ejected nanoparticles, which are byproducts of laser exposure, are shown in Figure 3.11.a. The transmission spectra of the pristine glass and the laser-affected zone are presented in Figure 3.11.b. The reason for the vast reduction in the transmission is the formation of t-Te, photodarkening due to rearrangement in the glass structure, increase in reflection and scattering due to surface nanostructures and nanoparticles. As for the Te nanoparticles [238], the absorption spectrum of the laser-affected zone shows broadband absorption with two distinct peaks around 400 nm and 1000 nm. Figure 3.11. displays the time-dependent temperature distribution of the focal volume calculated using the thermal diffusion model for the case of multi-pulse irradiation at 1 MHz. TeO_2 -based glass under the three-dimensional (3D) enclosure of a laser focal volume is subjected to high pressure and temperature. Under our experimental conditions, since the arrival of the next pulse (1 μs) is shorter than the lattice cooling time, the thermal accumulation regime is observed, subsequently leading to a melting of the glass surface.

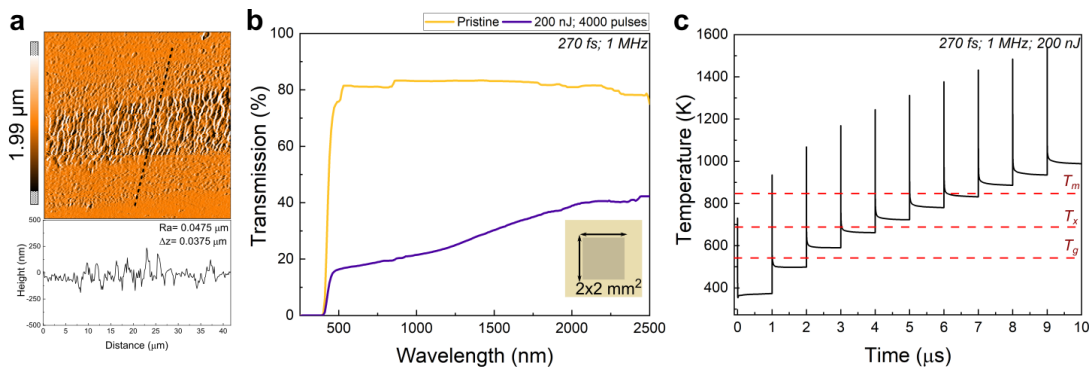


Figure 3.11: a) AFM image of surface nanostructures at $40.6 \times 40.6 \mu\text{m}$ area with z-direction intensity of $1.99 \mu\text{m}$. b) UV-VIS transmission spectra of TWK glass surface (thickness of 2 mm) and after fs-laser exposure of 200 nJ with ~ 4000 pulses (incoming pulse fluence: $262 \text{ J}/\text{mm}^2$). Inset: The schematic of laser-modified area ($2 \times 2 \text{ mm}^2$) on TWK glass for UV-VIS spectroscopy. c) Temporal temperature evolution during the first ten pulses within the focal volume. The dashed lines indicate the glass transition (T_g), crystallization (T_x), and melting (T_m) temperature of the TWK glass after fs-laser exposure of 200 nJ with ~ 4000 pulses (incoming pulse fluence: $262 \text{ J}/\text{mm}^2$).

Figure 3.12 shows BSE and TEM images of the laser-affected zone on the tellurite glass surface upon multi-pulse fs-laser inscription at the thermal accumulation regime. The typical BSE image of self-organized surface structures perpendicular to the laser polarization is presented in Figure 3.12.a. Figure 3.12.b presents the TEM image of the cross-section of the laser-affected zone with the schematic of the laser focal point. Figure 3.12.c shows the TEM image of the tellurite glass surface at the border of the focal volume with an inset image of the SAED pattern. The SAED pattern exhibits the polycrystalline nature of the area, which contains ejected

nanoparticles with subsurface nanocrystals. The relatively large grains result in bright single diffraction spots, whereas the ring pattern originates from several nanocrystals with different crystallographic orientations. The details of the SAED pattern can be found in Appendix C. The X-ray diffraction (XRD) pattern of the SAED pattern shows a slight shift from t-Te (Te-I), which corresponds to t-Te (Te-I) at 2 GPa [259]. Undefined weak diffractions show a possible match with the Te-II phase [260], although further confirmation is needed with advanced characterization techniques. The electron-lattice energy transfer in the fs-laser process results in lattice heating in μs time scale with shock wave (pressure-wave) generation. The pressure is estimated to be around a few TPa in the volume of the fused silica and on its surface with an energy density of 40 J/cm^2 [261]. The generated pressure results in high-density silica [262] and a new crystalline phase [263] in fused silica or elemental aluminum formation in the sapphire (single crystal of $\alpha\text{-Al}_2\text{O}_3$) [264]. Additionally, the surface cracks along the laser writing direction upon fs-laser irradiation in Appendix C indicate the stress level exceeds Young's modulus of TeO_2 -based glass ($\sim 42 \text{ GPa}$) [160].

From surface to subsurface, there are three different characteristics along its depth similar to the one at 1 kHz, i.e., nanoparticles, densely packed irregularly shaped nanocrystals, and spherical nanocrystals. Figure 3.12.d displays the morphology of typical ejected particles with an inset of the FFT pattern. Crystalline nanoparticles indicate the material ejection after the surface melting, re-solidification, and re-deposition to the surface. The HRTEM and SAED confirm that nanoparticles are excellent crystallinity of [100] t-Te with an average diameter of 54 nm. Figure 3.12.e-g shows TEM images of the center of the laser-affected zone at focal volume with inset images of SAED patterns. The SAED pattern in Figure 3.12.e shows polycrystalline t-Te, and unidentified diffractions with t-Te in Appendix C. Similarly, those diffractions fit well with Te-I with a weak signal of Te-II rather than the oxide polymorphs of Te and known compounds of each element present in the pristine [205, 260, 265–267]. The results are not surprising since at least tens of GPa of pressure is generated on the surface of dielectrics upon the fs-laser process, yet, it needs advanced techniques to confirm high-pressure Te phases. It is assumed that the peak pressure at the front of the shock wave driven by the laser is at least a few times the pressure value necessary to induce structural phase changes near the point where the energy is deposited. The first subsurface layer in Figure 3.12.f displays densely packed irregularly distributed nanocrystals with double diffraction. The interplanar spacings of the nanocrystals are 1.2, 0.38, 0.32, and 0.22 nm, corresponding to the double diffraction of (001), the diffraction of (100), (101), and (110) of the t-Te structure, respectively. The average nanocrystal size is $12.78 \pm 2.84 \text{ nm}$. Below the first $\sim 330 \text{ nm}$, the scattered spherical nanocrystals are located without overlapping each other. The interface between two types of nanocrystalline morphology is presented in Figure 3.12.g. The interplanar spacings are 0.38 and 1.75 nm, corresponding to (100) and (013), respectively. The average thickness of the third layer is 420 nm. The SAED pattern of the scattered spherical nanocrystals shows diffraction of t-Te.

Another characteristic of laser modification in dielectrics is the formation of self-organized nanocracks, perpendicular to the laser polarization [62]. The cracks were enlarged during

TEM lamella preparation by FIB, and hence, their dimensions after the milling appear larger than they actually are. The nanocracks under the surface are surrounded by alternating glass and polycrystalline t-Te layers. The very first layer of 10-20 nm is an amorphous material. Polycrystalline layers show Moiré fringes due to the same reason mentioned above. The polycrystalline t-Te around nanocracks shows densely packed irregularly distributed spherical morphology similar to the ones observed in the first layer laser-affected zone. We note that the oxidation of the t-Te nanocrystals into TeO_2 crystals in a multi-pulse regime is not detected by Raman spectroscopy and is not observed in high-resolution imaging.

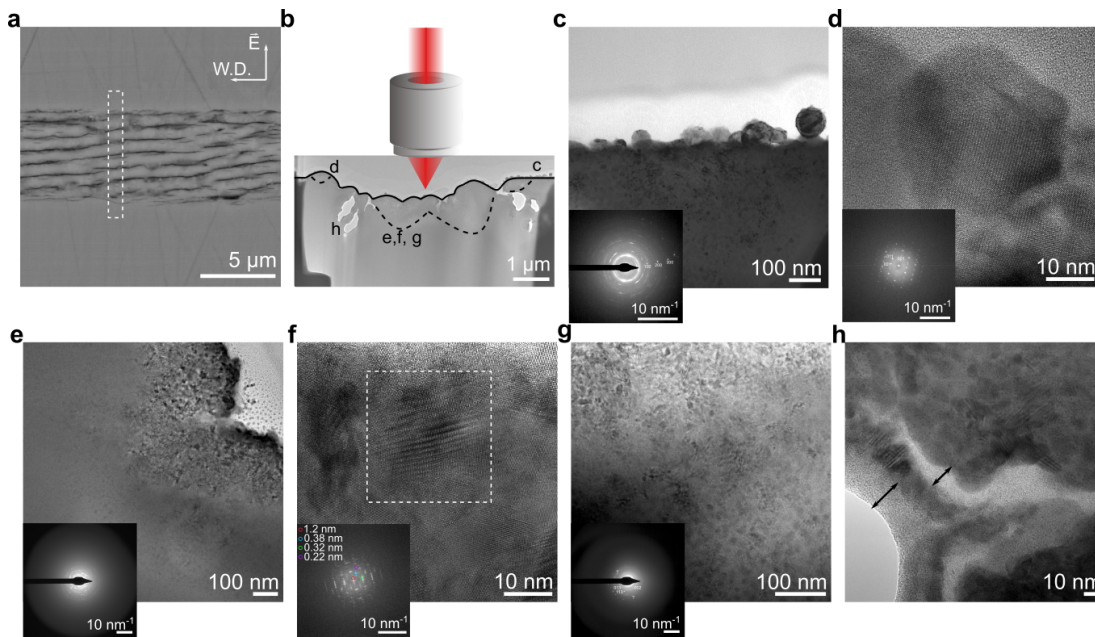


Figure 3.12: a) BSE image of self-organized nanostructures on the surface of TWK glass upon fs-laser inscription at 1 MHz with 200 nJ and 4000 pulses (incoming pulse fluence: 262 J/mm^2). b) TEM image of the cross-section indicated by a dashed line in (a) with the schematic of the laser focal point. c) TEM image of the surface with an inset image of the SAED pattern, d-e) HR-TEM image of the ejected particles and subsurface with inset images of FFT patterns. The zone axis of d) is [100]. f-g) TEM images of the laser-affected zone at focal volume with inset images of SAED patterns with the zone axis of [0-31] and h) the TEM image of nanostructures in the volume. The location of c-h images is marked in b.

The investigation in this section emphasizes the formation of nanocrystals in extreme conditions, such as high temperature and pressure under irradiation with 4000 pulses at 1 MHz. The crystallinity of the ejected nanoparticles is improved. The number and the average size of particles increase with the multi-pulse exposure; the average size of nanocrystals is slightly larger than the one at a few kHz. The effect of the thermal-cumulative regime on the nucleation rate, grain growth, and connectivity of the nanocrystals can be highlighted, for example, by nano-tomography, high-resolution X-ray diffraction techniques (synchrotron radiation), photo-luminescence spectra, or electrical resistivity measurement. The image of the spatial photoluminescence (PL) intensity distribution of the processed samples is illustrated in Figure

3.13.a, obtained by illuminating with 808 nm [204]. The photoluminescence is enhanced mainly due to elemental crystallization, the intensity rises with the laser repetition rate from 1 kHz to 1 MHz. High intensity in PL image taken after 10 seconds of exposure indicates the long recombination lifetime of the laser-affected zone, potentially useful for solar cell applications. In addition, early post-mortem by X-ray diffraction techniques (via synchrotron radiation) on the same sample has been exploited. The results at 100 kHz and 1 MHz are displayed in Appendix C. Besides, the DC resistivity is tested on a single laser-inscribed track with a length of 10 mm, and the results obtained by 4-probe measurement are presented in Table 3.3. The electrical resistivity of the laser-affected zone at the thermal-cumulative regime shows the lowest value, similar to polycrystalline bulk Te [268, 269]. At last, we present the laser-processing window (incoming pulse fluence vs. repetition rate) in Figure 3.12.a. Three distinct regions, namely visible modifications by optical tools, self-organized nanostructures, and ablation are revealed by various characterization techniques.

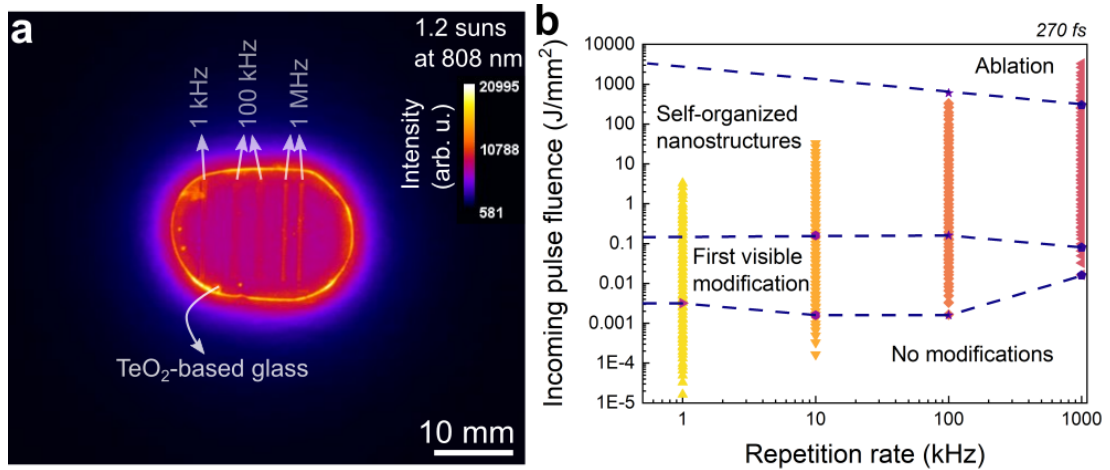


Figure 3.13: a) The laser-processing window (incoming pulse fluence vs. repetition rate) on the surface of TWK at 270 fs. b) PL image of sets of laser-written tracks at a rate from 1 kHz to 1 MHz on TWK glass. The color bar indicates the intensity of electron-hole recombination. The measurement lasted 10 s under constant illumination at 808 nm at 1.2 suns equivalent.

Table 3.3: The electrical resistivity of the laser-irradiated tracks on the surface of TWK with various laser-writing conditions. Note that the length of the laser tracks is 5 mm, and the cross-sectional area is calculated from TEM analysis.

Laser processing parameters	DC Resistivity ($\Omega \cdot m$)
1 kHz; 200 nJ; 10 pulses (0.66 J/mm ²)	188.143
1 kHz; 200 nJ; 4000 pulses (262 J/mm ²)	0.53981
100 kHz; 200 nJ; 4000 pulses (262 J/mm ²)	0.16028
1 MHz; 200 nJ; 4000 pulses (262 J/mm ²)	0.00445

3.4.4 Effect of ambient conditions on laser-induced modifications

So far, upon the fs-laser writing process under an open-air atmosphere, the formation of the laser-induced defects may indicate the interaction of the glass surface with an ambient environment. The purpose of this part of the study is to investigate the effect of environmental conditions on the formation of t-Te, a crucial step for establishing a general understanding. In this section, fs-laser writing is performed on a sample in a sealed chamber with a controlled dry air atmosphere [$O_{2(g)}+N_{2(g)}$], a dry pure nitrogen atmosphere [$N_{2(g)}$], and a vacuum ($<10^{-3}$ Pa). The results are compared with the open-air atmosphere ($O_{2(g)}+N_{2(g)}$, relative humidity level is 40%, constantly measured.).

Figure 3.14 shows the experimental setup, the Raman spectra of the laser-affected zone, the relative intensity ratio of the main peaks, and possible scenarios of polyatomic-ion migration processes occurring at the TeO_2 -based glass surface upon fs-laser inscription under various atmospheres. Figure 3.14.a presents the experimental setup of the sealed chamber used in this study for different atmospheres. The same laser exposure conditions were applied with the same laser for all four atmospheric conditions.

At 1 kHz with two-pulse irradiation, the sharp peak at 238 cm^{-1} exists in the Raman spectra for all atmospheric conditions. Figure 3.14.b shows the Raman spectra of the laser-affected zone under open-air, dry air, dry nitrogen, and under a vacuum at 1 MHz. Compared to irradiation in open-air, the peak at $\sim 238\text{ cm}^{-1}$ is present in dry air, a vacuum, and dry nitrogen conditions, whose intensity varies as follows: $I_{\text{nitrogen}} > I_{\text{vacuum}} > I_{\text{dry air}}$. The surface of the glass substrates was free from chemically bonded water and $-OH$ groups before fs-laser irradiation. Therefore, the experimental results under various atmospheres indicate that the origin of the peak at $\sim 238\text{ cm}^{-1}$ can be only Te^- dimers or Te_n clusters. Even though the nature of the peak is identified, the intensity of the t-Te peaks at 119, 139, and 260 cm^{-1} decreases with an increase in the intensity of 238 cm^{-1} in Figure 3.14.c. This evidence indicates that the presence of an open-air atmosphere (relative humidity and oxygen) plays a significant role in the formation of Te and supports the reduction reactions of (3.3) and (3.4).

Let us examine the fs-laser irradiation under dry nitrogen flow, indicating the minimum level of t-Te formation. Figure 3.14.d-e shows the Raman spectra of the laser-affected zone irradiated under dry nitrogen and the intensity ratios of the Raman peaks (A to E are the fractions of t-Te/glass, a-Te/glass, $238\text{ cm}^{-1}/a\text{-Te}$, $238\text{ cm}^{-1}/t\text{-Te}$, and $238\text{ cm}^{-1}/\text{glass}$, respectively). Under open-air exposure, the peak of 238 cm^{-1} disappears upon exposure to ten pulses at 1 kHz. Even at lower pulse energy, the focal volume is converted into t-Te. However, after exposure to 4000 pulses under dry nitrogen flow, the peak is still present, whose intensity increases with the pulse energy. The presence of 238 cm^{-1} indicates that the conversion of glass units to t-Te in the laser-affected zone is not completed effectively. The polarizability of the molecules can decrease under different atmospheres, resulting in lower peak intensity in Raman spectra. Similarly, Figure 3.14.f-g highlights the spatial peak distribution along the laser-affected zone under open-air and under nitrogen atmospheres. Validating the suppression of t-Te formation

under dry nitrogen flow, interpreted from Raman data, a 4-probe electrical measurement is performed to the laser-affected zone inscribed under nitrogen. Under the same conditions as in Table 1 (200 nJ with 4000 pulses at 1 MHz; incoming pulse fluence of 262 J/mm²), the DC resistivity of the laser-written track is 115.9 Ω·m.

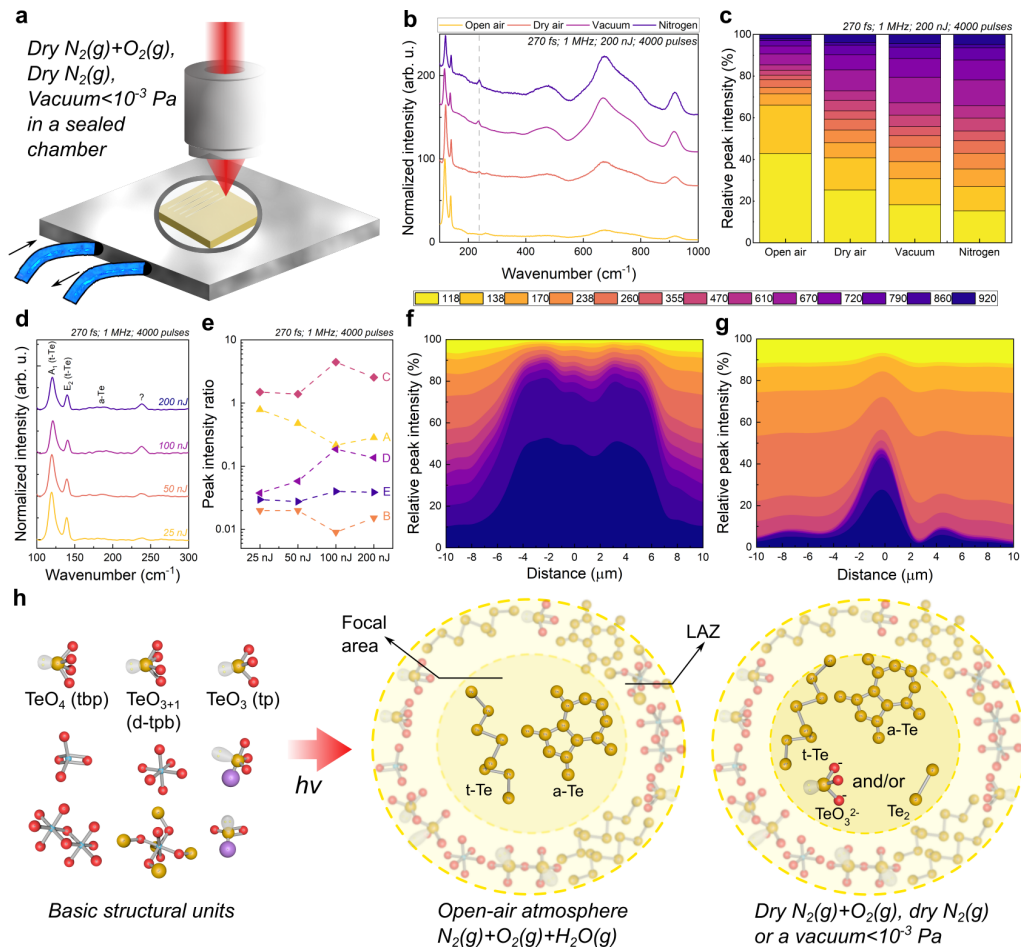


Figure 3.14: a) Schematic representation of experimental setup with a sealed chamber. b) Normalized Raman spectra of the center of the laser-affected zone under different atmospheres at 1 MHz. c) The relative intensity of the main peaks along the laser-affected zone under different atmospheres. d) Normalized Raman spectra of the center of the laser-affected zone under the dry nitrogen atmosphere. The laser parameters are 4000 pulses at various energies (25, 50, 100, and 200 nJ; incoming pulse fluence from 33 to 262 J/mm²) at a rate of 1 MHz on the surface of TeO₂-WO₃-K₂O. e) The intensity ratio of the peaks. A to E indicate the peak intensity ratios of t-Te/glass, a-Te/glass, 238 cm⁻¹/a-Te, 238 cm⁻¹/t-Te, and 238 cm⁻¹/glass, respectively. Spatial distribution of the ratio of peaks along the laser-affected zone, prepared under f) open-air atmosphere and g) a constant dry nitrogen flow at 25 nJ with 4000 pulses (incoming pulse fluence: 33 J/mm²). h) Schematic representation of the t-Te formation under different atmospheres.

Interestingly, the effect of the atmosphere has been investigated for conventional TeO₂-based

glass melting [270]. There, among argon, oxygen, and room atmospheres, Te^{4+} ion formation is inhibited in the inert atmosphere, and more Te^{4+} concentration is obtained when the glass is prepared in an oxygen-rich atmosphere. From our experiments, we show the fs-laser exposure similar situation to a glass melting. Similarly, during the fiber drawing process, tellurium-doped silica fibers drawn under an argon atmosphere show a formation of Te_2 dimers compared to fibers drawn in oxidizing conditions [212]. Although, in this case, the oxidation of Te_2 dimer causes a diminish of this peak under an oxidizing atmosphere, in our case, oxygen is removed quickly from the laser-affected zone, leaving a plasma rich in terms of Te atoms under fs-laser irradiation.

A possible explanation can be that as in an open-air atmosphere, the formation of Te^- dimers and Te_n clusters is an essential step for the completing t-Te transformation. It means the energy delivered by each subsequent pulse is enough to break the Te-O bonds to form free Te atoms and deoxygenate the laser-affected zone. Subsequently, the abundance of Te atoms in the plasma facilitates the formation of Te nanoclusters and nanocrystals. On the contrary, under the dry nitrogen atmosphere, the transformation of Te^- dimers and Te_n clusters to Te nanocrystals remains challenging. It shows that oxygen and humidity (-H or -OH groups) are necessary for the reduction reaction, whose absence eventually hinders the formation of the t-Te. Note that Raman analysis did not reveal the formation of any compound containing nitrogen. The schematic illustration displaying the effect of atmosphere is presented in Figure 3.14.h. Post-exposure experiment shows that the irradiation atmosphere is one of the key elements to modulate the content of t-Te at the laser-affected zone.

3.4.5 Effect of glass composition on laser-induced modifications

We interpret the formation t-Te nanocrystals and self-organized nanoplanes are accompanied by elemental redistribution and deoxygenation, and their growth outside the focal volume. While the glass decomposition and nanostructures surprisingly extending outside the optical exposure zone are unusual, the question remains whether these phenomena are universal in the field of fs-laser machining [62, 64]. Here, our goal is two-fold. One is to evaluate the validity of t-Te formation for all TeO_2 -based glass systems. The second one is to investigate how self-organization processes are influenced by variations in glass structure and compositions for glass systems sharing a same TeO_2 back-bone network.

Various compositions of multi-component tellurite glasses, TWA, TZNB and TNGPZ [271–274] have been selected due to technical importance and compared with the previous test sample (TWK). For instance, the presence of heavy-metal ions further increases the nonlinear refractive index in femtosecond regime [167]. Another example is that the addition of Ag or Li ions may confer TeO_2 glasses into high ionic conductive glasses that are interesting for solid-state energy conversion applications and immobilization of radioactive wastes in nuclear applications [271]. The details on the physical properties of the substrates and fs-laser modification thresholds are presented in Table 3.1.

First, we investigate the formation mechanism in a non-cumulative regime for another glass system other than TWK. OM image and Raman spectra of TZNB glass with few pulse exposure at 1 kHz are presented in Figure 3.15. 3.15.b presents Raman spectra of the center of the laser-affected zone demonstrated in 3.15.a. Unlike TWK, the signature of t-Te at 119 and 139 cm^{-1} , a-Te at 180 cm^{-1} and Te_2 dimers at 238 cm^{-1} are present after a single shot in the laser-affected zone of TZNB. In addition, their intensity increases with upcoming pulse and pulse energy as in Figure 3.15.c. This initial observation confirms the formation of t-Te nanocrystals upon a single laser pulse irradiation without further characterization by advanced techniques. In addition, we observe all the selected tellurite glass systems in a thermal-cumulative regime.

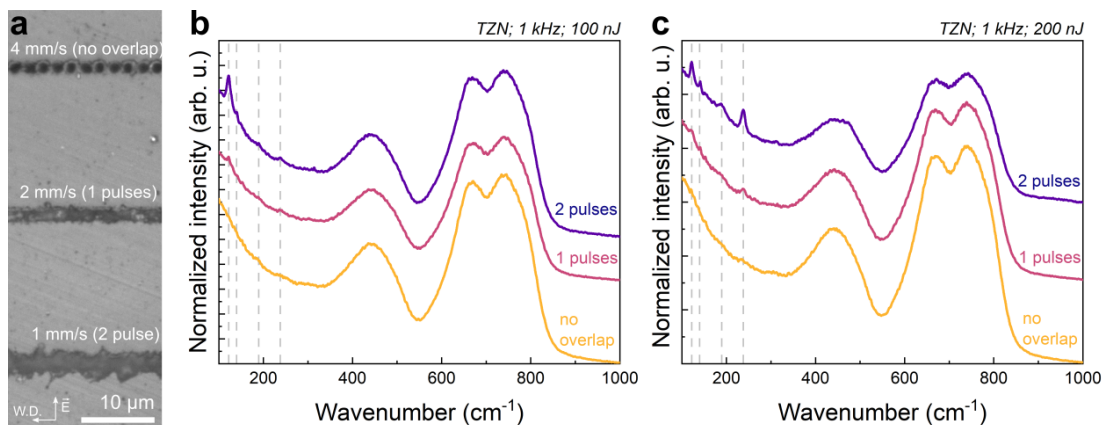


Figure 3.15: a) OM images of the laser-affected zone of TZNB at 1 kHz. Raman spectra of the center of laser-affected zone inscribed with b) 100 nJ with few pulses and c) 200 nJ with few pulses (ablation) at 1 kHz.

The Raman spectra of the laser-affected zone, the spatial distribution of relative peak intensity of t-Te, SE images of the laser-affected zone, and the DC resistivity of the laser-inscribed lines at thermal-cumulative regime in the open-air atmosphere are shown in Figure 3.16. The Raman bands and nomenclatures are summarized in Appendix C. Figure 3.16.a shows the Raman spectra of the laser-affected zone in the TWA glass. A few peculiar behaviors are observed in the laser-affected zone at a pulse energy of 25 nJ. The one is the strong intensity of the boson peak, associated with the existence of nanocrystals, transversal phonons, or changes of the MRO in a glass [275–277]. Its position depends on the thermal or pressure history of the glass [278]. Another one is weak low wavenumber peaks, which are associated with t-Te. The peak at around 240 cm^{-1} is associated with the Te-dimers or Te_n clusters. At the onset of ablation (the pulse energy of 50 nJ), no peaks at low wavenumber are observed, and the main glass peak gets narrower. Combined with the result of SEM-EDS in Appendix C, the oxidation of the laser-affected zone of TWA is observed.

Figure 3.16.b-c shows the Raman spectra of the laser-affected zone in the TZNB and TNGPZ, respectively. The increase of the 238 cm^{-1} is observed with pulse energy, accompanying the reduction of the intensity ratio of t-Te/glass. The formation of t-Te accompanied by the peak at 238 cm^{-1} is a common feature in three different compositions regardless of the processing

parameters in the open-air atmosphere; however, the crystal-to-glass ratio in focal volume differs.

Figure 3.16.d shows the spatial distribution of the ratio of t-Te/glass along the laser-affected zone. The compositions of Te in TWA, TWK, TNGPZ, and TZNB glass are around 35, 60, 65, and 70 wt%, respectively. The relative intensity of t-Te at the laser-affected zone is the highest in TWK since the Te-dimers and clusters are effectively converted to t-Te. Note that the peak at 238 cm^{-1} overlaps with the peak at 230 cm^{-1} which corresponds to Nb-O-Nb bridge in NbO_6 . Therefore, the intensity may not be representing a single peak. The content of t-Te at the laser-affected zone in TZNB and TNGPZ is around the same as in the pristine glass, showing the almost effective transformation of TeO_2 -glass to t-Te in the focal volume. TWA exhibits the lowest elemental crystallization ratio of t-Te/glass and an extremely narrow laser-processing window.

The tellurite glass systems used in this study have a composition of Te between 35 to 70 wt% (TeO_2 content is above 55 wt%). Similarly, the prerequisite for the formation of homopolar bonds of Te-Te or Te-cluster, the Te content should be above 40 wt% for amorphous telluride alloys [249]. In addition, the amount of glass modifiers and their stability define the nature of the reaction of each element (reduction or oxidation) in the laser-affected zone. For instance, thermodynamically, in the presence of Te, Ag_2O can be reduced to Ag by Te, and lead to the TeO_2 formation. These results highlight other requirements to obtain t-Te locally from TeO_2 -based glass upon fs-laser irradiation: the rich glass composition in terms of Te, and the quantity of glass modifier oxides, which can reduce TeO_2 .

Figure 3.16.e shows the SEM images of the laser-affected zone of TWA, TZNB, and TNGPZ at 1 MHz. The typical self-organized nanostructures on tellurite glass are perpendicular to the electric field of the laser extending beyond the focal volume, common for all selected tellurite glass systems. In addition, all selected glass systems preserves peak at around 238 cm^{-1} upon laser exposure in thermal-cumulative regime under nitrogen atmosphere. Detailed figures of self-organized nanostructures and Raman spectra with respect to laser parameters in thermal-cumulative regime are presented in Appendix C.

At last, Figure 3.16.f shows the DC electrical resistivity of the laser-written tracks in the thermal-cumulative regime of all compositions. The resistivity results are close in each composition at 25 nJ. TZNB, TNGPZ, and TWK show a similar trend over pulse energy, whereas TWA shows a steep increase due to oxidation at the onset of ablation. Since the onset of ablation of TWK is higher than TZNB and TNGPZ, it reaches a similar value as polycrystalline bulk Te resistivity at 200 nJ ($0.00445\ \Omega\cdot\text{m}$ as indicated in Table 3.3). These results indicate not only the potential for combining multiple material phases in a single substrate as a means for functionalizing tellurite glass but also enable the direct-write of functional 2.5 dimensional (2.5D) nanocomposites with physical properties easily tailored by the laser parameters.

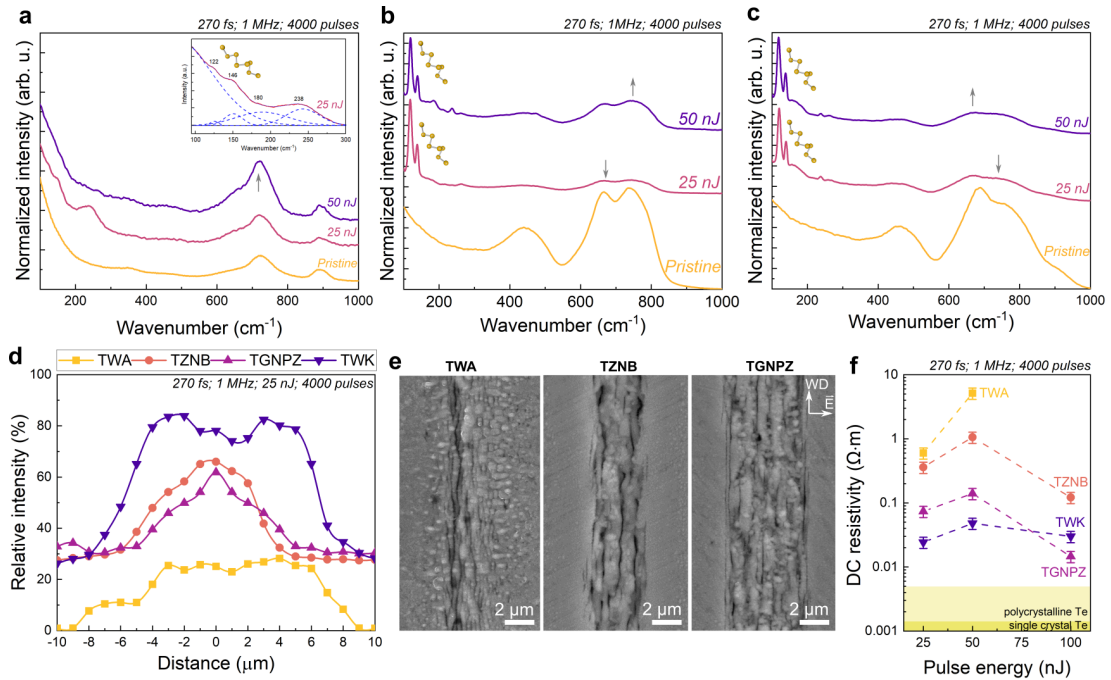


Figure 3.16: Raman spectra of the pristine glass and the laser-affected zone of a) TWA, b) TZNB, and c) TGNPZ at 4000 pulses with various pulse energies of 25 and 50 nJ (incoming pulse fluence of 33 and 66 J/mm², respectively) at 1 MHz. The inset image shows the deconvolution of the lower wavenumbers of TWA. d) Spatial distribution of the ratio of t-Te/glass along the laser-affected zone at 25 nJ. e) SE images of laser-affected zone written with 50 nJ and 4000 pulses at 1 MHz. f) The DC resistivity of the laser-written tracks of all compositions used in this study.

3.4.6 Phenomenological interpretation of self-organization in cumulative regime

In this section, we propose the following interpretation explaining self-organization beyond the focal volume in thermal-cumulative regime, as described in section 3.4.3

Let us first examine the steps leading towards self-organized structures that span beyond the focal volume in cumulative regime (at 1 MHz) and examine the key events occurring during laser exposure according to our phenomenological model in Figure 3.17.a-b. In the light of our recent observation [144], the Figure 3.17.a presented in [143] has been slightly modified to indicate the new findings.

Step 1: During fs-laser inscription, multi-photon ionization seeds the first electrons that further lead, through avalanche ionization, to the build-up of an under-dense plasma. As bonds are broken within the main structural units of the glass, weakly bonded ions, such as O²⁻ and Te⁴⁺ form.

Step 2: With the single pulse exposure, nanocrystals of t-Te is generated from the glass matrix within the focal volume. Besides, in terms of morphological modifications, the first few pulses

create an electric-field enhancement through the formation of surface plasmon-polariton (SPPs) pairs that initiate the formation of seeds for self-organized nanostructures within the focal volume [279, 280]. For specific conditions, surface electromagnetic waves (SEWs) through SPP coupling can be excited. SPPs may originate from delocalized coherent electron density oscillations and propagate along the interfaces between the two different materials (such as t-Te/TeO₂) emerging locally during the self-organization process. Driven by the laser electromagnetic field, SPPs propagate and dissipate away from both sides of the laser-affected zone with a preferential direction defined by the self-organized nanoplanes orientation. For the excitation of SPPs, specific conditions for the dielectric permittivity of the involved media have to be fulfilled. Particularly, for an irradiation with ultra-short laser pulses, this excitation channel can be enabled even for semiconductors and dielectrics, as the initially non-plasmonic material can transiently be turned into a metallic state, enabling SPPs once a critical density of electrons in the conduction band is exceeded. The merge of SPPs leads to a spatial modulation of the local energy field distribution, which, through absorption mechanism, is imprinted in the specimen. Note that SPPs formation has been showed theoretically and experimentally on silicon upon fs-laser irradiation [281].

Step 3: As laser pulses accumulate, seeds anticipate the formation of self-organized nanostructures at about 10 pulses. Likewise, the transformation of the focal volume into t-Te nanocrystals is completed in about a 10 pulses. In thermal cumulative regime, thermal melting and elemental decomposition with deoxygenation events stimulate further crystallization of t-Te in and beyond the focal volume. As the molten state of modified tellurite glass includes charged entities, intra-/inter-molecular charges exchanges further promotes crystallization [205]. Under strong electrical field, the molten material becomes polarized and forms elongated clusters as a result of the balance between electrical forces on induced surface charges and interfacial tension forces. The retention of local electrical neutrality has structurally an effect on the connection and coordination of the polyhedra. As observed with the Raman spectra, migration of W results in decrease of Te-O-Te linkages and W=O bonds and facilitates the formation of W-O-Te linkages, similar to WO₃-rich tellurite glass due to elemental redistribution.

Step 4: As heat builds up locally, illustrated in Figure 3.17.b, an area of nanocrystalline t-Te extends spatially. Thermal accumulation is important also because Te becomes metallized near melting temperature. Here, we make the hypothesis that a SPP field propagates at the interface between crystalline t-Te and tellurite glass. As a dipole moment is created, forces between polarized particles arise and keep them apart. This mechanism would explain the periodicity of the nanostructures observed *outside* the zone under direct-laser exposure. Note that a plasmonic effect on interfacial energy transfer across the silicon-silicon oxide interface was showed by Derrien *et al.* [282]. In addition, the TEM results indicate possible grain growth of nanocrystals with an increase in the number of pulses, which explains the crystallization outside the zone under direct-laser exposure.

Step 5: Depending on the pulse overlapping ratio, the temperature in the focal volume may

stay high, long enough, to allow for crystalline layer to grow. During cooling, due to the thermal expansion coefficients mismatch between modified and parent material phases, high stress concentration builds up at the interface and causes the formation of interstitial micro-cracks localized in between nanoplanes, and notably, where stress-concentration occurs at the boundary between pristine and modified materials.

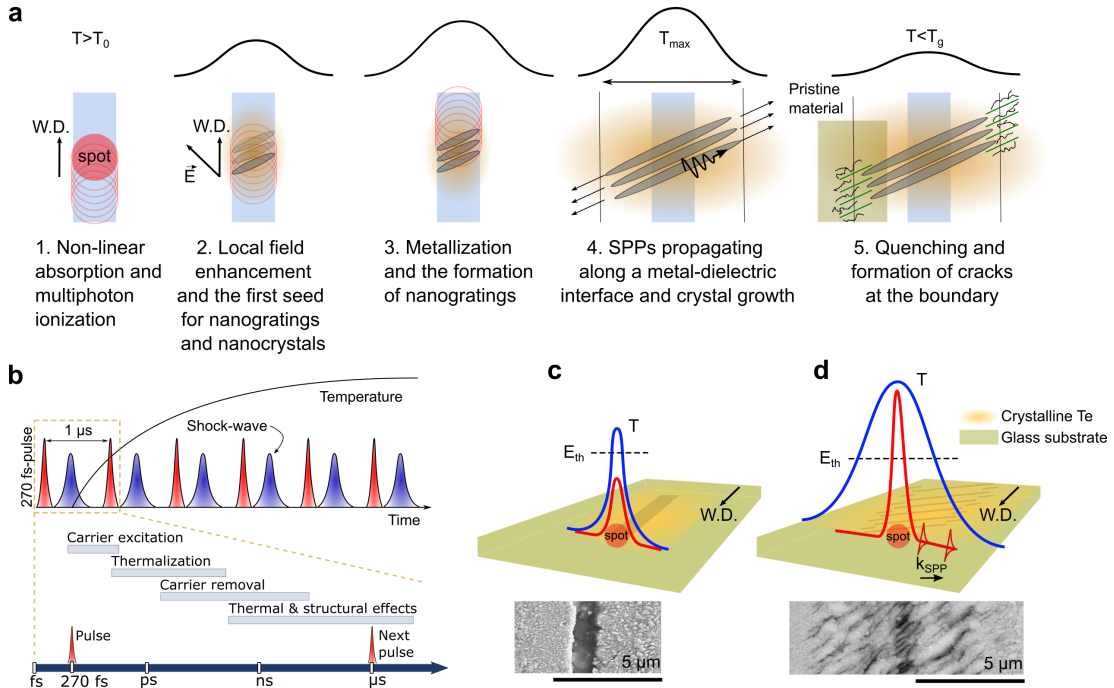


Figure 3.17: a) Phenomenological interpretation for the sequential formation of self-organized nanostructures beyond the focal volume and its related metallization on ternary-tellurite glass surface: *Step 1*. Nonlinear absorption, multi-photon and avalanche ionizations, *Step 2*. The formation of seeds for nanogratings by local field enhancement and the formation of t-Te upon single fs-laser pulse, *Step 3*. Completion of self-organized nanostructures and metallization by elemental decomposition and deoxygenation followed by thermal melting, *Step 4*. SPP propagation at the metal/dielectric interface with the grain growth of nanocrystals and finally, *Step 5*. Ultrafast cooling accompanied by the formation of the cracks due to thermal expansion mismatch between modified and parent glass. b) The characteristic time scale of fs-laser-induced events in thermal-cumulative regime. c-d) Phenomenological interpretation of the wider nanostructures formation on TWK glass. When multiple pulses accumulate, the temperature rise causes the material under exposure to melt. Despite the thermal-cumulative regime leading to the bulk heating of the material, nanostructures form at higher pulse energy, but are not found for lower pulse energy. Temperature gradient indicated as blue and field strength illustrated as red line on modified zone c) 10 nJ, 0.5 mm/s (13 J/mm²); d) 200 nJ, 0.5 mm/s (262 J/mm²) (both at 1 MHz).

Let us now discuss the effect of field strength as observed in Figure 3.17.c-d. Our interpretation is as follows. The laser intense electrical field determines the field-strength atoms are exposed. It will affect the condition for SPPs to exist [283] as it will impact the plasma electron density.

In such model, below a given threshold (here found around 20 nJ), the field-intensity is not high enough to sustain the self-organization mechanism described before. Note that a similar mechanism was proposed by Liao *et al.* [48].

In summary, the formation dynamics of these structures is complex. The structure under exposure is not static and evolve dynamically as the materials heat up and as nanostructures gradually form. Our interpretation is based on final state of matter, out of which we reconstruct a possible scenario. As ‘metallic seeds’ form through elemental decomposition and deoxygenation, the main hypothesis is that they start promoting SPPs due at their interface when subsequent fs-laser pulse arrives. In this quasi-static evolution scenario, we assume that after each pulse, the system can be considered as a ‘metastable’ configuration for the next incoming pulse, which supposes that viscosity remains sufficiently high, so that this approximation is valid, otherwise, the inhomogeneity (and phase separation) could not be maintained from pulse-to-pulse. From the material phase evidences collected, we observe the formation of crystalline Te surrounding the glassy phase itself localized within the nanoplanes. The growth of these nanoplanes outside the laser focus is explained by localized field-enhancement. Here, we have considered the hypothetical presence of SPPs to explain the field-enhancement that certainly also involves quasi-cylindrical waves that may play a constructive role in this field-enhancement mechanism, adding to the effect of the SPPs through cross-conversion mechanism [284]. To confirm this scenario, pump-probe experiments or alike could be considered for identifying the onset and sequence of intermediate events proposed here.

3.4.7 Morphological and structural changes in the volume

Up to now, we focused on modifications on a tellurite glass surface. In this final section, we cover the femtosecond laser-induced modifications in tellurite glass volume.

Previously, only two studies have shown tellurite-based glass decomposition by fs-laser irradiation. 370 fs-laser pulses emitted at 500 kHz and 1050 mW with 100,000 pulses have generated a cavity filled with air-bubble and t-Te nanocrystals in the oxyfluoride tellurite glass volume [199]. In addition, by the same group of researchers, the study on the effect of repetition rate at 1 and 250 kHz suggests the glass decomposition as a thermal process since no t-Te nanocrystals except Te clusters have been observed at 1 kHz even with longer exposure durations in phospho-tellurite glass [200].

Here, we aim to elaborate on our understanding of morphological and structural volume modifications in tellurite glass. Figure 3.18.a shows OM images of the cross-section of laser-affected zone 100 μm below the glass surface. The first modifications are visible optically at 50 nJ with a few pulses (for 20 pulses; incoming pulse fluence of 0.36 J/mm^2). The dimensions of the modifications increase with pulse energy further, and at around 200 nJ, self-focusing is observed. The chemically etched (with NaOH 2.5% for 30 seconds at room temperature) reveals the structures for further characterization. Figure 3.18.b-c demonstrates OM and SE

images of the cross-section of the laser-affected zone after the etching. Note that further etching with NaOH solution more than 300 seconds results degradation of the optical quality of the glass. Limited or no particular preferential etching of laser-affected zone is observed. In contrast, the surface structures can be smoothed by this method, illustrated in Appendix C.

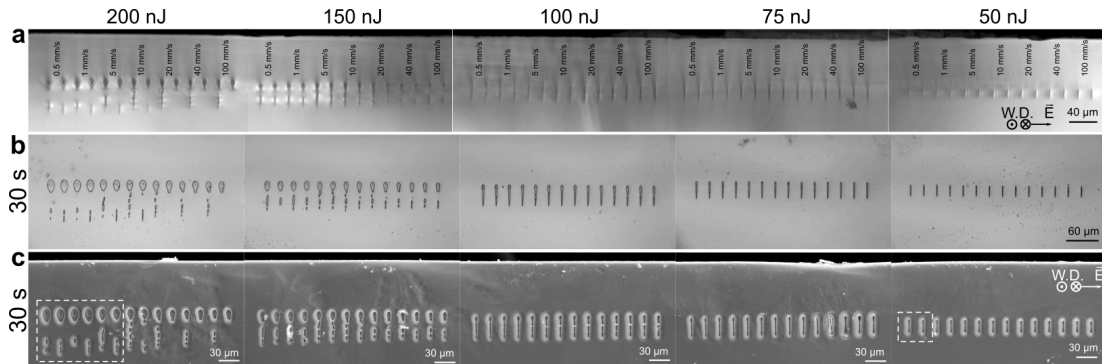


Figure 3.18: a) OM images of laser-affected zones in TWK glass at 1 MHz for various pulse fluences ranging from 0.36 to 262 J/mm². b) OM images after etching with NaOH 2.5% for 30 seconds at room temperature and c) the corresponding SE images of the laser-affected zone at 1 MHz in TWK.

In Figure 3.19.a-c, magnified SE images with their elemental maps present a dual-ion migration similar to various tellurite glass compositions reported earlier. At low pulse energy, while W is present in the top part of the modifications, Te migrates from the center to the bottom of the modified zone. Likewise, a similar trend is observed with higher pulse energy, even in a modification generated from self-focusing. The magnified images highlight the formation of black spots at the center of the modifications.

SE images illustrate that the laser-affected zone consists of circular regions associated with melting and resolidification upon multi-pulse exposure in a thermal cumulative regime. At low energy, the laser-affected area contains homogeneous modifications with black precipitates at the center. With the pulse energy, the laser-affected zone enlarges and transforms into an oval-shaped discontinuous region due to self-focusing. The center of the modification again contains darker-contrast precipitates. Unlike the surface of the glass, there are no self-organized nanogratings observed within the processing window. This might be either because the porous phase cannot be obtained due to the low viscosity of the glass, fast molecular oxygen is recombining with the glass upon irradiation, or the porous phase is too small to resolve with current characterization methods. Note that the high refractive index of the tellurite glass resulting in the heterogeneous distribution of the absorbed energy and self-focusing might alter the types of modifications. Let us investigate their nature by Raman spectroscopy.

At last, Figure 3.20 presents the OM images and Raman spectra across the laser-affected zone at 50 nJ, with its corresponding relative intensities. Nevertheless, Raman spectra highlight the signature of t-Te, whose peaks are located at 120 and 140 cm⁻¹. These peaks indicate

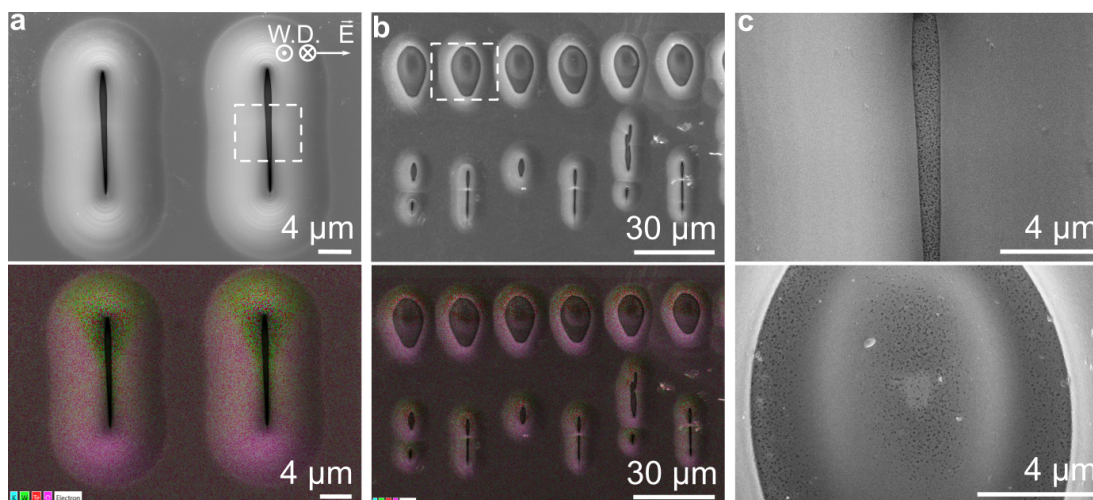


Figure 3.19: a) SE images and elemental map of laser-affected zones in TWK glass at 1 MHz for 50 nJ (incoming pulse fluence of 66 J/mm^2). b) SE images and elemental map of laser-affected zones in TWK glass at 1 MHz for 200 nJ (262 J/mm^2). c) Magnified images of SE images indicated in a-b).

that the oxygen disintegration from the glass and forming t-Te are possible with the current parameters, however, no molecular oxygen is detected by Raman spectroscopy. High oxygen diffusivity might indeed lead to the dissolution of molecular oxygen if it has ever generated during the process [285].

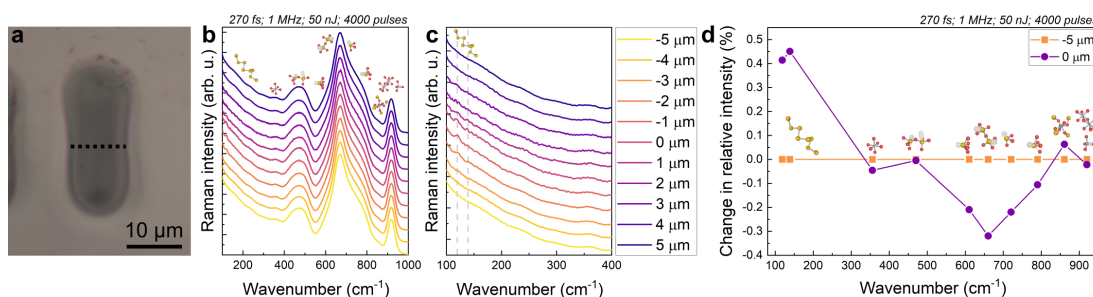


Figure 3.20: a) An OM image and b) Raman spectra of laser-affected zone in TWK at 1 MHz with 50 nJ and 4000 pulses (incoming pulse fluence of 66 J/mm^2). c) The magnified Raman spectra indicated in b). d) The relative change in main glass bands compared to pristine material at 1 MHz with 50 nJ and 4000 pulses (incoming pulse fluence of 66 J/mm^2)

3.5 Summary

In this chapter, we showed various photo-induced modifications on the surface and in the volume for both thermally cumulative and non-cumulative regimes of the tellurite glass family. Our findings triggered the following observations:

- The formation of self-organized nanostructures, perpendicular to the laser polarization on the glass surface is unraveled by pulse-to-pulse exposure. The structural characterization revealed a photo-decomposition of fs-laser-modified tellurite glass into an elemental t-Te, accompanied by elemental redistribution and deoxygenation. Under near-IR fs-laser irradiation, *a single pulse* is sufficient to form elemental t-Te, as revealed by high-resolution imaging and analysis. An intriguing fact is that self-organized nanostructures are first observed when the transformation of the laser-affected zone to t-Te is mostly completed. The formation of nanostructures and t-Te nanocrystals causes photo-darkening resulting in a decrease in total transmission of the inscribed area.
- The underlying elemental crystallization phenomenon is investigated by altering laser parameters in tellurite glass systems under various ambient conditions. Interestingly, the formation of t-Te is greatly suppressed under a dry nitrogen atmosphere as there is limited interaction of glass network units, and Te_2 or Te_n clusters with an open-air atmosphere have a detrimental effect on the formation process.
- The formation of elemental t-Te and elemental redistribution is a common feature in all compositions; the composition should be rich in Te to obtain a large laser-processing window. In addition, surface oxidation is observed in which there is an oxidizing modifier oxide, such as Ag.
- Polarization-dependent self-organized nanostructures in thermal-cumulative regimes extend beyond the zone under direct laser exposure. Under the thermal-cumulative exposure regime, increasing the temperature at the focal spot leads to further elemental crystallization or “glass decomposition” and promotes connectivity and grain growth in the focal volume. The typical cross-section of the laser-affected zone displays three different characteristics over its depth regardless of laser parameters.
- The femtosecond laser-induced modifications in the volume resulted in the dual-ion migration process and crystallization of t-Te nanocrystals. The threshold of nanocrystal formation in the volume is five times higher than the one on the surface.

In conclusion, the fs-laser direct writing offers an opportunity for producing integrated t-Te/ TeO_2 -glass nanocomposite, particularly attractive as future functional devices fabricated without adding or subtracting any other materials, and through a single-step process. The fs-laser direct-write technology is simple and scalable. Here, it led to millimeter-sized bilayer nanosheets with controllable nanostructures, physical properties, and multiple functionalities. As we will see in Chapter 5, our findings open up interesting applications, such as photoconductive devices. In the volume, waveguiding through densification and glass decomposition opens up even more possibilities for optoelectronic devices.

4 Non-oxide glass systems: Chalcogenide glass¹

¹This work has been partially published as *G.Torun, A. Yadav, K.A. Richardson and Y. Bellouard, Ultrafast laser direct-writing of self-organized microstructures in Ge-Sb-S chalcogenide glass, Frontiers in Physics, 316 (2022)* and cited in the text as [286].

External contributions: In this study, the bulk chalcogenide glass systems ($\text{Ge}_{23}\text{Sb}_7\text{S}_{70}$, $\text{Ge}_{23}\text{As}_7\text{S}_{70}$, and $\text{Ge}_{23}\text{Sb}_7\text{Se}_{70}$) were fabricated and characterized before femtosecond laser irradiation by Dr. Anupama Yadav and Prof. Dr. Kathleen A. Richardson at University of Central Florida.

In this chapter, let us consider the case of non-oxide glass systems under femtosecond laser exposure. Similar to Te, other chalcogens, such as S and Se, can form an amorphous solid and/or glass without its oxide. Here, we introduce chalcogenide glass systems, the current status of their research, use, and interaction with femtosecond lasers. Then, morphological and structural modifications on the surface and in their volume are performed by altering exposure parameters in well-studied ternary chalcogenide glass. Further, we discuss the stability and the reversibility of the modifications. Finally, by changing glass formers, we focus on the influence of basic structural units on key mechanisms sustaining self-organization and photo-induced modifications.

4.1 Glass structure and properties

Chalcogenide glass (ChG) systems have been considered as relatively new type of non-crystalline solids since their typical nature differs from those of oxide glass systems. Compared with the long history of oxide glass, the first report on ChGs has been available since 1870 [287]. Later, the interest for this particular glass started to expand with the study on As_2S_3 in the 1950s [288].

ChG systems consist of chalcogens from group 6A of the periodic table, such as S, Se, and Te, which are covalently-bonded to their nearest neighbor atoms by p electrons in the s^2p^4 configuration. Similar to TeO_2 , unbounded or lone-pair (LP) electrons do not participate in bonding but they can stimulate weak Van der Waals interaction between chains and ring molecules [289]. The glass network made of a single element, such as Se, refers to molecular glass systems. They also form a glass network by covalently bonding to other network formers, such as As, Ge, Sb, Ga, Si, and P, etc. [290]

With the combination of both types of interaction, ChG may form both homopolar and heteropolar bonds in multi-element systems [291]. The homopolar bonds may be found in a particular situation where non-chalcogen metal cations (e.g., Ge) are fully coordinated with chalcogens. The residual chalcogens can only bond to themselves, resulting in chalcogen-chalcogen homopolar bonds. In the case of insufficient chalcogen species available to fully meet the cation's coordination requirement, one observes metal-metal homopolar bonds [292]. As a general condition to complete the coordination number (CN) of the cations, the atomic structure should consist of two bonds for S or Se (CN=2), three bonds for As or Sb (CN=3), and four bonds for Ge (CN=4); such defines the bonding configuration of the elements in the glass.

Among all the compositions in chalcogenide systems, Ge-rich systems have one of the highest stability since GeS_4 tetrahedra is a rigid structural unit, and the germanium disulfide (GeS_2) exhibits the highest glass transition temperature [293]. Since GeS_4 tetrahedra has higher effective sulfur content so that highly reactive excess sulfur stabilized, Ge leads to a rise in the glass forming tendency with the melting temperature. In contrast, the rigidity and compactness of the Ge-S network are reduced by the addition of ternary inclusion (Ga, Sb,

etc.), causing rearrangement of the bonds and allowing structural changes with external stimuli [294]. Some Ge-based chalcogenide glass systems are already commercially available [295].

In this chapter, we focus on the ternary chalcogenide glass system, namely, $\text{Ge}_{23}\text{Sb}_7\text{S}_{70}$. Further, we explore variations in the structural evolution and photo-induced modifications when the identity of the iso-structural anion (S and Se) or cation (Sb and As) is changed. We investigate $\text{Ge}_{23}\text{Sb}_7\text{S}_{70}$ glass system more than the other compositions due to its low toxicity and high transparency in the visible part of the electromagnetic spectrum.

The structure of the Ge-Sb-S system was under investigation by Raman spectroscopy, X-ray diffraction (XRD), extended X-ray absorption fine structure (EXAFS), and neutron diffraction (ND) [294, 296–298]. Their results agree on the glass structure: The main structural units are $\text{GeS}_{4/2}$ tetrahedra and $\text{SbS}_{3/2}$ pyramids. In addition, S-S bonds are found in S-rich systems, whereas homopolar metal bonds of Ge and Sb and Ge-Sb bonds can be present in S-deficient glass systems, as shown in Figure 4.1.a. These structural units form short- to medium-range order (MRO) glass networks. Recent results obtained by Monte-Carlo simulation display similar bonding preferences, bond distances, and coordination numbers to previous reports except for longer Sb-S bonds [298].

They possess several rather unusual properties compared to oxide glass systems. Their interatomic bonds are weaker between covalently-bonded heavy elements compared to ionic bonding. Similar to some of the tellurite glass [166], they display semiconducting properties. However, unlike tellurite glass, chalcogenide glass is network formers having relatively well-defined intermediate range order and can form a glass upon quenching. Unlike tellurite glass, doping can be challenging since all atoms satisfy the valence requirements, and thus, donors or acceptors are not formed [299]. In some cases, chalcogenide glass with Ga can be doped thanks to a lower charge of Ga where dopants act as charge-balancing cations [300].

The most salient features of chalcogenide glass systems are wide transmission windows spanning the mid- and long-wave infrared (MIR and LWIR), high refractive index, and higher nonlinear optical properties owing to their heavy atoms and low vibrational energies. Figure 4.1.b shows the transmission window of a few chalcogenide glass systems, such as sulfides, selenides, and tellurides, and compares them with silicates. Furthermore, thanks to their photosensitivity due to their coordination defects, various temporary and permanent modifications have been reported, including photo-darkening, photo-expansion/contraction, and photo-crystallization [301]. In addition, they exhibit moderate environmental stability while having low strength, hardness, and low glass transition temperature due to their highly covalent nature [302]. Their aging due to light irradiation or environmental interaction has been discussed before [303] and shown that well-selected annealing is required to have a stable optical response over a long period. In addition, as a glass former, an increase in the relative atomic mass of chalcogens, i.e., from S to Te, leads to a reduction in the bond strength, softening temperature, the hardness, and increases the thermal expansion coefficient in the

glass. In the chalcogen group, the metallic character increases with an atomic number. That is why making Ge-Sb-Te glass under normal quenching conditions is difficult [304].

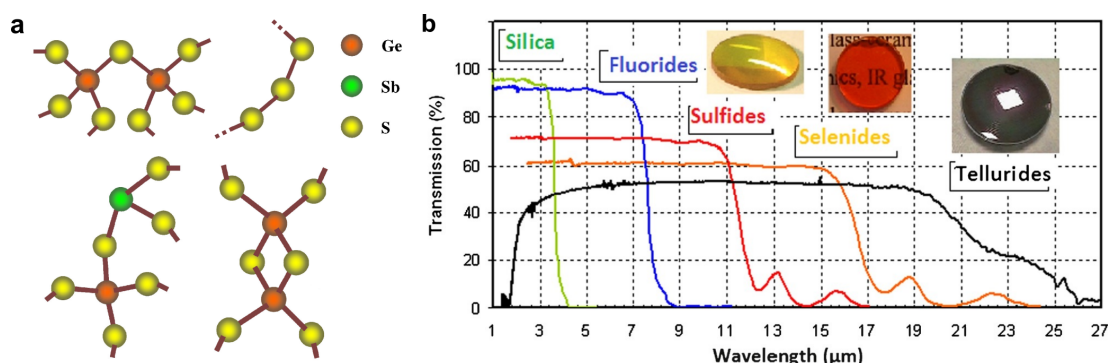


Figure 4.1: a) Structural units in S-rich Ge-Sb-S chalcogenide glass (adapted from [305]). b) The transmission window of S-, Se-, and Te-based chalcogenide glass systems. The insets are representative examples are sulfide As₂S₃, selenide As₂Se₃, and telluride Te₂₀As₃₀Se₅₀ glass systems (taken from [306]).

From an application point of view, chalcogenide glass has prompted diverse glass compositions to expand the number of available technologies. Their use span from infrared optical imaging and sensing [307, 308], optical communication systems and photonic devices [309–312], laser power delivery [313], super-continuum generation [314] as well as non-volatile memory and switching devices [315]. Over the past decade, various geometries have been explored to expand chalcogenide glass usage, including bulk materials, fibers, thin films, and nanoscale waveguides [292, 309, 311].

4.2 Femtosecond laser and chalcogenide glass interaction

Photo-induced transformations with illumination around the band gap of chalcogenide glass have been reported as early as the 1970s to develop data storage [316, 317]. Such modifications are due to photo-darkening, found as reversible with thermal treatment below the glass transition. Some of the other modifications are photo-anisotropy [318], phase change [319], photo-expansion [320], photo-contraction [321], etc. Both reversible and irreversible photo-modifications were outlined previously [301]. The reversibility of femtosecond laser-induced modifications is covered for the Ge-Sb-S system further in this chapter.

Focusing ultrafast laser pulses on the surface or in the volume of materials induces diverse and localized permanent structural, morphological, and chemical modifications. For chalcogenide glass, our knowledge about ultrashort pulses interaction with these substrates is widened in the last decade with avalanches of studies [286, 302, 322–353]. Some selected examples of femtosecond laser-induced modifications are illustrated in Figure 4.2. Here, we classify all the modifications reported in the literature. In these studies, the commonly reported facts of femtosecond laser interaction with binary to quaternary chalcogenide glass compositions are

divided into four different categories as below:

- the laser damage threshold [322–326, 328–330, 333–335, 340, 342] primarily using for fiber-based applications,
- photo-induced morphological modifications, e.g., self-organized nanostructures on the surface [286, 322–324, 339, 349–353], voids [347], and micro-explosion [354],
- laser fluence-dependent photo-induced structural modifications, e.g., photo-expansion and photo-contraction [302, 326, 329, 331, 332, 343–345], photo-darkening [337, 338, 346], photo-oxidation [325, 328], photo-anisotropy [327], photo-crystallization [336], ion migration [341] and subsequently,
- the performance of the laser-induced modifications as future photonic devices, such as waveguides [76, 355–359], gratings [360], relief diffraction gratings [361], micro-lenses [362], embedded spectrometers and interferometers [363], optical directional couplers [364], and so on.

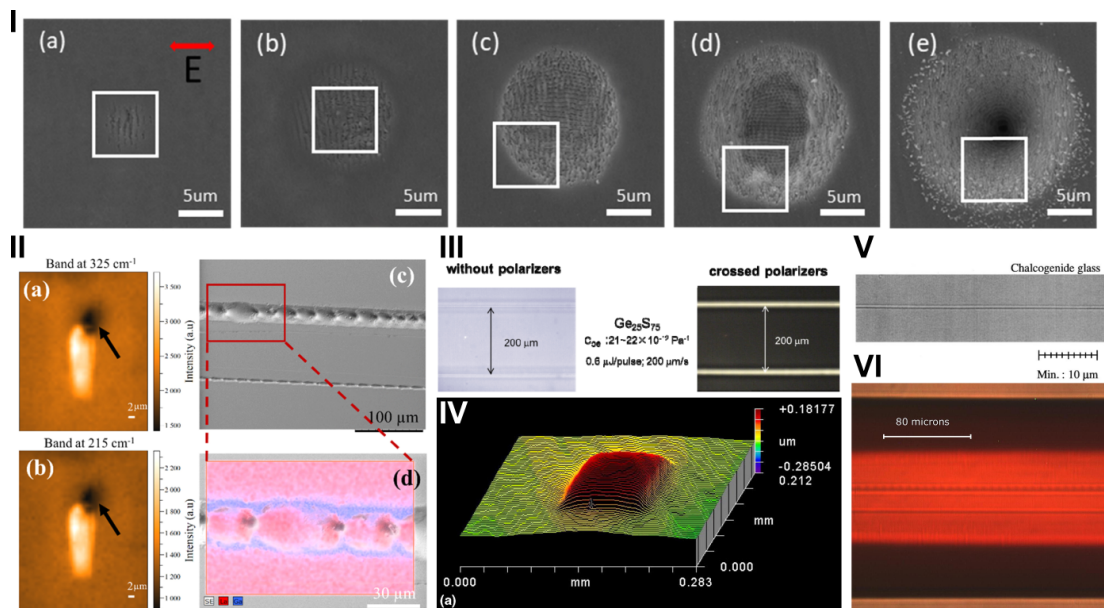


Figure 4.2: I) SE images of the characteristic stages of the morphological evolution of As_2S_3 after different irradiation pulse shots: a) 2, b) 5, c) 10, d) 20, e) 50 under fluence of $6.20 \text{ mJ}/\text{cm}^2$ (taken from [350]). II) Raman intensity maps of different bands in a waveguide at a) 325 cm^{-1} and b) 215 cm^{-1} in Ga-La-S. c-d) BSE image and the compositional map (La red, Ga blue) (taken from [347]). III) microscope images of the femtosecond laser written tracks in chalcogenide with/without polarizers (taken from [327]). IV) Surface profile of a square on $\text{Ge}_{0.23}\text{Sb}_{0.07}\text{S}_{0.60}\text{Se}_{0.10}$ using white light interferometer (taken from [326]). V) OM image of the waveguide (taken from [76]). VI) OM image of As_2S_3 fiber gratings with the $7.8 \mu\text{m}$ period (taken from [360]).

In this chapter, we first report morphological and structural modifications in the volume of the ternary chalcogenide glass to ultrafast laser pulses in non-cumulative and thermal-cumulative regimes. This work sets the baseline for our understanding of laser-induced structural changes and self-organization processes mainly in the $\text{Ge}_{23}\text{Sb}_7\text{S}_{70}$. The laser intensity and the peak power are varied by changing the pulse duration, the pulse energy (or field strength), and the pulse overlapping ratio. In addition, systematic research on morphological and structural photo-induced modifications on the surface of chalcogenide glass is reported. Further, the stability of the modifications is investigated by annealing at various temperatures since aging is a pronounced question in chalcogenide glass systems. This investigation also points out the type of reversibility of the femtosecond laser modifications. Finally, we exposed $\text{Ge}_{23}\text{Sb}_7\text{S}_{70}$, $\text{Ge}_{23}\text{As}_7\text{S}_{70}$, and $\text{Ge}_{23}\text{Sb}_7\text{Se}_{70}$ glass substrates to femtosecond laser pulses, for which we observe the pulse-to-pulse nanostructure formation that we correlate to the structural evolution of the material using elemental and systematic micro-Raman and UV-VIS observations.

4.3 Experimental procedure

4.3.1 Glass specimens preparation and characterization

The nominal composition of the glass used in this study is $\text{Ge}_{23}\text{Sb}_7\text{S}_{70}$. 100 g of elemental materials were weighed and batched in a nitrogen-purged glove box with a controlled atmosphere. The weighed batch was loaded into fused quartz tubes (30 mm in diameter) and sealed under a vacuum using a methane-oxygen torch to form ampoules. The glass batch was melted in a rocking furnace overnight at 1123 K. After overnight rocking at an elevated temperature, the molten glass was quenched at 1023 K by natural convection. Bulk glass specimens were subsequently annealed at 543 K for 2 hours to relax quench-related stress. The annealing is a key aspect while studying the photo-modifications since the response of rapidly quenched glass may differ from the glass structure close to equilibrium. The density was determined by Archimedes' method with distilled water as immersion fluid at room temperature. The specific heat and thermal conductivity were determined by the transient planar source method. The thermal analysis was performed using a differential scanning calorimeter (DSC from Netzsch DSC 204 F1 Phoenix). The instrument error on temperature was ± 2 K. Transmission data was obtained using Fourier transform infrared spectroscopy (FT-IR from ThermoFisher Scientific Nicolet iS5). Measurements were operated over a range of wavelengths from 1.4 to 25 μm on ~ 4.13 mm thick double-sided polished specimens. Below 1.4 μm , the transmission was measured by UV-VIS-NIR spectrometer. X-ray diffraction (PANalytical Empyrean) was performed to confirm the amorphous nature of the glass. The specimens were cut and polished to optical quality for fs-laser machining. Table 4.1 summarizes various physical properties of glass compositions investigated in this study.

Table 4.1: Physical properties of chalcogenide glass investigated in this study.

Sample	ρ (g/cm ³)	n @1.064 μ m	E _g (eV)	T%	T _g (K)	α (m ² /s)
Ge ₂₃ Sb ₇ S ₇₀	2.95±0.0015	2.25	2.3	0.593 - 8.3	584±2	0.2 x 10 ⁻⁶
Ge ₂₃ As ₇ S ₇₀	2.8±0.02	-	2.71	-	590±5	-
Ge ₂₃ Sb ₇ Se ₇₀	4.55±0.02	2.62	1.7	0.745 - 15	519±5	-

4.3.2 Femtosecond laser irradiation

Three different femtosecond laser systems were used, emitting pulses of different durations: 50 and 100 fs pulses at 850 nm (Yb-doped fiber, Satsuma with an OPA from Amplitude), 150 fs pulses at 1030 nm (Regen amplifier, S-pulse from Amplitude), and finally, 270 fs pulses also at 1030 nm (Yb-doped femtosecond fiber laser, Yuzu from Amplitude). This choice of two wavelengths is a compromise for investigating pulse durations, only motivated by the availability of laser sources. Although the 50 and 100 fs pulses are emitted at 850 nm, instead of 1030 nm like for the other pulse durations, we assume that it remains close enough to 1030 nm [365, 366], at least for a phenomenological interpretation and discussion. The reasoning is that the wavelength mostly affects the rate of creation of multiphoton seed electrons, igniting cascading events that eventually lead to a plasma formation, mainly sustained by carrier-carrier excitations and avalanche ionization processes. 100 fs pulses were obtained by negatively chirping the pulse in the compressor, which is the maximum pulse duration in the OPA laser configuration. The specimen was translated under the laser focus with the help of a high-precision motorized stage (Ultra-HR from PI Micos). The laser beam was focused at the surface and in the volume of the specimen with a 0.4-numerical aperture (NA) objective (OFR-20x-1064 nm from Thorlabs), resulting in a spot-size (defined at $1/e^2$) of 1.94 μ m for 1030 nm, 1.6 μ m for 850 nm.

First, static laser exposure was performed to determine the repetition rate to observe thermal accumulation outside the exposed volume. Specifically (and following a method proposed in [367]), the transition from non-cumulative to thermal cumulative exposure regime was determined by observing the evolution of the width of the static modifications with the increasing number of pulses and pulse repetition rates from 1 kHz to 1 MHz, for the various laser fluence values. The transition was found around 500 kHz. It was confirmed with a time-dependent temperature distribution model. The repetition rate was then fixed at 100 kHz for most of this study, which lies well below the thermal cumulative regime for this glass. Translation velocity was selected as one of the main variables to vary laser net fluence (or deposited energy, see Appendix A for details). Here, pulse-to-pulse overlapping ratios were varied from 0 to 99.9 %, and the pulse energy was ranging from 1 nJ to 1 μ J.

The laser patterns, consisting of 10 mm-long lines were inscribed at the surface interface, and just below the surface (between 10 and 20 μ m) to limit effects related to spherical aberrations (due to the high-index value of the chalcogenide glass). Furthermore, the patterns were inscribed using opposite directions of laser beam movement along with a single writing

axis and under three different linear-polarization states (and therefore, the orientation of the electrical field E) defined as parallel, at 45° , and perpendicular to the writing direction, respectively. For refractive index measurement, a pattern consisting of a single layer of parallel lines, spaced $2\ \mu\text{m}$ apart and covering a surface of $1 \times 1\ \text{mm}^2$, was written in the volume. For absorptivity measurement, a similar pattern was written, this time in the bulk defining an area of $100 \times 100\ \mu\text{m}^2$ of modified materials. The thickness of the written layer in the volume was defined by the length of the laser-affected zone along the propagation axis.

Finally, the glass specimens were subjected to accelerated aging by classical heat treatment after the laser irradiation to discuss the nature and erasure mechanism of the modifications. The samples were annealed at 513, 553, and 593 K for 15 hrs with a 1 K/min heating and cooling rate. Then, samples were subjected to further characterization.

4.3.3 Specimen characterization

After fs-laser exposure, specimens were first observed using a digital OM with standard lighting conditions (KH-8700 from Hirox). The cross-polarizer optical images were obtained using a polarized light microscope (Olympus BX51). A digital holographic microscope (DHM) was used to measure the optical path differences (OPD) and subsequently to estimate the refractive index changes at 633 nm. The surface profile was obtained by laser confocal microscopy (VK-X from Keyence).

Specimens having volume modifications were polished to reveal the structures and etched with NaOH (2.5 %) for less than 5 seconds. NaOH has proven itself as an effective etchant for the laser-affected zone for chalcogenide [368–370]. Specimens coated with a carbon film were observed using a field-emission scanning electron microscope (FE-SEM, Gemini 2 from Zeiss) equipped with energy-dispersive X-ray spectroscopy (EDS) operated at 5 kV for high-resolution imaging and 20 kV for elemental analysis. A Raman spectrometer (LabRam HR from Horiba), equipped with a 633 nm-laser excitation source attenuated down to 4 mW (to prevent damaging the specimen), was used to record Raman spectra of the modified zones. This wavelength is selected to minimize the absorption in the material. The linearly-polarized Raman laser beam was focused at the surface of the specimen using a 0.9 NA objective (100x-532 nm from Thorlabs). A series of scans were performed at room temperature on each laser-modified zone, with acquisition times of 30 s for each spot.

Finally, the transmission and reflection spectra were measured at room temperature for wavelengths ranging from 250 to 2000 nm using a UV-VIS-NIR spectrometer (Lambda 950 from Perkin Elmer). A mask with a hole of around $1 \times 1\ \text{mm}^2$ is prepared from black paper for broadband absorbance. For the measurement, the reference beam power is attenuated to 1%, to compensate for the presence of the mask and the ensuing effective drastic reduction of the beam size from the original 2 cm in diameter. The thickness of the sample used for this transmission measurement was 2.5 mm.

4.4 Results and discussion

4.4.1 Self-organization and photo-modifications in the volume

Figure 4.3.a summarizes various modifications obtained by dynamic laser exposure in the volume as a function of a pulse duration ranging from 50 to 270 fs at 100 kHz. Let us explain each modification step-by-step at 270 fs. At the lowest pulse energy, a homogeneous modification has been observed, leading to a change in the density and a concurrent rise in the refractive index. In fused silica, this regime (observed typically at low pulse energy with a pulse duration shorter than 200 fs) has been linked to localized densification, which results in positive refractive index change [17, 131, 371]. Here, densification was observed at the lowest pulse energy for all the selected pulse durations.

At higher pulse energies, another regime, namely porosification, is observed. This modification may be related to the formation of void-like structures at a molecular level, triggered by photo-dissociation processes at high field densities (Figure 4.3.a). Two types of contrast in refractive index as a function of laser fluence have been demonstrated in $\text{Ge}_{23}\text{Sb}_7\text{S}_{70}$, which are similar in terms of the sign and magnitude for its thin-film counterparts as well as for $\text{Ge}_{15}\text{As}_{15}\text{S}_{70}$ [302, 332]. Similarly, the change in amplitude of the refractive index increases with the pulse energy, showing that the glass connectivity progressively cleaved with laser fluence. This regime was explained by hydrodynamic expansion followed by thermomechanical relaxation, although they are annihilated by annealing above glass transition temperature for $\text{Ge}_{15}\text{As}_{15}\text{S}_{70}$ [332]. We discuss the effect of heat treatment later in this chapter.

Once the critical threshold is exceeded, anisotropic birefringent modifications are observed. We specifically investigate the occurrence of self-organized nanostructures consisting of periodically organized parallel nanoplanes, with sub-wavelength periodic features oriented perpendicular to the electric field vector of a linearly polarized femtosecond laser beam. The presence of nanogratings was first reported in fused silica [1]. In this class system, this type of modification exhibited form-birefringence [372], an increase in etch rate selectivity [36], and stress-induced birefringence [373] resulting from a noticeable localized volume expansion [40]. The nanogratings in fused silica exhibit high thermal stability due to the formation of nanoporous structures as a by-product of the laser-induced decomposition of the glass matrix [33, 374]. Like in silica, self-organized nanogratings in this chalcogenide glass studied here are observed inside the glass volume as well as on the glass surface interface, as will be discussed in the next section.

Figure 4.3.b displays the effect of photo modifications at various pulse energy on the change in refractive index. While photo-contraction is associated with the densification regime, porosification leads to photo expansion, similar to other studies [320, 321]. Densification or porosification alters the refractive index, which was characterized by measuring the optical path difference (OPD) changes (see detailed results in Appendix D). The densification regime is mostly used to fabricate optical components, such as waveguides and diffractive elements;

the latter has been used to fabricate micro-lenses [375]. Further increase in the net fluence promotes photo expansion in a regime where we observed anisotropic birefringent structures. From a practical point of view, such modifications have been utilized to produce birefringent and monolithic multifunctional devices for 5D optical data storage, micro-optics, photonics, telecommunications, imaging, and so on [80, 373, 376].

Figure 4.3.c shows the effect of laser processing parameters on the induced morphological changes at 10, 100, and 1000 kHz. A clear evolution of the modification from a low repetition rate to a higher one is visible in OM images, highlighting the feedback mechanism in the femtosecond laser interaction with chalcogenide glass. Above 500 kHz, in a thermally cumulative regime in which pulses are accumulating faster than the lattice cooling time, melting and resolidification lead to the generation of self-organized periodic patterns consisting of single or multiple spherical morphologies. In this condition, the repetition rate is at 1 MHz, which lies well within the cumulative regime for chalcogenide glass.

The formation of periodic spherical patterns starts at a pulse energy of 25 nJ, corresponding to an exposure fluence threshold of $\sim 13 \text{ J/cm}^2$. As the laser net fluence increases, the outer shell of the patterns gets wider, associated with a temperature-driven process. Above 50 nJ ($> \sim 165 \text{ J/cm}^2$), a formation of catastrophic fracture, removal of a top surface, and the creation of a crater were observed as shown in Appendix D, similar to a previous study [354]. Patterns consisting of bubbles with spherical cavities have been demonstrated in fused silica as a consequence of cumulative energy deposition [22], yet, we did not observe, at least at the scale of our observations, the formation of trapped gas pockets. Further characterization is needed to explore the existence of voids in chalcogenide glasses in the thermal cumulative regime. The self-organized periodic spherical patterns can be used for numerous applications, such as 3D data storage, photonic crystals, optical memories, waveguides, gratings, couplers, chemical and biological membranes, and other devices [377, 378].

Figure 4.4.a-b presents cross-polarizer images of laser-induced modifications in the volume. The polarization anisotropy observed here is attributed to a form-birefringence effect caused by the periodic structures with alternating refractive index [372]. Figure 4.4.c-g shows SE images of volume modifications with varying laser polarizations. SE images were obtained after polishing the specimen surface down to the level of the modifications and subsequently exposed to a flash etching (2.5% NaOH). Even merely polishing the specimen tends to affect the softer material preferentially and thus distort or possibly erase any small features. In $\text{Ge}_{23}\text{Sb}_7\text{S}_{70}$, this subwavelength periodicity reduces with the pulse energy, from 270 nm at 100 nJ (13 J/mm^2) down to around 220 nm at 200 nJ (26 J/mm^2) at an exposure dose of 400 pulses per spot. The periodicity dependence on the laser fluence as a function of pulse duration is shown in Appendix D. To investigate the elemental distribution in the laser-affected zone, SEM-EDS was performed. The measured composition of nanogratings was $\text{Ge}_{23.2}\text{Sb}_{7.1}\text{S}_{69.7}$. While near the resolution capability of EDS, the laser-affected zone consists of alternating S-deficient and S-depleted structures. The formation mechanism of these nanogratings remains unclear.

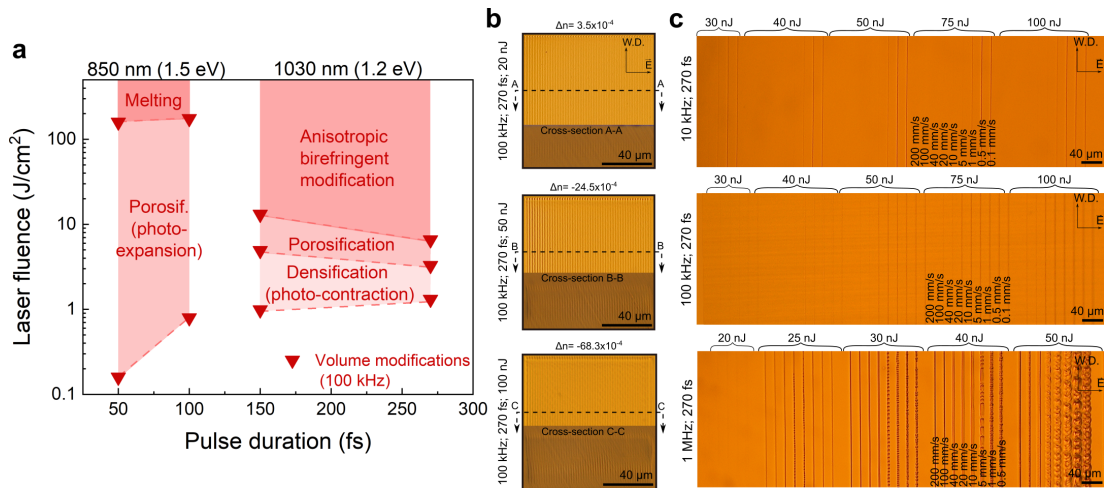


Figure 4.3: a) Laser-induced volume modifications of $\text{Ge}_{23}\text{Sb}_7\text{S}_{70}$ as a function of pulse energy and duration in dynamic laser exposure. The number of effective pulses is fixed at 400, and the repetition rate is 100 kHz. b) OM images of $100 \times 100 \mu\text{m}^2$ laser-modified single plane inscribed with various pulse energies at 100 kHz with a pulse duration of 270 fs. The square planes are $20 \mu\text{m}$ below the surface. The refractive index changes are estimated based on the optical path difference (OPD) measured by a digital holographic microscope (DHM). The standard deviation of the method is estimated to be 2×10^{-4} . c) OM images of laser inscribed lines with 270 fs-pulses emitted at different repetition rates (lines are located at $20 \mu\text{m}$ below the surface): 10 kHz, 100 kHz, and 1 MHz.

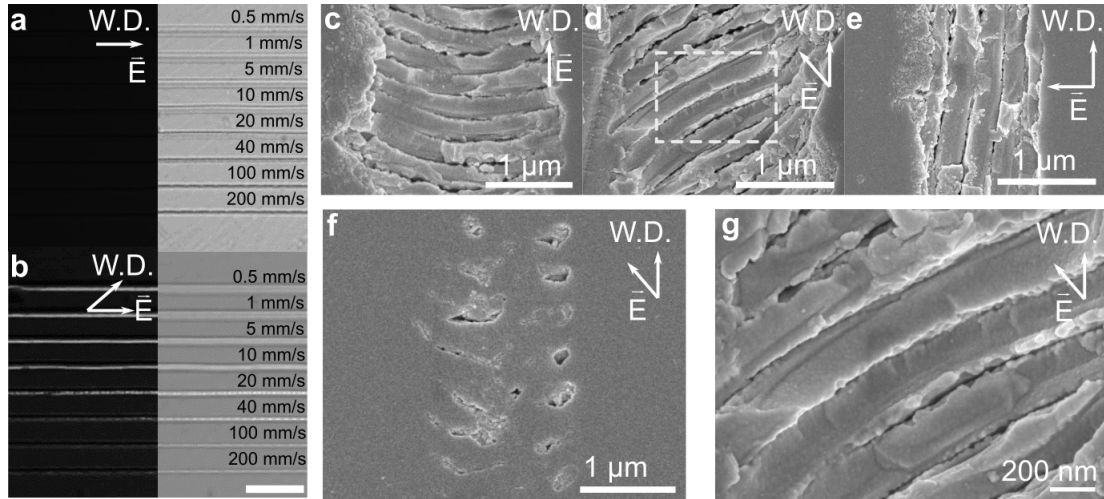


Figure 4.4: OM and cross-polarizer images of laser-inscribed lines with a) parallel and b) 45° polarization orientation to the laser-writing direction. The pulse energy is fixed at 100 nJ. c-e) SE images of laser-induced modifications (270 fs pulse length with 100 kHz repetition rate) for three polarization orientations: c) parallel, d) 45° , and e) perpendicular polarization. The pulse energy is 100 nJ with 400 pulses. f) The laser modification with two effective pulses per spot (writing speed of 100 mm/s). g) The higher magnification of the modification in d).

Figure 4.5.a shows the transmission spectra of the laser-affected zone in the glass volume. Light-induced defects and the formation of anisotropic self-organized nanostructures cause a notable decrease in the transmission spectra. The decrease in transmission is proportional to an increase in reflection (see Appendix D). In addition, structural changes near these modified regions are investigated using Raman spectroscopy. Since the Raman laser spot size is around $1\ \mu\text{m}$ at 633 nm, it integrates across the overall bond structure within the full, laser-affected zone, not allowing for a more spatially resolved analysis. However, it does provide some insight into structural changes associated with the laser-induced chemical modification seen by EDS. Figure 4.5.b compares Raman spectra of pristine and laser-modified glass. Let us first explain the $\text{Ge}_{23}\text{As}_7\text{S}_{70}$ glass network. The glass network consists of $\text{GeS}_{4/2}$ tetrahedra and $\text{SbS}_{3/2}$ pyramid, which are randomly connected [379]. In addition, S-S bonds are found in S-rich systems, whereas homopolar metal bonds are observed in S-deficient glass systems [380].

The spectrum of the pristine glass in Figure 4.5.b consists of peaks between 275 to $485\ \text{cm}^{-1}$. The band at $302\ \text{cm}^{-1}$ belongs to SbS_3 pyramids, while $340\ \text{cm}^{-1}$ is assigned to GeS_4 tetrahedra [302, 332]. 330 and $402\ \text{cm}^{-1}$ are assigned to corner-sharing $\text{GeS}_{4/2}$ tetrahedra, and $375\ \text{cm}^{-1}$ are attributed to edge-sharing $\text{GeS}_{4/2}$ tetrahedra. Two tetrahedra are connected with bridging sulfur, namely $\text{S}_3\text{Ge-S-Ge}_3\text{S}$, resulting in a band at $427\ \text{cm}^{-1}$. In addition, excess sulfur causes bands at $475\ \text{cm}^{-1}$ as a S_8 ring and $485\ \text{cm}^{-1}$ as a S_n chain [302]. A slight redshift - associated with a decrease in a backbone structure - is observed in the main band of the laser-affected zone. Moreover, a noticeable increase in the band intensity of the S_8 ring, S_n chain, and corner-sharing $\text{GeS}_{4/2}$ tetrahedra is observed in the laser-affected zone. There is a slight decrease in the bands at around $340\ \text{cm}^{-1}$. These results indicate the presence of fewer isolated $\text{GeS}_{4/2}$ groups and more connectivity of Ge-S-Ge and S-S homopolar bonds. The level of sulfur dissociation as a ring or a chain increases with laser fluence. As consistent with elemental analysis, we observe a minor decrease in GeS_4 content, whereas Sb_2S_3 content is unaltered. The laser-affected zone shows a random glass network due to local photo-induced decomposition.

4.4.2 Self-organization and photo-modifications on the surface

Let us now consider the surface modification on chalcogenide glass. Figure 4.6.a outlines the various surface modifications of $\text{Ge}_{23}\text{Sb}_7\text{S}_{70}$ in a pulse-duration and fluence space, qualitatively. A first regime, observed at the surface and for low pulse energies, consists of homogeneous and continuous structural changes (i.e., zones without a visible heterogeneity with the instruments considered in this study). At higher pulse energies, above this homogeneous regime, a second regime consisting of self-organized nanostructures is found for all pulse durations considered here (i.e., 50 to 270 fs). Although self-organized nanostructures are detected in a narrower region for the shortest pulse duration (50 fs), it is comparable between 150 fs to 270 fs. The surface self-organization threshold, $1.7\ \text{J}/\text{cm}^2$ for a single shot at 100 fs and $1.3\ \text{J}/\text{cm}^2$ for a single shot at 270 fs, is two to three times lower than fused silica [68], due to lower bond energy, smaller band gaps, photosensitivity, and higher absorptivity at $1\ \mu\text{m}$

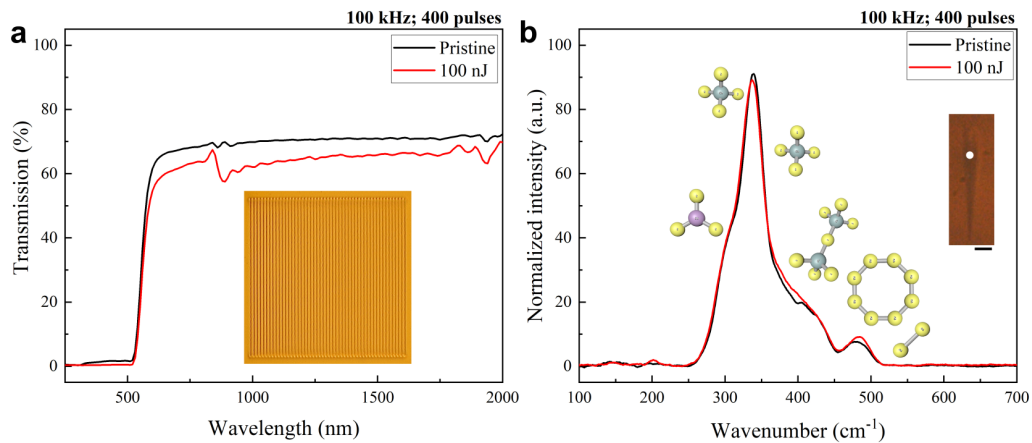


Figure 4.5: a) Transmission spectra of the laser-affected zone. The inset shows a reflective OM of a single plane ($1 \times 1 \text{ mm}^2$) formed with parallel lines generated from overlapping pulses at 100 nJ. The peaks around 800 nm are measurement artifacts due to the change of the detector measuring visible to the one measuring NIR during spectral measurement. b) Raman spectra of bulk $\text{Ge}_{23}\text{As}_7\text{S}_{70}$ versus laser-induced volume modifications (red curve). Note that the production parameters are similar to the ones reported in Figure 4.4.c. The inset image shows the cross-section of the measured laser-affected zone. The scale bar is $4 \mu\text{m}$.

(i.e., the laser wavelength), which is around 25%.

The time-dependent temperature distribution of focal volume calculated by thermal diffusion [136] of multi-pulse irradiation for 10 kHz is shown in Figure 4.6.b. The temperature rises quickly in the focal volume, and thermal quenching with a typical cooling rate of approximately $10^{14} \text{ K}\cdot\text{s}^{-1}$ eventually leads to supercooling of new dense phases, and/or metastable phases recovered under extreme conditions [137]. As the pulse interval (approximately a few μs) is longer than the lattice cooling time, the temperature rise is not affected by the second pulse around 250 kHz. Above this rate, thermal effects can lead to softening, melting, and resolidification of the laser-affected zone. Figure 4.6.c shows the OM images of inscribed laser tracks on the surface of $\text{Ge}_{23}\text{Sb}_7\text{S}_{70}$. The transition from a non-cumulative to a cumulative regime is highlighted from 100 kHz to 1 MHz. In addition, ablation in the cumulative regime is accompanied by catastrophic fracture and ejection of material.

Figure 4.7 displays the surface profile and the temporal evolution of the temperature upon multi-pulse irradiation with various pulse energies. Surface characterization is performed at 100 kHz, as presented in Figure 4.7.a. The homogeneous modification refers to non-visible modifications, yet, photo-expansion is revealed by surface profile measurement. The local temperature gradient remains below the glass transition ($T_g = 584 \text{ K}$) temperature in this type of modification, as emphasized in Figure 4.7.b. Higher laser fluence, or field strength, in this case, results collapse of the homogeneous modifications into cavitation with self-organized nanostructures. Although the temperature remains lower than T_g with few pulses around

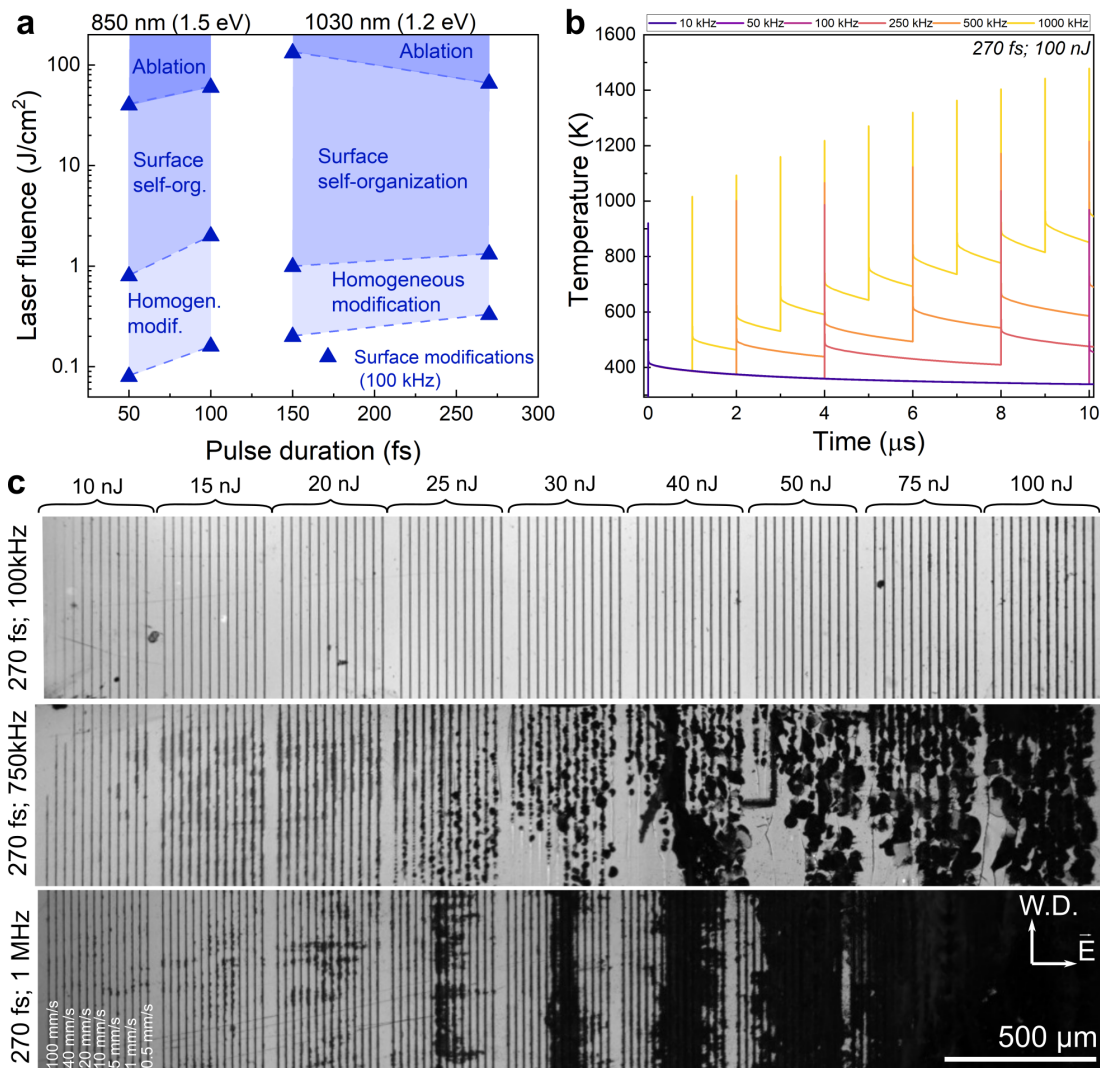


Figure 4.6: a) Laser-induced surface modifications of $\text{Ge}_{23}\text{As}_7\text{S}_{70}$ as a function of pulse energy and duration by dynamic laser exposure at 100 kHz. b) The time-dependent temperature distribution of focal volume ($2 \times 2 \times 10 \mu\text{m}^3$) during multi-pulse irradiation of $\text{Ge}_{23}\text{As}_7\text{S}_{70}$ surface at various repetition rates. c) OM images of surface tracks inscribed at 100 kHz, 750 kHz, and 1 MHz.

10-20 nJ, the temperature exceeds the T_g upon multiple pulses with a pulse energy of 50 nJ. Further rise in the pulse energy leads to melting and ablation of the laser-affected zone.

Figure 4.8 shows SE images of self-organized nanostructures visible on the glass surface as a function of pulse energy and the number of effective pulses per spot. The structures observed have an average periodicity of about 250 nm that decreases with the increase of laser fluence (achieved by increasing the number of pulses) down to 170 nm. At higher peak fluence (e.g., above 50 nJ), partial ablation leads to randomly distributed spherical nanoparticles, with average sizes of 150 nm and compositions similar to the bulk material. Traces of self-organized

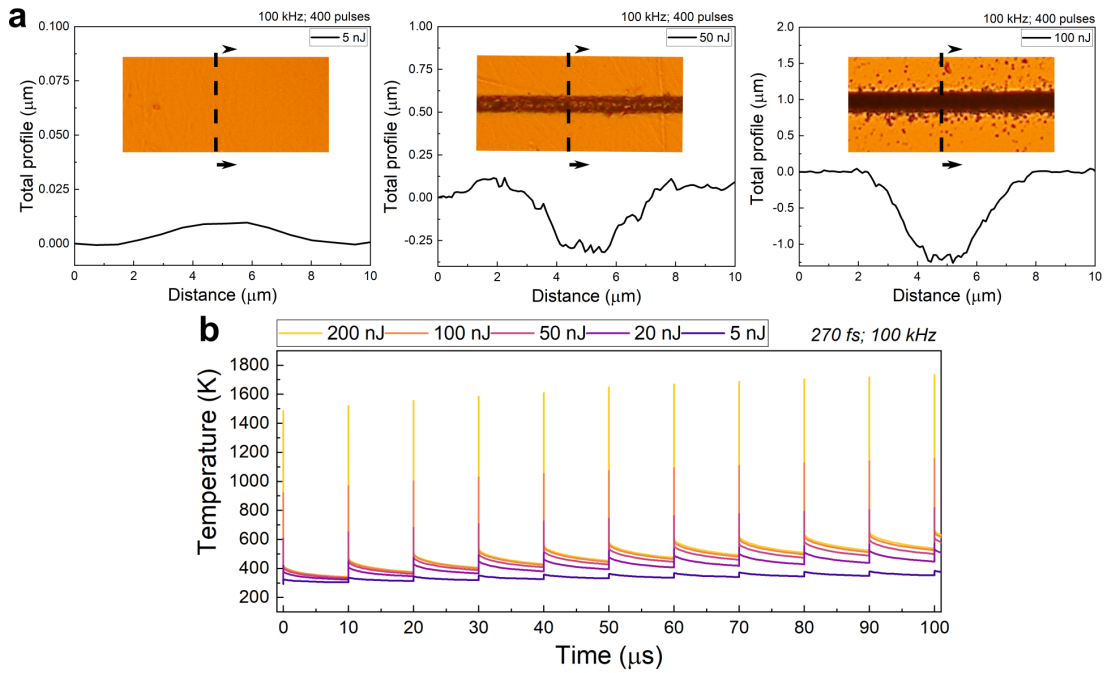


Figure 4.7: a) Surface profile obtained for three different surface regimes, emitted at 270 fs pulses at 100 kHz. The inset images show transmission OM images of the surface, corresponding to homogeneous modifications at 10 nJ, self-organized surface structures at 50 nJ, and ablation patterns at 100 nJ; achieved with 400 pulses overlapping. b) The time-dependent temperature distribution of focal volume during multi-pulse irradiation with various pulse energies at 100 kHz.

nanostructures are observed and, interestingly, in cases for which there is no overlapping of two consecutive pulses. The observation of subwavelength periodic structures in single pulse exposure is rather specific to chalcogenides [349], unlike other substrates [68]. Table in Appendix D summarizes the periodicity observed in chalcogenide glass. Interestingly, in some cases, As_2S_3 shows low spatial periodicity (~ 800 nm) at low fluence and high spatial periodicity around 200 nm at higher fluence [349–351]. The possible mechanism has been interpreted with the pump-probe experiment previously [350]. The other two systems observed are Ge-S and As-Se, having low spatial periodicity around ~ 750 nm [352, 353]. It suggests that the first step of the self-organization process is driven by the plasma-pulse interaction rather than by pulse-to-pulse accumulation effects. The formation of surface self-organized structures in materials has been summarized with a great effort elsewhere [62]. Lower spatial periodicity was explained by surface plasmon wave formation on the surface upon the first shot and the interference phenomenon appears resulting in a redistribution of the laser fluence on the surface. However, the formation of high spatial periodicity remains unclear.

$\text{Ge}_{23}\text{Sb}_7\text{S}_{70}$ glass is known as resistant to oxidation, which might occur during the laser-inscription process in an open-air atmosphere [319]. The elemental composition as measured in the self-organized nanostructures reveals the composition of nanoplanes in Figure 4.8.f

as $\text{Ge}_{22.5}\text{Sb}_{7.7}\text{S}_{64.9}\text{O}_{4.9}$. SEM-EDS results indicate that the Ge/Sb ratio seems to be slightly affected, that mostly S is removed, and photo-oxidation is taking place. During fs-laser irradiation, chemical bonds are broken upon the ionization process, and therefore photo-oxidation is a result of trapped oxygen by ionized elements in the ambient conditions. The high sulfur loss might be attributed to low bond energy and high volatility of sulfur.

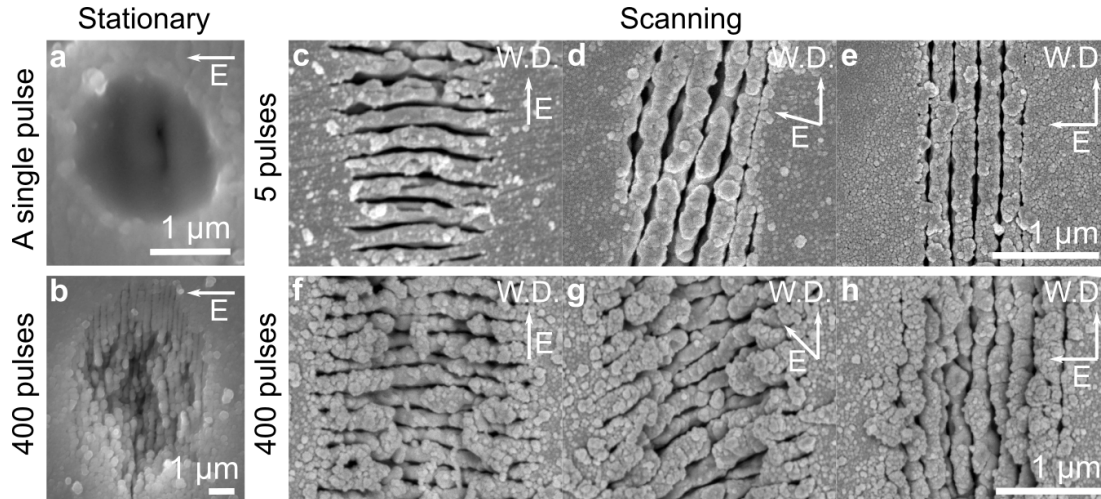


Figure 4.8: a-b) SE images of surface self-organized nanostructures on $\text{Ge}_{23}\text{Sb}_7\text{S}_{70}$ under non-scanning conditions: a) A single pulse and b) 400 pulses. c-h) Self-organized nanostructures while scanning along a line at 50 nJ for which 5 pulses overlap and for c) parallel, d) 45° , and e) perpendicular polarization with respect to the writing direction, respectively. Same conditions but this time with 400 pulses overlapping and for f) parallel, g) 45° , and h) perpendicular polarization defined with respect to the writing direction.

Figure 4.9 shows the transmission and Raman spectra of the pristine glass and the laser-affected zone. While we discuss the effect of laser parameters in the following sections in detail, let us cover the transmission spectra briefly as a comparison to volume modifications. The decay in the transmission is correlated with an increase in reflection (shown in Appendix D) and scattering due to surface structures and roughness as presented in Figure 4.8.c. The transmission decreases with the pulse energy, accompanied by photo-darkening. In addition to morphological changes and defects, decay in transmission by photo-darkening is a common phenomenon, observed in multiple chalcogenide glass systems [380]. The photo-darkening is a rather complex phenomenon, the structural evolution might be helpful for understanding. It can be reversed via heat treatment close to the glass-transition temperature [301].

Figure 4.9.b exhibits the Raman spectra of the pristine glass and the laser-affected zone. Upon ultrafast laser irradiation, both the left and right shoulder of the main band, related to SbS_3 pyramids at 302 cm^{-1} and corner-sharing $\text{GeS}_{4/2}$ tetrahedra at 402 cm^{-1} , respectively, are altered. On one hand, the intensity of bands at 302 , 330 , and 375 cm^{-1} grow with pulse energy, whereas the intensity of the band at 340 cm^{-1} decay with the pulse energy. These modifications, along with the rise of 475 cm^{-1} , indicate the reconfiguration of GeS_4 tetrahedra to corner-

sharing GeS_4 tetrahedra due to a decaying concentration of sulfur in the glass backbone. Overall, the Ge/Sb ratio seems slightly affected by laser irradiation. On the other hand, by changing the number of pulses, the peak intensity of the right and left shoulders of the main band shows an increase, indicating the onset of glass decomposition. In addition, with both the increasing pulse energy and the number of pulses, the main band is broadened due to a disorder in the glass network [319]. The effect of the laser parameters and the comparison with various different compositions are demonstrated further in this chapter.

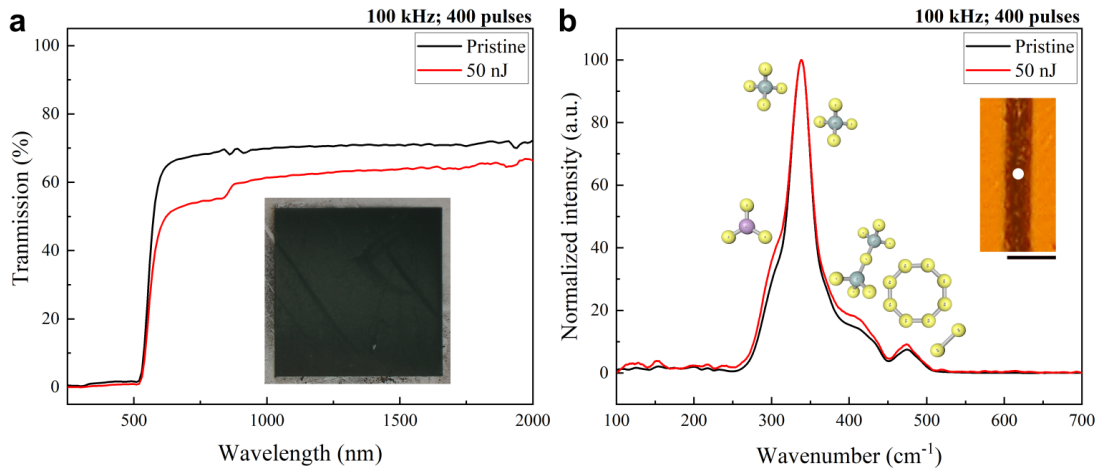


Figure 4.9: a) Transmission spectra of pristine and the laser-affected zone of $\text{Ge}_{23}\text{Sb}_7\text{S}_{70}$. The inset shows a reflective OM of a single plane ($1 \times 1 \text{ mm}^2$) formed with lines written at 50 nJ with 400 pulses per spot. b) Raman observations of the surface of the pristine and the laser-affected zone of $\text{Ge}_{23}\text{Sb}_7\text{S}_{70}$. In these experiments, the pulse repetition is set to 100 kHz. The inset image shows the measurement point of the laser-affected zone. The scale bar is $4 \mu\text{m}$.

4.4.3 Stability of morphological and structural modifications

Up to now, we explained numerous photo-induced modifications on the glass surface and in the volume upon femtosecond laser irradiation. Photosensitivity of chalcogenides can lead to diverse modifications depending on the irradiation conditions. The classification of these modifications is based on reversibility/irreversibility [301]. For instance, metastable states are present as high as glass transition temperature, while transient ones are present only during illumination. Here, we only consider stable and metastable modifications since our investigation starts only after the illumination. In addition, physical aging is the dominant effect in chalcogenide glass systems at room temperature due to their relatively low glass transition temperature. In general, the time-dependent modification in the physical properties and chemical degradation have been reported [303, 381]. Similar to photo-induced changes, photo-induced aging has been reported in chalcogenide glass [382].

The purpose of this section is to shed light on a few points about the femtosecond laser-induced modifications of $\text{Ge}_{23}\text{Sb}_7\text{S}_{70}$ glass. One is to understand the type of the modifications,

such as temporary or permanent modifications, along with their thermal stabilities. Another one is to investigate the erasure mechanism of photo modifications. We report the nature and the stability of femtosecond laser-induced modifications of $\text{Ge}_{23}\text{Sb}_7\text{S}_{70}$ glass by annealing. Several temperatures are selected following previous studies, where the erasure of certain defects leads to the disappearance of such modifications [343].

Let us explain the aging by the typical enthalpy (or volume) vs. temperature graph of glass in Figure 4.10.a. A rapid cooling above melting temperature leads to supercooled and glass regimes. The enthalpy curve deviates from the liquid curve depending on the cooling rate. This deviation results in different glass transition temperatures while heating the glass. For example, while T_{g1} represents a glass transition for slowly cooled glass, T_{g2} indicates the glass transition of fast cooled glass. Even though the glassy state is obtained, the material continues to relax towards a lower energy state (or thermodynamic equilibrium, where there is a lower enthalpy or volume). The relaxation time can be enhanced by keeping the glass at a certain temperature and time, known as physical aging. The blue points indicate the selected temperatures for further investigation of thermal stability.

Figure 4.10.b displays the stability of various modifications over temperature based on optical and spectroscopy observations after annealing. After keeping the irradiated glass at 513 K for 15 hours, homogeneous modifications on the surface and the densified zone in the volume are not optically visible. In contrast, a short annealing time has resulted in a more efficient waveguide response in densification regime [332]. Above 553 K, modifications so-called porosification, anisotropic nanostructures (in Figure 4.10.c), and bubbles in the volume survive (see Appendix D). Reversing such modifications is possible above the glass transition temperature. However, exceeding the glass transition temperature results in randomly distributed crystalline precipitates in the glass, causing the decomposition of the glass network and degradation of the optical properties. Similarly, surface self-organized nanostructures start to be erased around glass transition temperature, shown in Figure 4.10.d. The periodic nanoplanes leave their places in a few pores, making the nanostructure indistinguishable after five pulse exposure. The precipitate nucleated at the border of nanostructures accelerates the deformation of the laser-affected zone. Finally, the erasure of surface modifications such as self-organization, cavitation, and ablation requires remelting of the glass.

Figure 4.11 presents the Raman spectra of the bulk modifications before and after the heat treatment at 553 K for 15 hrs. The characteristic changes in the laser-affected zone are redshift of the main peak, intensity increase in both shoulders, i.e., SbS_3 pyramids and $\text{S}_3\text{Ge-S-Ge}_3\text{S}$ units, reconfiguration of main units and incorporation of sulfur from the glass backbone, in Figure 4.11.a. The changes in the glass spectra are proportional to the laser fluence (specifically to the optical field strength). With annealing in Figure 4.11.b, although the structures are visible optically, the shift in the main peak is resolved. In addition, there is a decrease in the intensity of the shoulders of the main band. It highlights the recovery of the defects in the form of corner-sharing $\text{GeS}_{4/2}$ tetrahedra being rearranged to edge-sharing. However, slightly excess sulphur still present as S_8 ring and S_n chains.

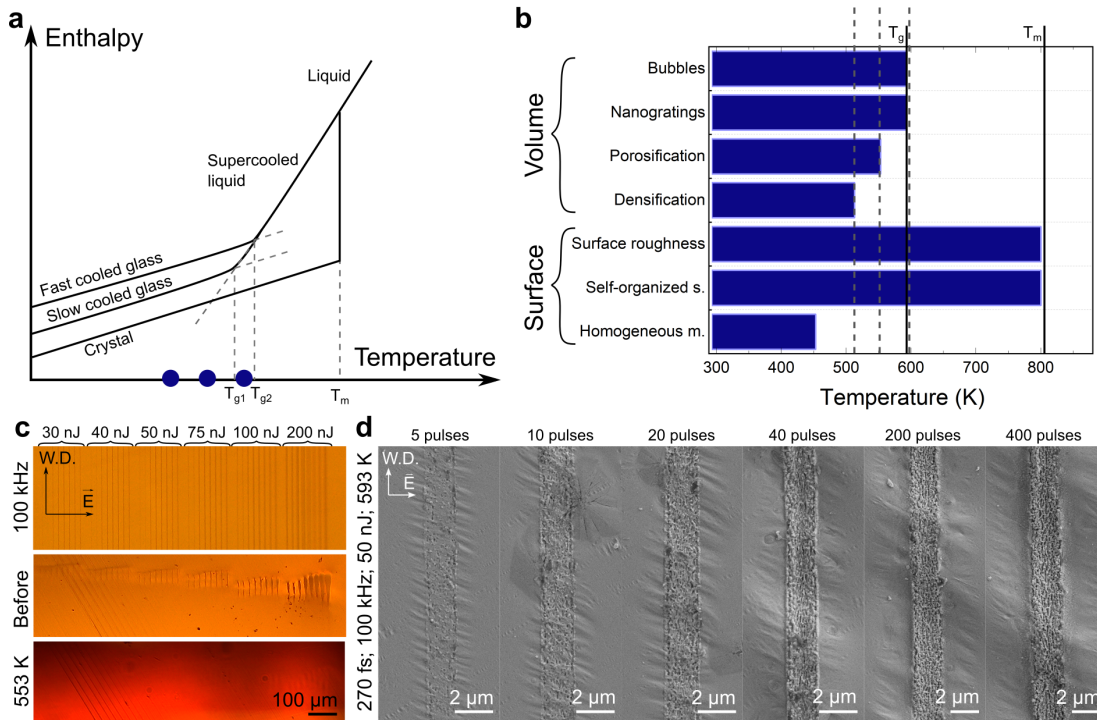


Figure 4.10: a) Typical enthalpy graph of glass over a temperature, presenting the transition from glassy state to supercooled liquid and molten state. Blue circles represent annealing temperatures. b) The graph representing the stability of each modification over a temperature on the surface and in the volume. The dashed lines denote the selected heat-treatment temperatures. c) OM images of bulk modifications (at 100 kHz) before and after the heat treatment at 553 K for 15 hrs. d) SE images of self-organized nanostructures (at 100 kHz) before and after the heat treatment at 593 K for 15 hrs.

Figure 4.12.a-d displays surface modifications and Raman spectra after annealing at 593 K for 15 hrs. Figure 4.12.e shows Raman spectra of the morphologies after annealing, along with their peak assignments [383–385]. Crystalline precipitates exhibit similar Raman spectra as monoclinic α -GeS₂ with high-intensity peaks at ~ 361 and 432 cm^{-1} . Still, the peak at 340 cm^{-1} at laser-affected zones is defined less clearly in the literature. It can be generated from both the A_1 mode of the Ge(S_{1/2})₄ tetrahedra and the A_{1g} mode of Ge(S_{1/2})_{4-x} with a companion A_{c1} mode at $\sim 370\text{ cm}^{-1}$. Peaks located at 340 and 370 are related to β -GeS₂ [336]. Orthorhombic sulfur peaks are located at $\sim 151, 232, 472\text{ cm}^{-1}$. Above the glass transition, all the structural changes, such as photo-expansion, and photo-darkening are reversed. However, the crystallization takes place in the entire volume. Overall, we validate the temperature window of all the modifications observed in Ge₂₃Sb₇S₇₀ glass.

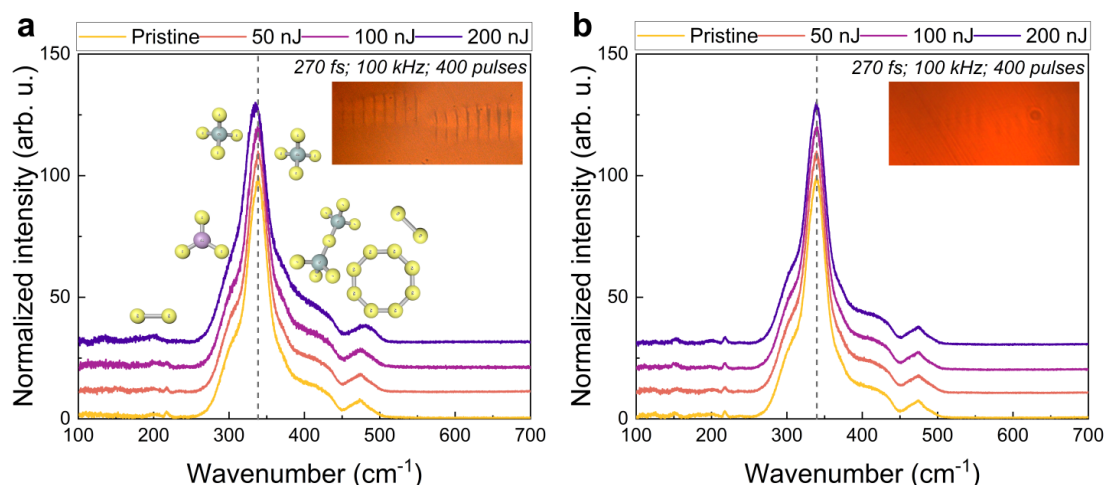


Figure 4.11: Raman spectra at the surface of both pristine and laser-affected zones in $\text{Ge}_{23}\text{Sb}_7\text{S}_{70}$ glass volume a) before the heat-treatment and b) after the heat-treatment at 553 K for 15 hrs. In these experiments, the pulse repetition is set to 100 kHz. The inset image shows the measurement point of the laser-affected zone.

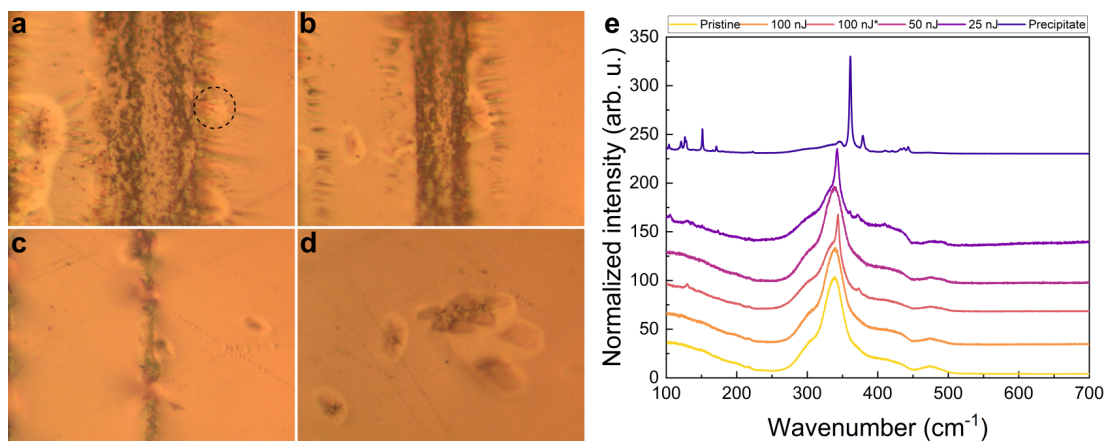


Figure 4.12: OM images of surface modifications (at 100 kHz) before and after the annealing above the glass-transition temperature at 593 K for 15 hrs with laser parameters of a) 100 nJ; b) 50 nJ; c) 25 nJ and d) pristine glass with the precipitate at the center. e) Raman observations of the surface of the pristine and the laser-affected zone on $\text{Ge}_{23}\text{Sb}_7\text{S}_{70}$ surface after the annealing at 593 K for 15 hrs. The dashed circle in a) represents the precipitate nucleated at the border of the laser-affected zone, corresponding to the 100 nJ* in e). In these experiments, the pulse repetition is set to 100 kHz with 400 pulses per spot.

4.4.4 Effect of the glass network on laser-induced modifications

So far, we investigated various photo-modifications and self-organization of $\text{Ge}_{23}\text{Sb}_7\text{S}_{70}$ and their thermal stability. In this final section, we unravel how photo-induced modifications (including the self-organization process) are influenced by variations in glass-forming elements, i.e., bond energy, atomic weight, short-range order, etc., for glass systems sharing similar

iso-structural units. For that purpose, we compare the findings of our systematic investigation by replacing Sb with As and S with Se, keeping the same proportion in the bulk glass. In this case, the heavier nature of Se enhances refractive index and nonlinearity compared to S, while As leads to higher photo-darkening and ablation threshold compared to Sb [337, 386].

Table 4.2 presents various thresholds leading to the surface modifications for single pulse irradiation. While the modification threshold indicates the first observable modification optically, the ablation threshold is rather determined by the collapse of self-organized nanogratings, ejection of matter, and melting. It has been shown that bond energies $\text{Ge}_{23}\text{As}_7\text{S}_{70}$ and $\text{Ge}_{23}\text{Sb}_7\text{Se}_{70}$ differ, and consequently some physical properties, although the number of lone electron pairs is quite similar [387]. During the nonlinear absorption process, the critical free electron density plays an important role in the formation of the final microstructure.

Table 4.2: Thresholds for modifications and ablation of $\text{Ge}_{23}\text{Sb}_7\text{S}_{70}$, $\text{Ge}_{23}\text{As}_7\text{S}_{70}$ and $\text{Ge}_{23}\text{Sb}_7\text{Se}_{70}$ per pulse.

Sample	Modification threshold	Onset of ablation
$\text{Ge}_{23}\text{Sb}_7\text{S}_{70}$	10 nJ	125 nJ
$\text{Ge}_{23}\text{As}_7\text{S}_{70}$	15 nJ	150 nJ
$\text{Ge}_{23}\text{Sb}_7\text{Se}_{70}$	50 nJ	100 nJ

Figure 4.13.a-b shows SE images of the surface self-organized structures of $\text{Ge}_{23}\text{As}_7\text{S}_{70}$ and $\text{Ge}_{23}\text{Sb}_7\text{Se}_{70}$. Likewise, the orientation of self-organized nanostructures is perpendicular to the laser electric field. The periodicity and continuity differ greatly from one another. Smaller periodicity and threshold are obtained in $\text{Ge}_{23}\text{As}_7\text{S}_{70}$ compared to $\text{Ge}_{23}\text{Sb}_7\text{S}_{70}$. Since the wavelength is close to the band gap energy of $\text{Ge}_{23}\text{Sb}_7\text{Se}_{70}$, continuous self-organized nanostructures are not observed. Alternately, discontinuous irregular nanostructure in a small processing window.

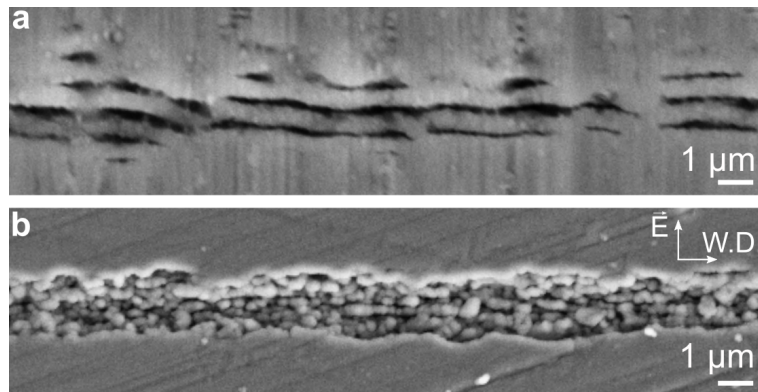


Figure 4.13: SE images of self-organized structures on the surface of $\text{Ge}_{23}\text{As}_7\text{S}_{70}$ and $\text{Ge}_{23}\text{Sb}_7\text{Se}_{70}$ at 100 kHz with 50 nJ and 400 pulses.

The relative compositions of the nanoplanes are $\text{Ge}_{22.5}\text{As}_{6.4}\text{S}_{67.9}\text{O}_{3.2}$ and $\text{Ge}_{23.3}\text{Sb}_{7.0}\text{Se}_{69.5}\text{O}_{0.2}$ for nominal compositions of $\text{Ge}_{23}\text{As}_7\text{S}_{70}$ and $\text{Ge}_{23}\text{Sb}_7\text{Se}_{70}$, respectively. The ratio of existing

structural units is altered by the ultrafast laser. In the case of $\text{Ge}_{23}\text{As}_7\text{S}_{70}$, Ge/As ratio decreases dramatically as Ge/Sb in $\text{Ge}_{23}\text{Sb}_7\text{S}_{70}$. However, instead of $\text{SbSe}_{3/2}$, $\text{GeSe}_{4/2}$ units are modified in selenide glass. In addition, photo-induced oxidation takes place for both of the compositions. The main chalcogen, Se, can be reduced easier than S, resulting in less oxygen incorporation into the laser-affected zone upon multi-pulse exposure.

Let us examine the influence of laser parameters on structural modifications in detail. Figure 4.14 presents Raman spectra and the relative peak intensities changing with pulse energy and the number of pulses per focal area for $\text{Ge}_{23}\text{Sb}_7\text{S}_{70}$. The peak assignments are reported in section 4.4.2 and Appendix D in detail. Figure 4.14.c highlight the effect of pulses as such that a shoulder related to $\text{SbS}_{3/2}$ peak after around 10th pulse changes dramatically and preserves its position up to 400 pulses. On the contrary, the shoulder related to $\text{S}_3\text{Ge-S-Ge}_3\text{S}$ bridge continuously modified with each subsequent pulse. Similarly, the intensity of S rings and chains increases with each pulse. In Figure 4.14.d, dramatic increases in individual $\text{SbS}_{3/2}$ units, S rings, and chains generate glass decomposition.

Figure 4.15.a,d shows transmission spectra with respect to pristine glass of $\text{Ge}_{23}\text{As}_7\text{S}_{70}$ and $\text{Ge}_{23}\text{Sb}_7\text{Se}_{70}$. The absorption increases with laser pulse energy for both glass compositions due to photodarkening, similar to $\text{Ge}_{23}\text{Sb}_7\text{S}_{70}$. As inset OM images indicate, at the onset of ablation, both glass compositions reach to their the highest absorption values. Band gap of a glass depends on the average electron affinity of anions, the average bonding energy of ions and the average polarization energy of ions. Chalcogenide glass with smaller band gap energy likely to show higher refractive index. When refractive index increases, chalcogenide glass subjected to photodarkening [322]. To explain the evolution of glass structure and to correlate properties with photodarkening, Raman spectra collected from the center of the laser-affected zone are investigated in detail.

Resembling similar glass network as in $\text{Ge}_{23}\text{Sb}_7\text{S}_{70}$, $\text{Ge}_{23}\text{Sb}_7\text{Se}_{70}$ the main structural units are $\text{GeSe}_{4/2}$ and $\text{SbSe}_{3/2}$ with excessive Se. Likewise, $\text{GeS}_{4/2}$ and $\text{AsS}_{3/2}$ with excessive S are present in $\text{Ge}_{23}\text{As}_7\text{S}_{70}$. The peak assignments are described in Appendix D. Figure 4.15.b,c,e,f presents Raman spectra and changes in the main peak intensity of laser-affected zones. $\text{Ge}_{23}\text{As}_7\text{S}_{70}$ shows strong effect in main band of 340 cm^{-1} , resulting in sulphur diminution in GeS_4 tetrahedra, as previously reported [360]. The bandwidth of the main band widened due to an increase in disorder in the glass network. The content of edge and corner-sharing $\text{GeS}_{4/2}$ and $\text{AsS}_{3/2}$ structural units increases, whereas there is a slight decrease in the free S-rings and S-chains. We can conclude that the ultrafast laser irradiation primarily disturbs the network connectivity and subsequently causes the removal of excess S. Alteration of Ge/As ratio prompts the rise of the amplitude of the band around 475 and 489 cm^{-1} , the amplitude of the shoulder at 309 cm^{-1} , and broader the main band, indicating less GeS_4 units in the glass network and more AsS_3 units.

Raman spectra of $\text{Ge}_{23}\text{Sb}_7\text{Se}_{70}$ shows that the main structural units are GeSe_4 tetrahedra and Sb_2Se_3 pyramids. Figure 4.14.d-f shows almost no change in Se chains and rings at 250 ,

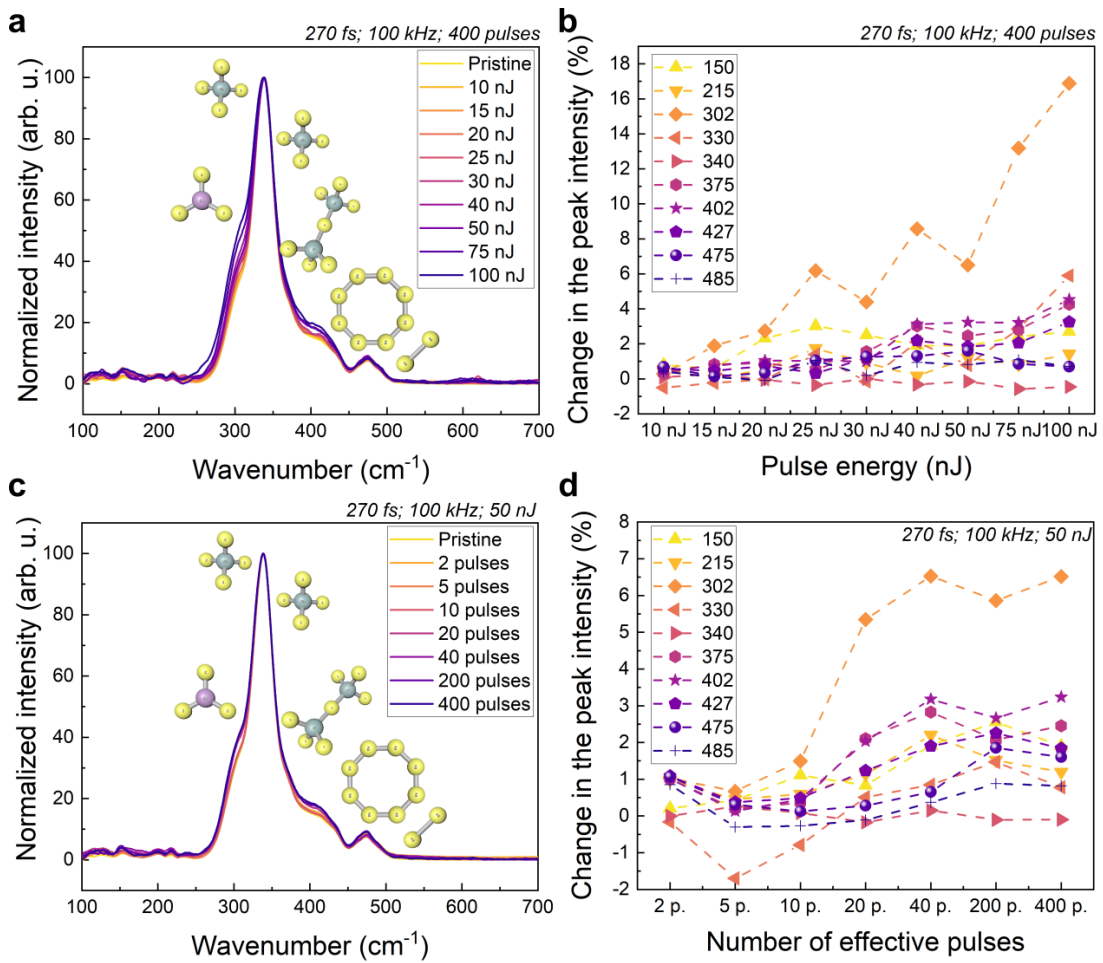


Figure 4.14: a) Effect of pulse energy and c) effect of the number of pulses on Raman spectra of the center of laser affected area of $\text{Ge}_{23}\text{Sb}_7\text{S}_{70}$ glass surface at 100 kHz. b,d) The ratio of main peaks for the pulse energy.

266, and 300 cm^{-1} , up to the onset of ablation. At the onset of ablation, however, Se content decreases below the value of pristine glass, consistent with elemental analysis. The $\text{GeSe}_{4/2}$ tetrahedra peak at 200 cm^{-1} , exhibiting the highest peak intensity, seems not affected by the laser-irradiation. In contrast, the peak at 215 cm^{-1} , the edge-sharing $\text{Ge}_2\text{Se}_{8/2}$ bi-tetrahedra, exhibits large variation with pulse energy. The same trend is observed in 190 cm^{-1} , correlated with $\text{SbSe}_{3/2}$ pyramids. The ratio of Ge/Sb is slightly varied with pulse energy and eventually increases at the onset of ablation. Finally, as opposed to $\text{Ge}_{23}\text{Sb}_7\text{S}_{70}$, the accumulation of pulses from a few to a few hundred does not play a significant role to control the structural modifications in $\text{Ge}_{23}\text{As}_7\text{S}_{70}$ and $\text{Ge}_{23}\text{Sb}_7\text{Se}_{70}$.

Ge-based ternary chalcogenide glass systems display a few similar photo-modifications, such as photo-oxidation, elemental redistribution, and photo-darkening whereas, their modification threshold, conditions to obtain and sustain self-organized nanostructures, and the final chemical structure differ tremendously. These findings pinpoint the importance of the bond

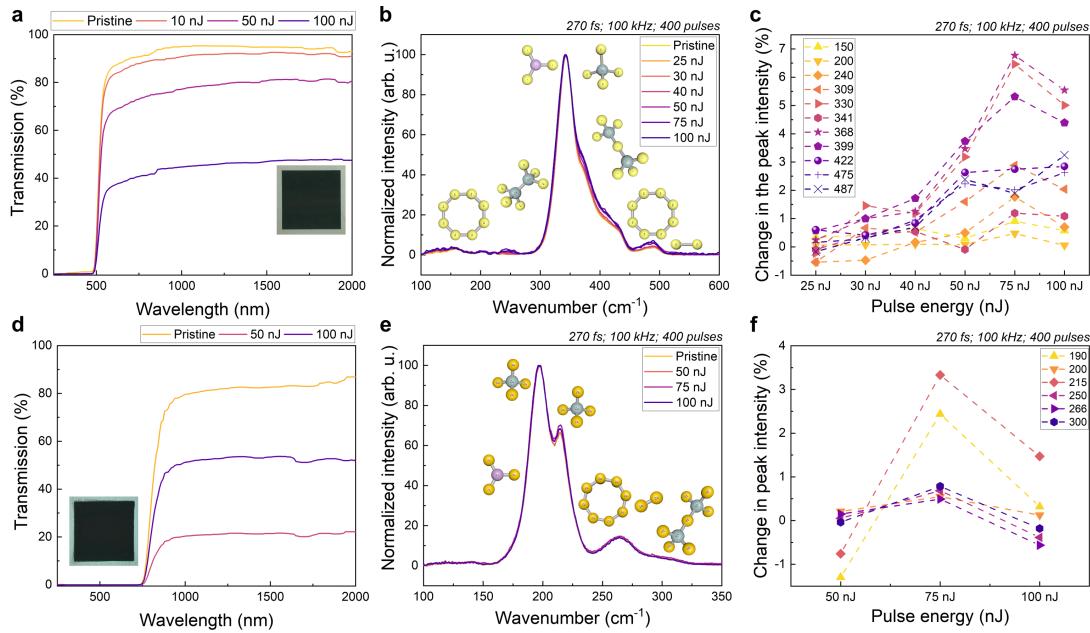


Figure 4.15: Transmission spectra of laser-affected area in a) $\text{Ge}_{23}\text{As}_7\text{S}_{70}$ and b) $\text{Ge}_{23}\text{Sb}_7\text{Se}_{70}$. Inset images show the reflected optical micrographs of $1 \times 1 \text{ mm}^2$ squares inscribed at 100 kHz with 100 nJ and 400 pulses. Raman spectra of the center of laser affected area and effect of pulse energy on c) $\text{Ge}_{23}\text{As}_7\text{S}_{70}$ and d) $\text{Ge}_{23}\text{Sb}_7\text{Se}_{70}$ glass surface. e-f) The relative intensities of main peaks to the pulse energy.

strength, glass-forming abilities, etc., to obtain desired photo-modifications, while explaining the fundamentals of the formation mechanism of each modification based on experimental observations.

4.5 Summary

In this chapter, we investigated various photo-induced modifications on the surface and in the volume and both thermally cumulative and non-cumulative regimes of the chalcogenide glass family. Our findings triggered the following observations:

- In $\text{Ge}_{23}\text{Sb}_7\text{S}_{70}$, various photo-structural modifications in the volume, ranging from refractive index changes to the formation of highly periodic spherical patterns were observed. At the lower fluence level, the laser-affected zones display a change in positive and negative refractive index. At higher levels, the formation of self-organized laser patterns, consisting of parallel nano-planes perpendicular to the laser polarization resembling similar structures found in other glass systems, is observed experimentally, both at and under the surface.
- Similarly, self-organization at the surface was shown with pulse-to-pulse evolution with a threshold of 1.3 J/cm^2 . We observed that the magnitude of photo modifications was

triggered by the laser fluence. The photo-modified areas at the surface of the glass revealed evidence of photo-oxidation, photo-darkening, and restructuring of the glass network.

- While self-organized surface nanostructures start to erase above the glass transition temperature, the removal of cavitation and the surface roughness requires melting of the glass. In bulk, bubbles and nanogratings dissolve before the glass transition, while the densification regime disappears at lower temperatures.
- Substituting Sb with As and S with Se, while keeping the concentration the same, results in fluctuations in modification thresholds and degradation in self-organized nanostructures.
- $\text{Ge}_{23}\text{Sb}_7\text{S}_{70}$ shows photo-contraction, photo-expansion in the glass volume. In addition, all compositions display photo-darkening, photo-decomposition and photo-oxidation phenomena on the glass surface.

In summary, the self-organization process occurring during ultrafast laser exposure of continuous patterns is one efficient method for nanostructuring of mid-IR material for the fabrication of photonic devices micro- to nanometer scale. Understanding the relationship between the optical properties and physical modifications upon ultrafast laser exposure is crucial for successful photonic devices by femtosecond laser direct writing. From the application point of view, these results may enable the direct write of functional 2.5D or 3D structures with physical properties tailored to the laser inscription parameters.

5 Device fabrications and applications¹

¹This work has been partially submitted to peer-reviewed journals as *G. Torun, A. Romashkina, T. Kishi, and Y. Bellouard, Femtosecond laser direct-write photoconductive patterns on tellurite glass, (2023)*, which are cited in the text as [388].

External contributions: The femtosecond laser machining of wall roughness was machined by Dr. Pieter Vlugter. The tellurite glass was produced by Prof. Dr. Tetsuo Kishi at the Tokyo Institute of Technology. The effect of temperature on resistivity was performed by Ms. Anastasia Romashkina. The PCB was designed with Samuel Benketaf. The chalcogenide glass rods were produced and characterized initially by Dr. Anupama Yadav and Prof. Dr. Kathleen A. Richardson at the University of Central Florida. Finally, the coating of chalcogenide glass substrates with amorphous-SiO₂ was done by Ruben Ricca.

In previous chapters, we cover the laser-induced modifications and self-organization by femtosecond laser exposure in complex glass systems in great detail. Let us here explore the application point of view of our findings.

5.1 ULE@Glass

In Chapter 2, numerous laser-induced modifications in ULE glass, driven by rearrangement of network and localized defects. In this section, we report the microstructuring of ULE glass by femtosecond laser micromachining combined with chemical etching as a fabrication technique for future optical elements and devices.

5.1.1 3D microstructures of ULE@Glass

Ultra-low expansion (ULE) glass offers broad transparency, lightweight, high mechanical, and dimensional stability against environmental fluctuations. The knowledge of femtosecond laser interaction with ULE glass has started to build up along with several different glass systems other than fused silica. Still, the preferential etching of the laser-affected zone remains elusive. Here, we report 3D glass microstructuring of ULE glass by femtosecond laser exposure combined with chemical etching. Specifically, we explore the effect of the laser processing parameters on the etching rate of laser-modified ULE glass. The selectivity highly depends on the glass structure in the laser-affected zone, which we correlate to the etching rate by systematic Raman analysis presented in Chapter 2. In addition, we investigate the role of etchants on laser-modified areas, namely HF and NaOH solutions. A strong preferential etching with a high aspect ratio is accomplished in ULE glass, attractive particularly for precision manufacturing and space applications.

Introduction

One of the transparent materials attractive for devices and applications requiring lightweight, high accuracy, mechanical and dimensional stability against environmental fluctuations is ultra-low expansion glass (so-called ULE@Glass). ULE glass, consisting of SiO_2 with 7.4 wt% TiO_2 , exhibits near zero thermal expansion coefficient (0 ± 30 ppb/K from 278 to 308 K) at room temperature [106]. Thanks to its impressive thermomechanical properties, this glass has been practiced as mirrors and optics in large astronomical telescopes, space satellites, and interferometers in metrology.

Femtosecond laser exposure has become a critical tool in recent decades not only for producing optical and photonic devices but also for implementing three-dimensional (3D) multi-functional micro-components in bulk transparent materials when combined with wet chemical etching. Based on non-linear absorption within the focal volume, this process tailors the material structure locally and eventually leads to enhanced chemical selectivity. When it

comes to femtosecond laser interaction with ULE glass, one might expect similar behavior as fused silica since both share a comparable glass network. However, numerous unusual modifications, more than the ones in fused silica, have been reported. To date, the reported facts on femtosecond laser-ULE glass interaction are the formation of self-organized nanogratings [52] and their erasure mechanism [128], a photo-darkening [126], local structural transformations [127] and crystallization of TiO_2 , which are discussed in Chapter 2 extensively. Although these early studies form the fundamental basis of such interaction, to the best of our knowledge, no report on an etching study of fs-laser irradiated ULE glass has been shown.

In this complementary study, we introduce a step-by-step approach to test relevant laser parameters toward the 3D structuring of ULE glass at micro-/nanoscales. Specifically, the pulse duration, laser polarization, and repetition rate as a function of pulse energy and the number of pulses per spot are investigated to a larger extent. In addition, two different etchant solutions, i.e., HF 2.5% and NaOH 5% are selected as they are practiced for fused silica extensively [43]. The selectivity highly depends on the glass structure in the laser-affected zone, which we correlate to the etching rate by systematic Raman analysis, presented in Chapter 2. Finally, the parametric window revealing a minimal surface roughness with a high aspect ratio after etching has been presented to fabricate practical parts on demand.

Experimental procedure

Commercial Corning ULE®Glass (7972), consisting of SiO_2 with 7.4 wt% TiO_2 was used to study in this chapter. Several different patterns were inscribed in ULE glass. First, parallel line patterns were inscribed in the volume (with a depth of 100 μm) of the ULE glass with a length of 10 mm to measure the etching rate. Further, numerous plane patterns consist of parallel lines along the x-y and y-z planes to observe the final surface profile.

For those, three different femtosecond laser systems were used, emitting pulses of different durations: 150 fs pulses at 1030 nm (Regen amplifier, S-pulse from Amplitude), 270 fs pulses also at 1030 nm (Yb-doped femtosecond fiber laser, Yuzu from Amplitude), and finally, 500 fs pulses at 1030 nm (Yuja from Amplitude). Note that the beam quality (M^2) is slightly different for different laser systems. The specimen was translated under the laser focus with the help of a high-precision motorized stage (Ultra-HR from PI Micos). The laser beam was focused on the surface of the specimen with a 0.4 numerical aperture (NA) objective (OFR-20x-1064 nm from Thorlabs). In Chapter 2, the femtosecond laser processing map has been reported for this glass system. In addition to several pulse durations, a wide range of pulse repetition rates (1 kHz-1 MHz) was employed at 270 fs. Here, pulse-to-pulse overlapping ratios were varying from 0 to 99.9%, and the pulse energy was ranging from 100 nJ to 1600 nJ, as measured after focusing with the objective lens. Furthermore, tracks were inscribed using opposite directions of laser beam movement along a single writing axis and under three different linear polarization states (and therefore, the orientation of the electrical field E) defined as parallel, at 45° , and perpendicular to the writing direction, respectively. All irradiated specimens were cut into a few pieces to reveal the structures. Later, specimens were etched using HF (2.5%)

at room temperature and NaOH (5 %) at 363 K for three hours to estimate the etching rate quantitatively and for several hours to observe surface profiles. The weight loss of pristine ULE in 5% NaOH is 0.9 mg/cm^2 at 368 K [107] and measured etching rate of $0.5 \text{ }\mu\text{m/hr}$ at 363 K. The etching rate of ULE in 2.5% HF at room temperature is $3 \text{ }\mu\text{m/hr}$.

After laser exposure, specimens were observed using an optical microscope (BX51 from Olympus) and a digital optical microscope (KH-8700 from Hirox). The etching rate was calculated based on the length observed in the OM over three hours of etching time. For statistical purposes, the measurement was performed for two different specimens. The surface profile and the roughness were obtained using laser confocal microscopy (VK-X from Keyence) and confirmed with atomic force microscopy (AFM from Nanosurf). A Raman spectrometer (LabRam HR from Horiba), equipped with a 532 nm laser excitation source attenuated down to 4 mW was used to record Raman spectra with acquisition times of 30 s for an individual spot. For high-resolution imaging and elemental analysis, a thin film of carbon was sputtered (from JEOL) on specimens using a field-emission scanning electron microscope equipped with EDS (FE-SEM, Gemini 2 from Zeiss, operated at 5 kV for imaging and 20 kV for elemental analysis).

Let us first explore the effect of pulse duration, polarization, and repetition rate on the etching selectivity in fused silica. First, the etching of fused silica has been reported using HF solution [38]. The reported facts are polarization sensitivity [36], the surface roughness of $\sim 100 \text{ nm}$ [43], selectivity of 1:100 [83], high aspect ratio, and so on. Later, several less dangerous solutions compared to HF, such as KOH and NaOH, have demonstrated an immense etching selectivity [43, 389]. Another reason to utilize NaOH, for example, is that little or no etching of pristine material is observed. First, the etching selectivity is explained by the localized fluctuations and densification in the laser-affected zone due to the change in bond angle of SiO_4 tetrahedra. This event leads to the chemical reactivity of oxygen atoms, leading to dissolution with a few solutions. Since higher localized defect formation, fluctuations, and densification has been observed in the nanograting regime, researchers initially focused on this particular regime. Later, it has been shown that before the nanograting regime, a few pulse regime results in a better etching rate ($\sim 300 \text{ }\mu\text{m/hr}$) with a higher aspect ratio (~ 500) thanks to defect selective solution of NaOH [43]. The anisotropy of these defects guides to polarization-sensitive few pulse regimes.

The effect of laser parameters on the etching rate

The etching rate of the laser-affected zone for different pulse durations (150-500 fs) at 100 kHz is presented in Figure 5.1. For 150 fs, the maximum pulse energy that can be obtained with the laser system is 783 nJ, leading to a fluence range of $0.05\text{-}2540 \text{ J/mm}^2$. While much higher can be achieved in the laser system emitting 270 fs pulses ($0.22\text{-}3580 \text{ J/mm}^2$) and 500 fs pulses ($0.071\text{-}635 \text{ J/mm}^2$) at 100 kHz. The polarization is perpendicular to the writing directions, providing the highest etching rate for fused silica [36].

The threshold of HF etching in Figure 5.1.a-c starts below 200 nJ for all pulse durations. Above the threshold, the maps exhibit a common trend over a number of pulses. Here, we divide the maps into three regimes namely, a few pulses (<10 pulses), transition (10-100 pulses), and multi-pulse (>100 pulses) regimes. The first regime is associated with a low etching rate located between a few pulses and tens of pulses. Once pulse duration gets longer, etching with few pulses is enhanced. Further, a rise in the number of pulses up to ~ 100 leads to an almost complete diminish in the etching selectivity. Yet, in the multi-pulse regime associated with reestablished and enhanced etching rate, the highest etching rate for all pulse durations is found (>100 pulses). While the maximum etching rate in the investigated range is 130, 134, and 124 $\mu\text{m/hr}$ for 150, 270, and 500 fs, respectively, the rate is enhanced twice by NaOH solution as in Figure 5.1.d-f. The same trend from lower etching rate in a few pulse regime and enhanced etching rate in multi-pulse regime persists, albeit the etching rate is also strengthened twice in a few pulse regime. While the minimum pulse energy requirement for NaOH solution to etch is higher for inscription parameters at 150 fs, a lower threshold signifies the rise in the sensitivity at 270 fs. The maximum etching rate for each pulse duration is 220, 260, and 257 $\mu\text{m/hr}$ for 150, 270, and 500 fs, respectively. Note that no etching selectivity is obtained in a specimen irradiated with 50 fs laser pulses.

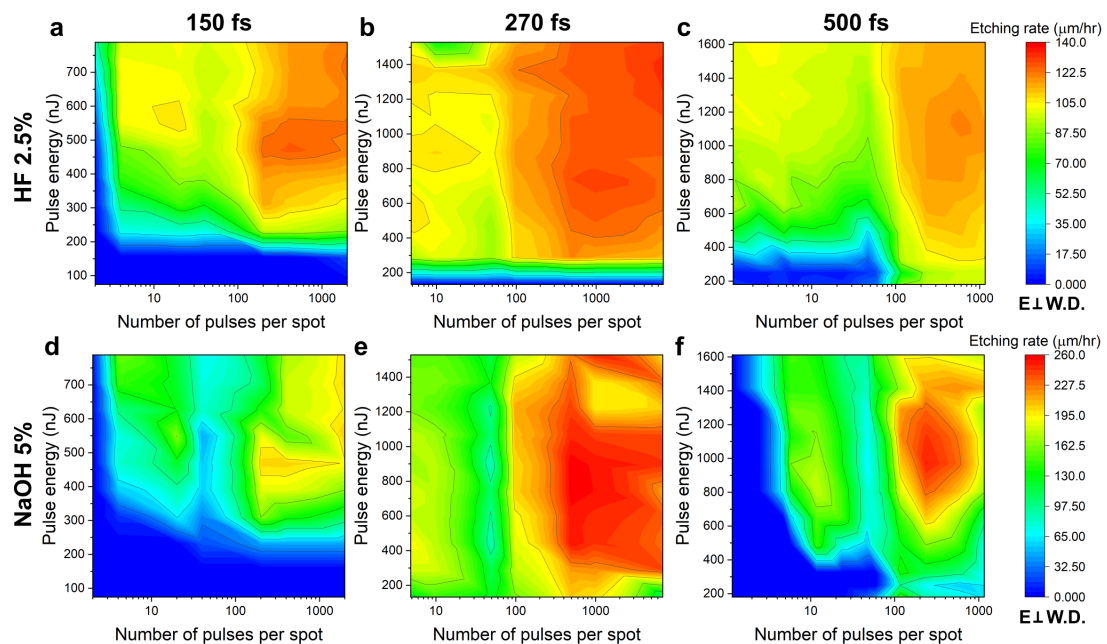


Figure 5.1: Comparison of etching rate versus pulse duration at 100 kHz. 3D map of etching rate for a-c) 2.5% HF and d-f) 5% NaOH solutions as a function of pulse energy and number of pulses for 150, 270, and 500 fs-laser pulses.

In Chapter 2, we unveil the microstructure after laser irradiation for all the pulse durations. While a few pulse regime exhibits rather disorganized morphology with the presence of localized defects, which are slowly transforming to self-organized nanogratings with many pulses. In Figure 5.1, the threshold of etching in a few pulse regimes is higher than the

nanograting regime. Above certain pulse energy for each pulse duration, localized defects, such as defects related to the silica network leads to a little enhancement in the etching rate in a few pulse regime. Above 100 pulses per spot, the nanograting regime enhances the etching rate to even higher values thanks to defects mediated not only by Si-O-based network defects and nanopore formation but also by the transformation of Ti^{4+} to Ti^{3+} . It highlights that the number of pulses greatly affects the etching rate due to the structural rearrangement and possibly transformation of defects into pores [43]. Above ~ 1000 nJ with more than 100 pulses, we determined the glass dissociation and subsequent crystallization of β - TiO_2 . The highest etching rate persists at high pulse energies since the crystalline form can be dissolved in both NaOH and HF solution dissolves TiO_2 [135, 390].

Defect-mediated random morphologies in a few pulse regimes perform twice less etching than the nanograting regime both for HF and NaOH solutions. We strengthen this statement by SEM observation. SE images of cross-sections after 3 hours of etching with HF and NaOH are reported in Appendix E for 500 fs-laser pulses as a representative case. While HF solution leads to etching in the entire investigated fluence range, NaOH solution results in more selective etching. Extraordinary selectivity of NaOH (approximately $300 \mu\text{m/hr}$) was experimentally demonstrated for fused silica previously, relying on the reorientation of defects in a few pulses [43].

In Chapter 2, we examined that at a certain threshold, nanogratings perpendicular to the laser polarization form. They are associated with chemical etching selectivity due to the formation of localized defects. In this direction, we investigate the effect of polarization on the etching rate at various pulse durations. Figure 5.2 displays the etching rate with three orthogonal linear polarizations for the writing direction for the pulse duration of 500 fs.

Starting with HF etching at a few pulse regime, no significant difference in both threshold and etching rate is observed in Figure 5.2.a-c. However, followed by the transition regime, a sensitivity of HF etching is visible in the multi-pulse regime. While the highest etching rate of almost $130 \mu\text{m/hr}$ is obtained thanks to nanogratings, which are parallel to the writing direction in Figure 5.2.a, the etching rate is halved by other polarizations Figure 5.2.b-c. Although the NaOH solution reinforces the etching rate up to $260 \mu\text{m/hr}$ in Figure 5.2.d-f, a similar behavior to the laser polarization is observed, i.e., three different regimes and the decay of the etching rate in the multi-pulse regime by turning the polarization. Unlike fused silica at 333 kHz [43], both HF and NaOH solutions are less sensitive to the anisotropy occurring with a few pulses. The polarization-independent behavior has been reported for fused silica recently at 100 kHz [391]. The difference might originate from the variation in the type of defects generated in fused silica versus ULE glass as well as due to the difference in laser parameters. Similar to fused silica and many other materials, the etching rate is higher in the case of a linear polarization state perpendicular to the writing direction in the nanograting regime. Moreover, SE images of cross-sections after three hours of etching are presented in Appendix E. While HF etching is relatively less sensitive to the anisotropy of defects and nanogratings at a sufficiently long time, the cross-section etched with NaOH solution results in higher selectivity

and sensitivity to the type of defects in the investigated parametric window.

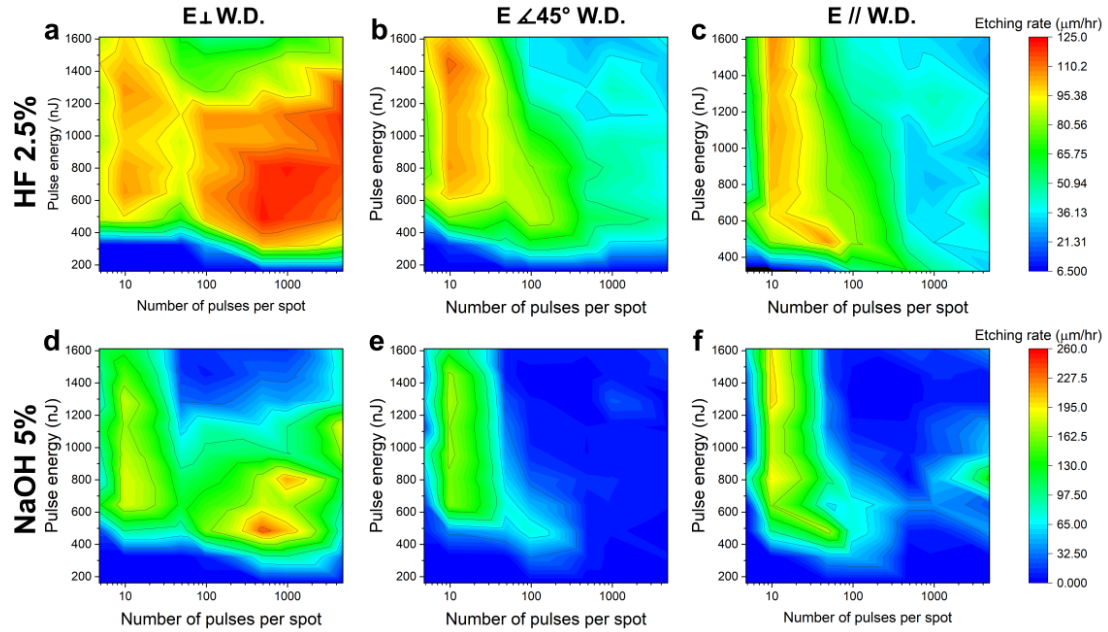


Figure 5.2: Comparison of etching rate versus laser polarization for 500 fs laser pulses at 240 kHz. 3D map of etching rate for a-c) 2.5% HF and d-f) 5% NaOH solutions as a function of pulse energy and number of pulses.

Together with the discussion in Chapter 2, the transition from non-cumulative to the thermal-cumulative regime is observed around 500 kHz for ULE glass, which is relatively lower than fused silica (~ 1 MHz). Yet, a high repetition rate with faster writing is desired for industrial implementations. In addition, as displayed in this section, multi-pulse irradiation is desired to achieve a higher etching rate in ULE glass. Here, we present the effect of repetition rate from 100 kHz to 1 MHz not only for an understanding of the case of accelerated etching but also for practical purposes.

Figure 5.3 illustrates the etching rate varying with several repetition rates. In general, various studies consider a 100-333 kHz regime for micromachining of fused silica [43, 83]. Starting with a few pulse regimes at 100 kHz, polarization-insensitive defects form immediately. These defects were observed for all repetition rates, although the etching rate with HF solution decreases with repetition rate, i.e., $106 \mu\text{m/hr}$ for 100 kHz versus $93 \mu\text{m/hr}$ for 1 MHz. After the transition regime between ~ 10 -100 pulses, the multi-pulse regime, associated with nanogratings enhances the etching rate at 100 kHz. However, this window shrinks with the repetition rate, and the threshold falls below 200 nJ. Further rise leads to zero etching rate, since this region is related to bubble formation, i.e., densified zone with trapped molecular oxygen at the center [22].

The final microstructures after etching with HF solutions are demonstrated in Appendix E. In the investigated parameter window, higher laser fluence results in distortion of the beam and

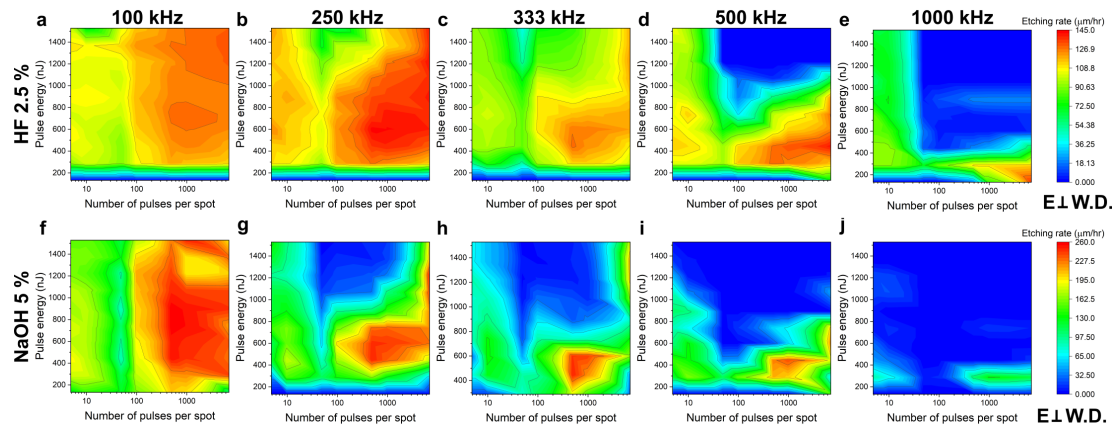


Figure 5.3: Comparison of etching rate versus repetition rate for 270 fs. 3D map of etching rate for a-e) 2.5% HF and f-j) 5% NaOH solutions as a function of pulse energy and number of pulses.

self-focusing. Since HF solution can dissolve the pristine glass network, all modifications are left in their place into a hollow channel after etching. At a repetition rate equal to and higher than 500 kHz, the previous statement becomes invalid since the modification is associated with a densified glass network accompanied by pores in nano- to micrometer scales.

Extended parametric window at 270 fs

So far, we observe a large parametric window, demonstrating the possibility to apply various laser systems. Now, we systematically investigate fine parametric windows with 270 fs laser pulses rather below self-focusing phenomena.

Figure 5.4.a-f presents the 2D map of the etching rate as a function of deposited energy (or net laser fluence). Above the threshold of ~ 143 nJ at 100 kHz with 270 fs laser pulses, logarithmic increment in the both etching rates of HF and NaOH is visible with 160 nJ in Figure 5.4.a. Here, zero etching rate by HF and especially NaOH shows that there is little or no defect generation with a few pulses. A steep increase results in nanograting formation, as presented in Chapter 2. By increasing the field strength, or pulse energy, a few pulse regimes is exceeding the etching rate of nanogratings for a pulse energy of 190 and 210 nJ. Since the generation of localized defects rises proportionally to the laser fluence, etching without a significant pulse overlapping becomes visible. From 210 nJ and onwards, the transition region almost disappears, making the map consisting of two distinct regimes, i.e., localized defect-mediated and nanograting-driven etching.

Preferential etching of ULE glass has been demonstrated for numerous laser parameters. We find that two types of etching dominate the process over a very large laser fluence regardless of pulse duration and repetition rate. The first one is localized defect-driven, and the second one is based on nanograting formation, which leads to the highest etching rate. Unlike fused

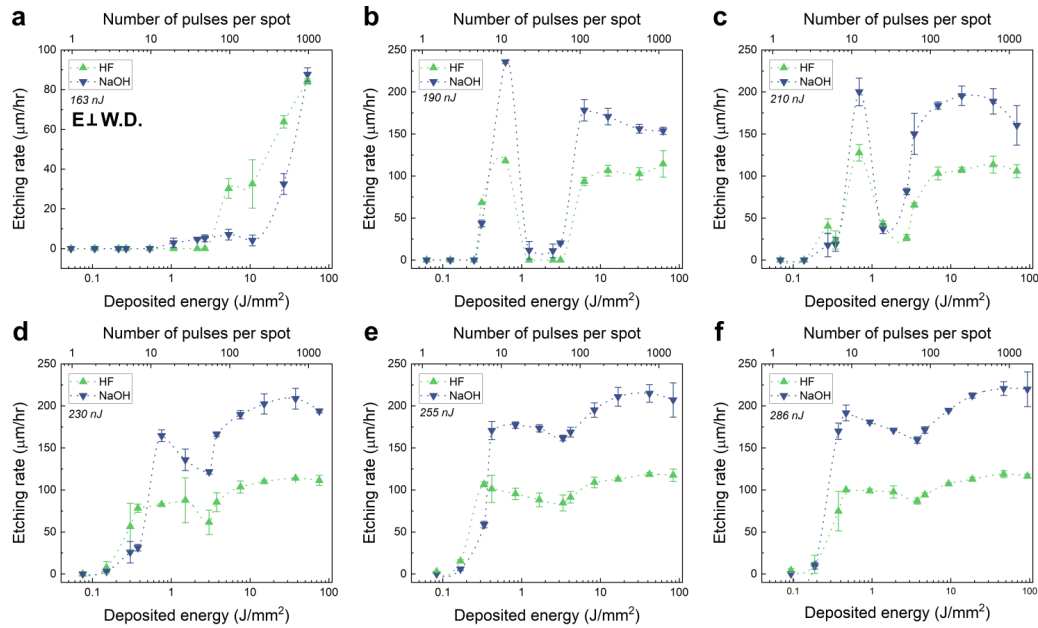


Figure 5.4: The average etching rate in a fine parametric window for HF and NaOH at 270 fs with 100 kHz and a) 160 nJ, b) 190 nJ, c) 210 nJ, d) 230 nJ, e) 255 nJ, and f) 286 nJ. The polarization is perpendicular to the laser writing direction.

silica, polarization has almost no impact on the few pulse regime due to different defects in ULE glass. To fabricate complex micro-/nanocomponents of ULE glass, a few considerations, such as the highest aspect ratio and the final roughness after etching, on the quality has to be investigated. Then, we display simple 3D shapes made out of ULE glass.

The aspect ratio and the surface roughness after etching

The aspect ratio, i.e., the etched length of the single channel over its width, is presented in Figure 5.5. The width was measured from the SEM images demonstrated in Appendix E. Figure 5.5.a-f shows the aspect ratio for various laser parameters after 3 hours of etching. The aspect ratio obtained by HF etching is comparable with one another. In addition, at 250 kHz with 270 fs laser pulses (not shown here), the ratio stays almost identical. In addition, NaOH etching exhibits a superior aspect ratio ~ 200 for 150 fs. Since NaOH does not attack to the pristine material as much as HF solution, thus the aspect ratio is expected to be higher for higher etching times. The longer the pulse duration, the worsen the aspect ratio. Not only the pulse duration, the rise in pulse energy also deteriorates the aspect ratio. Although the width of the few pulse regime is thinner, slightly higher aspect ratio is obtained in nanograting regime due to a longer etched channel length.

Figure 5.6.a-d displays average line roughness with SE images of the side wall after HF etching. The dominant laser parameters affecting the roughness of the etched structures are polarization and writing speed. A slower speed resulting in a higher number of pulses leads

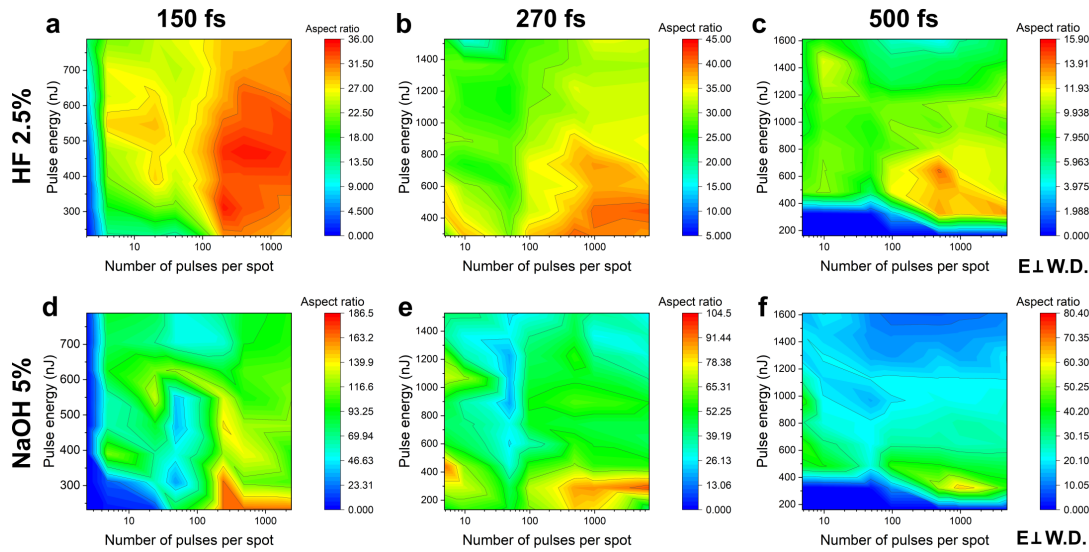


Figure 5.5: Comparison of aspect ratio versus pulse duration at 100 kHz. 3D map of etching rate with HF solution as a function of pulse energy and number of pulses for a) 150, b) 270, and c) 500 fs, and etching rate with NaOH solution as a function of pulse energy and number of pulses for d) 150, e) 270, and f) 500 fs.

to a smoother surface. The deterioration of the smoothness of the surface is intensified by pulse energy at a low number of pulses. At 5000 pulses, with the help of crystallized volume, dominating the laser-affected zone, leads to smoother structures. The more the crystalline phases in the laser-affected zone, the better the etching rate and the smaller roughness for both HF and NaOH solutions since β -TiO₂ is soluble in both of the solutions [135, 390].

Finally, Figure 5.7 displays the simple 3D squares carved out 60 μm below the glass surface for a demonstration of the capability of this process. The area roughness is around 700 nm at 250 nJ, while it rises above 1 μm with a pulse energy of 1000 nJ.

In summary, we investigate the 3D microstructuring of ULE glass by femtosecond laser micromachining and chemical etching. We observe that a longer pulse duration gives twice higher etching rate ($\sim 260 \mu\text{m/hr}$ at 500 fs) compared to shorter pulse durations at 150 fs as it leads to more complex laser-induced modifications, such as localized defect formation based on valence state change of Ti ions, phase dissociation and crystallization of β -TiO₂ (anatase). Similarly, a higher number of pulses (>100 , hence lower net fluences) is required to reach a higher etching rate for every pulse duration above 100 fs. The highest etching rate is obtained when a polarization state is perpendicular to the laser writing direction. The thermal-cumulative regime starts at 500 kHz at 270 fs, deteriorating the etching rate due to melting and re-solidification. In addition, we explore the role of etchants on laser-modified volumes, namely HF and NaOH solutions. The etching behavior is somewhat comparable to the one observed in fused silica, in terms of etching selectivity. Finally, the minimum final roughness (between 90 to 400 nm), aspect ratio (~ 190), and examples of simple 3D geometries

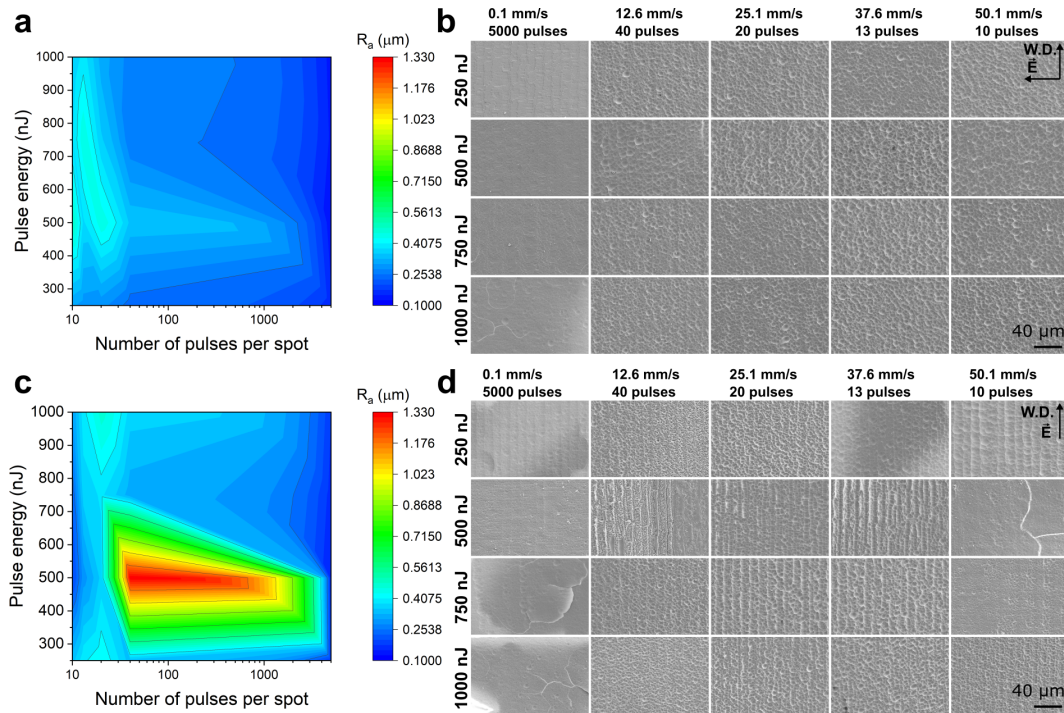


Figure 5.6: 3D map of etching rate with HF solution as a function of pulse energy and number of pulses for 500 fs with a) perpendicular polarization and b) SE images of the cross-sections. c) The parallel polarization with respect to writing direction and d) SE images of the cross-sections.

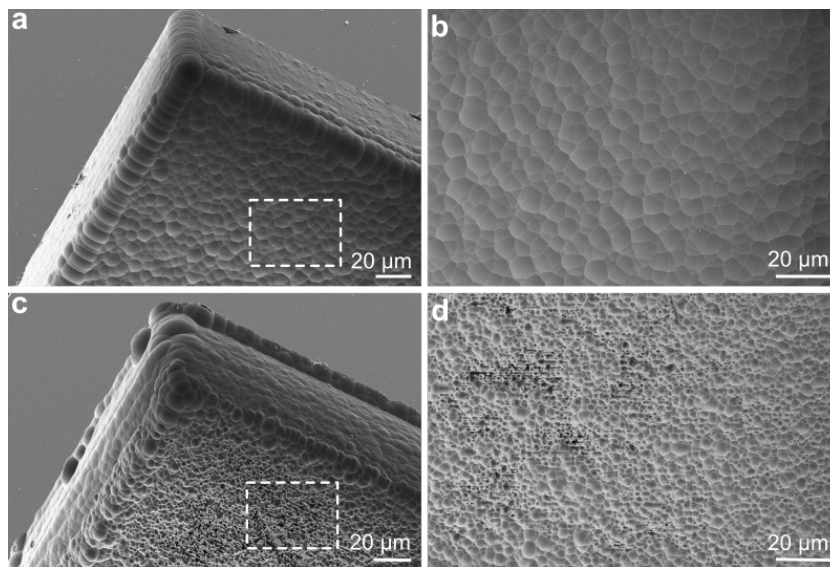


Figure 5.7: SE and magnified SE images of the 3D squares removed from the ULE glass by femtosecond laser combined with HF etching. The laser parameters are a-b) 250 nJ and c-d) 1000 nJ at 500 fs, 250 kHz, and 12 mm/s.

have been presented. A high etching rate and contrast are accomplished by the femtosecond laser-assisted etching processing of ULE glass, attractive for many applications, particularly for precision manufacturing and space applications.

5.2 Tellurite glass

In Chapter 3, our investigation of femtosecond laser interaction with tellurite glass led to the observation of the formation of t-Te. In this section, we demonstrate femtosecond laser direct-write UV photodetectors made from tellurite glass based on surface crystallization.

5.2.1 Direct-write UV photodetectors

We report the formation of arbitrary photoconductive patterns made of tellurium (Te) nanocrystals by exposing a tellurite glass to femtosecond laser pulses. During this process, Te/TeO₂-glass nanocomposite interfaces with photoconductive properties form on the tellurite glass substrate. We show that these laser-inscribed patterns have a highly reproducible photo-response, from the near ultraviolet (263 nm) to the visible spectrum, stable over a few months. Specifically, high responsivity (~ 16.55 A/W) and detectivity (5.25 ± 10^{11} Jones) of a single laser-written line pattern are measured for an illumination dose of 0.07 mW/cm² at 400 nm. This work illustrates a pathway for locally turning a tellurite glass into functional photoconductor of arbitrary shape, without adding materials and using a single laser process step.

Introduction

We demonstrated that upon near-IR fs-laser exposure, the tellurite glass evolves into a semiconductor/glass composite [143], consisting of t-Te nanocrystals embedded in a TeO₂ glass matrix. Extensive investigation revealed that the laser-modified areas show evidence of t-Te nanoparticles and nanocrystals with a low amount of a-Te upon a single fs-laser pulse exposure of TeO₂-based glass [144]. In particular, it leads to the formation Te/TeO₂-glass interface at the surface, at which the ratio of phases depends on the laser processing parameters. This process is based on a scalable laser direct-write technology by focusing a femtosecond laser on the surface of a glass substrate and scanning the laser spot as a pattern with an arbitrary length and shape.

Previously, several authors reported that the TeO₂/Te interface produced by surface oxidation of Te (such as obtained by UV irradiation of Te thin films [392–395], or by continuous-wave (CW) lasers operating at 440–520 nm [209]) have functional properties, such as photoconductivity [392, 393, 396, 397], ultrahigh chemical sensitivity [398, 399], and better optical properties than Te and TeO₂ [400]. Here, in our case, the transparent substrate of TeO₂, adding further flexibility to use in optics and photonics, requires high peak irradiance and non-linear absorption to transform into t-Te locally. Surrounded by a stable amorphous matrix, Te nanocrystals

are further protected against environmental modulations. Adding the possibility of controlling the formation of nanocrystals in the dielectric matrix give a further degree of freedom in the engineering of nanocomposite photonic structures, in particular, considering that tellurium has plasmonic-like properties.

In the sequel, we further investigate the photoconductive properties of the Te/TeO₂-glass interface produced by direct-write femtosecond laser exposure. Specifically, we unravel a highly reproducible and sensitive photo-response under different illumination conditions in the near UV-VIS spectrum that we characterize for various laser exposure parameters and illumination conditions. This process is particularly appealing for light-sensing devices made by functionalizing a single piece of material and, hence, obtained without adding or subtracting any other materials.

Experimental procedure

In this study, the test composition is selected as 10K₂O-10WO₃-80TeO₂ (mol%). An Yb-doped femtosecond fiber laser (Yuzu from Amplitude) emitting 270 fs pulses at 1030 nm was used in this experiment. Arbitrary laser patterns were inscribed on the surface of the tellurite glass as parallel lines with several lengths from 5 to 10 mm. The repetition rate was fixed at 1 MHz, corresponding to a thermal cumulative regime for the tellurite glass. Here, the number of effective pulses per spot was varied from 20 to 4000, and the range of pulse energy was spanned from 1 to 200 nJ, resulting in an incoming net fluence range of 0.0066 to 263 J/mm². Further details on the glass production and laser parameters can be found in Chapter 3.

After laser exposure, the tellurite glass samples were first observed using an optical microscope (BX51 from Olympus). A Raman spectrometer (LabRam HR from Horiba), equipped with a 532 nm laser excitation source attenuated down to 4 mW, focused on 0.9 NA objective (100x-532 nm from Thorlabs) was then used to confirm the presence of elemental Te nanocrystals in laser-modified areas. Further, another Raman spectrometer (MonoVista CRS+ from Spectroscopy and Imaging GmbH), equipped with a 442 nm laser (He-Cd laser from Kimmon Koha) excitation source with an incident power of 115 mW was used to investigate the degradation mechanism under UV-light irradiation. The linearly-polarized Raman laser beam was focused at the surface of the glass sample using a 0.9 NA objective (50x-532 nm from Thorlabs). A series of point scans were performed with acquisition times of 60 s per individual spot. Finally, the absorption spectra were measured at room temperature for wavelengths ranging from 250 to 2500 nm using an ultraviolet-visible-near-infrared spectrometer ((UV-VIS-NIR, Lambda 950 from Perkin Elmer). For this purpose and to isolate the functionalized regions in the substrate, a mask with a hole of around 2x2 mm² is prepared from black paper for broadband absorbance. For the measurement, the reference beam power is attenuated to 10%, to compensate for the presence of the mask and the ensuing effective drastic reduction of the beam size from the original 2 cm in diameter. The thickness of the sample used for this transmission and reflection measurement was 2 mm.

First, the DC resistivity of the laser-written tracks was measured by the 4-probe station equipped with a microscope connected to the source measurement unit (SMU B2902A from Keysight) applying a bias voltage of 40 V. A control software (Quick I/V Measurement Software from Keysight) was used to obtain the data. The tungsten probes were placed on the sample with the help of high-precision adjustments. Temperature dependence of the conductivity was measured with slow heating of the sample from room temperature to 368 K.

To fabricate a device for probing the photoconductivity, electrodes in the form of thin Au (with a thickness of ~ 20 nm) were sputtered (JFC-1200 Fine Coater from JEOL), covering the end of the laser-inscribed patterns, identified as electrical contacts. For obtaining the desired shape of electrodes, a mask made from fused silica glass by femtosecond laser machining-assisted etching process was placed on the tellurite glass before sputtering, shown in Appendix E. Later, wire bonding (HB10 wedge and ball bonder from TPT) with the Au and/or Al wires was performed attached to the printed circuit board (PCB) designed in KiCAD software. To ensure the wires were attached to the sample and the PCB over long measurement periods, the end of electrodes were covered with Ag-based electrically conductive epoxy (H20E-FC from epoxy technology; the resistivity is less than $0.04 \Omega \cdot \text{m}$ at room temperature). The epoxy was later cured at 393 K for 15 minutes. After the device fabrication, characteristic transient current-voltage responses were collected with the source measurement unit (SMU B2902A from Keysight). As a light source for the photoconductivity measurement, a LED of white light (spectral range of 450 to 750 nm) and other LEDs of 460 nm, 400 nm, and 263 nm were used with various optical intensities (0 - $2.1 \text{ mW}/\text{cm}^2$). The spectral profiles of the LEDs are presented in Appendix E. After obtaining a collimated beam with a positive lens, a cylindrical lens was used to create a stretched elliptical profile illumination covering the laser-written patterns with an area of approximately 200 mm^2 . The same measurement was performed for at least ten different lines for statistical purposes. Figure 5.8 illustrates the schematic representation of the device fabrication and characterization procedure.

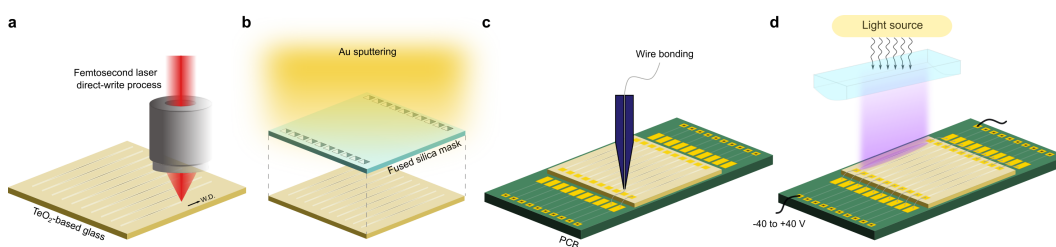


Figure 5.8: Schematic representation of the sample and device preparation and characterization steps. a) The femtosecond laser direct-write process on tellurite glass. b) The fabrication of Au electrodes at both ends of the sample by sputtering through a mask to protect the central portion of the laser-written patterns. c) A wire bonding between PCB and electrodes once the sample was fixed on a PCB. d) The device characterization by applying a bias voltage ranging from -40 to $+40$ V and light focus into a thin elliptical line, while an elliptical illumination source is focused, covering individual line-pattern separately.

Electrical properties

The electrical conductivity of pure TeO₂ glass and binary glass systems are based on a small-radius polaron hopping mechanism at and above room temperature [401]. Depending on the glass modifier oxides, there is an additional contribution from ionic conductivity. The TWK glass studied in this work has a reported electrical resistivity (DC) of at room temperature $1.4 \cdot 10^{18} \Omega \cdot \text{m}$ [402].

Figure 5.9 illustrates the effect of laser-inscription parameters and temperature on the DC electrical resistivity, absorption spectra, and direct and indirect band gap plots of the pristine and laser-inscribed patterns. The resistivity of the patterns is calculated by the resistance measured with a 4-probe setup and the dimensions. The line length and cross-section of the crystallized area were measured from images taken by OM and TEM [144], respectively. The resistivity of the patterns varies from ~ 0.001 to $\sim 50 \Omega \cdot \text{m}$ with the laser-writing parameters in Figure 5.9.a. Several parameters, such as the surface area of grain boundaries, preferred grain orientation, presence of impurities, and structural defects, influence DC resistivity [269]. We showed that the laser-inscribed zone consists of Te nanocrystals (with a grain size range of ~ 5 -15 nm), growing proportionally with the number of laser pulses and the laser electric field intensity. Low laser-inscription fluence results in thinner crystallized areas with disconnected nanocrystals, which are more susceptible to charges and impurities at the interface, as well as surface scattering. Through grain growth stimulated by higher laser-inscription fluence in the thermal-cumulative regime, the value reaches the resistivity of polycrystalline bulk Te [268, 403, 404]. No correlation was detected between the orientation of the electric field and the dark resistivity of line patterns. All patterns were written at a pulse energy of 200 nJ and 4000 pulses per focal spot (corresponding to an incoming pulse fluence of $262 \text{ J}/\text{mm}^2$). Figure 5.9.b shows the temperature-dependent relative dark resistivity of the laser-inscribed line patterns, reflecting a typical semiconductor behavior due to the thermally-active charge transportation. The inset shows the activation energy, estimated to be $\sim 0.6 \text{ meV}$ using an Arrhenius-law fitting procedure ($\ln RT$ vs. $10^3/T$) [269, 405, 406]. Similarly, the resistivity of the pristine glass drops with temperature ($1.14 \cdot 10^{14} \Omega \cdot \text{m}$ at 373 K [402]).

Figure 5.9.c presents the absorption spectra of the pristine glass versus the laser-inscribed area of $2 \times 2 \text{ mm}^2$. The laser-inscribed area shows broadband absorption in the solar spectral emission range, decreasing continuously towards the band gap energy of t-Te ($\sim 3600 \text{ nm}$). While it is above 80% in the visible spectrum, there is a sharp rise in absorption below 460 nm, reaching the maximum value between 330-410 nm. Two broad peaks in the absorption curve are also observed, at $\sim 400 \text{ nm}$ and $\sim 1000 \text{ nm}$, respectively, similar to previously reported results [205]. Theoretical and experimental studies related to the optical absorption of pure Te indicate the presence of two peaks: one in the range of ~ 3 -6 eV (~ 400 -200 nm), associated with the direct transition from the valence band (p-bonding triplet) to the conduction band (p-antibonding triplet), and another one in the range of ~ 0 -3 eV (\sim from mid-IR to 400 nm), assigned to forbidden direct-transition from the valence band (p-lone pair) to the conduction band (p-antibonding triplet). In addition, the absorption spectrum of Te-nanorods shows

some differences when compared to that of pure bulk Te, presenting a broad absorption peak due to the allowed direct transition located at approximately 300 nm [407]. For Te nanoparticles, a broad absorption band at around 660 nm indicates a forbidden direction transition [408]. In our case, the peak around 330-410 nm is corresponding to the direct band gap transition, while the forbidden direct transition is reported in ~600-1000 nm. In another study, Te nanoparticles between 10 nm and 120 nm show a plasmonic-like resonance-dominated transition in the spectrum at ~300-400nm [238]. It is not completely a plasmonic resonance due to the absence of ground-state free carriers as it is in metals or doped semiconductors. Above 120 nm, Te nanoparticles exhibit all-dielectric (Mie-type) resonance. Similar to our study in which the size of nanocrystals and nanoparticles are ~5-55 nm, the absorption spectra of Te nanoparticles (their sizes from 10 nm to 300 nm) cover the entire solar emission spectrum from 300 nm to 2000 nm. The presence of localized states is due to interfaces at the surface, the grain boundary, and intra-grain regions. The impurities further absorb the photon energy below the band gap through one of the gap states within defect density, contributing to broadband absorption. The absorption spectra can be modulated by the laser-writing parameters, as shown in Appendix E.

Figure 5.9.d shows Tauc plots [138], for both direct and indirect bandgap model behaviors. While a linear region (and hence, a bandgap value) is clearly identifiable for the non-exposed case, the laser-exposed regions exhibits less pronounced linear zones that may account for their disorganized structures and interfacial effects. A shift towards lower energy, both in the direct and indirect optical band gap models, is observed, as an expected consequence of the presence of Te-nanocrystals after laser exposure.

Photoconductive properties and long-term stability

The p-type behavior of Te originates from the p-state lone-pair electrons that form the upper level of the valence band [409]. The population of holes in p-type conduction comes from the interaction of these lone-pair electrons with dangling bonds. A region enriched with holes forms at interfaces such as the surface, the grain boundary, and intra-grain regions due to impurities. The photoconductivity can occur at the interface due to the variation in hole concentration [399]. In addition, there can be an adsorption process, i.e., gas atoms adsorbed during the measurement [393, 394, 399], affecting the population of holes. In another Te/TeO₂ system, photoconduction is explained by the presence of photo-excited carriers in the Te-layer, which are trapped at the interface of the Te/TeO₂ layer [393, 396]. In our case, the laser-inscribed zone consists of a mixture of polycrystalline Te (t-Te nanoparticles and nanocrystals), amorphous Te (a-Te), and TeO₂-glass [144] and as such as forms of a heterogeneous assembly. The photoconductivity mechanism is hence likely more complicated than in well-defined Te/TeO₂ interfaces [392, 393, 396]. We designed a specific device in coplanar configuration, illustrated in Figure 5.8.d, to avoid manual manipulations while testing the photoconductivity of the laser-inscribed patterns. The electrodes in the form of a thin film of Au at both ends of the line patterns are connected to a printed circuit board

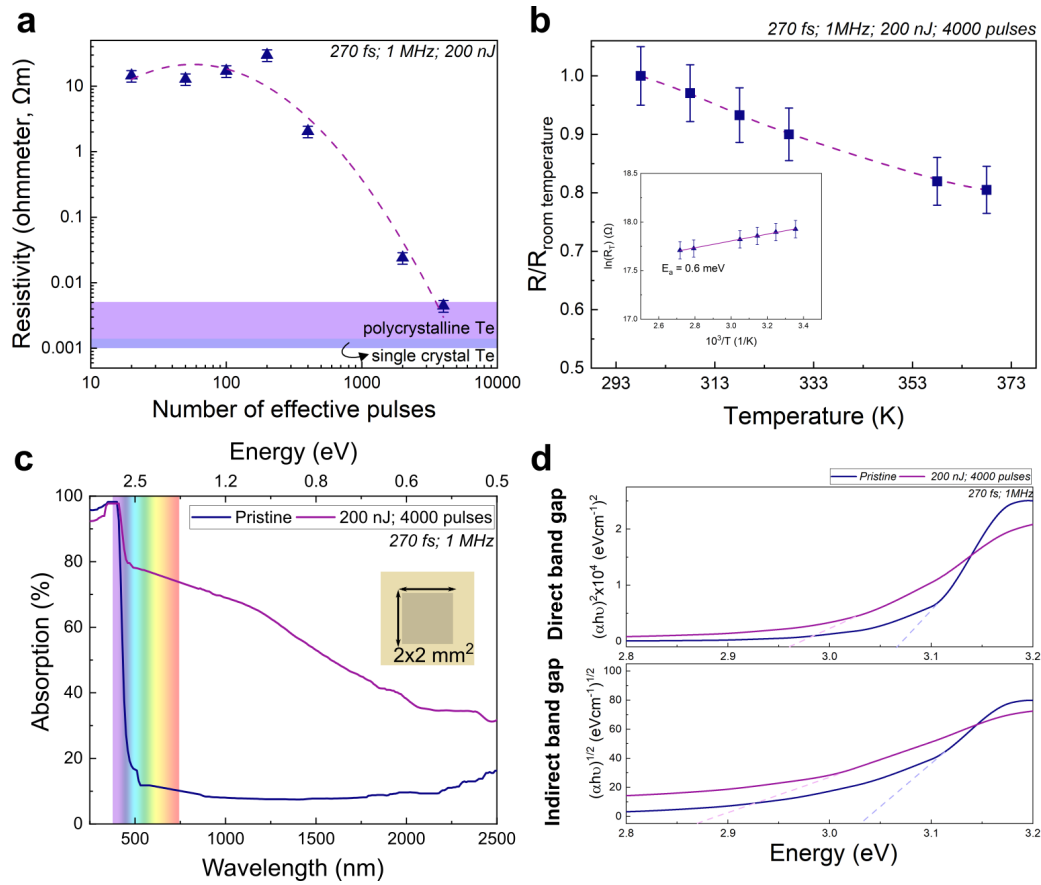


Figure 5.9: a) Effect of the laser writing parameters on electrical (DC) resistivity of line patterns. b) Effect of the temperature on the resistivity of laser-inscribed patterns with the inset image of the Arrhenius-law fitting. c) Measured UV-VIS-NIR absorption spectra of the pristine and laser-inscribed area (2×2 mm²), d) Corresponding Tauc plots of pristine and the laser-inscribed area, considering both indirect and direct bandgap absorption models.

(PCB) by wire bonding. We conducted a current-voltage (I-V) characterization and calculated their responsivity, detectivity, external quantum efficiency, and generated photocurrent by varying optical power density. Additionally, we determined the spectral and temporal photo-responses of the patterns. The results are gathered in Figure 5.10. The spectral response of the Te/TeO₂-glass nanocomposite is demonstrated in Figure 5.10.a. It exhibits a strong absorption at ~ 400 nm, leading to the highest photocurrent output. The spectrum of the white light is presented in Appendix E. Although the center peak is at ~ 600 nm, radiation below 460 nm can contribute to the observed photo-response under white light illumination. I-V curves obtained without and with illumination in both forward and reverse bias are displayed in Figure 5.10.b. The typical I-V curve is deviating from ohmic contact in the range of -40 V to +40 V. The absolute semi-log I-V curve is presented in Appendix E. In the dark current for a zero bias voltage, we measure near-zero current ($3.7 \cdot 10^{-10} \pm 1 \cdot 10^{-10}$ A). The electrical conductivity in the device is controlled mainly by the conductive part of the laser-inscribed

zones, interfaces, and structural impurities and defects [410]. For the current to flow, the device in this scheme requires a bias voltage above zero. Once the bias voltage is exceeded internal barrier voltage (around 1 V in this case) and the knee voltage (or breakdown voltage for reverse bias) is surpassed, the external electric field supplies extra carriers. By illuminating the active area of the device, the current rises as a function of optical power density. The photocurrent at 400 nm versus optical power density follows a typical square root-like relation, typically observed in the case of high resistances.

Figure 5.10.c shows the temporal response of laser-inscribed patterns under the illumination of 400 nm with different optical power densities. From this graph, we calculated the responsivity (R_{ph}), detectivity (D^*), and external quantum efficiency (EQE), which are a figure of merit (FOM) for the photo-detecting properties of our laser-inscribed patterns on tellurite glass. R indicates the generated photocurrent per unit area, D^* displays the ability to differentiate weak signals from noise, and EQE the number of charge carriers (electron-hole pairs) collected per photon incident on the photodetector [411]. They are expressed as:

$$R_{ph} = \frac{\Delta I}{AP} \quad \text{where } \Delta I = I_{ph} = I_{light} - I_{dark} \quad (5.1)$$

$$D^* = \frac{R_{ph}\sqrt{A}}{\sqrt{2eI_{dark}}} \quad (5.2)$$

$$EQE(\%) = \frac{(hcR_{ph})}{e\lambda} \times 100 \approx \frac{R_{ph}}{\lambda 1240} (W \cdot A/nm) \times 100 \quad (5.3)$$

where I_{ph} , I_{light} , I_{dark} , P , A , e , h , c , λ are the generated photocurrent, the current measured under illumination, the dark current, optical power density, the effective covered area with Te on the TeO_2 -based glass, the charge of an electron, the Planck constant, the speed of light and the illumination source wavelength, respectively. At 400 nm and under an exposure dose of 0.07 mW/cm^2 , the responsivity and detectivity of the device are calculated to be $\sim 16.55 \text{ A/W}$ and $5.25 \cdot 10^{11} \text{ Jones}$, respectively. The responsivity is reduced with the optical power density, a behavior similar to various Te photodetectors [246, 393, 396, 405, 407, 412, 413], which is attributed to defect states in the laser-inscribed zones. Photo-generated holes under low optical intensity are captured by the defect states near the valence band and reduce the number of recombination of electron-hole pairs. However, under high optical intensity, a low number of photo-generated holes will be captured due to the limited number of defect states. Therefore, the laser-inscribed zone is more sensitive under lower light intensities. A similar trend is observed in the EQE (%) plot, which is directly proportional to the responsivity and inversely proportional to the light intensity. Note that the calculated responsivity, detectivity and EQE indicate the peak values, which can alternate due to geometrical uncertainties, i.e., fluctuation in the active part of the laser-affected width, connectivity and homogeneity of nanocrystals in the laser-affected zone, etc. The generated photocurrent follows an empiric

power law in the form:

$$I_{\text{ph}} = \beta P^\alpha \quad (5.4)$$

where α is the dimensionless exponent (≤ 1), providing the information of traps (or defect states) present, and β is a parameter related to the photodetector responsivity [414]. α equals 1 in an ideal trap-free photodetector but becomes less than 1 in the presence of trap states. In our case, α is 0.46, implying that most traps are already filled at lower optical power densities, and additional illumination power does not efficiently increase the photocurrent. The internal quantum efficiency (IQE), the ratio of the number of charge carriers or electron-hole pairs generated to the number of photons absorbed [415], is 5012% for the same illumination conditions (with 97.73% absorption at 400 nm). There are a few possible reasons why an apparent high responsivity and high EQE (i.e. >100%) are measured. First of all, the photogain is not taken into account in EQE. Then, the higher external bias voltage above the barrier voltage leads to the generation of additional 'non-light driven' electron-hole pairs. At the illumination wavelength, which is much higher than the bandgap of Te, which is 0.34 eV [416] in homogeneous bulk tellurium, but can be engineered up to ~ 1.42 eV [235] by modulating its size at nanoscales [235], hence, more electron-hole pair can be stimulated by avalanche multiplication per photon in the active region of the device. In addition, trapped minority carriers, hence electrons in our case, in the device due to the various defective states in our system, further enhance the apparent photoconductive gain. Although more than 100% EQE is not common, it is possible by avalanche carrier multiplication [417].

The temporal evolution of the Te/TeO₂-glass nanocomposite is displayed in Figure 5.10.e. The rise time, the time required for current to increase from 10% to 90% of its peak value under illumination, is one of the key parameters to evaluate a photodetector performance. We measured an average rise time of about 20 s, which is rather low. The carrier mobility in Te is temperature-dependent and typically ranges from 20 to 50 cm²/Vs at room temperature [418]. The mobility is also affected by the contribution of carriers present near the Te/TeO₂ interface [407]. Therefore, the delay in the rise time of the Te/TeO₂-glass interface is attributed to several factors, such as the existence of charge impurities or defect states. A decrease in the mobility of carriers is due to surface texture originating from the laser-induced self-organized nanostructures [143]. Conversely, the decay time, which is the time required for the current to decrease from 90% to 10% of its peak value, is rather slow. Likewise, slow photoconductive decay response can be attributed to a large number of recombination centers, the presence of trap levels and defect states within the band gap [419]. Relaxation curves are fitted best with a sum of two exponential functions, expressed as:

$$I_{\text{ph}} = I_{\text{dark}} + A_1 e^{(-t/\tau_1)} + A_2 e^{(-t/\tau_2)} \quad (5.5)$$

where A_1 and A_2 are weight coefficients, and τ_1 and τ_2 are the characteristic decay constants (effective relaxation times) [420, 421]. While the average rise time is approximately 20 s, the decay time is about an order of magnitude longer. This persistent photoconductivity is also

observed in amorphous, metal-oxide semiconductors and wide-bandgap semiconductors [422, 423]. Various reasons for the persistent photoconductivity are the presence of oxygen vacancies located within the bandgap [422], large spatial fluctuations of the potential energy of charge carriers [423], point defects, and metastable defects [424]. In some cases, the persistent behavior can take a few hrs to days without illumination. This behavior can be eliminated by designing a device with a three-gated terminal in a sandwich configuration, such as a field-effect transistor device structure, and subsequently by applying a short pulse positive gate voltage [422, 425]. The persistent photoconduction indicates that in Te/TeO₂-glass interface, there is a complex recombination process of free carriers by both radiative and non-radiative. For different wavelengths, Appendix shows the spectro-temporal evolution of the line patterns. The rise time is 82 s for white light, 55 s for 463 nm, and 41 s for 263 nm. The decay times for white light, 463 nm and 263 nm under the same illumination conditions are 411 s, 207 s, and 286 s, respectively. Various Te-based photodetector (whether macro- or nano-scale, from ultraviolet to near-infrared) shows the rise and decay times in the range of micros to a few hrs [246, 393, 396, 405, 407, 412, 413].

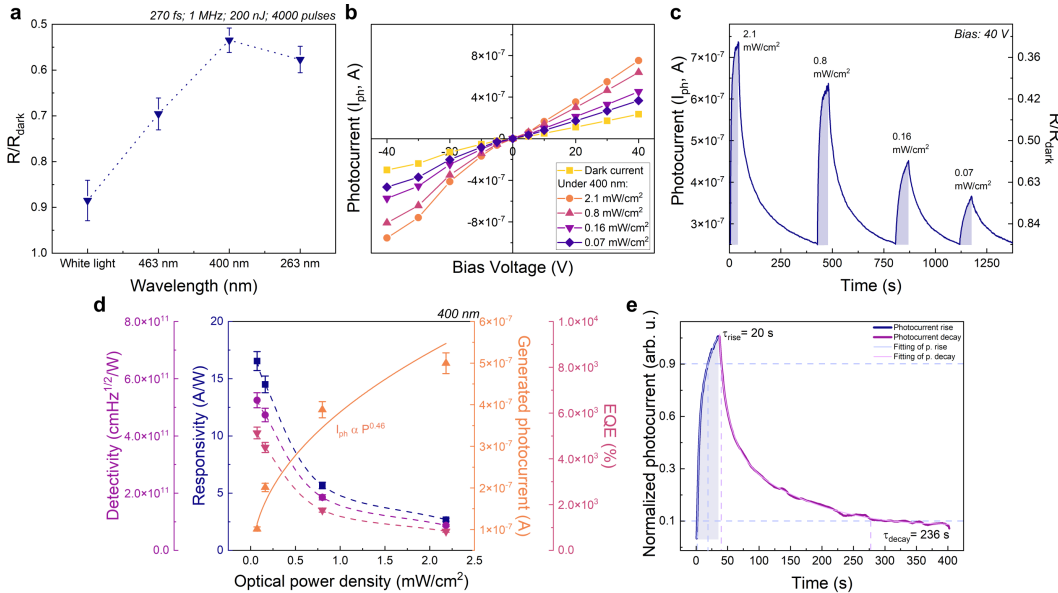


Figure 5.10: a) Spectral response of the device per unit of incident light power. b) I-V curve with and without illumination with various biases (- 40 V to 40 V). c) Typical temporal evolution with different optical power densities (0.07 to 2.1 mW/cm²). e) Responsivity, detectivity, EQE (%), and generated photocurrent of Te/TeO₂-glass nanocomposite structure. e) Temporal evolution of the line patterns: the photocurrent rise and decay time. All measurements are performed under an open-air atmosphere at room temperature.

Table 5.1 summarizes the performance of various Te nanostructures and other nanostructures of photoconductive semiconductors such as CdS, CdSe, t-Se, and ZnO. While the size of the other Te devices is in the order of nano-/micro-scale, the laser-inscribed patterns range from a few millimeters to a centimeter in length and hundreds of nanometers to a few micrometers in thickness. The responsivity and the detectivity vary with the optical power density. While

this device exhibits comparable responsivity and detectivity to devices based on other manufacturing principles, there is still room to improve the time response. Let us investigate the stability of the device over time, which is an essential aspect of practical applications.

Figure 5.11 presents the photoconduction characteristics of the same device (as in Figure 5.10) from the day of fabrication to after a few months of utilization. Figure 5.11.a shows I-V curves obtained without and with illumination at 400 nm after one month. We notice that the dark current decreases from $0.24 \mu\text{A}$ to $0.09 \mu\text{A}$ with a bias of 40 V after a month, and the current under illumination at 400 nm follows a similar trend. Figure 5.11.b-c displays the temporal response upon various optical densities at 400 nm and corresponding responsivity, detectivity, quantum efficiency, and generated photocurrent values. R , D^* , and EQE (%) values degrade over a month under illumination at 400 nm, while the exponent of generated photocurrent, α , stays the same. This behavior is because trap states are still present and do not change over time. Finally, a repetitive measurement on the first day of the device fabrication is presented in Figure 5.11.d, indicating the robustness and stability of the device. The amount of photo-response and the dark resistivity after 10 hrs of a cyclic test has not changed. Figure 5.11.e-f shows the multiple on-off cycles after a few months of usage. The rise and decay time does not change after a month, except for the photocurrent value. However, after two months, there is a noticeable baseline drift of the generated photocurrent and response times. There are a few possibilities to explain this dramatic change in the photo-response of the device over a few months. The first reason is the irreversible photo-induced oxidation upon UV illumination, observed previously in Te [209, 393]. The oxidation of Te starts immediately after the first test of the device and forms $\text{TeO}_2/\text{Te}/\text{TeO}_2$ -glass interface. However, the interface TeO_2/Te moves over time, as suggested by the dark current value being less than the value on the first day. Further illumination causes the oxidation of Te nanocrystals and nanoparticles, which results in the dark current approaching zero. To understand the degradation mechanism under UV irradiation, Raman spectra of pristine glass and the laser-inscribed line patterns were collected over time with a Raman laser emitting at 445 nm.

Raman spectra of the structural evolution of the tellurite glass under a Raman laser emitting at 445 nm are shown in Figure 5.12.a. The glass network of the glass is composed of TeO_4 trigonal bipyramids (tbp), TeO_{3+1} distorted trigonal bipyramids (d-tbp), TeO_3 trigonal pyramids (tp), WO_4 , and WO_6 polyhedra. It results in the presence of Raman peaks located at around 355, 490, 610, 670, 720, 790, 860, and 920 cm^{-1} , and assigned to bending vibrations of W-O-W in WO_6 octahedra, a symmetrical stretching of Te-O-Te linkages, continuous network of TeO_4 , antisymmetric stretching of Te-O-Te linkages consisting two inequivalent Te-O bonds, Te and NBO of TeO_{3+1} and TeO_3 , stretching of Te-O⁻ in TeO_{3+1} and TeO_3 , the stretching of W-O, W-O⁻ and W=O bonds associated with WO_4 and WO_6 polyhedra, respectively [163, 164]. There is no change in the peak intensity and ratio of the peaks in each spectrum collected at every 300 s. Hence, the pristine material is not altered while characterizing the device.

Figure 5.12.b-c displays the Raman spectra of the center of the laser-inscribed pattern and the ratio of the Te versus TeO_2 -glass. The characteristic vibration peaks of Te in the laser-inscribed

Table 5.1: Comparison of spectral range, responsivity, detectivity, the rise and decay time, and the stability of Te nanomaterials and common photoconductive materials.

Sample	Spectral range (nm)	R (A/W)	D* (Jones)	τ_{rise} and τ_{decay}	Stability
This work (10 mm tracks)	263, 400, 463 nm and white light	16.54 at 400 nm and 0.07 mW/cm ²	5.25·10 ¹¹ at 400 nm	20 and 236 s	cycling more than 2 months
Te nanowires[426]	633 nm	-	-	40 and 40 s	cycling for 100 times
Te nanoplates[240]	413-550 nm	389.5 at 473 nm and 76.2 mW/cm ²	-	4.4 and 2.8 s	bending for 100 times
Te nanoflakes[413]	1550 nm	51.85 at 1550 nm and 0.51 mW/mm ²	1.88 × 10 ¹⁰	19 and 21 μ s	-
Te nanoflakes[427]	520, 1550 and 3390 nm	383 at 520 nm and 1.6 nW	-	-	-
Te nanoflakes[425]	1400-2400 nm	16 at 1700 nm	2·10 ⁹	few s each	-
Te nanosheets[246]	350-400 nm	13.4·10 ⁻⁶ at 350 nm and 2.17 mW/cm ²	3.1·10 ⁷	54.5 and 70.2 ms	cycle stability for 10000s
Te nanoparticles in PMMA[407]	310-2200 nm	7.5·10 ⁻⁸ at 400 nm and 4.2 mW/cm ²	-	-	-
Te nanosheets and nanowires[428]	830, 1310, 1550, 2000 nm and blackbody	6650 at 1550 nm and 0.01 mW/mm ²	1.23·10 ¹²	31.7 and 25.5 μ s	+3 months
Te nanorods[408]	300-785 nm	6.1 at 0.94 mW/cm ²	1.2·10 ¹¹	tens of s	~30 days
CdS nanobelts[429]	490 nm	7.3·10 ⁴ at 3 mW/cm ²	-	~20 μ s	more than 73 hrs
CdS nanorod[430]	365, 420, 450, 500 nm	1.23·10 ⁴ at 450 nm and 0.5 mW/cm ²	2.8·10 ¹¹	0.82 and 0.84 s	-
CdSe nanocrystals[431]	500-532 nm	9.72 at 532 nm and 0.9 W/cm ²	6.9 × 10 ¹⁰	both below 2 μ s	-
t-Se nanoparticles[432]	300-700 nm	19·10 ⁻³ at 610 nm and 0.4 mW/cm ²	-	0.32 and 0.23 μ s	-
ZnO nanowires[433]	350-500 nm	1109 at 356 nm	-	both ~tens of s	-

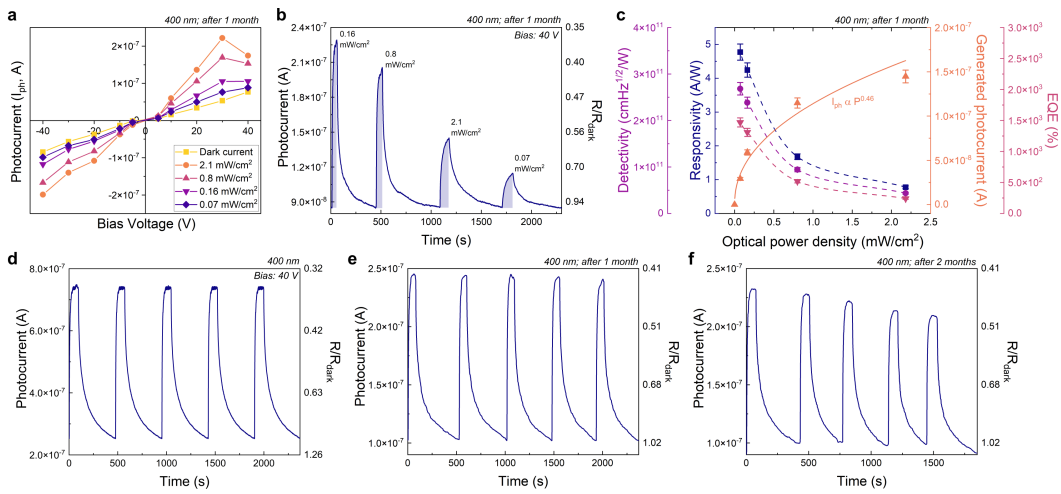


Figure 5.11: a) I-V curve without and with illumination at 400 nm for various biases. The measurement was carried out 1 month after the fabrication of the device. b) Typical temporal evolution of photocurrent with different optical power densities (0.07 to 2.1 mW/cm²) under 400 nm illumination 1 month after the fabrication of the device. c) Responsivity, detectivity, EQE (%), and generated photocurrent of Te/TeO₂-glass nanocomposite structure 1 month after the fabrication of the device. d-f) Repetitive temporal response at 400 nm with a flux of 2.1 mW/cm² the day of the fabrication, after 1 month and 2 months, respectively.

zone are at 93, 118, 139, 170, and 260 cm⁻¹, corresponding to E₁, A₁, and E₂ modes, Te-Te homopolar bonds in amorphous Te (a-Te), and two second-order spectra, respectively [205, 207–209]. After irradiating for 300 s, the Raman spectra do not show any crystalline-TeO₂ peaks but rather a decrease in the intensity ratio of Te/TeO₂-glass and an increase the intensity of in main glass bands. The photo-oxidation process further explains the longer decay time of the device after the fabrication. There can be a chemical reaction among existing structures and defects or with ambient air during the measurement. Due to oxidation, the zones enriched with holes at the surface, the grain boundary, and intragrain regions decrease. After two months of device usage, both rise and decay times decrease proportionally. Yet, time constants do not change, implying the presence of trap states as recombination centers. There are fewer carriers, generating less photocurrent in each cycle resulting in shorter recombination times. Transparent thin films of coating of SiO₂ or Si₃N₄ can overcome the degradation of the patterns [410]. Another reason is the degradation of the electrical contacts or the reaction between Te and contacts (Au and Ag) [410]. Typical metal-contacted Te devices show a performance degradation over time and temperature (failure above 473K) due to the diffusion of metal atoms into the Te channels. A non-reactive interlayer, such as graphene [410], can be employed to prevent metal diffusion. In summary, the preventative steps against the photo-oxidation of Te and degradation of metallic contacts are necessary for the better stability of the device for future applications.

In summary, we observed a photo-response of a tellurium/tellurite glass (Te/TeO₂-glass) nanocomposite interface produced by a femtosecond laser direct-write process on a tellurite

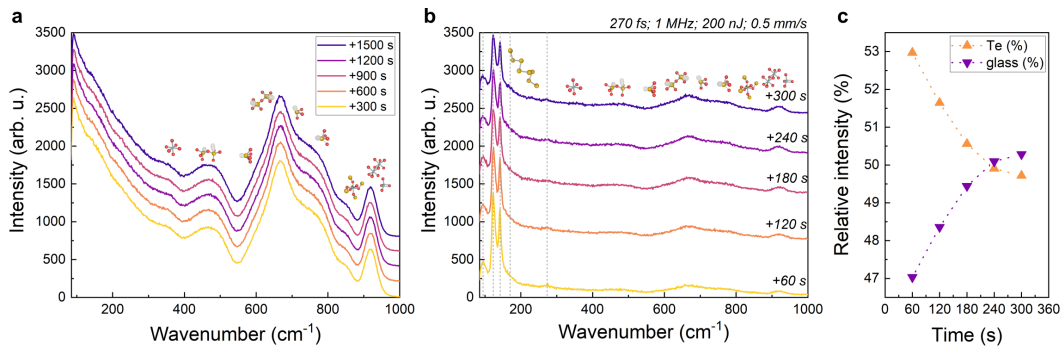


Figure 5.12: a) The Raman spectra of the pristine glass after irradiated with 445 nm Raman laser for 1500 s. b) The Raman spectra of laser-irradiated line pattern after irradiated for 300 s. The fs-laser processing parameters are 200 nJ with 0.5 mm/s at 1 MHz (corresponding to an incoming pulse fluence of 262 J/mm²). Note that Raman investigation is performed at the same day as the fabrication of the tested sample. c) The relative intensities of Te ($I_{93}+I_{122}+I_{141}+I_{170}+I_{260}$, (%)) and pristine glass peaks ($I_{356}+I_{470}+I_{610}+I_{670}+I_{720}+I_{790}+I_{860}+I_{920}$, (%)) at the laser-inscribed zone after irradiated with Raman laser for 300 s. The optical power density of the Raman laser is 115 mW/ μm^2

glass surface. After laser exposure, the measured resistivity is at least ten orders of magnitude lower than the one of the unmodified material, and is comparable to the one value measured for polycrystalline tellurium. By scanning a femtosecond laser beam over the tellurite glass substrate, one can form write a conductive path between arbitrarily distant locations. Furthermore, we show that line patterns produced in this manner can have a highly reproducible and sensitive photo-response, from the near ultraviolet to the visible spectrum, stable over a few months. This manufacturing process demonstrates that one can turn an otherwise non-photo responsive substrate, in the present case tellurite glass, into a photoconductive one by exposing it to femtosecond laser, and this, without adding any material to the substrate.

5.3 Chalcogenide glass

In Chapter 4, we presented that the photo-sensitivity of chalcogenide glass systems led to extensive photo-induced modifications. In this section, we report how our findings can be practiced to fabricate optical elements by femtosecond laser micromachining combined with chemical etching.

5.3.1 3D microstructures of chalcogenide glass

Among mid-IR materials, chalcogenide glass has the broadest reported transparency in the mid-IR, making it particularly attractive for spectroscopy and infrared imagery. Yet, it remains a challenging material to shape in an arbitrary form. Here, we explore the combination of femtosecond laser exposure and chemical etching steps to produce arbitrary 3D shapes. In

this context, we discuss how laser-induced defects in the glass matrix play a critical role in etching contrast and selectivity. Among variously known etchants of chalcogenides, high optical quality is obtained by alkali hydroxide solutions, yet, not all of them are effective for volume etching. The volume etching by NaOH solution results in a maximum etching rate of $190 \mu\text{m/hr}$. Still, the laser-affected zone exhibits relatively low etching selectivity compared to one in fused silica since similar defects are also present in the glass network. Nevertheless, various 2.5D and 3D microstructures are presented for the first time as a proof-of-concept. With further optimization, this simple and scalable laser direct writing method allows a new route in developing optical functionalities and new platforms for future devices.

Introduction

Chalcogenide glass is an attractive glass system thanks to its broadband transparency spanning from the visible to the mid-infrared range, from $\sim 400 \text{ nm}$ to up to $25 \mu\text{m}$. It is widely used in optics [307, 333], in particular for sensing [308], supercontinuum generation [314], integrated THz photonics [387], as well as ultrahigh-bandwidth signal processing [309] applications. Over the past decade, various geometries have been explored for expanding the usage of chalcogenide glass, including bulk materials, fibers, thin films, or in the form of gratings and rib waveguides [292, 309, 311]. However, controlling the geometry and dimensions of sophisticated parts of chalcogenide glass components remains challenging at the micro-/nanometer scales. Surface structuring of these glass systems can be done using electron-beam lithography [434], dry etching [435], solution-based process [436], surface plasticizing [437], hot embossing [438], template fluid instabilities [439], thermal poling [440] or using laser direct writing [441]. Simple 3D shapes and geometries have been produced by molding [442] and thermal drawing [443] and recently, by additive manufacturing [444, 445]. In another study, we have shown the combination of femtosecond laser-assisted etching of a fused silica mold and pressure-assisted chalcogenide glass infiltration to obtain 3D microstructures in a micrometer scale [446], in particular for the production of free-form optics embedded in a silica matrix. Unfortunately, these processes are incapable of producing arbitrary 3D shapes [434–441] and/or free-standing chalcogenide shapes [446]. This work investigates the potential and limits of the femtosecond laser process combined with chemical etching in the context of chalcogenide free-form manufacturing.

As wide bandgap semiconductors, amorphous chalcogenides can readily react with a broad range of the electromagnetic spectrum. Due to excited electrons across the bandgap by the absorption of visible light, photo-structuring is another common technique to produce functional surfaces and devices. In addition, their significantly weaker and less rigid network structure makes them be exploited as, for example, a photoresist, which results in local structural and/or physicochemical changes upon light exposure [368]. Photosensitivity can lead to various reversible and irreversible phenomena, as discussed in Chapter 4. The high photo-sensitivity of chalcogenides makes them also favorable candidates for a process based on ultrafast laser exposure, followed by an etching step, as thoroughly demonstrated for

other glass systems, and, in particular, fused silica [43]. The process is based on in-volume modifications induced through non-linear absorption mechanisms triggered by multiphoton absorption that is subsequently dissolved using wet etching.

Previous attempts of preferential etching triggered by femtosecond laser modification on chalcogenide glass have been reported for the fabrication of specific 2D and 2.5D components, such as micro-lenses [447]- through single-pulse exposure, and gratings [448] done by scanning the laser beam. Recently, another pathway, different than the one discussed here, has been reported for the fabrication of photonic crystals [449] and infrared anti-reflective coatings and meta-optics [450] made by two-photon polymerization to define the volume to keep rather than subtracting it. Yet, systematic study and 3D geometries from the bulk glass are not shown before, which motivates this work. Specifically, we investigate the role of various etchants and laser-writing conditions in the context of process optimization. We further discuss how laser-induced defects in the glass matrix can play a critical role in etching contrast and selectivity. Finally, we conclude with an illustration of various 2.5D and 3D microstructures produced with an optimized process.

Experimental procedure

The nominal composition of the glass used in this study is $\text{Ge}_{23}\text{Sb}_7\text{S}_{70}$. The femtosecond laser system, emitting pulses of 270 fs pulses at 1030 nm (Yb-doped femtosecond fiber laser, Yuzu from Amplitude) was used. The specimen was translated under the laser focus with the help of a high-precision motorized stage (Ultra-HR from PI Micos). The laser beam was focused at the surface and in the volume of the specimen using a 0.4-NA objective (OFR-20x-1064 nm from Thorlabs). Translation velocity and pulse energy were selected to vary laser fluence (or deposited energy). Here, while pulse-to-pulse overlapping ratios were adjusted between 0 to 99.9%, the pulse energy was ranging from 1 nJ to 200 nJ. The repetition rate was alternating between 1-100 kHz. Furthermore, two different linear polarization states, i.e., parallel and perpendicular to the writing direction, were utilized to test the effect of polarization on the etching rate.

In Chapter 4, the femtosecond laser processing map has been reported for this glass system. For surface structures, the sample surface was irradiated with a net fluence ranging from 0.0016 to 26.25 J/mm². A similar parameter window was utilized for in-volume irradiation between 0.0032 and 52.5 J/mm². Single tracks, consisting of 10 mm-long lines, were written 20 μm under the surface to estimate the etching rate contrast between exposed and non-exposed regions, whereas microchannels, consisting of multiple adjacent lines, were written at a depth of 100 μm . A shallow depth was chosen to limit effects related to spherical aberrations due to the high-index value of the chalcogenide glass ($n = 2.25$). Samples having volume modifications were polished to reveal the structures. Later, all irradiated samples were etched using four different chemicals at room temperature: NaOH (2.5 %), KOH (44%), HF (1%), and propylamine (99% from Sigma Aldrich) at room temperature for a few seconds to several hours (without stirring).

The optimum process to obtain the highest etching selectivity was determined by performing a systematic experiment with different concentrations of the etchants, time, and temperature (not shown here). Specimens were observed using a digital optical microscope with standard lighting conditions (KH-8700 from Hirox). The surface profile and the roughness were obtained using laser confocal microscopy (VK-X from Keyence) and confirmed with atomic force microscopy (AFM from Nanosurf). Finally, carbon thin film-coated samples were observed using a field-emission scanning electron microscope (FE-SEM, Gemini 2 from Zeiss) operated at 5 kV for high-resolution imaging.

Finally, to reduce the etching of pristine glass, both surfaces of the samples were coated with amorphous-SiO₂ by plasma enhanced chemical vapor deposition (PECVD from Oxford PlasmaLab) with a thickness of 1.6 μm at 373 K before femtosecond laser inscription. These samples were used for calculating the volume etching rate and glass cutting along the z-direction.

Wet chemical etching of surface structures

Wet chemical etchants already known for chalcogenide glass are summarized previously [368–370, 451]. First, selected etchants such as the non-aqueous solvent of propylamine (CH₃(CH₂)₂NH₂) and the aqueous solutions of potassium and sodium hydroxide (KOH and NaOH) are investigated for the pristine material. Even though chalcogenides are known to have high chemical resistance to acids [368], such as hydrofluoric acid or hydrochloric acid (HF and HCl, respectively), etc., etching with HF is performed for comparison. The etching rate of the pristine glass for various known etchants, i.e., NaOH, KOH, HF, and propylamine is shown in Table 5.2.

Table 5.2: The etching rate of the Ge₂₃Sb₇S₇₀ glass with NaOH, KOH, HF, and CH₃(CH₂)₂NH₂.

Etchant solutions/solvents	gr/hour	cm ³ /hour	μm/hour (per 1 cm ²)
NaOH (2.5%)	0.00852	0.00289	28.9
KOH (44%)	0.4272	0.14503	1450.3
CH ₃ (CH ₂) ₂ NH ₂ (99%)	0.00456	0.00159	15.9
HF (2.5%)	0.000024	8*10 ⁻⁵	0.8

Those etchants have been used mainly for various lithographic processes. Their selectivity to femtosecond laser-modified zones in Ge₂₃Sb₇S₇₀ glass remains elusive. First, the surface structures in the form of a single spot to continuous tracks are inscribed to observe the etching selectivity. Figure 5.13 shows SE images of 2D surface-structures and the surface profile of Ge₂₃Sb₇S₇₀ under various laser-writing conditions and etchants. Figure 5.13.a-c shows the unetched sample surface, where the separation of laser spots is controlled by the laser-writing speed. Figure 5.13.d-f shows the sample surface after 60 seconds of etching with KOH at room temperature. Enlarged and smooth laser surface structures are obtained due to the evenly etching of pristine material and laser-affected zone simultaneously. In the case of NaOH etching in Figure 5.13.g-i, sharp features are obtained since the etching rate of pristine material

is lower compared to KOH. Finally, propylamine makes surface scratches enlarged and visible, giving a little etching contrast to the femtosecond laser-modified zone. Chalcogenide glasses are etched relatively easily by alkaline solutions [368]. In our case, NaOH and KOH give the best etching contrast on the surface structures. Then, the determining factor of etch rate of the microstructure are the laser exposure conditions.

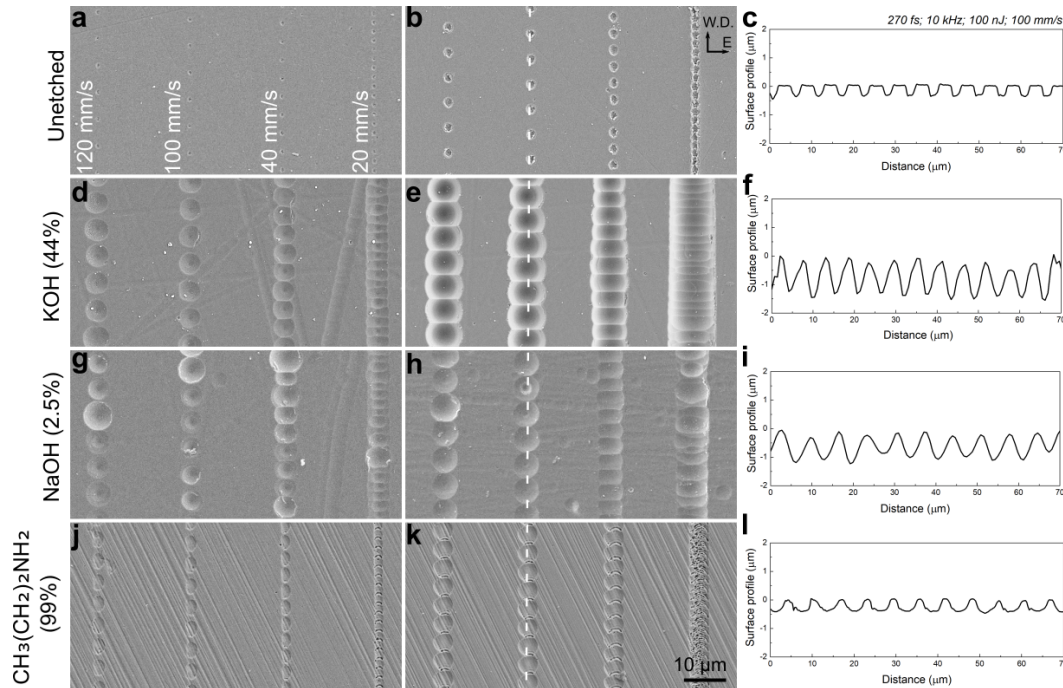


Figure 5.13: Secondary electron (SE) images of 2D surface structures and surface profile of $\text{Ge}_{23}\text{Sb}_7\text{S}_{70}$ under various laser writing conditions and etchants. a-b) Unetched glass surface, and c) the surface profile. d-e) After 60 s of etching with KOH (44%), and f) the surface profile. g-h) After 60 s of NaOH (2.5%), and i) the surface profile. j-k) After 60 s of Propylamine (99%), and l) the surface profile. The laser writing parameters are a-d-g-j) 10 nJ ($0.0055\text{-}0.033\text{ J/mm}^2$) and b-e-h-k) 100 nJ ($0.055\text{-}0.33\text{ J/mm}^2$) at 10 kHz.

NaOH solution shows the highest etching contrast, defined as preferentially removed exposed materials compared to the removal of unexposed material, among other etchants. From this point on, only results obtained with NaOH etching are presented. Before moving to etching selectivity in volume, let us explain the glass structure of $\text{Ge}_{23}\text{Sb}_7\text{S}_{70}$. The glass network of $\text{Ge}_{23}\text{Sb}_7\text{S}_{70}$ consists of $\text{GeS}_{4/2}$ tetrahedra and $\text{SbS}_{3/2}$ pyramids, connected randomly [379], and S-S homopolar bonds in Ge-S_n-Ge bridges [379]. It is also known that the Ge-Sb-S glass undergoes various structural changes under femtosecond laser exposure [286, 302]. At low fluence, $\text{Ge}_{23}\text{Sb}_7\text{S}_{70}$ exhibits a photo-contraction regime, resulting in densification. However, at a higher fluence, a local photo-decomposition or porosification regime results in an increase in the band intensity of the broken S in the form of S_8 rings and S_n chains and corner-sharing $\text{GeS}_{4/2}$ tetrahedra. The conversion of structural units leads to a reconfiguration in the backbone glass structure. Let us now present possible chemical reactions that may

occur between femtosecond laser-affected zones in $\text{Ge}_{23}\text{Sb}_7\text{S}_{70}$ and NaOH solution at room temperature. There, the corner-sharing $\text{GeS}_{4/2}$ are chemically transformed according to the following reactions [452]:



The reaction with NaOH occurs by a two-step dissolution: first the interaction of glass structure with NaOH solution (5.6) and the second, the adsorption of the intermediate product (5.7) [451]. Similar to a previous study [452], as OH^- reacts with the glass and produces the intermediate product, a decrease in OH^- concentration in the solution leads to different dissolution rates. In addition, the excess sulphur, produced as S_8 rings, and S_n chains upon the laser irradiation, can react with Na^+ and OH^- and dissolve in the solution. According to a previous study, the $\text{GeS}_{4/2}$ tetrahedra, S_8 rings, and S_n chains can dissolve easier compared to $\text{SbS}_{3/2}$ [451], hence resulting in selective etching of the laser-affected zone. Unfortunately, those units are also present in the pristine glass, causing the dissolution of the pristine material simultaneously, and therefore yielding a much lower etching contrast compared to femtosecond laser-assisted etching of fused silica [43].

Wet chemical etching of volume structures

Here, we investigate single laser tracks to determine the etching rate. Further, we demonstrate how multiple lines interact with each other to form a microchannel. Figure 5.14 shows the OM and SE images after etching, and the etching rate for a given set of pulse energies, writing speed, and laser polarization, i.e., the orientation of the laser electric field. By inscribing tracks in the glass volume, etching selectivity is obtained for bulk modifications. Figure 5.14.a shows the SE image of the cross-section and OM images of the top view of laser-written tracks after etching. Significant widening is observed resulting in a low aspect ratio (1:3), i.e., the ratio of etched length and the width of the etched track at the enclosed point (marked with a white arrow in Figure 5.14.a). As the pristine material continues to be etched (with an average speed of $26.3 \mu\text{m/hr}$), the entrance point of the laser-written tracks keeps being removed at the speed indicated Table 5.2.

Figure 5.14.b-c displays the etching rate for a given set of pulse energies, writing speed, and polarization. Overall, the high field strength with relatively low net fluence ($\sim 0.33\text{-}6.56 \text{ J/mm}^2$) gives the best etching rate ($150\text{-}200 \mu\text{m/hr}$). This behavior follows a sharp decay at high field strength with high net fluence ($\sim 6.56 \text{ J/mm}^2$). A few pulses (refer to high writing speed) are effective enough to reach the highest etching rate, showing intriguing similarity with another study conducted for the laser-modified fused silica with NaOH etching [43]. Note that the

same experiment was performed for KOH (not shown here), however, no preferential etching over time is observed.

Two different polarization states show significant differences in the etching rate. Perpendicular polarization is shown as the highest etching rate for fused silica or other glass systems showing anisotropic birefringent structures [43, 286]. The highest etching rate for laser-modified tracks in $\text{Ge}_{23}\text{Sb}_7\text{S}_{70}$ glass is also obtained by the tracks written with perpendicular polarization.

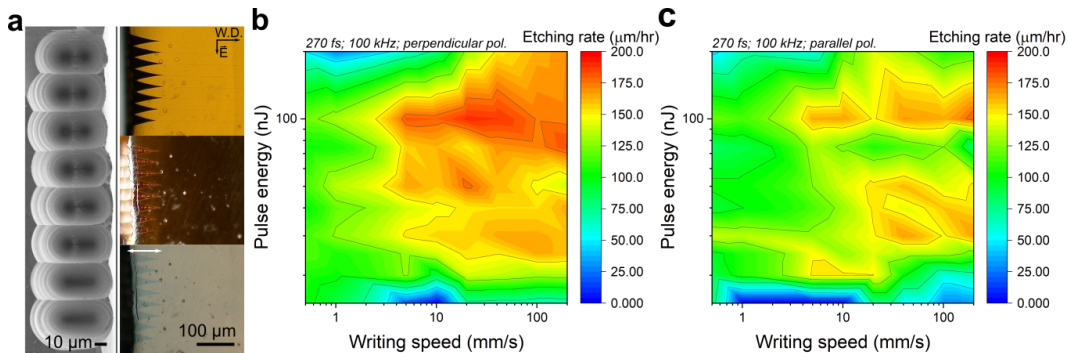


Figure 5.14: a) SE image of the cross-section and OM images of top view of single laser-written tracks $20\ \mu\text{m}$ in depth under the $\text{Ge}_{23}\text{Sb}_7\text{S}_{70}$ glass surface after 30 minutes of etching. Laser-writing parameters are 30 nJ with a net fluence from 0.0098 to $3.94\ \text{J}/\text{mm}^2$. b) Volume etching rate of single laser-written tracks from 0.0016 to $26.25\ \text{J}/\text{mm}^2$ at 100 kHz. The etching was performed for 3 hrs at room temperature.

In addition, sets of lines are written alongside each other to create micro-channels in different regimes. Figure 5.15 displays SE images of the cross-section and OM images of a top view of a set of laser-written tracks under $100\ \mu\text{m}$ of the $\text{Ge}_{23}\text{Sb}_7\text{S}_{70}$ glass surface after etching. Figure 5.15.a show the effect of the densification regime in-volume modifications, in there is no etching contrast or selectivity. Furthermore, the micro-channel in Figure 5.15.b is written in the porosification regime, demonstrating smooth structures with a high selective etching rate and contrast. Finally, sets of channels next to each other are written in Figure 5.15.c at the onset of the porosification regime. $\sim 100\ \mu\text{m}$ depth is achieved after 1 hour of NaOH etching at room temperature. This is an excellent example of why a higher field strength is required with the same net fluence to obtain smoother microstructures with a higher aspect ratio.

Wet chemical etching of 2.5D and 3D structures

As a proof of concept, 2.5D near-surface structures such as pillars, prisms, and free-standing over-hanged structures are investigated with NaOH etching. Figure 5.16.a-b shows square prisms with different dimensions written at two different regimes and their surface profiles. The writing conditions of Figure 5.16.a are in the densification regime. The cliff near the edge of the structures is due to higher net fluence exposure (slower writing speed) related to the acceleration of the stage. Towards the center of the microstructure, when the accurate speed (so is the desired fluence) is achieved, the etching rate instantly drops. The process window

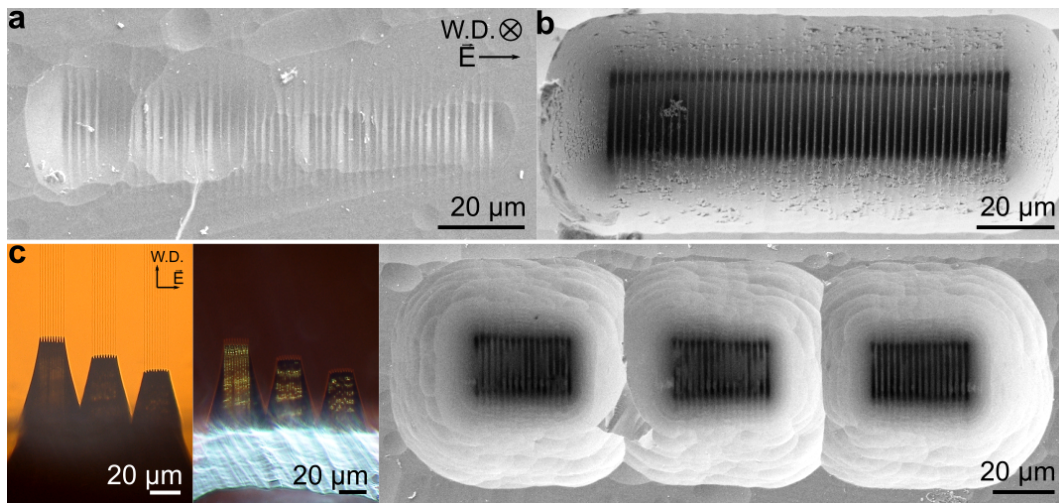


Figure 5.15: SE images of 3D micro-channels written as a set of laser-written tracks under $100\ \mu\text{m}$ of the $\text{Ge}_{23}\text{Sb}_7\text{S}_{70}$ glass surface after 1 hr of etching. a) 10 nJ with $0.65\ \text{J}/\text{mm}^2$ and b) 50 nJ with $3.28\ \text{J}/\text{mm}^2$. c) OM images of a top view and the SE image of the cross-section of sets of channels under $100\ \mu\text{m}$ in-depth of the $\text{Ge}_{23}\text{Sb}_7\text{S}_{70}$ glass surface. The set of channels are written at 25 nJ with $3.28\ \text{J}/\text{mm}^2$ at 100 kHz.

in this regime is extremely narrow and requires extra care while selecting the parameters. The microstructures in Figure 5.16.b are written in the porosification regime, where the glass-backbone structure decomposed. Since this regime requires higher net fluence, there is no step along the laser writing direction, and a uniform surface profile is achieved.

Figure 5.16.c shows SE image of the set of pillars with dimensions ranging from 2 to $100\ \mu\text{m}$ laterally and $100\ \mu\text{m}$ in depth before and after etching. The lowest diameter obtained after etching is $13\ \mu\text{m}$ with a depth of $100\ \mu\text{m}$. Figure 5.16.d presents over-hanged structures written with various step sizes and laser parameters. The over-hanged structures are achieved only at the high net fluence in the porosification regime. The thickness difference of the top layer comes from the variation in the step size in the z -direction.

In addition, removal of a glass window with various shapes are performed by femtosecond laser-assisted wet chemical etching of the $\text{Ge}_{23}\text{Sb}_7\text{S}_{70}$ glass as industrial relevance. OM images demonstrates that the glass is removed from top to bottom in Figure 5.17.a-b. Figure 5.17.a,c-e displays glass windows with a final size of $560\ \mu\text{m}$ in the lateral distance and 1 mm in depth after 22 hours of etching. The starting glass thickness is 1.1 mm, and the size of the inner edge of the square was $500\ \mu\text{m}$. Again, the fastest etching regime in processing window is somewhat lies between porosification and anisotropic birefringent structures. Magnified SE images highlight the smoothness of the inner walls in Figure 5.17.c-d, although further optimization is needed to obtain the desired final design. The final roughness of the cross-section of the cut is $\sim 167\ \text{nm}$, fulfilling an optical quality requirement for various optics and photonics applications in near-IR to mid-IR.

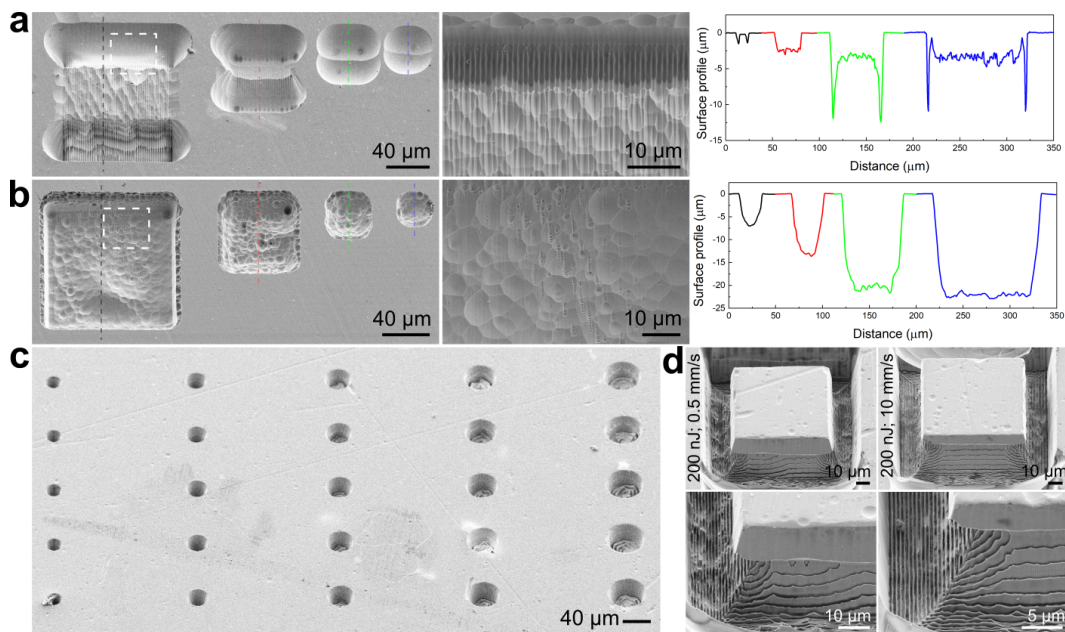


Figure 5.16: SE images of 2.5D near-surface structures on $\text{Ge}_{23}\text{Sb}_7\text{S}_{70}$ before and after NaOH etching. a-b) 2.5D near-surface structures in two different regimes with their surface profile after etching with a depth of $20\ \mu\text{m}$ for 10 mins. c) After etching of pillars with a depth of $100\ \mu\text{m}$ for 30 mins. d) After the etching of over-hanged microstructures for 1 hour. Samples were observed every 5 mins to avoid over-etching. Laser writing parameters are 0.0016 to $26.25\ \text{J}/\text{mm}^2$ at $100\ \text{kHz}$.

Finally, glass-cutting is performed by scanning along the z-direction of a glass coated with amorphous- SiO_2 , reported in Appendix E. The starting thickness of the pristine glass with a coating on both surfaces is $650\ \mu\text{m}$. After the glass is cut into two pieces by etching with NaOH for 14 hours, the glass is dipped into HF to remove the SiO_2 coating. The first few tens of micrometers of the cross-section shows rather over-etched structures due to removal by ablation or delamination of the coating during laser writing. The OM image is taken after 1 hour of etching to observe the progress of the etching.

A few limitations have to be overcome in this process, such as avoiding crack formation, obtaining a low surface roughness, and a high aspect ratio with a high resolution. Cracks can be present in the complex geometry samples of this work, depending on the density of the laser-written tracks in a given volume. However, we avoid cracks by carefully selecting the laser processing window and an overlapping distance between the adjacent tracks, kept at $\sim 1\text{-}2\ \mu\text{m}$. The final surface texture (or the roughness) inherited from this process can be eliminated by post-processing methods. A high-aspect ratio can be obtained by extensive research on glass chemistry and its interaction with etchants. Regarding resolution, the smallest structure produced in this study is about $13\ \mu\text{m}$ in diameter after etching; however, it is possible to push such limits further by tuning laser parameters such as the wavelength of the laser, focusing conditions, or careful tuning of the glass composition. In this demonstration,

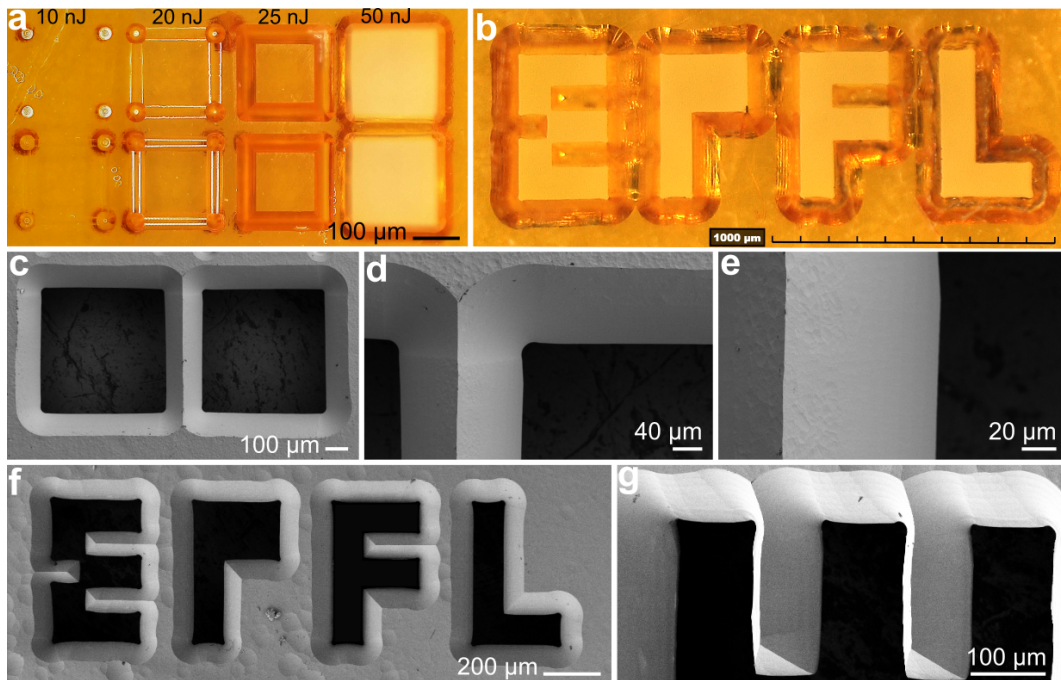


Figure 5.17: OM and SE images of 3D glass windows with various designs along the z-direction of the $\text{Ge}_{23}\text{Sb}_7\text{S}_{70}$ glass after etching for 12 hours with 2.5% NaOH at room temperature. a-c) Glass windows after etching for 12 hr. The laser parameters are a) 10-50 nJ and b-g) 50 nJ with 6.56 J/mm^2 at 100 kHz.

although we employed $\text{Ge}_{23}\text{Sb}_7\text{S}_{70}$ glass, this technique can be applied to a wide range of glass compositions both within and outside the chalcogenide glass systems and laser writing conditions. As examples illustrated above, the process enables the fabrication of 2D to 3D chalcogenide structures with micrometer precision. By the present process, complex shapes from micrometer to centimeter scale such as 3D waveguides, lenses, etc. can be produced without time-consuming procedures.

In summary, the utility of femtosecond laser-assisted selective wet etching as a fabrication technique of chalcogenide glasses is presented. Various etchants to selectively attack the laser-modified glass structure are discussed and among them, the NaOH solution is found as having the highest selectivity. We further discuss how the laser-induced defects in the glass matrix play a key role in etching contrast and selectivity. The fabrication of elements in various dimensions is explored through direct laser writing combined with selective etching both on the surface and in the glass volume. In particular, various 2.5D and 3D microstructures are presented as proof-of-concept. This simple and scalable laser direct writing method develops the new fundamental understanding into energy and matter interactions, which can be used in future to guide, design and fabrication of chalcogenide glass based sensors and optical devices.

5.4 Summary

In this chapter, we showed various photo-induced modifications on the surface and in the volume and both thermally cumulative and non-cumulative regimes of ULE glass, tellurite, and chalcogenide glass families. Our findings triggered the following observations:

- The selective etching of femtosecond laser-modified ULE glass presents a high etching rate with an excellent aspect ratio by NaOH solution. The highest etching rate is obtained when a polarization state is perpendicular to the laser writing direction. A high etching rate and contrast are accomplished by the femtosecond laser-assisted etching processing of ULE glass, attractive for many applications, particularly for precision manufacturing and space applications.
- In tellurite glass, we investigated the photo-response of the Te/TeO₂-glass nanocomposite interface produced by the femtosecond laser direct-write process on a tellurite glass surface. Furthermore, we show that the line patterns can have a highly reproducible and sensitive photo-response in the near ultraviolet to visible spectrum stable over a few months. These results may enable the direct write of functional 2.5D nanocomposites with physical properties easily tailored by the inscription parameters.
- In chalcogenide glass, the utility of femtosecond laser-assisted selective wet etching as a fabrication technique of chalcogenide glasses is presented. Among various etchants, the NaOH solution results in the highest selectivity. The fabrication of elements in various dimensions is explored through direct laser writing combined with selective etching both on the surface and in the glass volume. In particular, various 2.5D and 3D microstructures are presented as a proof-of-concept.

6 Conclusions

Femtosecond lasers have become an irreplaceable tool in the last few decades not only for implementing three-dimensional (3D) multi-functional micro-devices in bulk transparent materials but also for studying a light-matter interaction with a high peak irradiance at various time scales. Based on the non-linear phenomena occurring within the focal volume where the energy is confined, this process eventually leads to local structural modifications on the surface or inside transparent materials.

In this context, this thesis aimed to explore a generalized framework for understanding ultra-fast laser-matter interaction in complex glass systems. Specifically, we investigated the role of the material's properties on the formation of laser-induced modifications and, in particular, self-organization. For this purpose, this thesis is based on a comparative study of complex glass systems bringing answers to the following questions:

- How do chemical and physical properties influence each type of laser-induced modification? What are the final properties of the laser-affected zones, in particular, similarities and differences among complex glass systems?
- Does self-organization occur in any glass? How do glass structure and properties influence the formation of self-organization phenomena? What are the conditions to sustain/hinder self-organized nanostructures in the volume and on the glass surface?
- Parallel to photo-induced modifications, how can we achieve superior properties, monolithic substrates, and devices by tuning glass properties based on femtosecond laser technology?

To investigate the questions listed above, in this study, ULE, chalcogenide, and tellurite glass systems were selected as complex glass systems because of a few reasons. Altogether, they form a representative group to cover the range of glassy materials. For example, almost all UV-VIS-NIR-MIR range of the optical transmission windows can be enveloped by the combination of ULE ($\sim 0.25\text{-}2.8\ \mu\text{m}$), tellurite ($0.4\text{-}5\ \mu\text{m}$), and chalcogenide ($0.6\text{-}8.3\ \mu\text{m}$) glass systems.

Similarly, their electrical properties span from a range of wide-bandgap semiconductors to insulative. Various bonding types and bond strengths set a wide range of views to multi-component glass families. The physical properties of the selected complex glass systems are reproduced in Table 6.1. Moreover, each has certain properties that are considerably in common in their own systems. For example, titania-silicate glass (ULE) shares 93 wt% of the composition of fused silica. Both glass systems are categorized under silicate glass, sharing multiple common physical properties. While tellurite glass tolerably represents non-silicate glass systems, chalcogenide glass portrays non-oxide glass systems. Although each glass system has unique features determined by its chemical composition, in the big picture, one can be represented by another only up to a certain extent. Therefore, we carefully chose different compositions of each complex glass system while preserving the structural network. Several different compositions of tellurite and chalcogenide glass systems were also studied while keeping the TeO₂- and Ge-based networks the same. For ULE glass, well-studied fused silica was used as a benchmark to correlate the structural modifications.

Table 6.1: The physical properties of ULE@Glass, tellurite, and chalcogenide glass [106, 107, 163, 165]. The table displays the sample name, density, refractive index, softening temperature, heat capacity, and Young's modulus.

Sample	ρ (g/cm ³)	n	T _m (K)	C _p (J/kg·K)	E (GPa)
ULE 7972	2.21	1.48	1763	767	67.6
TWK	5.31	2.025	892	460	41.95
Ge ₂₃ Sb ₇ S ₇₀	2.95	2.25	850	422	-

6.1 Main results

Before answering the questions above, let us summarize all of the findings in this thesis. We investigated three different glass systems as follows:

Case study I: Silicate glass systems

- *Laser-induced modifications in ULE glass*

In Chapter 2, we covered modifications in ULE glass, specifically, the volume and surface nanogratings, densification, photo-darkening, glass decomposition, crystallization, and the formation of bubbles. Starting with homogeneous modifications associated with densification at low pulse duration (~ 14 J/mm²), self-organized nanogratings are started to occur around 150 fs and above (~ 30 -40 J/mm²) in the glass volume. The modifications above 150 fs are accompanied by photo-darkening due to the valence state change of the glass modifier, TiO₂, from Ti⁴⁺ to Ti³⁺, leading to the high absorption of the laser-affected area. In addition, molecular oxygen is found at the laser-affected zone in the nanograting regime above 150 fs. Additional pulse energy above 150 fs leads to glass decomposition and subsequent crystallization of metastable TiO₂ (β -TiO₂, anatase)

phase. While amorphous precipitates, possibly composed of Ti_2O_3 , are formed at low laser fluence, higher laser fluence (90 J/mm^2) presents the polycrystalline TiO_2 with an average size of 5 nm. Finally, in the thermal cumulative regime above 500 kHz, the bubbles filled with molecular oxygen, surrounded by densified matrix are obtained.

- *The fabrication of monolithic substrates through selective etching*

In Chapter 5, we reported femtosecond laser exposure combined with chemical etching of ULE glass not only to implement 3D glass micromachining but also to better understand the nature of the photo-induced modifications. We found that a longer pulse duration gives twice higher etching rate ($\sim 260 \mu\text{m/hr}$ at 500 fs) compared to shorter pulse durations at 150 fs as it leads to more complex laser-induced modifications, such as localized defect formation based on valence state change of Ti ions, phase dissociation, and crystallization of $\beta\text{-TiO}_2$. The highest etching rate is obtained when a polarization state is perpendicular to the laser writing direction due to the anisotropy of nanogratings. In addition, we investigated the role of etchants on laser-modified volumes, namely HF and NaOH solutions. Twice higher etching rate by NaOH etching ($\sim 260 \mu\text{m/hr}$ with a high aspect ratio of ~ 200) was accomplished. Finally, the average roughness range after etching is in the range of 90 to 400 nm.

Case study II: Non-silicate glass systems

- *Laser-induced modifications in tellurite glass*

In Chapter 3, we showed various photo-induced modifications on the surface and in the volume, such as self-organization beyond the focal volume, photo-darkening, glass decomposition, crystallization, and densification. The photo-decomposition of laser-modified tellurite glass leads to an elemental t-Te, accompanied by elemental redistribution and deoxygenation. A single pulse is sufficient to form elemental t-Te on the tellurite glass surface. The formation of nanostructures and t-Te nanocrystals causes photo-darkening resulting in a decrease in total transmission of the laser-affected area. Polarization-dependent self-organized nanostructures in thermal-cumulative regimes extend beyond the zone under direct laser exposure on the surface. At the same time, elemental crystallization and growth are promoted in the thermal-cumulative regime. The underlying elemental crystallization phenomenon was investigated by altering laser parameters in tellurite glass systems under various ambient conditions. Interestingly, the formation of t-Te is greatly suppressed under a dry nitrogen atmosphere as there is limited interaction of glass network units, and Te_2 or Te_n clusters with an open-air atmosphere have a detrimental effect on the formation process. The femtosecond laser-induced modifications in the volume results in the dual-ion migration process and crystallization of t-Te nanocrystals. The threshold of nanocrystal formation in the volume was found to be five times higher than the one on the surface. No volume nanogratings were observed in tellurite glass systems under the selected irradiation conditions.

- *The fabrication of UV photodetector based on Te-TeO₂ nanocomposite interface*

In Chapter 5, we demonstrated a pathway for locally turning a tellurite glass into functional photoconductive Te/TeO₂-glass tracks of arbitrary shapes without adding materials and through a high-precision single process thanks to glass decomposition and surface crystallization phenomena. We showed that these laser-inscribed patterns have a highly reproducible photo-response from the near ultraviolet (263 nm) to the visible spectrum and are stable over a few months. Furthermore, high responsivity and detectivity of a single line pattern are achieved as ~ 16.55 A/W and 5.25×10^{11} Jones, respectively, for an illumination dose of 0.07 mW/cm² at 400 nm.

Case study III: Non-oxide glass systems

- *Laser-induced modifications in chalcogenide glass*

In Chapter 4, we investigated various photo-induced modifications on the surface and in the volume of chalcogenide glass. Refractive index change, the formation of self-organization and highly periodic spherical patterns, photo-oxidation, photo-darkening, and restructuring of the glass network were observed. At the lower fluence level (~ 0.1 J/mm²), the laser-affected zones display a change in positive and negative refractive index, leading to photo-contraction and photo-expansion in the glass volume. At higher levels (13 J/mm²), the formation of self-organized laser patterns, consisting of parallel nano-planes perpendicular to the laser polarization, is observed both at and under the surface. While self-organized surface nanostructures (generated at 1.3 J/cm²) start to erase after annealing above the glass transition temperature, the removal of cavitation and the surface roughness requires melting of the glass. In contrast, bubbles and nanogratings in the volume dissolve before the glass transition, while the densification regime disappears at lower temperatures (513 K). Furthermore, substituting Sb with As and S with Se results in fluctuations in the modification threshold and degradation in self-organized surface nanostructures. All compositions display photo-darkening, elemental decomposition, and photo-oxidation phenomena on the glass surface. In our parameter range with subsequent characterization techniques, crystallization was not detected in chalcogenide glass.

- *The fabrication of monolithic substrates through selective etching*

In Chapter 5, we explored the combination of femtosecond laser exposure and chemical etching steps to produce arbitrary 3D shapes in Chapter 5. The volume etching by NaOH solution results in a maximum etching rate of 190 μ m/hr. Still, the laser-affected zone exhibits relatively low etching selectivity (and an aspect ratio of 1:3) since similar defects are also present in the glass network. Nevertheless, various 2.5D and 3D microstructures are presented for the first time as proof of concept.

6.2 General discussion

Let us decode the questions above one by one based on this thesis work.

How do chemical and physical properties influence each type of laser-induced modification? What are the final properties of the laser-affected zones, in particular, similarities and differences among complex glass systems?

Relying on the non-linear absorption process, various properties, including electronic structure and optical properties (but not limited to), play a key role in the initial ionization process and the generation of seed electrons. Once the energy is transferred to the lattice, the dynamics of the lattice come into play. Some physical properties, such as density, Young's modulus, heat capacity, thermal conductivity, etc., determines the final laser-induced modification. However, once the first pulse arrives, the subsequent pulse interacts with a modified material whose properties can be deviating from the pristine material.

Starting with the damage threshold, the general determining factors are the bond strength, the bandgap, and the absorption. In this study, the pulse energy thresholds on the surface of selected glass systems are as follows: ULE (90 nJ) > TeO₂-WO₃-K₂O (10 nJ) \approx Ge₂₃Sb₇S₇₀ (10 nJ) for a single 270 fs-laser pulse emitted at 1030 nm. Even though chalcogenide and tellurite glass are categorized in separate families, they can be considered "soft glass" systems, which display lower bond energy, low glass-transition, and melting temperature compared to silicate glass systems. Thanks to chalcogen atoms (S, Se, and Te) in both systems, they exhibit similar physical properties. Still, tellurite glass possesses a higher ablation threshold owing to the stronger oxide bonds and the presence of heavy-metal oxides as glass modifiers (WO₃ in the case of TWK). In contrast, the ablation threshold of ULE glass is five times higher than tellurite glass, thanks to strong Si-O bonds and the well-connected glass network.

The final modifications are demonstrated and discussed in great detail. Let us have a look at the similarities and differences among modifications. A few common chemical modifications, such as photo-induced density change, glass decomposition, photo-darkening, ion migration, and valence state change, were observed in entire selected systems. Even though the multi-component chemistry of the complex glass system allows us to observe these modifications, the underlying reason for each differs on a great scale. For example, while the densification in ULE glass is because of the smaller ring formation and change of Si-O angle in addition to the transformation of the valence state of Ti, it is due to the rearrangement of corner-sharing and edge-sharing units in chalcogenide. In contrast, the densification is a result of the local increase of Te content in the laser-affected zone of tellurite glass.

Ion migration is also a common modification. The generation of exceptionally dense plasma with a highly localized and intense electromagnetic field can cause the movement of charged species in the glass. This movement also can be supported by the local thermal and pressure gradients. Once the laser pulse is gone, the material starts to relax, and the charge transfer among species, generation of defects, and/or structural changes lead to various modifications.

As a result, ion migration towards the laser-affected zone and valence state change of Ti were determined in ULE glass. Similarly, ion migration and valence state change of Te with W in tellurite were also observed. In addition, photo-darkening is a consequence of valence state change, crystallization, and bond cleavage of S with an increase in interchain bonds in ULE, tellurite, and chalcogenide glass, respectively.

Another common modification is glass decomposition, which led to crystallization in tellurite and ULE glass. We obtained dramatic increases in individual $\text{SbS}_{3/2}$ units, S rings, and chains upon glass composition process in Ge-Sb-S glass. However, no crystalline peaks were detected, which was correlated with very large glass-forming range of Ge-Sb-S glass systems. Note that some studies argue that the phase separation and crystallization of $\text{SbS}_{3/2}$ in chalcogenide glass due to an increase in $\text{SbS}_{3/2}$ peak in Raman spectra [385].

Observed only in ULE and tellurite, crystallization is obtained in the non-cumulative regime for both systems. Extremely high pulse energy (~ 1000 nJ) is required for the formation of β - TiO_2 nanocrystals in ULE glass. In contrast, we obtained t-Te crystals at ~ 10 nJ on the surface and 50 nJ in the tellurite glass volume. Thermodynamically speaking, tellurite glass is known to be fragile upon thermal cycles, which can easily go under glass decomposition [163]. On the tellurite glass surface, the single pulse crystallization is also identified.

Another morphological modification is periodic bubble patterns in the volume. Upon thermal cumulative effects, the periodic bubble patterns due to melting and resolidification are observed with a slight difference in each glass system. For example, the gaseous cavity of the resolidified shell is only detected in ULE glass although it has been reported for tellurite glass [200] and chalcogenide glass [347] previously.

Does self-organization occur in any glass? How do glass structure and properties influence the formation of self-organization phenomena? What are the conditions to sustain/hinder self-organized nanostructures in the volume and on the glass surface?

We observed that self-organized nanostructures on the surface of each complex glass system are achievable and highly dependent on the laser processing window. Specifically, a low threshold of tellurite and chalcogenide glass results from weak bond strength, a smaller band gap, relatively higher absorbance, and low thermomechanical stability. On one hand, surface phenomena are known to be universal regardless of material systems. On the other hand, their features, e.g., periodicity, threshold, and composition, are highly material-dependent. For example, tellurite and chalcogenide glass systems require between 1 to 10 pulses to obtain periodic self-organized nanostructures perpendicular to the laser polarization. On ULE glass, above 10 pulses are required in a non-cumulative regime.

In addition, we observed the formation of self-organized nanostructures oriented perpendicular to the laser polarization that spans beyond the focal volume in the thermal-cumulative regime of tellurite glass. Furthermore, our observations indicate a localized laser-induced metallization occurring under femtosecond laser irradiation combined with a self-organization

process. We argue that the formation of these intriguing nanostructures on the surface is through SPP propagation between the metal-dielectric interface thanks to crystallization and the effect of grain growth at the thermal cumulative regime. Moreover, we observed four different compositions of common tellurite glass systems, and we found that all compositions display crystallization and self-organization beyond the focal volume. Still, complementary work by numerical simulations is required to improve our phenomenological interpretation. Nanogratings in the thermal cumulative regime are not present for chalcogenide glass systems, while this remains an open question for ULE glass.

Furthermore, the self-organized nanostructures in the volume were only observed for ULE glass for an extensive range of parameters ($\sim 30\text{-}120\text{ J/mm}^2$) and chalcogenide glass just below the surface in a limited processing window. We did not observe volume nanogratings in tellurite glass, yet, the high refractive index of tellurite glass, resulting in non-uniform energy transfer due to spherical aberration limits further study in the volume. Therefore, nontrivial formation self-organized nanogratings in the volume remain unanswered for tellurite glass. However, one can argue that nanopores, inner structures of nanograting in silicate glass systems, consist of molecular oxygen due to glass decomposition. Since tellurite glass has low viscosity, cavitation in the nanoscale might be challenging. At the same time, high oxygen diffusivity might indeed lead to the dissolution of molecular oxygen, if it has ever generated during the process [285]

In general, self-organization requires glass decomposition, involving bond cleavage and rearrangement of the glass network. Several interplays between the chemical structure and thermodynamics of materials highlight the complexity of these modifications. Finally, we summarized the observed laser-induced modifications, self-organization, and their possible driving force in Table 6.2.

Parallel to photo-induced modifications, how can we achieve superior properties, monolithic substrates, and devices by tuning glass properties based on femtosecond laser technology?

Etching selectivity of the laser-affected zone in ULE and chalcogenide glass is accomplished by the femtosecond laser irradiation combined with chemical etching, attractive particularly for devices in optics and photonics, spectroscopic instruments, precision manufacturing, and space applications. For chalcogenide, the energy threshold for the highest etching rate is around 0.32 J/mm^2 , which results in $190\text{ }\mu\text{m/h}$, twice higher fluence leads to an exceptional etching rate of $260\text{ }\mu\text{m/h}$ in ULE glass (both irradiated with 270 fs-laser pulses emitted at 100 kHz and etched with NaOH). Additionally, with the help of crystallization, remarkable nanocomposite structures can be accomplished locally. In the case of tellurite glass, we achieved photoconductive tracks of arbitrary shapes by locally turning a tellurite glass into a functional Te/TeO₂-glass nanocomposite without adding materials and through a high-precision single process thanks to semiconducting nature of tellurium. These laser-inscribed patterns have a highly reproducible photo-response, from the near ultraviolet (263 nm) to the visible spectrum, stable over a few months.

6.3 Thesis outcome and insights for future works

Here, we review the ongoing effort and studies of femtosecond laser-induced modifications and self-organization in complex glass systems.

Complex self-organization problem at multi-scale

Experimentally, we demonstrated the volume nanogratings in some systems, such as chalcogenide and ULE glass. One can advance to a theoretical framework based on ultrafast laser physics and the observations, yet, the difficulty lies in the system-wide modeling of multi-component systems. Multiple unknown factors, multiple complex events occurring for a certain period during the irradiation, and interaction among species, make our understanding of the formation of nanogratings challenging. Still, the model covering the electromagnetic part with the hydrodynamics aspect of the process will advance our understanding.

Moreover, self-organized nanostructures on the surface are observed for all the glass systems. However, salient features are reported in tellurite glass, such as extending nanogratings beyond the focal volume. The formation of these nanostructures with surface crystallization remains an open question.

In-situ observations of the dynamics of the process

The time-resolved dynamics upon femtosecond laser irradiation remain unknown, such as glass decomposition and crystallization in tellurite and ULE glass. One way to observe dynamic events occurring during laser inscription is a time-resolved pump-probe experiment. A pump-probe experiment can provide valuable insights into the mechanisms involved in the interaction of ultrafast laser pulses with materials. By varying the time delay between the pump and probe pulses, the dynamics of the material can be studied on a femtosecond timescale.

Phase transformations, especially crystallization, can be resolved dynamically by high-energy X-ray-based techniques, such as synchrotron X-ray radiation and X-ray free electron laser (X-FEL). This technique enhances our understanding of the fundamental ionization process as well as the lattice dynamics once laser pulses are gone, such as the effect of cooling rate on the final structure. The post-mortem observation of femtosecond laser-induced crystallization of tellurite glass has been investigated in Swiss Light Source (SLS at PSI), shown in Appendix C.

Towards applications In the case of ULE glass, the remarkable localized crystallization can be used to engineer nanocomposites for future applications, including direct-write photocatalysts or solar-blind nanocomposites. Anisotropic birefringent nanogratings increase fabrication capabilities further to new devices, including Fresnel zone plates, birefringence quarter-wave plates, and beam splitters polarizers. A strong preferential etching is accomplished by the femtosecond laser irradiation combined with the etching, attractive particularly for precision manufacturing and space applications. In alignment with that, further process optimization can be realized to obtain higher aspect ratio structures as well as lower roughness upon

etching.

Numerous photo-induced modifications can help us to achieve optical and photonic devices in chalcogenide glass, such as waveguides, diffraction gratings, and micro-lenses based on direct-write photo-expansion or photo-contraction processes. An etching selectivity by the femtosecond laser-irradiated zone in chalcogenide glass further promotes the scale of production of new micromechanical or optomechanical components. Likewise, a better understanding of the chemistry of the chalcogenide systems is necessary for high-quality optical parts. This may involve the preparation of modification-specific chemical solutions or a multi-step approach to achieve high etching selectivity and optical quality.

At last, localized crystallization of tellurite glass can be used to engineer Te/TeO₂ nanocomposites, which is attractive not only for UV-VIS photo-detection but also for various applications, such as ultrahigh chemical sensitivity for gas detection or solar-blind nanocomposites. Further optimization is required to increase the lifetime of the Te/TeO₂ nanocomposite for UV photodetection. One can also realize various design configurations specific to desired applications. In addition, densification in the volume expands the possibilities further for fabricating optical microcomponents made of tellurite glass.

Table 6.2: The observed laser-induced modifications of the complex glass system: ULE, tellurite, and chalcogenide glass families. Y refers to "yes" as it is an observed modification, N refers to "no", and U is used for "unknown".

Photo-induced modification	ULE	TeO ₂	ChG	The formation mechanism
Photo-contraction and densification	Y	Y	Y	Compact glass network formation through a smaller bond angle or corner sharing species
Photo-expansion and porosification	U	Y	Y	Defects in molecular level causing loosening the glass network
Self-organized volume nanogratings	Y	U	Y	Possibly by local field enhancement and through self-organization
Self-organization on the surface	Y	Y	Y	Possibly by local field enhancement and through self-organization
Self-organization beyond the focal volume	U	Y	N	Possibly by local field enhancement and propagation of SPP through metal-glass interface
Nanopores with tapped gas	Y	U	U	Glass decomposition formation of gaseous species
Periodic bubble patterns	Y	Y	Y	Melting and resolidification in thermal cumulative regime
Ablation of the surface	Y	Y	Y	melting, vaporization and material ejection
Valence state change	Y	Y	U	Charge transfer upon high intense electric field
Photo-induced darkening	Y	Y	Y	The formation of defects and/or structural changes
Photo-induced oxidation	U	Y	Y	Reaction with environment
Ion migration	Y	Y	Y	Polarization under high electric field intensity and charge balance of species
Glass decomposition	Y	Y	Y	Bond cleavage of the main network
Crystallization	Y	Y	U	Glass decomposition or reduction reaction among species
Etching selectivity in the volume	Y	N	Y	Solubility of certain structures and defects

A Experimental details

A.1 Femtosecond laser parameters

In this thesis, the main variables are pulse duration, pulse energy, repetition rate, and writing speed to obtain various deposited energies. The effective number of pulses is calculated as

$$M = \omega \left(\frac{f}{v} \right) \quad (\text{A.1})$$

Accordingly, the deposited energy per unit surface (or ‘net fluence’) on the specimen can be approximated by

$$E_{\text{deposited}} = \frac{4E_p}{\pi\omega} \left(\frac{f}{v} \right) \quad (\text{A.2})$$

where E_p is the pulse energy, ω is the optical beam waist (defined at $1/e^2$), f is the laser repetition rate and v is the writing speed as described in Ref. [453]. This deposited energy is a dose of how much energy per unit surface is passing through the material but does not indicate how much of this energy is effectively absorbed. However, it remains a convenient and simple metric for comparing and reproducing experimental exposure conditions.

A.2 Laser spot diameter measurement

The focal spot size on the surface was first predicted based on the Zemax file provided by the manufacturer, and then, the non-linear affected zone was measured directly using SEM. This measurement is done in the non-cumulative regime, to make sure that only optical effects are accounted for. Additionally, the focal spot was measured with a commercial beam profiler.

According to Thorlabs’s datasheet and Zemax file, the predicted optical spot-diameter at $1/e^2$ at a wavelength of 1030 nm is 1.79 μm (and 1.85 μm at 1064 nm). We carefully measured the beam diameter with a beam profiler at the entrance pupil, so that it effectively fills up the aperture (effective diameter at $1/e^2$ is 7.92 mm). Even if would assume an improper aperture

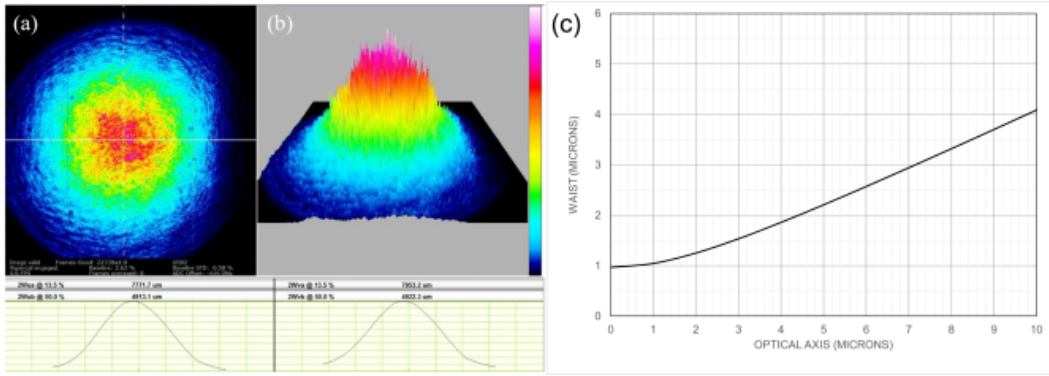


Figure A.1: Beam diameter at the entrance pupil. Results are obtained by beam profiler and DataRay software. a-b) The displayed profiles of the beam and c-d) the line profiles along the crosshairs at 13.5%. u and v notations are the orientation of the crosshairs. e) Beam waist vs. z-axis from the experimental result. c) Beam waist at the entrance pupil of the objective, beam waist, and diameter at focus at a given wavelength. Results were obtained in Zemax Optic Studio with the objective (LMH-20X-1064 from Thorlabs) used in our experiments. M^2 value is taken as 1.2.

Wavelength (nm)	Entrance pupil beam diameter (mm)	Beam diameter at focus (μm)
1030	8	1.79
1030	7	2.05
1030	6	2.39

filling (like for instance 7 mm, which is not the case here), the beam diameter at the spot would degrade to $2 \mu\text{m}$. In Table S1, we show various simulation results with Thorlabs Zemax file for the specific objective we used, for various aperture filling and with a conservative laser parameter (M^2 value of 1.2).

To do the additional measurement, we used a commercial beam profiler (WinCamD-LCM-1" CMOS Beam profiler from DataRay) that we translated at a fixed distance from the objective with high-precision positioning stages (with a resolution of $\pm 0.25 \mu\text{m}$, repeatability of $\pm 0.5 \mu\text{m}$, PI Micos, Ultra-HR). As the minimum spot size that can be detected by the beam profiler is $\sim 55 \mu\text{m}$, and in order not to damage the sensor, we extracted a profile of the Gaussian envelop while translating the sensor toward the focusing spot and after the focusing spot (with $100 \mu\text{m}$ -steps). We then used these points to match with the Gaussian envelop (taking into account the M^2 value of the laser) that we compared to the Zemax simulation based on the manufacturer parameters and the measured beam profile at the entrance pupil. Once the Gaussian envelop along the beam path after the objective is known, we extrapolate the exact value at the spot. This yields a value of about $1.94 \pm 0.2 \mu\text{m}$, which is, in fair agreement (within experimental errors) with the Zemax simulation based on the data provided by the manufacturer ($1.79 \mu\text{m}$).

We used third-harmonics to find the surface accurately that we are back with the expected

spot location (based on the Gaussian envelop with the actual measured data) and that we further confirmed with SEM measurements of the actual modified zones. The accuracy of the z-positioning is confirmed in Appendix C. The pulse energy is gradually increased. At low pulse energy, the affected is slightly smaller than the theoretical spot size (which is to be expected due to the non-linear absorption effect) and shows that the beam is effectively at the focal spot and the minimal waist along the z-axis. For the same z position, the laser-affected zones become much wider than the optical waist, which demonstrates the points that self-organization expands beyond the zone where the waist is minimum.

A.3 Time-dependent temperature distribution model

The time-dependent temperature distribution model is calculated in a commercial finite element analysis software (COMSOL Multiphysics) based on thermal diffusion [136].

$$\frac{\partial T(t, x, y, z)}{\partial t} = \nabla(D\nabla T(t, x, y, z)) + \left(\frac{1}{\rho c_p}\right) + \left(\frac{\partial Q(t, x, y, z)}{\partial t}\right) \quad (\text{A.3})$$

where T is the temperature, t is the time after laser exposure, D is the thermal diffusion coefficient, ρ is the mass density, c_p is the specific heat capacity, Q is the generated heat density calculated from the absorbed laser power density. The initial conditions are in open-air under normal atmospheric pressure with the ambient temperature set at 293.15 K. The more accurate calculation of temperature distribution, such as via the two-temperature model (TTM) is time-consuming, and complicated since most of the parameters are unknown for our custom-made glass specimens. The energy losses come mainly from heat conduction, convection, and thermal radiation, calculated by setting the boundary conditions in COMSOL Multiphysics.

Table A.1: The physical properties of ULE®Glass, tellurite, and chalcogenide glass used in thermal model [106, 107, 163, 165]. Material parameters used for time-dependent temperature distribution of focal volume calculated by thermal diffusion in COMSOL Multiphysics. The heat capacity values were from [163] between 455 K and 650 K for TWK glass. The properties of ULE glass were taken from the materials library in COMSOL Multiphysics. Other properties are assumed constant with the temperature due to a lack of information and in a first-order approximation.

Sample	ρ	$k(\text{W/m}\cdot\text{K})$	CTE (1/K)	C_p (J/kg·K)	Absorbance
ULE 7972	2.21	1.31	0	767	0.05
TWK	5.31	0.8	$18.5 \cdot 10^{-6}$	460	0.3
$\text{Ge}_{23}\text{Sb}_7\text{S}_{70}$	2.95	0.2509	$11 \cdot 10^{-6}$	422	0.35

B ULE®Glass

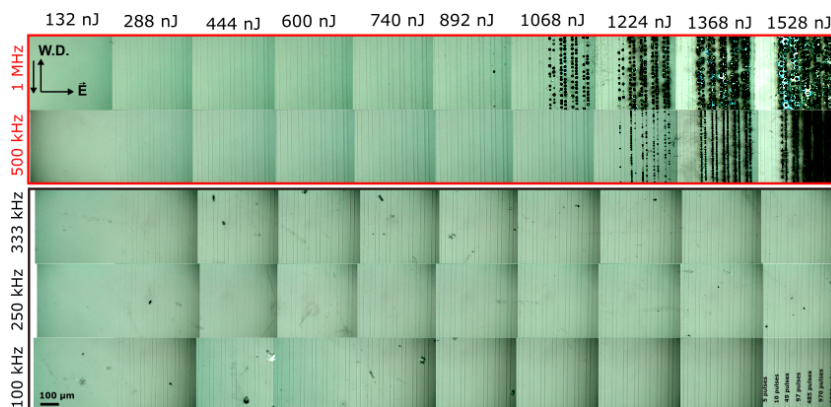


Figure B.1: OM images of laser-written tracks in ULE glass for different repetition rates spanning from non-cumulative to the thermal cumulative regime at 270 fs.

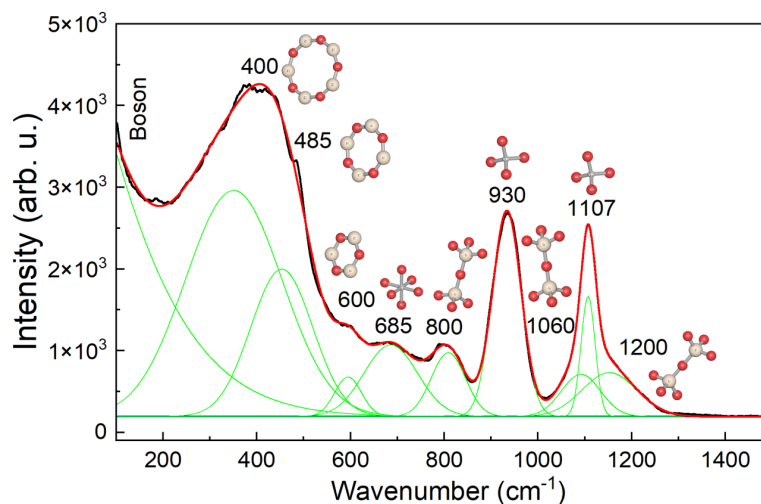


Figure B.2: Deconvoluted Raman spectra of the pristine ULE glass. Green bands are fitted peaks, the red line is overall spectra and the black line is experimental data.

Table B.1: Peak assignments of Raman spectra of the center of laser modified lines of ULE glass [54, 108, 132–134]

Wavenumber (cm ⁻¹)	Assignment
153	E _g band of β -TiO ₂
203	Ti ₂ O ₃ clusters or crystals related band
198	E _g band of β -TiO ₂
398	B _{1g} mode of β -TiO ₂
400	The symmetric stretching-bending vibration of Si-O-Si bridges in five to eight-membered rings of SiO ₄ tetrahedra
485	The symmetric oxygen ring breathing vibrations of four-membered silicate rings (D ₁ peak)
515	The doublet of A _{1g} and B _{1g} modes of β -TiO ₂
600	The symmetric oxygen ring breathing vibrations of three-membered silicate rings (D ₂ peak)
640	E _g band of β -TiO ₂
685	TiO ₆ symmetric stretching
796	The overtone of B _{1g} mode of β -TiO ₂
800	Si-O-Si bending modes
930	TiO ₄ asymmetric stretching
1060	Asymmetric stretching modes of Si-O-Si bridges
1107	The symmetric stretching of TiO ₄
1200	Asymmetric stretching modes of Si-O-Si bridges
1554	The stretching vibration of molecular oxygen

C Tellurite glass

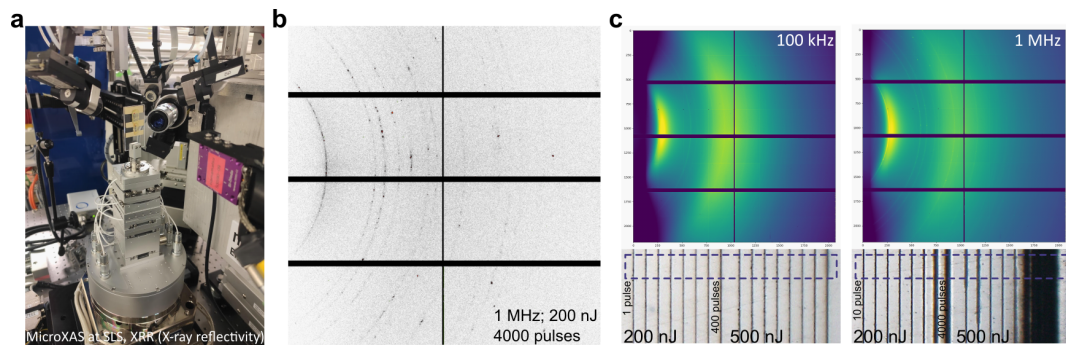


Figure C.1: a) Experimental setup in XRR mode (the sample was tilted 15 degrees) b) 1 MHz 500 nJ, c) 100 kHz vs d) 1 MHz. The experiment was performed in the MicroXAS beamline at PSI. The beam size is $1 \mu\text{m} \times 1 \mu\text{m}$. The photon energy was 12 keV. Eiger 4M detector was used with a collection time of 0.2 s.

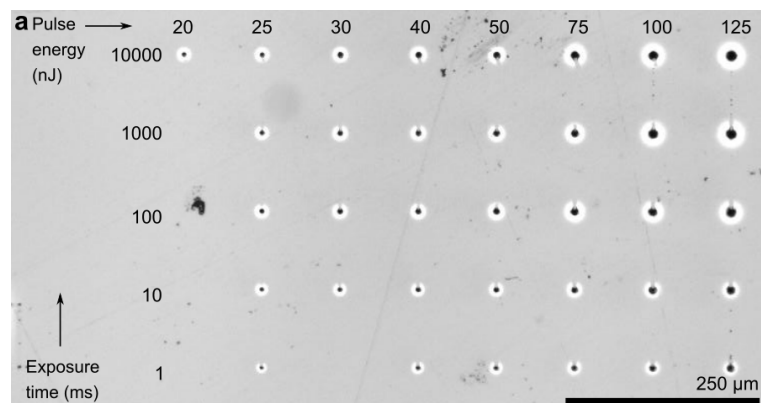


Figure C.2: OM image of the laser-affected zone after irradiating in the thermal accumulated regime of TWK at 1 MHz in static exposure conditions.

Table C.1: Peak assignments of Raman spectra of the center of laser modified lines of TAW [454], TZNB [147], TNGPZ [147], TWK [163]

Assignments	TAW	TZNB	TNGPZ	TWK
Symmetric stretching vibrations of crystalline Te (A_1 mode)	122	118	118	119
Doubly degenerated vibration modes of crystalline Te (E_{TO} mode)	146	138	138	139
Te-Te homopolar bonds in amorphous Te	180	179	179	170
β -TeO ₂ crystal	-	185	-	-
Doubly degenerated vibration modes of crystalline Te (E_{TO} mode)	-	220	220	220
β -TeO ₂ crystal	238	235	235	-
Second-order E vibrational mode of crystalline Te	-	260	260	260
Bending vibrations of W-O-W in WO ₆ octahedra	349	-	-	350
Symmetrical stretching vibration of Te-O-Te linkages	475	450	450	490
Vibration mode of continuous network composed of TeO ₄ trigonal bipyramid (tbp)	614	610	610	610
Antisymmetric vibration mode of Te-O-Te linkages constructed by two inequivalent Te-O bonds	665	660	660	670
Stretching vibrations between Te and non-bridging oxygen (NBO) of TeO ₃₊₁ (distorted tbp) polyhedra and TeO ₃ trigonal pyramid (tp)	723	715	715	720
Te-O- stretching vibrations of TeO ₃₊₁ polyhedra	778	775	770	790
W-O stretching vibration of both WO ₄ and WO ₆	832	-	-	860
Distorted NbO ₆ octahedra	-	-	875	-
Stretching vibration of the W-O- and W=O terminal bonds associated with WO ₄ and WO ₆ polyhedra	890	-	-	920

Table C.2: The tabular data of interplanar distances of the laser-affected zone compared with the bulk t-Te after a few pulse exposure of TWK glass at 1 kHz.

Interplanar distances (nm)	Bulk t-Te	Nanocrystals in the substrate after single laser shot	Nanoparticles after single laser shot	Nanocrystals in the substrate after two laser shot
(100)(010)	0.385	0.39	0.39	0.38
(101)(011)	0.3227	0.32	0.33	0.32
(102)(012)	0.2345	0.23	0.24	0.23
(200)	0.1925	-	-	0.19
(001)	0.5915	-	-	0.59
(002)	0.2957	-	-	0.29
(003)	0.1971	-	-	0.19

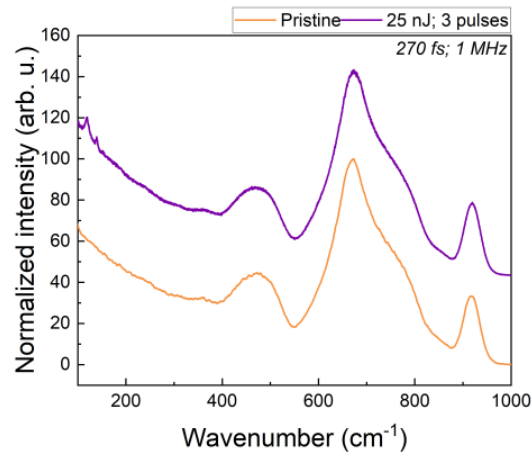


Figure C.3: Raman spectra of the laser-affected zone on TWK glass substrate, which was cooled with liquid nitrogen (77 K) in a chamber. The open-air atmosphere was utilized in the chamber.

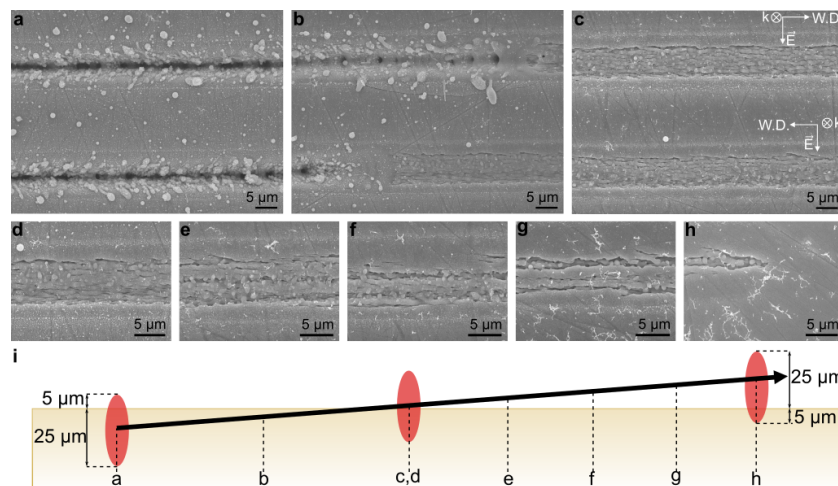


Figure C.4: SE images 200 nJ, 0.5 mm/s (262 J/mm^2). Colored values indicate the average composition along the scanned line. Dashed lines indicate the composition of pristine glass. All images correspond to a transverse polarization (with respect to the writing direction) and 1 MHz pulse repetition rate.

Table C.3: The tabular data of interplanar distances of the laser-affected zone compared with the bulk t-Te after exposure of TWK glass in the thermal cumulative regime at 1 MHz.

Interplanar distances (nm)	Bulk t-Te	Ejected nanoparticles
(001)	0.5915	0.59
(100)	0.385	0.38
(101)	0.3227	0.32
(102)	0.2345	0.23
(013)	0.1755	-

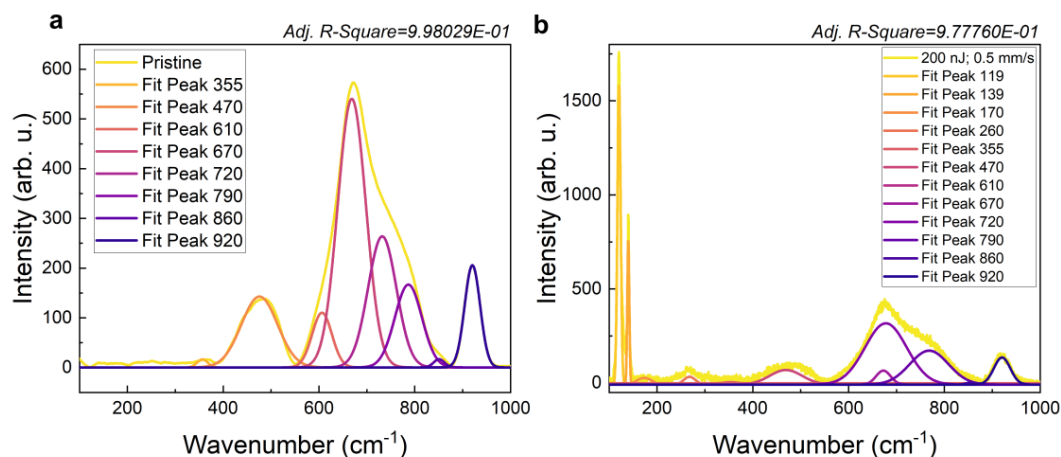


Figure C.5: Deconvolution of the Raman spectra of (a) the pristine material of TWK and (b) the laser-affected zone at 1 MHz (incoming pulse fluence: 262 J/mm²) in Figure 3.10.

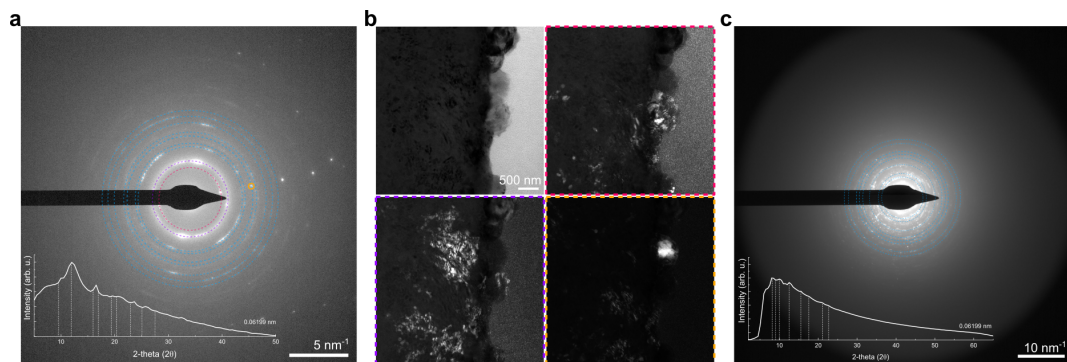


Figure C.6: SAED patterns of the laser-affected zone in TWK at 1 MHz and their corresponding XRD patterns, calculated by a computer program (EDP2XRD) [455]. The dashed lines in XRD indicate the highlighted ring patterns on SAED. a) SAED pattern of laser-affected zone shown in Figure 3.12.c, b) enlarged bright field (BF) TEM image of Figure 3.12.c and dark-field (DF) TEM images. The bright area in DF images is corresponding to the 1st ring, 2nd ring, and the diffraction spot indicated with colored circles in a). c) SAED pattern of laser-affected zone shown in Figure 3.12.e.

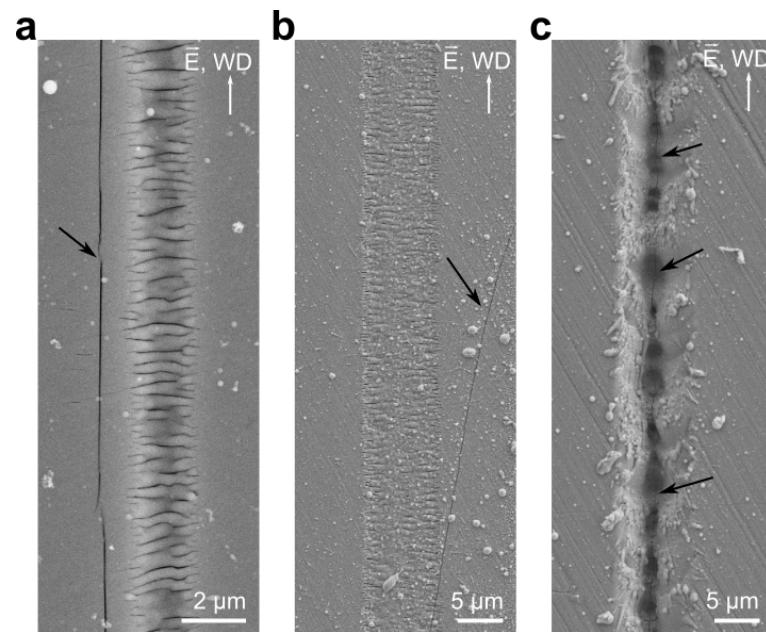


Figure C.7: SE images of cracks at and around the laser-affected zone of TWK glass with various pulse energies: a) 25 nJ, b) 200 nJ, and c) 500 nJ with 4000 pulses at 1 MHz.

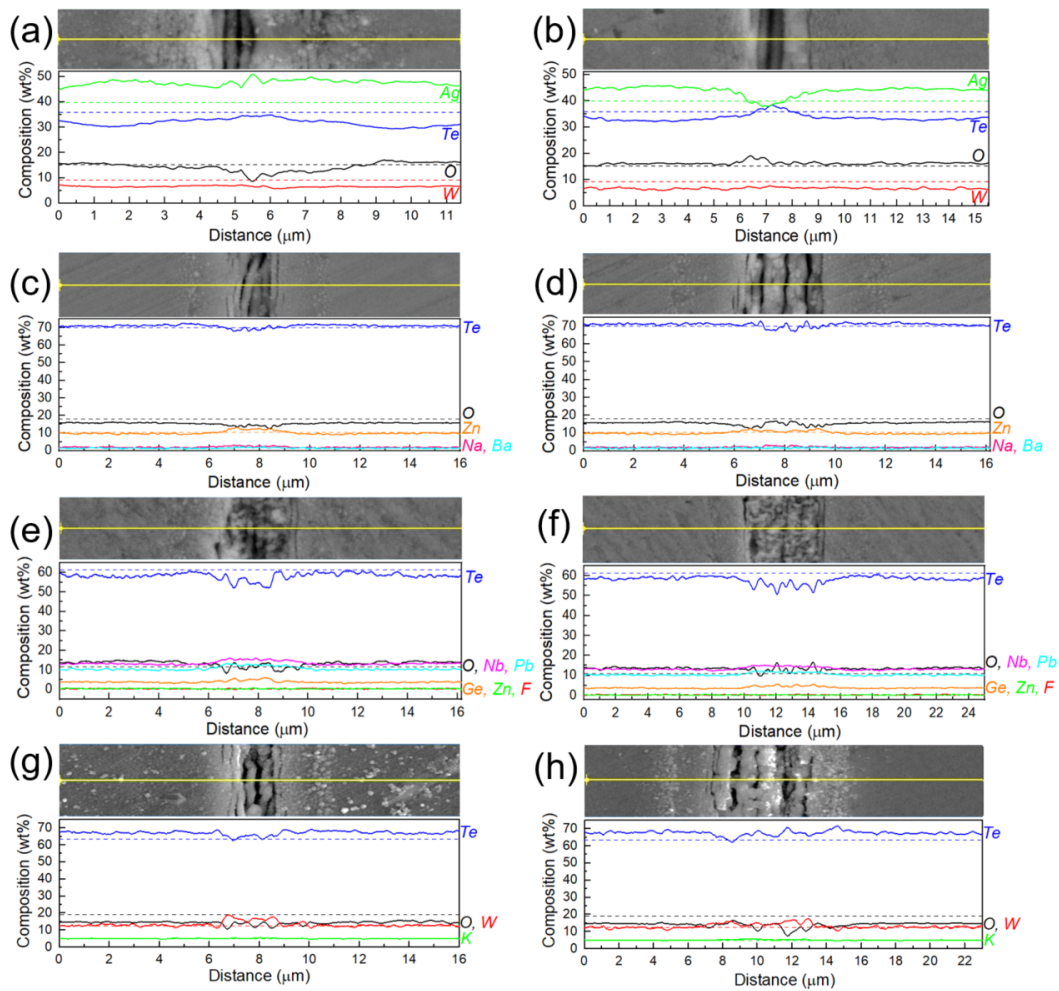


Figure C.8: SE images and elemental analysis determined by EDS along the laser-affected zone (line scans in yellow) of all the compositions. a-b) TWA, c-d) TZNB, e-f) TNGPZ and g-h) TWK. The pulse energy in a,c,e,g) is 25 nJ, and in b,d,f,h) 50 nJ at a fixed effective number of pulses (4000 pulses) at 1 MHz.

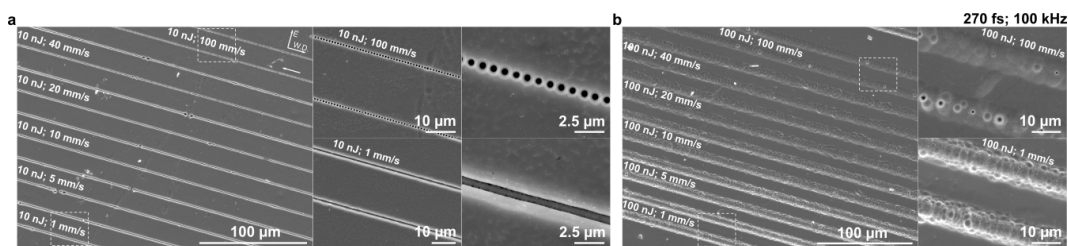


Figure C.9: SE images of the tellurite glass surface after etching with NaOH for 30 seconds. 270 fs laser pulses were used to inscribe lines at 100 kHz with a) 25 nJ and b) at 100 nJ.

D Chalcogenide glass

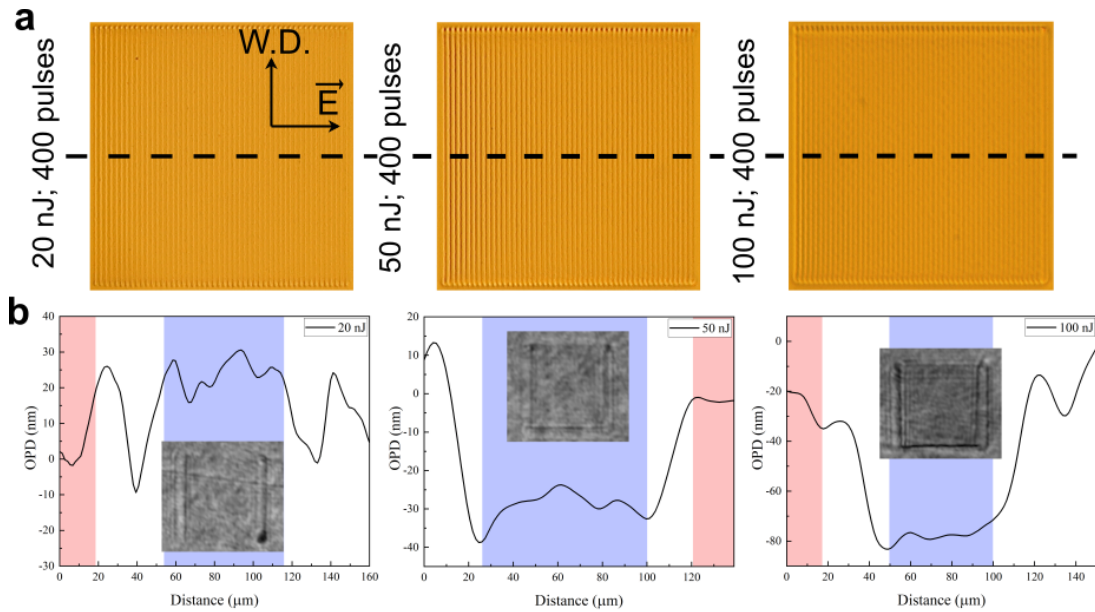


Figure D.1: a) Transmission optical microscope images of $1 \times 1 \text{ mm}^2$ laser-affected areas obtained at a pulse rate of 100 kHz with 400 overlapping pulses. b) Optical path difference across the laser-modified area (insets: digital holographic microscope images of the area). The average optical path differences are calculated from the red and blue areas. Red areas are considered pristine material, while blue areas are considered laser-modified zones.

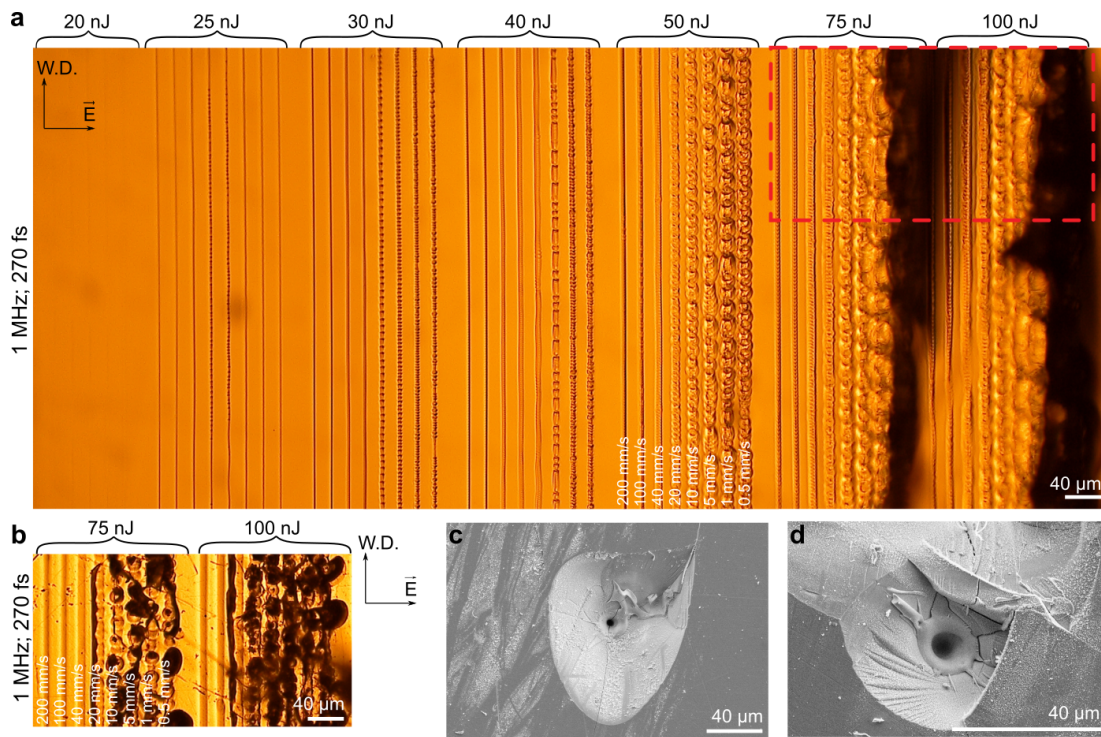


Figure D.2: a-b) Transmission OM images of laser-inscribed lines in $\text{Ge}_{23}\text{Sb}_7\text{S}_{70}$ glass volume at 1 MHz (thermal cumulative regime) with various writing speeds and pulse energies. c-d) SE images of the top surface of laser-inscribed lines at 75 nJ with 4000 pulses. Note that the focal spot was located at $20\ \mu\text{m}$ below the surface.

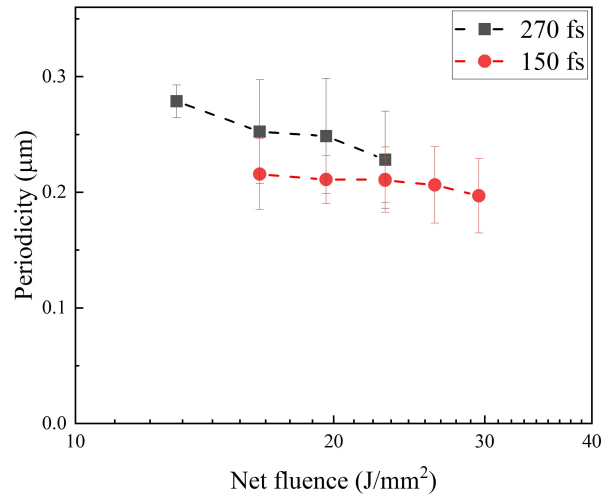


Figure D.3: Volume nanogratings periodicity of $\text{Ge}_{23}\text{Sb}_7\text{S}_{70}$ as a function of laser net fluence for a pulse duration of 150 and 270 fs emitted at a rate of 100 kHz.

Table D.1: Literature survey of the periodicity of self-organized structures on the surface of the chalcogenide glass.

Glass composition	τ (fs)	λ (nm)	Periodicity (nm) (number of pulses)
As ₂ S ₃ [350]	150	800	700 (2-5) and 250 (>10)
As ₂ S ₃ [351]	150	800	740 to 780 (overlapping of 65%-80%) and 300
As ₂ S ₃ [349]	100	800	(2) to 180 (10)
As ₂ S ₃ [323]	34	806	180 with 720 (10)
As ₂ S ₃ [353]	150	3000	599 (1000)
As ₂ Se ₃ [353]	150	3000	583 (1000)
Ge ₂₅ Ga ₁ As ₉ S ₆₅ [352]	34	806	720 (50)
Ge ₂₃ Sb ₇ S ₇₀ [This study]	150	1030	210 (5) and 170 (400)
Ge ₂₃ Sb ₇ S ₇₀ [This study]	270	1030	330 (1), 250 (5) and 170 (400)

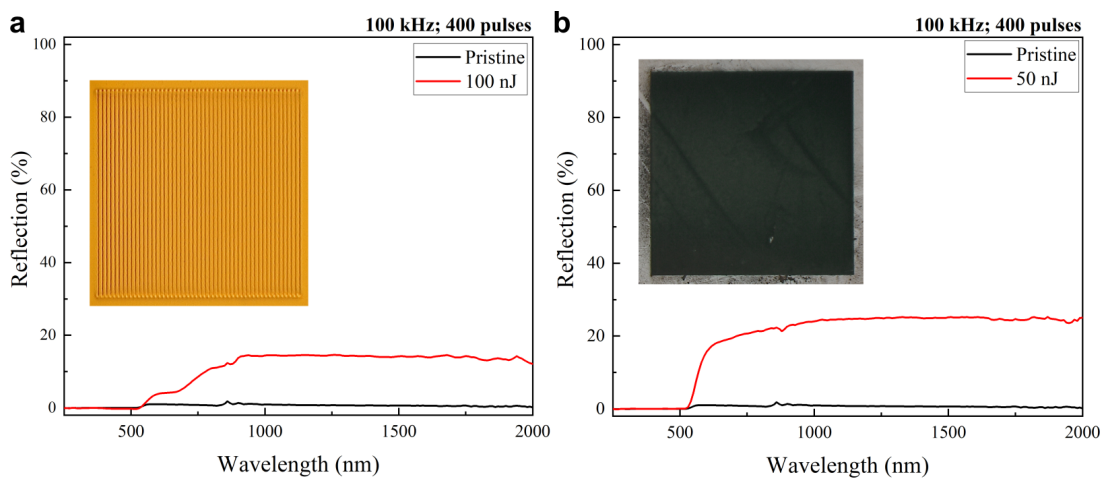


Figure D.4: Reflection spectra of laser-affected zones a) in the volume and b) on the surface. The inset shows a reflective optical micrograph of a single plane ($1 \times 1 \text{ mm}^2$) formed with parallel lines, themselves made of overlapping pulses with 100 nJ pulse energy. Note that the peaks around 800 nm are measurement artifacts due to the change of detector types from visible to NIR measuring spectral ranges.

Table D.2: Raman bond assignments of investigated chalcogenide glass systems used in this study.

Wavenumber (cm ⁻¹)	Raman bond assignment with references
150-154, 215	S-S bridge bonds or S chain [302, 332]
190	Sb-Se bond vibrations in the SbSe _{3/2} pyramids [380]
200	A ₁ mode of the corner-sharing GeSe _{4/2} tetrahedra [380]
215	The vibration mode of the edge-sharing Ge ₂ Se _{8/2} bi-tetrahedra [380, 386]
240	The vibration mode of S ₃ Ge-GeS ₃ unit [332]
250	A ₁ modes of vibration of Se rings [380]
263	A ₁ modes of vibration of Se chains [380]
300	Se-Se in chains along with Ge-Se-Ge bonds [386]
302	E modes of SbS _{3/2} pyramids [302]
309	E modes of AsS _{3/2} pyramids [380, 456]
330	A ₁ mode of corner-sharing GeS _{4/2} tetrahedra and AsS _{3/2} pyramids [380, 456]
340	A ₁ mode of isolated GeS ₄ tetrahedra [302, 332, 380, 456]
344	Symmetric stretching modes of AsS _{3/2} pyramids [328, 456]
368	T ₂ mode of two edge-sharing Ge ₂ S ₄ S _{2/2} [302, 332, 380, 456]
400-402	T ₂ mode of corner-sharing GeS _{4/2} tetrahedra [380, 456]
422-427	Vibrations of S ₃ Ge-S-GeS ₃ unit [380, 456]
475	A ₁ mode of S ₈ ring [456]
485-487	A ₁ mode of S chain [456]

E Device fabrication and applications

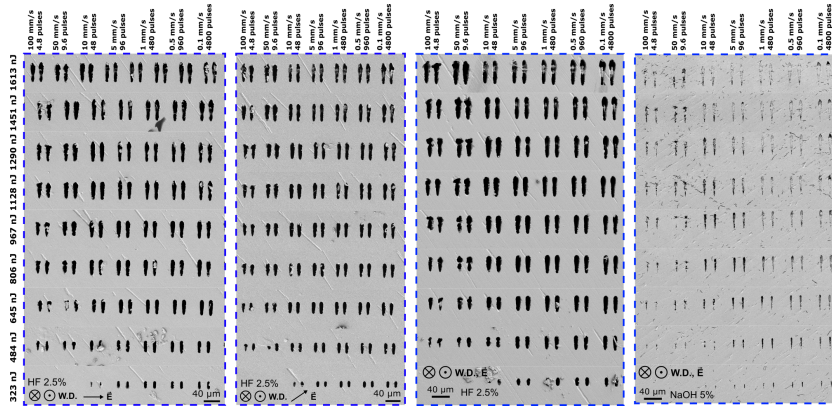


Figure E.1: SE images of cross-sections of the laser-affected zones with different polarization conditions after 3 hours of etching with HF and NaOH solutions. The irradiation parameters are 240 kHz at 500 fs.

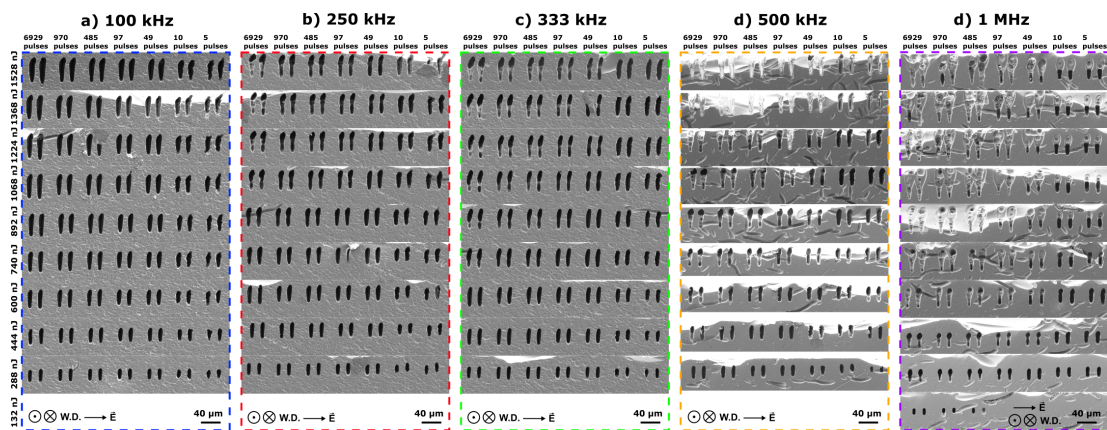


Figure E.2: SE images of cross-sections of the laser-affected zones with different repetition rates after 3 hours of etching with HF solution at 270 fs. a) 100 kHz, b) 250 kHz, c) 333 kHz, d) 500 kHz and e) 1 MHz.

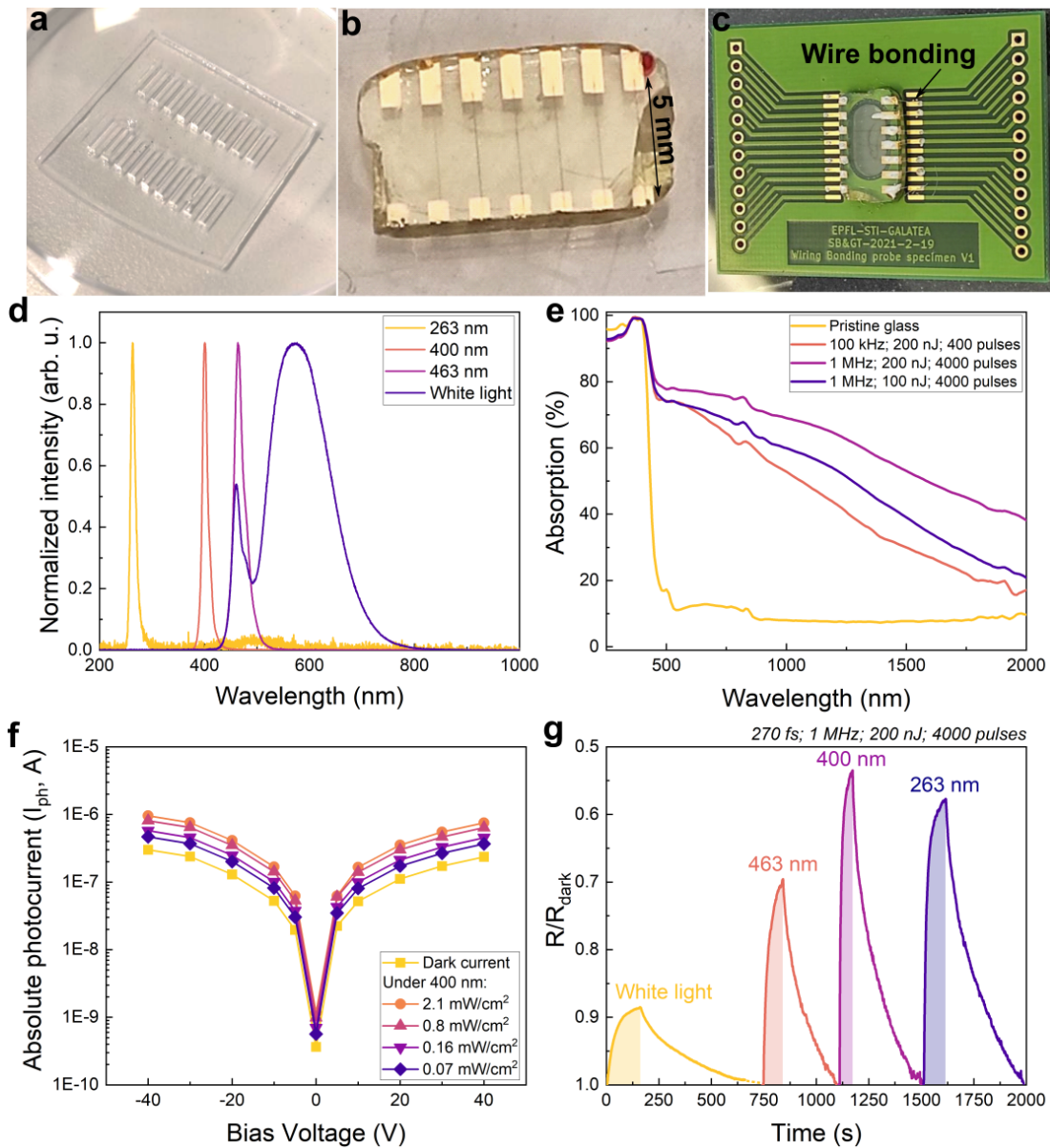


Figure E.3: a) Fused silica mask fabricated by femtosecond laser micromachining combined with chemical etching. b) Tellurite glass surface after femtosecond laser inscription and deposition of gold electrodes before the measurement and c) the image of the final device. d) LED spectra used in this study. e) Absorption spectra of the femtosecond laser writing on the tellurite glass surface. f) The semi-log absolute photocurrent versus bias voltage ($I-V$) curve without and with the illumination of 400 nm. g) The spatiotemporal spectra of on-off curves for different wavelengths.

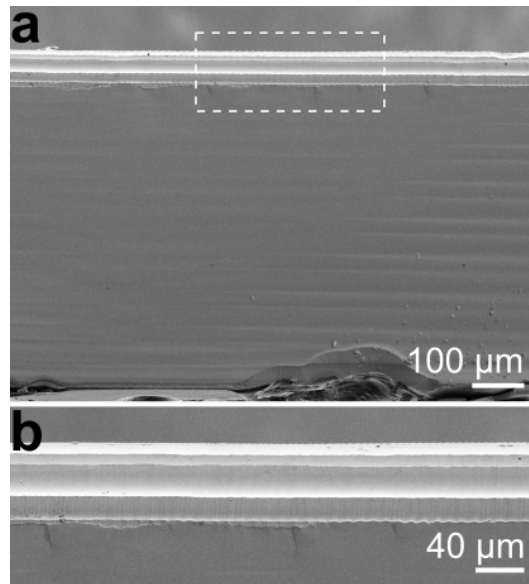


Figure E.4: a-b) SE images of a glass cutting scanned by the laser along the z-direction of the $\text{Ge}_{23}\text{Sb}_7\text{S}_{70}$ glass. After scanning with 100 nJ with 6.56 J/mm^2 at 100 kHz along the z-direction, the glass is etched for about 14 hr with NaOH. After obtaining two separate pieces, they are etched with HF for about 2 hrs to remove the coating.

Bibliography

- [1] Y. Shimotsuma, P. G. Kazansky, J. Qiu, and K. Hirao, "Self-organized nanogratings in glass irradiated by ultrashort light pulses," *Physical Review Letters*, vol. 91, p. 247 405, 24 2003. DOI: 10.1103/PhysRevLett.91.247405.
- [2] D. Tan, K. N. Sharafudeen, Y. Yue, and J. Qiu, "Femtosecond laser induced phenomena in transparent solid materials: fundamentals and applications," *Progress in Materials Science*, vol. 76, pp. 154–228, 2016. DOI: <https://doi.org/10.1016/j.pmatsci.2015.09.002>.
- [3] S. K. Sundaram, "First glass: formation of silicate in the early universe," *American Ceramic Society Bulletin*, vol. 101, no. 6, pp. 26–29, 2022. [Online]. Available: <https://ceramics.org/wp-content/bulletin/2022/pdf/August-2022.pdf>.
- [4] E. D. Zanotto and J. C. Mauro, "The glassy state of matter: Its definition and ultimate fate," *Journal of Non-Crystalline Solids*, vol. 471, pp. 490–495, 2017. DOI: <https://doi.org/10.1016/j.jnoncrysol.2017.05.019>.
- [5] P. K. Gupta, "Non-crystalline solids: glasses and amorphous solids," *Journal of Non-Crystalline Solids*, vol. 195, no. 1, pp. 158–164, 1996. DOI: [https://doi.org/10.1016/0022-3093\(95\)00502-1](https://doi.org/10.1016/0022-3093(95)00502-1).
- [6] R. Doremus, *Glass Science*. Wiley, 1973. [Online]. Available: <https://books.google.ch/books?id=18dTAAAAMAAJ>.
- [7] E. Mazur and R. Gattass, "Femtosecond laser micromachining in transparent materials," *Nature Photonics*, vol. 2, no. 4, pp. 219–225, 2008. DOI: 10.1038/nphoton.2008.48.
- [8] C. B. Schaffer, A. Brodeur, and E. Mazur, "Laser-induced breakdown and damage in bulk transparent materials induced by tightly focused femtosecond laser pulses," *Measurement Science and Technology*, vol. 12, no. 11, pp. 1784–1794, 2001. DOI: 10.1088/0957-0233/12/11/305.
- [9] L. V. Keldysh, "Ionization in the field of a strong electromagnetic wave," *Soviet Physics JETP*, vol. 20, p. 1307, 1965.
- [10] S. K. Sundaram and E. Mazur, "Inducing and probing non-thermal transitions in semiconductors using femtosecond laser pulses," *Nature Materials*, vol. 1, pp. 217–224, 2002. DOI: [doi:10.1038/nmat767](https://doi.org/10.1038/nmat767).

- [11] P. Stampfli and K. H. Bennemann, "Time dependence of the laser-induced femtosecond lattice instability of Si and GaAs: Role of longitudinal optical distortions," *Physical Review B*, vol. 49, pp. 7299–7305, 11 1994. DOI: 10.1103/PhysRevB.49.7299.
- [12] M. Beresna, M. Gecevicius, and P. G. Kazansky, "Ultrafast laser direct writing and nanostructuring in transparent materials," *Advances in Optics and Photonics*, vol. 6, no. 3, pp. 293–339, 2014. DOI: 10.1364/AOP.6.000293.
- [13] Amina, L. Ji, M. Uzair, and T. Yan, "Structural modifications induced by ultrafast IR laser pulses in sapphire," in *9th International Symposium on Advanced Optical Manufacturing and Testing Technologies: Subdiffraction-limited Plasmonic Lithography and Innovative Manufacturing Technology*, vol. 10842, SPIE, 2019, pp. 100–112. DOI: 10.1117/12.2506379.
- [14] K. M. Davis, K. Miura, N. Sugimoto, and K. Hirao, "Writing waveguides in glass with a femtosecond laser," *Optics Letters*, vol. 21, no. 21, pp. 1729–1731, 1996. DOI: 10.1364/OL.21.001729.
- [15] J. Chan, T. Huser, S. Risbud, and D. Krol, "Structural changes in fused silica after exposure to focused femtosecond laser pulses," *Optics Letters*, vol. 26, pp. 1726–8, 2001. DOI: 10.1364/OL.26.001726.
- [16] Y. Bellouard *et al.*, "Stress-state manipulation in fused silica via femtosecond laser irradiation," *Optica*, vol. 3, p. 1285, 2016. DOI: 10.1364/OPTICA.3.001285.
- [17] C. Hnatovsky *et al.*, "Pulse duration dependence of femtosecond-laser-fabricated nanogratings in fused silica," *Applied Physics Letters*, vol. 87, no. 1, p. 014 104, 2005. DOI: 10.1063/1.1991991.
- [18] J. W. Chan, T. R. Huser, S. H. Risbud, J. S. Hayden, and D. M. Krol, "Waveguide fabrication in phosphate glasses using femtosecond laser pulses," *Applied Physics Letters*, vol. 82, no. 15, pp. 2371–2373, 2003. DOI: 10.1063/1.1565708.
- [19] P. Delullier *et al.*, "Photosensitivity of infrared glasses under femtosecond laser direct writing for mid-IR applications," *Applied Sciences*, vol. 12, no. 17, 2022. DOI: 10.3390/app12178813.
- [20] R. Taylor, C. Hnatovsky, and E. Simova, "Applications of femtosecond laser induced self-organized planar nanocracks inside fused silica glass," *Laser & Photonics Reviews*, vol. 2, no. 1-2, pp. 26–46, 2008. DOI: <https://doi.org/10.1002/lpor.200710031>.
- [21] C. Hnatovsky, E. Simova, R. Pattathil, D. Rayner, P. Corkum, and R. Taylor, "Femtosecond laser writing of porous capillaries inside fused silica glass," *Optics letters*, vol. 32, pp. 1459–61, 2007. DOI: 10.1364/OL.32.001459.
- [22] Y. Bellouard and M.-O. Hongler, "Femtosecond-laser generation of self-organized bubble patterns in fused silica," *Optics Express*, vol. 19, no. 7, pp. 6807–6821, 2011. DOI: 10.1364/OE.19.006807.

- [23] J. W. Chan, T. Huser, J. S. Hayden, S. H. Risbud, and D. M. Krol, "Fluorescence spectroscopy of color centers generated in phosphate glasses after exposure to femtosecond laser pulses," *Journal of the American Ceramic Society*, vol. 85, no. 5, pp. 1037–1040, 2002. DOI: <https://doi.org/10.1111/j.1151-2916.2002.tb00219.x>.
- [24] S. Kanehira, K. Miura, and K. Hirao, "Ion exchange in glass using femtosecond laser irradiation," *Applied Physics Letters*, vol. 93, no. 2, p. 023 112, 2008. DOI: 10.1063/1.2959820.
- [25] T. Fernandez *et al.*, "Bespoke photonic devices using ultrafast laser driven ion migration in glasses," *Progress in Materials Science*, vol. 94, pp. 68–113, 2018. DOI: <https://doi.org/10.1016/j.pmatsci.2017.12.002>.
- [26] J. Qiu *et al.*, "Space-selective valence state manipulation of transition metal ions inside glasses by a femtosecond laser," *Applied Physics Letters*, vol. 79, no. 22, pp. 3567–3569, 2001. DOI: 10.1063/1.1421640.
- [27] Y. Kondo, T. Suzuki, H. Inouye, K. Miura, T. Mitsuyu, and K. Hirao, "Three-dimensional microscopic crystallization in photosensitive glass by femtosecond laser pulses at nonresonant wavelength," *Japanese Journal of Applied Physics*, vol. 37, no. 1A, p. L94, 1998. DOI: 10.1143/JJAP37.L94.
- [28] Y. Kondo, K. Miura, T. Suzuki, H. Inouye, T. Mitsuyu, and K. Hirao, "Three-dimensional arrays of crystallites within glass by using non-resonant femtosecond pulses," *Journal of Non-Crystalline Solids*, vol. 253, no. 1, pp. 143–156, 1999. DOI: [https://doi.org/10.1016/S0022-3093\(99\)00410-X](https://doi.org/10.1016/S0022-3093(99)00410-X).
- [29] J. Cao, M. Lancry, F. Brisset, L. Mazerolles, R. Saint-Martin, and B. Poumellec, "Femtosecond laser-induced crystallization in glasses: Growth dynamics for orientable nanostructure and nanocrystallization," *Crystal Growth & Design*, vol. 19, no. 4, pp. 2189–2205, 2019. DOI: 10.1021/acs.cgd.8b01802.
- [30] K. Miura, J. Qiu, T. Mitsuyu, and K. Hirao, "Space-selective growth of frequency-conversion crystals in glasses with ultrashort infrared laser pulses," *Optics Letters*, vol. 25, no. 6, pp. 408–410, 2000. DOI: 10.1364/OL.25.000408.
- [31] P. Bak, *How Nature Works: the science of self-organized criticality*. Springer New York, 2013. [Online]. Available: <https://books.google.ch/books?id=x8nSBwAAQBAJ>.
- [32] G. M. Whitesides and B. Grzybowski, "Self-assembly at all scales," *Science*, vol. 295, no. 5564, pp. 2418–2421, 2002. DOI: 10.1126/science.1070821.
- [33] M. Lancry, B. Poumellec, J. Canning, K. Cook, J.-C. Poulin, and F. Brisset, "Ultrafast nanoporous silica formation driven by femtosecond laser irradiation," *Laser & Photonics Reviews*, vol. 7, no. 6, pp. 953–962, 2013. DOI: <https://doi.org/10.1002/lpor.201300043>.
- [34] S. Richter *et al.*, "On the fundamental structure of femtosecond laser-induced nanogratings," *Laser & Photonics Reviews*, vol. 6, no. 6, pp. 787–792, 2012. DOI: <https://doi.org/10.1002/lpor.201200048>.

- [35] S. Richter *et al.*, “The role of self-trapped excitons and defects in the formation of nanogratings in fused silica,” *Optics Letters*, vol. 37, no. 4, pp. 482–484, 2012. DOI: 10.1364/OL.37.000482.
- [36] C. Hnatovsky, R. S. Taylor, E. Simova, V. R. Bhardwaj, D. M. Rayner, and P. B. Corkum, “Polarization-selective etching in femtosecond laser-assisted microfluidic channel fabrication in fused silica,” *Optics Letters*, vol. 30, no. 14, pp. 1867–1869, 2005. DOI: 10.1364/OL.30.001867.
- [37] L. Sudrie, M. Franco, B. Prade, and A. Mysyrowicz, “Writing of permanent birefringent microlayers in bulk fused silica with femtosecond laser pulses,” *Optics Communications*, vol. 171, no. 4, pp. 279–284, 1999. DOI: [https://doi.org/10.1016/S0030-4018\(99\)00562-3](https://doi.org/10.1016/S0030-4018(99)00562-3).
- [38] A. Marcinkevičius *et al.*, “Femtosecond laser-assisted three-dimensional microfabrication in silica,” *Optics Letters*, vol. 26, no. 5, pp. 277–279, 2001. DOI: 10.1364/OL.26.000277.
- [39] Y. Bellouard, T. Colomb, C. Depeursinge, M. Dugan, A. A. Said, and P. Bado, “Nanoindentation and birefringence measurements on fused silica specimen exposed to low-energy femtosecond pulses,” *Optics Express*, vol. 14, no. 18, pp. 8360–8366, 2006. DOI: 10.1364/OE.14.008360.
- [40] A. Champion and Y. Bellouard, “Direct volume variation measurements in fused silica specimens exposed to femtosecond laser,” *Optical Materials Express*, vol. 2, no. 6, pp. 789–798, 2012. DOI: 10.1364/OME.2.000789.
- [41] P. Vlugter and Y. Bellouard, “Elastic properties of self-organized nanogratings produced by femtosecond laser exposure of fused silica,” *Physical Review Materials*, vol. 4, p. 023 607, 2 2020. DOI: 10.1103/PhysRevMaterials.4.023607.
- [42] P. Vlugter, E. Block, and Y. Bellouard, “Local tuning of fused silica thermal expansion coefficient using femtosecond laser,” *Physical Review Materials*, vol. 3, p. 053 802, 5 2019. DOI: 10.1103/PhysRevMaterials.3.053802.
- [43] E. Casamenti, S. Pollonghini, and Y. Bellouard, “Few pulses femtosecond laser exposure for high efficiency 3d glass micromachining,” *Optics Express*, vol. 29, no. 22, pp. 35 054–35 066, 2021. DOI: 10.1364/OE.435163.
- [44] S. Richter, M. Heinrich, S. Döring, A. Tünnermann, S. Nolte, and U. Peschel, “Nanogratings in fused silica: formation, control, and applications,” *Journal of Laser Applications*, vol. 24, no. 4, p. 042 008, 2012. DOI: 10.2351/1.4718561.
- [45] R. S. Taylor, C. Hnatovsky, E. Simova, P. P. Rajeev, D. M. Rayner, and P. B. Corkum, “Femtosecond laser erasing and rewriting of self-organized planar nanocracks in fused silica glass,” *Optics Letters*, vol. 32, no. 19, pp. 2888–2890, 2007. DOI: 10.1364/OL.32.002888.

- [46] P. Temple and M. Soileau, "Polarization charge model for laser-induced ripple patterns in dielectric materials," *IEEE Journal of Quantum Electronics*, vol. 17, no. 10, pp. 2067–2072, 1981. DOI: 10.1109/JQE.1981.1070638.
- [47] V. R. Bhardwaj *et al.*, "Optically produced arrays of planar nanostructures inside fused silica," *Physical Review Letters*, vol. 96, p. 057 404, 5 2006. DOI: 10.1103/PhysRevLett.96.057404.
- [48] Y. Liao *et al.*, "Formation of in-volume nanogratings with sub-100-nm periods in glass by femtosecond laser irradiation," *Optics Letters*, vol. 40, no. 15, pp. 3623–3626, 2015. DOI: 10.1364/OL.40.003623.
- [49] M. Beresna, M. Gecevičius, P. G. Kazansky, T. Taylor, and A. V. Kavokin, "Exciton mediated self-organization in glass driven by ultrashort light pulses," *Applied Physics Letters*, vol. 101, no. 5, p. 053 120, 2012. DOI: 10.1063/1.4742899.
- [50] M. Lancry, B. Pournellec, A. Chahid-Erraji, M. Beresna, and P. G. Kazansky, "Dependence of the femtosecond laser refractive index change thresholds on the chemical composition of doped-silica glasses," *Optical Materials Express*, vol. 1, no. 4, pp. 711–723, 2011. DOI: 10.1364/OME.1.000711.
- [51] F. Zimmermann, A. Plech, S. Richter, A. Tünnermann, and S. Nolte, "Ultrashort laser pulse induced nanogratings in borosilicate glass," *Applied Physics Letters*, vol. 104, no. 21, p. 211 107, 2014. DOI: 10.1063/1.4880658.
- [52] S. Richter *et al.*, "Laser induced nanogratings beyond fused silica - periodic nanostructures in borosilicate glasses and ULE™," *Optical Materials Express*, vol. 3, no. 8, pp. 1161–1166, 2013. DOI: 10.1364/OME.3.001161.
- [53] J. Wang, X. Liu, Y. Dai, Z. Wang, and J. Qiu, "Effect of sodium oxide content on the formation of nanogratings in germanate glass by a femtosecond laser," *Optics Express*, vol. 26, no. 10, pp. 12 761–12 768, 2018. DOI: 10.1364/OE.26.012761.
- [54] M. Lancry *et al.*, "Nanogratings formation in multicomponent silicate glasses," *Applied Physics B*, vol. 122, no. 66, 2016. DOI: <https://doi.org/10.1007/s00340-016-6337-8>.
- [55] S. V. Lotarev, S. S. Fedotov, A. I. Kurina, A. S. Lipatiev, and V. N. Sigaev, "Ultrafast laser-induced nanogratings in sodium germanate glasses," *Optics Letters*, vol. 44, no. 7, pp. 1564–1567, 2019. DOI: 10.1364/OL.44.001564.
- [56] Y. Shimotsuma, S. Mori, Y. Nakanishii, E. Kim, M. Sakakura, and K. Miura, "Self-assembled glass/crystal periodic nanostructure in Al₂O₃-Dy₂O₃ binary glass," *Applied Physics A*, vol. 124, no. 82, 2018. DOI: <https://doi.org/10.1007/s00339-017-1507-z>.
- [57] Q. Xie, M. Cavillon, D. Pugliese, D. Janner, B. Pournellec, and M. Lancry, "On the formation of nanogratings in commercial oxide glasses by femtosecond laser direct writing," *Nanomaterials*, vol. 12, no. 17, 2022. DOI: 10.3390/nano12172986.
- [58] H. Yao *et al.*, "Formation of nanogratings driven by ultrafast laser irradiation in mid-IR heavy oxide glasses," *Ceramics International*, vol. 48, no. 21, pp. 31 363–31 369, 2022. DOI: <https://doi.org/10.1016/j.ceramint.2022.07.012>.

- [59] S. S. Fedotov *et al.*, “Direct writing of birefringent elements by ultrafast laser nanostructuring in multicomponent glass,” *Applied Physics Letters*, vol. 108, no. 7, p. 071 905, 2016. DOI: 10.1063/1.4941427.
- [60] Q. Zhai *et al.*, “Evolution of self-organized nanograting from the pre-induced nanocrack-assisted plasma-laser coupling in sapphire,” *Applied Physics B*, vol. 127, no. 74, 2021. DOI: <https://doi.org/10.1007/s00340-021-07625-6>.
- [61] T. O. Lipateva *et al.*, “Direct laser writing in YAG single crystal: Evolution from amorphization to nanograting formation and phase transformation,” *Journal of Alloys and Compounds*, vol. 942, p. 169 081, 2023. DOI: <https://doi.org/10.1016/j.jallcom.2023.169081>.
- [62] J. Bonse and S. Gräf, “Maxwell meets Marangoni—a review of theories on laser-induced periodic surface structures,” *Laser & Photonics Reviews*, vol. 14, no. 10, p. 2 000 215, 2020. DOI: <https://doi.org/10.1002/lpor.202000215>.
- [63] J. Bonse, J. Krüger, S. Höhm, and A. Rosenfeld, “Femtosecond laser-induced periodic surface structures,” *Journal of Laser Applications*, vol. 24, no. 4, p. 042 006, 2012. DOI: 10.2351/1.4712658.
- [64] H. M. van Driel, J. E. Sipe, and J. F. Young, “Laser-induced periodic surface structure on solids: a universal phenomenon,” *Physical Review Letters*, vol. 49, pp. 1955–1958, 26 1982. DOI: 10.1103/PhysRevLett.49.1955.
- [65] S. Höhm, A. Rosenfeld, J. Krüger, and J. Bonse, “Femtosecond laser-induced periodic surface structures on silica,” *Journal of Applied Physics*, vol. 112, no. 1, p. 014 901, 2012. DOI: 10.1063/1.4730902.
- [66] J. Z. P. Skolski, G. R. B. E. Römer, J. V. Obona, V. Ocelik, A. J. Huis in ’t Veld, and J. T. M. De Hosson, “Laser-induced periodic surface structures: Fingerprints of light localization,” *Physical Review B*, vol. 85, p. 075 320, 7 2012. DOI: 10.1103/PhysRevB.85.075320.
- [67] R. Buividas *et al.*, “Mechanism of fine ripple formation on surfaces of (semi)transparent materials via a half-wavelength cavity feedback,” *Nanotechnology*, vol. 22, no. 5, p. 055 304, 2010. DOI: 10.1088/0957-4484/22/5/055304.
- [68] F. Liang, R. Vallée, and S. L. Chin, “Mechanism of nanograting formation on the surface of fused silica,” *Optics Express*, vol. 20, no. 4, pp. 4389–4396, 2012. DOI: 10.1364/OE.20.004389.
- [69] A. Rudenko *et al.*, “Spontaneous periodic ordering on the surface and in the bulk of dielectrics irradiated by ultrafast laser: a shared electromagnetic origin,” *Scientific Reports*, vol. 7, no. 12306, 2017. DOI: <https://doi.org/10.1038/s41598-017-12502-4>.
- [70] A. Rudenko, C. Mauclair, F. Garrelie, R. Stoian, and J.-P. Colombier, “Self-organization of surfaces on the nanoscale by topography-mediated selection of quasi-cylindrical and plasmonic waves,” *Nanophotonics*, vol. 8, no. 3, pp. 459–465, 2019. DOI: doi:10.1515/nanoph-2018-0206.

- [71] A. Rudenko, C. Mauchair, F. Garrelie, R. Stoian, and J.-P. Colombier, "Amplification and regulation of periodic nanostructures in multipulse ultrashort laser-induced surface evolution by electromagnetic-hydrodynamic simulations," *Physical Review B*, vol. 99, p. 235 412, 23 2019. DOI: 10.1103/PhysRevB.99.235412.
- [72] S. A. Akhmanov, V. I. Emel'yanov, N. I. Koroteev, and V. N. Seminogov, "Interaction of powerful laser radiation with the surfaces of semiconductors and metals: nonlinear optical effects and nonlinear optical diagnostics," *Soviet Physics Uspekhi*, vol. 28, no. 12, p. 1084, 1985. DOI: 10.1070/PU1985v028n12ABEH003986.
- [73] V. I. Emel'yanov, "Self-organisation of ordered defect-deformation microstructures and nanostructures on the surfaces of solids under the action of laser radiation," *Quantum Electronics*, vol. 29, no. 7, p. 561, 1999. DOI: 10.1070/QE1999v029n07ABEH001533.
- [74] J. Reif, O. Varlamova, S. Varlamov, and M. Bestehorn, "The role of asymmetric excitation in self-organized nanostructure formation upon femtosecond laser ablation," *Applied Physics A*, vol. 104, pp. 969–973, 2011. DOI: <https://doi.org/10.1007/s00339-011-6472-3>.
- [75] Y. Bellouard *et al.*, "The Femtoprint project," *Journal of Laser Micro Nanoengineering*, vol. 7, no. 1, pp. 1–10, 2012. DOI: 10.2961/jlmn.2012.01.0001.
- [76] K. Miura, J. Qiu, H. Inouye, T. Mitsuyu, and K. Hirao, "Photowritten optical waveguides in various glasses with ultrashort pulse laser," *Applied Physics Letters*, vol. 71, no. 23, pp. 3329–3331, 1997. DOI: 10.1063/1.120327.
- [77] C. B. Schaffer, A. Brodeur, J. F. García, and E. Mazur, "Micromachining bulk glass by use of femtosecond laser pulses with nanojoule energy," *Optics Letters*, vol. 26, no. 2, pp. 93–95, 2001. DOI: 10.1364/OL.26.000093.
- [78] E. Bricchi, J. D. Mills, P. G. Kazansky, B. G. Klappauf, and J. J. Baumberg, "Birefringent Fresnel zone plates in silica fabricated by femtosecond laser machining," *Optics Letters*, vol. 27, no. 24, pp. 2200–2202, 2002. DOI: <https://doi.org/10.1364/ol.27.002200>.
- [79] M. Beresna, M. Gecevičius, and P. Kazansky, "Polarization sensitive elements fabricated by femtosecond laser nanostructuring of glass [Invited]," *Optical Materials Express*, vol. 1, 2011. DOI: 10.1364/OME.1.000783.
- [80] J. Zhang, M. Gecevičius, M. Beresna, and P. G. Kazansky, "Seemingly unlimited lifetime data storage in nanostructured glass," *Physical Review Letters*, vol. 112, p. 033 901, 3 2014. DOI: 10.1103/PhysRevLett.112.033901.
- [81] Y. Shimotsuma *et al.*, "Ultrafast manipulation of self-assembled form birefringence in glass," *Advanced Materials*, vol. 22, no. 36, pp. 4039–4043, 2010. DOI: <https://doi.org/10.1002/adma.201000921>.
- [82] Y. Kondo, J. Qiu, T. Mitsuyu, K. Hirao, and T. Yoko, "Three-dimensional microdrilling of glass by multiphoton process and chemical etching," *Japanese Journal of Applied Physics*, vol. 38, no. 10A, p. L1146, 1999. DOI: 10.1143/JJAP.38.L1146.

- [83] Y. Bellouard, A. Said, M. Dugan, and P. Bado, "Fabrication of high-aspect ratio, micro-fluidic channels and tunnels using femtosecond laser pulses and chemical etching," *Optics Express*, vol. 12, no. 10, pp. 2120–2129, 2004. DOI: 10.1364/OPEX.12.002120.
- [84] Y. Bellouard, A. A. Said, and P. Bado, "Integrating optics and micro-mechanics in a single substrate: a step toward monolithic integration in fused silica.," *Optics Express*, vol. 13, no. 17, pp. 6635–6644, 2005. DOI: 10.1364/OPEX.13.006635.
- [85] V. Tielen and Y. Bellouard, "Three-dimensional glass monolithic micro-flexure fabricated by femtosecond laser exposure and chemical etching," *Micromachines*, vol. 5, no. 3, pp. 697–710, 2014. DOI: 10.3390/mi5030697.
- [86] M. Zanaty *et al.*, "Programmable multistable mechanisms for safe surgical puncturing," *Journal of Medical Devices*, vol. 13, no. 2, 2019. DOI: 10.1115/1.4043016.
- [87] M. Haque, K. K. C. Lee, S. Ho, L. A. Fernandes, and P. R. Herman, "Chemical-assisted femtosecond laser writing of lab-in-fibers," *Lab Chip*, vol. 14, pp. 3817–3829, 19 2014. DOI: 10.1039/C4LC00648H.
- [88] A. Schaap, T. Rohrlack, and Y. Bellouard, "Optical classification of algae species with a glass lab-on-a-chip," *Lab Chip*, vol. 12, pp. 1527–1532, 8 2012. DOI: 10.1039/C2LC21091F.
- [89] S. I. Nazir and Y. Bellouard, "A monolithic gimbal micro-mirror fabricated and remotely tuned with a femtosecond laser," *Micromachines*, vol. 10, no. 9, 2019. DOI: 10.3390/mi10090611.
- [90] G. Marshall, M. Ams, and M. Withford, "Direct laser written waveguide-Bragg gratings in bulk fused silica," *Optics letters*, vol. 31, pp. 2690–1, 2006. DOI: 10.1364/OL.31.002690.
- [91] E. Stratakis *et al.*, "Laser engineering of biomimetic surfaces," *Materials Science and Engineering: R: Reports*, vol. 141, p. 100 562, 2020. DOI: <https://doi.org/10.1016/j.mser.2020.100562>.
- [92] Y. Lin *et al.*, "Durable and robust transparent superhydrophobic glass surfaces fabricated by a femtosecond laser with exceptional water repellency and thermostability," *Journal of Materials Chemistry A*, vol. 6, pp. 9049–9056, 19 2018. DOI: 10.1039/C8TA01965G.
- [93] A. Papadopoulos *et al.*, "Biomimetic omnidirectional antireflective glass via direct ultrafast laser nanostructuring," *Advanced Materials*, vol. 31, no. 32, p. 1 901 123, 2019. DOI: <https://doi.org/10.1002/adma.201901123>.
- [94] A. Y. Vorobyev and C. Guo, "Direct femtosecond laser surface nano/microstructuring and its applications," *Laser & Photonics Reviews*, vol. 7, no. 3, pp. 385–407, 2013. DOI: <https://doi.org/10.1002/lpor.201200017>.
- [95] J. Eichstädt, G. Römer, and A. H. in't Veld, "Towards friction control using laser-induced periodic surface structures," *Physics Procedia*, vol. 12, pp. 7–15, 2011. DOI: <https://doi.org/10.1016/j.phpro.2011.03.099>.
- [96] A. Y. Vorobyev and C. Guo, "Water sprints uphill on glass," *Journal of Applied Physics*, vol. 108, no. 12, p. 123 512, 2010. DOI: 10.1063/1.3511431.

- [97] E. L. Bourhis, "Applications of glass," in *Glass*. John Wiley Sons, Ltd, 2007, ch. 4, pp. 39–51. DOI: <https://doi.org/10.1002/9783527617029.ch4>.
- [98] L. Pauling, "The nature of silicon-oxygen bonds," *American Mineralogist*, vol. 65, no. 3-4, pp. 321–323, 1980.
- [99] A. K. Varshneya, "Fundamentals of inorganic glasses," in 1994, pp. 13–25. DOI: <https://doi.org/10.1016/B978-0-08-057150-8.50007-0>.
- [100] J. P. Rino, I. Ebbsjö, R. K. Kalia, A. Nakano, and P. Vashishta, "Structure of rings in vitreous SiO₂," *Physical Review B*, vol. 47, pp. 3053–3062, 6 1993. DOI: 10.1103/PhysRevB.47.3053.
- [101] R. Weeks, "Paramagnetic resonance of lattice defects in irradiated quartz," *Journal of Applied Physics*, vol. 27, no. 11, pp. 1376–1381, 1956. DOI: 10.1063/1.1722267.
- [102] L. Skuja, "Optically active oxygen-deficiency-related centers in amorphous silicon dioxide," *Journal of Non-Crystalline Solids*, vol. 239, no. 1, pp. 16–48, 1998. DOI: [https://doi.org/10.1016/S0022-3093\(98\)00720-0](https://doi.org/10.1016/S0022-3093(98)00720-0).
- [103] G. Pacchioni, L. Skuja, and D. Griscom, *Defects in SiO₂ and related dielectrics: Science and technology*. 2000. DOI: 10.1007/978-94-010-0944-7.
- [104] G. M. Lo Piccolo, M. Cannas, and S. Agnello, "Intrinsic point defects in silica for fiber optics applications," *Materials*, vol. 14, no. 24, 2021. DOI: 10.3390/ma14247682.
- [105] K. E. Hrdina, "Production and properties of ULE glass with regards to EUV masks," (The last access from [semanticscholar.org](https://www.semanticscholar.org) on 28.03.2023), 1999.
- [106] Corning. "ULE® Corning Code 7972 Ultra Low Expansion Glass." https://www.corning.com/media/worldwide/csm/documents/ULE_7972.pdf, The last access on 20.03.2023. (2016).
- [107] R. Sabia, M. J. Edwards, R. VanBrocklin, and B. Wells, "Corning 7972 ULE material for segmented and large monolithic mirror blanks," in *Optomechanical Technologies for Astronomy*, vol. 6273, SPIE, 2006, p. 627 302. DOI: 10.1117/12.672059.
- [108] M. C. Tobin and T. Baak, "Raman spectra of some low-expansion glasses," *Journal of the Optical Society of America*, vol. 58, no. 11, pp. 1459–1461, 1968. DOI: 10.1364/JOSA.58.001459.
- [109] R. B. Gregor, F. W. Lytle, D. R. Sandstrom, J. Wong, and P. Schultz, "Investigation of TiO₂-SiO₂ glasses by X-ray absorption spectroscopy," *Journal of Non-Crystalline Solids*, vol. 55, no. 1, pp. 27–43, 1983. DOI: [https://doi.org/10.1016/0022-3093\(83\)90005-4](https://doi.org/10.1016/0022-3093(83)90005-4).
- [110] S. M. Mukhopadhyay and S. H. Garofalini, "Surface studies of TiO₂-SiO₂ glasses by X-ray photoelectron spectroscopy," *Journal of Non-Crystalline Solids*, vol. 126, no. 3, pp. 202–208, 1990. DOI: [https://doi.org/10.1016/0022-3093\(90\)90820-C](https://doi.org/10.1016/0022-3093(90)90820-C).
- [111] L. Cormier, P. H. Gaskell, G. Calas, and A. K. Soper, "Medium-range order around titanium in a silicate glass studied by neutron diffraction with isotopic substitution," *Physical Review B*, vol. 58, pp. 11 322–11 330, 17 1998. DOI: 10.1103/PhysRevB.58.11322.

- [112] P. C. Schultz, "Binary titania-silica glasses containing 10 to 20 wt% TiO₂," *Journal of the American Ceramic Society*, vol. 59, no. 5-6, pp. 214–219, 1976. DOI: <https://doi.org/10.1111/j.1151-2916.1976.tb10936.x>.
- [113] T. I. Kwindt, D. Enke, and S. Koppka, "Effect of TiO₂ on microphase development during phase separation and crystallization in Na₂O-B₂O₃-SiO₂ glass system," *Journal of the American Ceramic Society*, vol. 105, no. 5, pp. 3261–3278, 2022. DOI: <https://doi.org/10.1111/jace.18288>.
- [114] G. Scannell, A. Koike, and L. Huang, "Structure and thermo-mechanical response of TiO₂-SiO₂ glasses to temperature," *Journal of Non-Crystalline Solids*, vol. 447, pp. 238–247, 2016. DOI: <https://doi.org/10.1016/j.jnoncrysol.2016.06.018>.
- [115] R. Limbach, S. Karlsson, G. Scannell, R. Mathew, M. Edén, and L. Wondraczek, "The effect of TiO₂ on the structure of Na₂O-CaO-SiO₂ glasses and its implications for thermal and mechanical properties," *Journal of Non-Crystalline Solids*, vol. 471, pp. 6–18, 2017. DOI: <https://doi.org/10.1016/j.jnoncrysol.2017.04.013>.
- [116] C. L. Rathmann, G. H. Mann, and M. E. Nordberg, "A new ultralow-expansion, modified fused-silica glass," *Applied Optics*, vol. 7, no. 5, pp. 819–823, 1968. DOI: 10.1364/AO.7.000819.
- [117] O. Mazurin, V. Leko, and L. Komarova, "Crystallization of silica and titanium oxide-silica corning glasses (codes 7940 and 7971)," *Journal of Non-Crystalline Solids*, vol. 18, no. 1, pp. 1–9, 1975. DOI: [https://doi.org/10.1016/0022-3093\(75\)90002-2](https://doi.org/10.1016/0022-3093(75)90002-2).
- [118] H. Zheng and G. C. Lim, "Laser-effected darkening in TPEs with TiO₂ additives," *Optics and Lasers in Engineering*, vol. 41, no. 5, pp. 791–800, 2004. DOI: [https://doi.org/10.1016/S0143-8166\(03\)00032-0](https://doi.org/10.1016/S0143-8166(03)00032-0).
- [119] D. O. Scanlon *et al.*, "Band alignment of rutile and anatase TiO₂," *Nature Materials*, vol. 12, pp. 798–801, 213. DOI: <https://doi.org/10.1038/nmat3697>.
- [120] H. Ma, J. Yang, Y. Dai, Y. Zhang, B. Lu, and G. Ma, "Raman study of phase transformation of TiO₂ rutile single crystal irradiated by infrared femtosecond laser," *Applied Surface Science*, vol. 253, no. 18, pp. 7497–7500, 2007. DOI: <https://doi.org/10.1016/j.apsusc.2007.03.047>.
- [121] A. L. Linsebigler, G. Lu, and J. T. Yates Jr, "Photocatalysis on TiO₂ surfaces: principles, mechanisms, and selected results," *Chemical Reviews*, vol. 95, no. 3, pp. 735–758, 1995.
- [122] A. Narazaki, Y. Kawaguchi, H. Niino, M. Shojiya, H. Koyo, and K. Tsunetomo, "Formation of a TiO₂ micronetwork on a UV-absorbing SiO₂-based glass surface by excimer laser irradiation," *Chemistry of Materials*, vol. 17, no. 26, pp. 6651–6655, 2005. DOI: 10.1021/cm0518372.
- [123] Y. Liu *et al.*, "Femtosecond laser direct writing of TiO₂ crystalline patterns in glass," *Applied Physics B*, vol. 93, pp. 613–617, 2008. DOI: <https://doi.org/10.1007/s00340-008-3166-4>.

- [124] Y. Dai *et al.*, “Direct writing three-dimensional Ba₂TiSi₂O₈ crystalline pattern in glass with ultrashort pulse laser,” *Applied Physics Letters*, vol. 90, no. 18, p. 181 109, 2007. DOI: 10.1063/1.2734919.
- [125] Y. Dai, B. Zhu, J. Qiu, H. Ma, B. Lu, and B. Yu, “Space-selective precipitation of functional crystals in glass by using a high repetition rate femtosecond laser,” *Chemical Physics Letters*, vol. 443, no. 4, pp. 253–257, 2007. DOI: <https://doi.org/10.1016/j.cplett.2007.06.076>.
- [126] S. Richter *et al.*, “Ultrashort pulse induced modifications in ULE - from nanograting formation to laser darkening,” *Optical Materials Express*, vol. 5, no. 8, pp. 1834–1850, 2015. DOI: 10.1364/OME.5.001834.
- [127] I. Efthimiopoulos *et al.*, “Femtosecond laser-induced transformations in ultra-low expansion glass: Microstructure and local density variations by vibrational spectroscopy,” *Journal of Applied Physics*, vol. 123, no. 23, p. 233 105, 2018. DOI: 10.1063/1.5030687.
- [128] M. Cavillon, Y. Wang, B. Poumellec, F. Brisset, and M. Lancry, “Erasure of nanopores in silicate glasses induced by femtosecond laser irradiation in the Type II regime,” *Applied Physics A*, vol. 126, no. 876, 2020. DOI: <https://doi.org/10.1007/s00339-020-04062-8>.
- [129] S.-E. Wei *et al.*, “Thermal stability of type II modifications by IR femtosecond laser in silica-based glasses,” *Sensors*, vol. 20, no. 3, 2020. DOI: 10.3390/s20030762.
- [130] C. Cayron, “GenOVa: A computer program to generate orientational variants,” *Journal of Applied Crystallography*, vol. 40, no. 6, pp. 1179–1182, 2007. DOI: 10.1107/S0021889807048741.
- [131] Y. Bellouard, E. Barthel, A. A. Said, M. Dugan, and P. Bado, “Scanning thermal microscopy and Raman analysis of bulk fused silica exposed to low-energy femtosecond laser pulses,” *Optics Express*, vol. 16, no. 24, pp. 19 520–19 534, 2008. DOI: 10.1364/OE.16.019520.
- [132] S. Sharma, J. Mammone, and M. Nicol, “Raman investigation of ring configurations in vitreous silica,” *Nature*, vol. 292, pp. 140–141, 1981. DOI: <https://doi.org/10.1038/292140a0>.
- [133] T. Ohsaka, F. Izumi, and Y. Fujiki, “Raman spectrum of anatase, TiO₂,” *Journal of Raman Spectroscopy*, vol. 7, no. 6, pp. 321–324, 1978. DOI: <https://doi.org/10.1002/jrs.1250070606>.
- [134] U. Balachandran and N. Eror, “Raman spectra of titanium dioxide,” *Journal of Solid State Chemistry*, vol. 42, no. 3, pp. 276–282, 1982. DOI: [https://doi.org/10.1016/0022-4596\(82\)90006-8](https://doi.org/10.1016/0022-4596(82)90006-8).
- [135] D. A. H. Hanaor and C. C. Sorrell, “Review of the anatase to rutile phase transformation,” *Journal of Materials Science*, vol. 46, pp. 855–874, 2011. DOI: <https://doi.org/10.1007/s10853-010-5113-0>.

- [136] M. Shimizu *et al.*, “Mechanism of heat-modification inside a glass after irradiation with high-repetition rate femtosecond laser pulses,” *Journal of Applied Physics*, vol. 108, no. 7, 2010. DOI: 10.1063/1.3483238.
- [137] E. G. Gamaly *et al.*, “Laser-matter interaction in the bulk of a transparent solid: Confined microexplosion and void formation,” *Physical Review B - Condensed Matter and Materials Physics*, vol. 73, no. 21, pp. 1–15, 2006. DOI: 10.1103/PhysRevB.73.214101.
- [138] P. Makuła, M. Pacia, and W. Macyk, “How To Correctly Determine the Band Gap Energy of Modified Semiconductor Photocatalysts Based on UV-Vis Spectra,” *Journal of Physical Chemistry Letters*, vol. 9, no. 23, pp. 6814–6817, 2018. DOI: 10.1021/acs.jpcclett.8b02892.
- [139] S. Liu, J. Yu, and M. Jaroniec, “Anatase TiO₂ with dominant high-energy 001 facets: Synthesis, properties, and applications,” *Chemistry of Materials*, vol. 23, no. 18, pp. 4085–4093, 2011. DOI: 10.1021/cm200597m.
- [140] F. Lin *et al.*, “Single-facet dominant anatase TiO₂ (101) and (001) model catalysts to elucidate the active sites for alkanol dehydration,” *ACS Catalysis*, vol. 10, no. 7, pp. 4268–4279, 2020. DOI: 10.1021/acscatal.9b04654.
- [141] A. Rezikyan and G. G. Moore, “Fluctuation electron microscopy study of crystal nucleation in TiO₂-SiO₂ glass with heat treatment,” *Journal of Physics: Condensed Matter*, vol. 32, no. 48, p. 485 402, 2020. DOI: 10.1088/1361-648X/abae19.
- [142] C. Cayron, “Diffraction artefacts from twins and stacking faults, and the mirage of hexagonal, polytypes or other superstructures,” *Scripta Materialia*, vol. 194, p. 113 629, 2021. DOI: 10.1016/j.scriptamat.2020.11.014.
- [143] G. Torun, T. Kishi, and Y. Bellouard, “Direct-write laser-induced self-organization and metallization beyond the focal volume in tellurite glass,” *Physical Review Materials*, vol. 5, p. 055 201, 5 2021. DOI: 10.1103/PhysRevMaterials.5.055201.
- [144] G. Torun, T. Kishi, D. Pugliese, D. Milanese, and Y. Bellouard, “Formation mechanism of elemental Te produced in tellurite glass systems by femtosecond laser irradiation,” *Advanced Materials*, vol. 35, no. 20, p. 2 210 446, DOI: <https://doi.org/10.1002/adma.202210446>.
- [145] J. J. Berzelius, “Untersuchung über die eigenschaften des tellurs,” *Annalen der Physik*, vol. 108, no. 37-41, pp. 577–627, 1834. DOI: <https://doi.org/10.1002/andp.18341083702>.
- [146] J. Stanworth, “Tellurite glasses,” *Nature*, vol. 169, pp. 581–582, 1952. DOI: <https://doi.org/10.1038/169581b0>.
- [147] R. El-Mallawany, *Tellurite Glasses Handbook: Physical Properties and Data, Second Edition*. Taylor & Francis, 2011. [Online]. Available: <https://books.google.ch/books?id=rEJhNu7XNcsC>.
- [148] P. T. Sarjeant and R. Roy, “New glassy and polymorphic oxide phases using rapid quenching techniques,” *Journal of the American Ceramic Society*, vol. 50, no. 10, pp. 500–503, 1967. DOI: <https://doi.org/10.1111/j.1151-2916.1967.tb14980.x>.

- [149] R. Al-Mukadam, A. Zandona, and J. Deubener, "Kinetic fragility of pure TeO₂ glass," *Journal of Non-Crystalline Solids*, vol. 554, p. 120 595, 2021. DOI: <https://doi.org/10.1016/j.jnoncrysol.2020.120595>.
- [150] N. Tagiara, D. Palles, E. Simandiras, V. Psycharis, A. Kyritsis, and E. Kamitsos, "Synthesis, thermal and structural properties of pure TeO₂ glass and zinc-tellurite glasses," *Journal of Non-Crystalline Solids*, vol. 457, pp. 116–125, 2017. DOI: <https://doi.org/10.1016/j.jnoncrysol.2016.11.033>.
- [151] R. Raghvender, A. Bouzid, S. Cadars, D. Hamani, P. Thomas, and O. Masson, "Structure of amorphous TeO₂ revisited: A hybrid functional ab initio molecular dynamics study," *Physical Review B*, vol. 106, p. 174 201, 17 2022. DOI: [10.1103/PhysRevB.106.174201](https://doi.org/10.1103/PhysRevB.106.174201).
- [152] M. A. Marple, M. Jesuit, I. Hung, Z. Gan, S. Feller, and S. Sen, "Structure of TeO₂ glass: Results from 2D 125Te NMR spectroscopy," *Journal of Non-Crystalline Solids*, vol. 513, pp. 183–190, 2019. DOI: <https://doi.org/10.1016/j.jnoncrysol.2019.03.019>.
- [153] J. C. Champarnaud-Mesjard, S. Blanchandin, P. Thomas, A. Mirgorodsky, T. Merle-Méjean, and B. Frit, "Crystal structure, Raman spectrum and lattice dynamics of a new metastable form of tellurium dioxide: γ -TeO₂," *Journal of Physics and Chemistry of Solids*, vol. 61, no. 9, pp. 1499–1507, 2000. DOI: [https://doi.org/10.1016/S0022-3697\(00\)00012-3](https://doi.org/10.1016/S0022-3697(00)00012-3).
- [154] O. Noguera, T. Merle-Méjean, A. Mirgorodsky, M. Smirnov, P. Thomas, and J. C. C-Mesjard, "Vibrational and structural properties of glass and crystalline phases of TeO₂," *Journal of Non-Crystalline Solids*, vol. 330, no. 1, pp. 50–60, 2003. DOI: <https://doi.org/10.1016/j.jnoncrysol.2003.08.052>.
- [155] M. N. Garaga *et al.*, "Short-range structure of TeO₂ glass," *The Journal of Physical Chemistry C*, vol. 121, no. 50, pp. 28 117–28 124, 2017. DOI: [10.1021/acs.jpcc.7b08978](https://doi.org/10.1021/acs.jpcc.7b08978).
- [156] O. L. G. Alderman *et al.*, "Short-range disorder in TeO₂ melt and glass," *The Journal of Physical Chemistry Letters*, vol. 11, no. 2, pp. 427–431, 2020. DOI: [10.1021/acs.jpcclett.9b03231](https://doi.org/10.1021/acs.jpcclett.9b03231).
- [157] A. G. Kalampounias, G. Tsilomelekis, and S. Boghosian, "Glass-forming ability of TeO₂ and temperature induced changes on the structure of the glassy, supercooled, and molten states," *Journal of Chemical Physics*, vol. 142, no. 15, 2015. DOI: [10.1063/1.4917536](https://doi.org/10.1063/1.4917536).
- [158] A. P. Mirgorodsky, T. Merle-Méjean, J. C. Champarnaud, P. Thomas, and B. Frit, "Dynamics and structure of TeO₂ polymorphs: Model treatment of paratellurite and tellurite; Raman scattering evidence for new γ - and δ -phases," *Journal of Physics and Chemistry of Solids*, vol. 61, no. 4, pp. 501–509, 2000. DOI: [10.1016/S0022-3697\(99\)00263-2](https://doi.org/10.1016/S0022-3697(99)00263-2).
- [159] A. G. Papadopoulos, N. S. Tagiara, E. D. Simandiras, and E. I. Kamitsos, "On the absence of doubly bonded TeO groups in TeO₂ glass," *Journal of Physical Chemistry B*, vol. 124, no. 27, pp. 5746–5753, 2020. DOI: [10.1021/acs.jpcc.0c02499](https://doi.org/10.1021/acs.jpcc.0c02499).

- [160] M. A. Sidkey and M. S. Gaafar, "Ultrasonic studies on network structure of ternary TeO_2 - WO_3 - K_2O glass system," *Physica B: Condensed Matter*, vol. 348, no. 1-4, pp. 46–55, 2004. DOI: 10.1016/j.physb.2003.11.005.
- [161] S.-H. Kim, T. Yoko, and S. Sakka, "Linear and nonlinear optical properties of TeO_2 glass," *Journal of the American Ceramic Society*, vol. 76, no. 10, pp. 2486–2490, 1993. DOI: <https://doi.org/10.1111/j.1151-2916.1993.tb03970.x>.
- [162] S. Manning, H. Ebendorff-Heidepriem, and T. M. Monro, "Ternary tellurite glasses for the fabrication of nonlinear optical fibres," *Optical Materials Express*, vol. 2, no. 2, pp. 140–152, 2012. DOI: 10.1364/OME.2.000140.
- [163] T. Kosuge, Y. Benino, V. Dimitrov, R. Sato, and T. Komatsu, "Thermal stability and heat capacity changes at the glass transition in K_2O - WO_3 - TeO_2 glasses," *Journal of Non-Crystalline Solids*, vol. 242, no. 2-3, pp. 154–164, 1998. DOI: 10.1016/S0022-3093(98)00800-X.
- [164] M. Celikbilek Ersundu, A. Ersundu, M. Sayyed, G. Lakshminarayana, and S. Aydin, "Evaluation of physical, structural properties and shielding parameters for K_2O - WO_3 - TeO_2 glasses for gamma ray shielding applications," *Journal of Alloys and Compounds*, vol. 714, pp. 278–286, 2017. DOI: <https://doi.org/10.1016/j.jallcom.2017.04.223>.
- [165] M. Sidkey and M. Gaafar, "Ultrasonic studies on network structure of ternary TeO_2 - WO_3 - K_2O glass system," *Physica B: Condensed Matter*, vol. 348, no. 1, pp. 46–55, 2004. DOI: <https://doi.org/10.1016/j.physb.2003.11.005>.
- [166] M. Celikbilek, A. Ersundu, E. Zayim, and S. Aydin, "Thermochromic behavior of tellurite glasses," *Journal of Alloys and Compounds*, vol. 637, pp. 162–170, 2015. DOI: <https://doi.org/10.1016/j.jallcom.2015.03.013>.
- [167] R. F. Souza, M. A. R. C. Alencar, J. M. Hickmann, R. Kobayashi, and L. R. P. Kassab, "Femtosecond nonlinear optical properties of tellurite glasses," *Applied Physics Letters*, vol. 89, no. 17, p. 171 917, 2006. DOI: 10.1063/1.2364467.
- [168] B. Ferreira *et al.*, "Second harmonic generation in poled tellurite glass," *Journal of Non-Crystalline Solids*, vol. 332, no. 1, pp. 207–218, 2003. DOI: <https://doi.org/10.1016/j.jnoncrysol.2003.09.015>.
- [169] H. Nasu, O. Matsushita, K. Kamiya, H. Kobayashi, and K. Kubodera, "Third harmonic generation from Li_2O - TiO_2 - TeO_2 glasses," *Journal of Non-Crystalline Solids*, vol. 124, no. 2, pp. 275–277, 1990. DOI: [https://doi.org/10.1016/0022-3093\(90\)90274-P](https://doi.org/10.1016/0022-3093(90)90274-P).
- [170] T. Kishi, T. Kumagai, S. Shibuya, F. Prudenzano, T. Yano, and S. Shibata, "Quasi-single mode laser output from a terrace structure added on a Nd^{3+} -doped tellurite-glass microsphere prepared using localized laser heating," *Optics Express*, vol. 23, no. 16, pp. 20 629–20 635, 2015. DOI: 10.1364/OE.23.020629.
- [171] M. Liao, C. Chaudhari, G. Qin, X. Yan, T. Suzuki, and Y. Ohishi, "Tellurite microstructure fibers with small hexagonal core for supercontinuum generation," *Optics Express*, vol. 17, no. 14, pp. 12 174–12 182, 2009. DOI: 10.1364/OE.17.012174.

- [172] S. J. Madden and K. T. Vu, "Very low loss reactively ion etched Tellurium Dioxide planar rib waveguides for linear and non-linear optics," *Optics Express*, vol. 17, no. 20, pp. 17 645–17 651, 2009. DOI: 10.1364/OE.17.017645.
- [173] S. J. Madden and K. T. Vu, "High-performance integrated optics with tellurite glasses: status and prospects," *International Journal of Applied Glass Science*, vol. 3, no. 4, pp. 289–298, 2012. DOI: <https://doi.org/10.1111/ijag.12002>.
- [174] K. Kimura, "Optical recording materials based on TeO_x films," *Japanese Journal of Applied Physics*, vol. 28, no. 5R, p. 810, 1989. DOI: 10.1143/JJAP28.810.
- [175] J. Wang, E. Vogel, and E. Snitzer, "Tellurite glass: a new candidate for fiber devices," *Optical Materials*, vol. 3, no. 3, pp. 187–203, 1994. DOI: [https://doi.org/10.1016/0925-3467\(94\)90004-3](https://doi.org/10.1016/0925-3467(94)90004-3).
- [176] G. S. Murugan, T. Suzuki, and Y. Ohishi, "Tellurite glasses for ultrabroadband fiber Raman amplifiers," *Applied Physics Letters*, vol. 86, no. 16, p. 161 109, 2005. DOI: 10.1063/1.1906323.
- [177] J. Fan, Y. Zhang, G. Li, and Y. Yue, "Tellurium nanoparticles enhanced electrochemical performances of TeO₂-V₂O₅-Al₂O₃ glass anode for Lithium-ion batteries," *Journal of Non-Crystalline Solids*, vol. 521, p. 119 491, 2019. DOI: <https://doi.org/10.1016/j.jnoncrysol.2019.119491>.
- [178] S. Inoue, A. Nukui, K. Yamamoto, T. Yano, S. Shibata, and M. Yamane, "Refractive index patterning of tellurite glass surfaces by ultra short pulse laser spot heating," *Journal of Materials Science*, vol. 37, no. 16, pp. 3459–3465, 2002. DOI: 10.1023/A:1016511106180.
- [179] Y. Tokuda *et al.*, "Waveguide formation in niobium tellurite glasses by pico- and femtosecond laser pulses," *Journal of Non-Crystalline Solids*, vol. 326-327, pp. 472–475, 2003. DOI: [https://doi.org/10.1016/S0022-3093\(03\)00455-1](https://doi.org/10.1016/S0022-3093(03)00455-1).
- [180] M. Smayev, V. Dorofeev, A. Moiseev, and A. Okhrimchuk, "Femtosecond laser writing of a depressed cladding single mode channel waveguide in high-purity tellurite glass," *Journal of Non-Crystalline Solids*, vol. 480, pp. 100–106, 2018. DOI: <https://doi.org/10.1016/j.jnoncrysol.2017.11.007>.
- [181] S. Gross *et al.*, "Ultrafast laser inscription in soft glasses: A comparative study of athermal and thermal processing regimes for guided wave optics," *International Journal of Applied Glass Science*, vol. 3, no. 4, pp. 332–348, 2012. DOI: <https://doi.org/10.1111/ijag.12005>.
- [182] P. Nandi *et al.*, "Femtosecond laser written channel waveguides in tellurite glass," *Optics Express*, vol. 14, no. 25, pp. 12 145–12 150, 2006. DOI: 10.1364/OE.14.012145.
- [183] K. C. Vishnubhatla, S. V. Rao, R. S. S. Kumar, K. S. Prasad, P. S. R. Prasad, and D. N. Rao, "Inscription and characterization of micro-structures in silicate, Foturan and tellurite glasses by femtosecond laser direct writing," in *Commercial and Biomedical Applications of Ultrafast Lasers VIII*, SPIE, vol. 6881, 2008, p. 688 113. DOI: 10.1117/12.762907.

- [184] T. T. Fernandez *et al.*, “Active waveguides written by femtosecond laser irradiation in an erbium-doped phospho-tellurite glass,” *Optics Express*, vol. 16, no. 19, pp. 15 198–15 205, 2008. DOI: 10.1364/OE.16.015198.
- [185] M. Ramme, T. Anderson, J. Choi, H. Ebendorff-Heidepriem, T. Monroe, and M. Richardson, “Waveguide writing and characterization in tellurite glass,” 2009. DOI: <https://doi.org/10.1364/CLEO.2009.JWA4>.
- [186] T. T. Fernandez *et al.*, “Femtosecond laser written optical waveguide amplifier in phospho-tellurite glass,” *Optics Express*, vol. 18, no. 19, pp. 20 289–20 297, 2010. DOI: 10.1364/OE.18.020289.
- [187] D. S. da Silva, N. U. Wetter, W. de Rossi, L. R. P. Kassab, and R. E. Samad, “Production and characterization of femtosecond laser-written double line waveguides in heavy metal oxide glasses,” *Optical Materials*, vol. 75, pp. 267–273, 2018. DOI: <https://doi.org/10.1016/j.optmat.2017.10.033>.
- [188] T. T. Fernandez *et al.*, “Role of ion migrations in ultrafast laser written tellurite glass waveguides,” *Optics Express*, vol. 22, no. 12, pp. 15 298–15 304, 2014. DOI: 10.1364/OE.22.015298.
- [189] T. T. Fernandez *et al.*, “Dual regimes of ion migration in high repetition rate femtosecond laser inscribed waveguides,” *IEEE Photonics Technology Letters*, vol. 27, no. 10, pp. 1068–1071, 2015. DOI: 10.1109/LPT.2015.2407378.
- [190] G. C. Righini *et al.*, “Laser irradiation, ion implantation and e-beam writing of integrated optical structures,” in *Photonic Materials, Devices, and Applications*, vol. 5840, 2005, pp. 649–657. DOI: 10.1117/12.609231.
- [191] J. M. Oliveira, A. J. Jesus-Silva, A. C. Silva, N. O. Dantas, and E. J. Fonseca, “Waveguides written in silver-doped tellurite glasses,” *Optical Materials*, vol. 101, p. 109 767, 2020. DOI: <https://doi.org/10.1016/j.optmat.2020.109767>.
- [192] S. K. Sundaram, C. B. Schaffer, and E. Mazur, “Microexplosions in tellurite glasses,” *Applied Physics A: Materials Science and Processing*, vol. 76, no. 3, pp. 379–384, 2003. DOI: 10.1007/s00339-002-1824-7.
- [193] T. Mann, R. Mathieson, M. Murray, B. Richards, and G. Jose, “Femtosecond laser ablation properties of Er³⁺ ion doped zinc-sodium tellurite glass,” *Journal of Applied Physics*, vol. 124, no. 4, p. 044 903, 2018. DOI: 10.1063/1.5040947.
- [194] Y. Shimotsuma, K. Hirao, Q. J., and P. Kazansky, “Nano-modification inside transparent materials by femtosecond laser single beam,” *Modern Physics Letters B*, vol. 19, no. 05, pp. 225–238, 2005. DOI: 10.1142/S0217984905008281.
- [195] Y. Shimotsuma, K. Hirao, J. Qiu, and K. Miura, “Nanofabrication in transparent materials with a femtosecond pulse laser,” *Journal of Non-Crystalline Solids*, vol. 352, no. 6, pp. 646–656, 2006. DOI: <https://doi.org/10.1016/j.jnoncrysol.2005.11.060>.

- [196] Y. Teng, J. Zhou, S. N. Khisro, S. Zhou, and J. Qiu, "Elemental redistribution behavior in tellurite glass induced by high repetition rate femtosecond laser irradiation," *Journal of Alloys and Compounds*, vol. 601, pp. 212–216, 2014. DOI: <https://doi.org/10.1016/j.jallcom.2014.02.178>.
- [197] R. Akagi, K. Handa, N. Ohtori, M. Hannon A.C. and Tatsumisago, and N. Umesaki, "High-temperature structure of K_2O - TeO_2 glasses," *Journal of Non-Crystalline Solids*, vol. 256-257, pp. 111–118, 1999. DOI: [https://doi.org/10.1016/S0022-3093\(99\)00392-0](https://doi.org/10.1016/S0022-3093(99)00392-0).
- [198] Z. Li, H. Wang, Y. Li, Y. Ma, T. Cui, and G. Zou, "Pressure-induced elemental dissociation in zinc chalcogenides," *New Journal of Physics*, vol. 12, no. 4, p. 043 058, 2010. DOI: [10.1088/1367-2630/12/4/043058](https://doi.org/10.1088/1367-2630/12/4/043058).
- [199] C. Cheng, Y. Yu, F. Zhang, H. Zhang, and J. Qiu, "Femtosecond laser induced microstructure and luminescence changes in oxyfluoride tellurite glasses," *Journal of Non-Crystalline Solids*, vol. 406, pp. 1–4, 2014. DOI: <https://doi.org/10.1016/j.jnoncrysol.2014.09.025>.
- [200] Q. Chen *et al.*, "A strategy for fabrication of controllable 3D pattern containing clusters and nanoparticles inside a solid material," *Nanoscale*, vol. 9, pp. 9083–9088, 26 2017. DOI: [10.1039/C7NR01615H](https://doi.org/10.1039/C7NR01615H).
- [201] R. G. Capelo *et al.*, "Controlled formation of metallic tellurium nanocrystals in tellurite glasses using femtosecond direct laser writing," *Journal of Materials Research and Technology*, vol. 13, pp. 1296–1304, 2021. DOI: <https://doi.org/10.1016/j.jmrt.2021.05.037>.
- [202] M. Celikbilek, A. Ersundu, N. Solak, and S. Aydin, "Crystallization kinetics of the tungsten-tellurite glasses," *Journal of Non-Crystalline Solids*, vol. 357, no. 1, pp. 88–95, 2011. DOI: <https://doi.org/10.1016/j.jnoncrysol.2010.09.012>.
- [203] L. Bressel *et al.*, "Femtosecond laser induced density changes in GeO_2 and SiO_2 glasses: fictive temperature effect," *Optical Materials Express*, vol. 1, no. 4, pp. 605–613, 2011. DOI: [10.1364/OME.1.000605](https://doi.org/10.1364/OME.1.000605).
- [204] M. Lehmann *et al.*, "Bulk defects and hydrogenation kinetics in crystalline silicon solar cells with fired passivating contacts," *IEEE Journal of Photovoltaics*, vol. 12, no. 3, pp. 711–721, 2022. DOI: [10.1109/JPHOTOV.2022.3161871](https://doi.org/10.1109/JPHOTOV.2022.3161871).
- [205] C. Marini *et al.*, "High-pressure phases of crystalline tellurium: A combined Raman and ab-initio study," *Physical Review B - Condensed Matter and Materials Physics*, vol. 86, no. 6, pp. 1–5, 2012. DOI: [10.1103/PhysRevB.86.064103](https://doi.org/10.1103/PhysRevB.86.064103).
- [206] B. Torrie, "Raman spectrum of tellurium," *Solid State Communications*, vol. 8, no. 22, pp. 1899–1901, 1970. DOI: [10.1016/0038-1098\(70\)90343-1](https://doi.org/10.1016/0038-1098(70)90343-1).
- [207] Y. H. Cheng, S. W. Teitelbaum, F. Y. Gao, and K. A. Nelson, "Femtosecond laser amorphization of tellurium," *Physical Review B*, vol. 98, no. 13, pp. 1–5, 2018. DOI: [10.1103/PhysRevB.98.134112](https://doi.org/10.1103/PhysRevB.98.134112).

- [208] R. T. Ananth Kumar, H. A. Mousa, P. Chithra Lekha, S. T. Mahmoud, and N. Qamhieh, "Scrutiny of structural disorder using Raman spectra and Tauc parameter in GeTe₂ thin films," *Journal of Physics: Conference Series*, vol. 869, no. 1, 2017. DOI: 10.1088/1742-6596/869/1/012018.
- [209] T. Vasileiadis and S. N. Yannopoulos, "Photo-induced oxidation and amorphization of trigonal tellurium: A means to engineer hybrid nanostructures and explore glass structure under spatial confinement," *Journal of Applied Physics*, vol. 116, no. 10, p. 103510, 2014. DOI: 10.1063/1.4894868.
- [210] D. Reinen and G. G. Lindner, "The nature of the chalcogen colour centres in ultramarine-type solids," *Chemical Society Reviews*, vol. 28, no. 2, pp. 75–84, 1999. DOI: 10.1039/a704920j.
- [211] C. Heinemann and W. Koch, "The tellurium dimer and its anion," *Molecular Physics*, vol. 92, no. 3, pp. 463–470, 1997. DOI: 10.1080/002689797170202.
- [212] A. S. Zlenko *et al.*, "Tellurium-doped silica fibers: spectroscopic properties and nature of active centers," *Journal of the Optical Society of America B*, vol. 33, no. 4, p. 675, 2016. DOI: 10.1364/josab.33.000675.
- [213] R. L. Frost and E. C. Keeffe, "Raman spectroscopic study of the tellurite mineral: Rodalquilarite H₃Fe₂³⁺(Te⁴⁺O₃)₄Cl," *Spectrochimica Acta - Part A: Molecular and Biomolecular Spectroscopy*, vol. 73, no. 1, pp. 146–149, 2009. DOI: 10.1016/j.saa.2009.02.019.
- [214] M. R. Zaki, D. Hamani, M. Dutreilh-Colas, J. R. Duclère, O. Masson, and P. Thomas, "Synthesis, thermal, structural and linear optical properties of new glasses within the TeO₂-TiO₂-WO₃ system," *Journal of Non-Crystalline Solids*, vol. 484, pp. 139–148, 2018. DOI: 10.1016/j.jnoncrysol.2018.01.034.
- [215] M. Daniel, B. Desbat, J. Lassegues, B. Gerand, and M. Figlarz, "Infrared and Raman study of WO₃ tungsten trioxides and WO₃, xH₂O tungsten trioxide hydrates," *Journal of Solid State Chemistry*, vol. 67, no. 2, pp. 235–247, 1987. DOI: 10.1016/0022-4596(87)90359-8.
- [216] J. Cornette *et al.*, "Vibrational spectra of rhombohedral TeO₃ compared to those of ReO₃-like proto-phase and α-TeO₂ (paratellurite): Lattice dynamic and crystal chemistry aspects," *Journal of Raman Spectroscopy*, vol. 42, no. 4, pp. 758–764, 2011. DOI: 10.1002/jrs.2757.
- [217] A. Zavabeti *et al.*, "High-mobility p-type semiconducting two-dimensional β-TeO₂," *Nature Electronics*, vol. 4, no. 4, pp. 277–283, 2021. DOI: 10.1038/s41928-021-00561-5.
- [218] J. Xie, J. Yan, D. Zhu, and G. He, "Atomic-level insight into the formation of subsurface dislocation layer and its effect on mechanical properties during ultrafast laser micro/nano fabrication," *Advanced Functional Materials*, vol. 32, no. 15, 2022. DOI: 10.1002/adfm.202108802.

- [219] M. Yankowitz *et al.*, “Tuning superconductivity in twisted bilayer graphene,” *Science*, vol. 363, no. 6431, pp. 1059–1064, 2019. DOI: [10.1126/science.aav1910](https://doi.org/10.1126/science.aav1910).
- [220] B. Oz, I. Kabalci, M. Ovecoglu, and G. Ozen, “Thermal properties and crystallization behavior of some TeO₂-K₂O glasses,” *Journal of the European Ceramic Society*, vol. 27, no. 2, pp. 1823–1827, 2007. DOI: <https://doi.org/10.1016/j.jeurceramsoc.2006.04.143>.
- [221] A. Ersundu, G. Karaduman, M. Celikbilek, N. Solak, and S. Aydin, “Stability of the δ -TeO₂ phase in the binary and ternary TeO₂ glasses,” *Journal of the European Ceramic Society*, vol. 30, no. 15, pp. 3087–3092, 2010. DOI: <https://doi.org/10.1016/j.jeurceramsoc.2010.07.018>.
- [222] T. M. Machado and M. A. Silva, “The reduction of tellurium in binary glasses in the system TeO₂-Sb₂O₃,” *Materials Chemistry and Physics*, vol. 201, pp. 86–91, 2017. DOI: <https://doi.org/10.1016/j.matchemphys.2017.08.031>.
- [223] T. M. Machado and M. A. Pereira da Silva, “Preparation and properties of antimony sodium polyphosphate glasses containing tellurium particles,” *Materials Chemistry and Physics*, vol. 244, p. 122 731, 2020. DOI: <https://doi.org/10.1016/j.matchemphys.2020.122731>.
- [224] Z. Jiang, T. Zhao, J. Ren, Y. Zhang, and Y. Yue, “NMR evidence for the charge-discharge induced structural evolution in a Li-ion battery glass anode and its impact on the electrochemical performances,” *Nano Energy*, vol. 80, p. 105 589, 2021. DOI: <https://doi.org/10.1016/j.nanoen.2020.105589>.
- [225] G. Qiu, A. Charnas, C. Niu, Y. Wang, W. Wu, and P. D. Ye, “The resurrection of tellurium as an elemental two-dimensional semiconductor,” *npj 2D Materials and Applications*, vol. 6, no. 1, pp. 1–10, 2022. DOI: [10.1038/s41699-022-00293-w](https://doi.org/10.1038/s41699-022-00293-w).
- [226] Z. Y. Chen and R. Qin, “Probing structural chirality of crystals using high-order harmonic generation in solids,” *Physical Review A*, vol. 101, no. 5, p. 53 423, 2020. DOI: [10.1103/PhysRevA.101.053423](https://doi.org/10.1103/PhysRevA.101.053423).
- [227] A. Ben-Moshe *et al.*, “The chain of chirality transfer in tellurium nanocrystals,” *Science*, vol. 372, no. 6543, pp. 729–733, 2021. DOI: [10.1126/science.abf9645](https://doi.org/10.1126/science.abf9645).
- [228] F. Calavalle *et al.*, “Gate-tuneable and chirality-dependent charge-to-spin conversion in tellurium nanowires,” *Nature Materials*, 2022. DOI: [10.1038/s41563-022-01211-7](https://doi.org/10.1038/s41563-022-01211-7).
- [229] Y. Wang *et al.*, “Strain-Engineered Anisotropic Optical and Electrical Properties in 2D Chiral-Chain Tellurium,” *Advanced Materials*, vol. 32, no. 29, pp. 1–9, 2020. DOI: [10.1002/adma.202002342](https://doi.org/10.1002/adma.202002342).
- [230] B. Y. Xia *et al.*, “One-Dimensional Nanostructures: Synthesis, Characterization, and Applications**,” *Advanced Materials*, vol. 15, no. 5, pp. 353–389, 2003. DOI: <https://doi.org/10.1002/adma.200390087>.
- [231] T. I. Lee *et al.*, “High-power density piezoelectric energy harvesting using radially strained ultrathin trigonal tellurium nanowire assembly,” *Advanced Materials*, vol. 25, no. 21, pp. 2920–2925, 2013. DOI: [10.1002/adma.201300657](https://doi.org/10.1002/adma.201300657).

- [232] S. Lin, W. Li, Z. Chen, J. Shen, B. Ge, and Y. Pei, "Tellurium as a high-performance elemental thermoelectric," *Nature Communications*, vol. 7, pp. 1–6, 2016. DOI: 10.1038/ncomms10287.
- [233] P. Li, "Mid-infrared photoconductivity spectra of single tellurium nanowires," *Journal of Applied Physics*, vol. 128, no. 6, 2020. DOI: 10.1063/5.0013188.
- [234] Y. Wang *et al.*, "Field-effect transistors made from solution-grown two-dimensional tellurene," *Nature Electronics*, vol. 1, no. 4, pp. 228–236, 2018. DOI: 10.1038/s41928-018-0058-4.
- [235] A. Kramer, M. L. Van de Put, C. L. Hinkle, and W. G. Vandenberghe, "Tellurium as a successor of silicon for extremely scaled nanowires: a first-principles study," *npj 2D Materials and Applications*, vol. 4, no. 1, pp. 1–8, 2020. DOI: 10.1038/s41699-020-0143-1.
- [236] J. K. Qin *et al.*, "Raman response and transport properties of tellurium atomic chains encapsulated in nanotubes," *Nature Electronics*, vol. 3, no. 3, pp. 141–147, 2020. DOI: 10.1038/s41928-020-0365-4.
- [237] J. Shen *et al.*, "Elemental electrical switch enabling phase segregation-free operation," *Science*, vol. 374, no. 6573, pp. 1390–1394, 2021. DOI: 10.1126/science.abi6332.
- [238] C. Ma, J. Yan, Y. Huang, C. Wang, and G. Yang, "The optical duality of tellurium nanoparticles for broadband solar energy harvesting and efficient photothermal conversion," *Science Advances*, vol. 4, no. 8, pp. 1–10, 2018. DOI: 10.1126/sciadv.aas9894.
- [239] Z. Shi *et al.*, "Two-Dimensional Tellurium: Progress, Challenges, and Prospects," *Nano-Micro Letters*, vol. 12, no. 1, pp. 1–34, 2020. DOI: 10.1007/s40820-020-00427-z.
- [240] Q. Wang, M. Safdar, K. Xu, M. Mirza, Z. Wang, and J. He, "Van der Waals epitaxy and photoresponse of hexagonal tellurium nanoplates on flexible mica sheets," *ACS Nano*, vol. 8, no. 7, pp. 7497–7505, 2014. DOI: 10.1021/nn5028104.
- [241] J. Chen, Y. Dai, Y. Ma, X. Dai, W. Ho, and M. Xie, "Ultrathin β -tellurium layers grown on highly oriented pyrolytic graphite by molecular-beam epitaxy," *Nanoscale*, vol. 9, no. 41, pp. 15 945–15 948, 2017. DOI: 10.1039/c7nr04085g.
- [242] X. Huang *et al.*, "Epitaxial Growth and Band Structure of Te Film on Graphene," *Nano Letters*, vol. 17, no. 8, pp. 4619–4623, 2017. DOI: 10.1021/acs.nanolett.7b01029.
- [243] B. Mayers and Y. Xia, "One-dimensional nanostructures of trigonal tellurium with various morphologies can be synthesized using a solution-phase approach," *Journal of Materials Chemistry*, vol. 12, no. 6, pp. 1875–1881, 2002. DOI: 10.1039/b201058e.
- [244] A. Apte *et al.*, "Polytypism in ultrathin tellurium," *2D Materials*, vol. 6, no. 1, 2019. DOI: 10.1088/2053-1583/aae7f6.
- [245] E. Bianco *et al.*, "Large-area ultrathin Te films with substrate-tunable orientation," *Nanoscale*, vol. 12, no. 23, pp. 12 613–12 622, 2020. DOI: 10.1039/d0nr01251c.

- [246] Z. Xie *et al.*, “Ultrathin 2D Nonlayered Tellurium Nanosheets: Facile Liquid-Phase Exfoliation, Characterization, and Photoresponse with High Performance and Enhanced Stability,” *Advanced Functional Materials*, vol. 28, no. 16, pp. 1–11, 2018. DOI: 10.1002/adfm.201705833.
- [247] K. Itoh, “Structure of Se-Te glasses studied using neutron, X-ray diffraction and reverse Monte Carlo modelling,” *Journal of Solid State Chemistry*, vol. 246, pp. 372–378, 2017. DOI: 10.1016/j.jssc.2016.12.012.
- [248] Y. M. Azhniuk, V. V. Lopushansky, Y. I. Hutych, M. V. Prymak, A. V. Gomonnai, and D. R. Zahn, “Precipitates of selenium and tellurium in II-VI nanocrystal-doped glass probed by Raman scattering,” *Physica Status Solidi (B) Basic Research*, vol. 248, no. 3, pp. 674–679, 2011. DOI: 10.1002/pssb.201046112.
- [249] B. Sari, H. Batiz, C. Zhao, and M. C. Scott, “Structural heterogeneity in non-crystalline Structural heterogeneity in non-crystalline $\text{Te}_x\text{Se}_{1-x}$ thin films,” *Applied Physics Letters*, vol. 121, no. 012101, 2022. DOI: 10.1063/5.0094600.
- [250] M. Aspiala, D. Sukhomlinov, and P. Taskinen, “Standard Gibbs energy of formation of tellurium dioxide measurement by a solid-oxide electrolyte EMF technique,” *Thermochimica Acta*, vol. 573, pp. 95–100, 2013. DOI: <https://doi.org/10.1016/j.tca.2013.08.006>.
- [251] R. J. Ackermann and E. G. Rauh, “A thermodynamic study of the tungsten-oxygen system at high temperatures,” *Journal of Physical Chemistry*, vol. 67, no. 12, pp. 2596–2601, 1963. DOI: <https://doi.org/10.1021/j100806a023>.
- [252] A. Krywonos, J. E. Harvey, and N. Choi, “Linear systems formulation of scattering theory for rough surfaces with arbitrary incident and scattering angles,” *Journal of the Optical Society of America A*, vol. 28, no. 6, pp. 1121–1138, 2011. DOI: 10.1364/JOSAA.28.001121.
- [253] R.-J. Jeng, T. Kishi, N. Matsushita, and T. Yano, “Optical bonding of tellurite glass film on silicate glass,” *International Journal of Applied Glass Science*, vol. 10, no. 2, pp. 248–258, 2019. DOI: <https://doi.org/10.1111/ijag.13094>.
- [254] A.-E. Pasi, H. Glänneskog, M. R. S.-J. Foreman, and C. Ekberg, “Tellurium behavior in the containment sump: dissolution, redox, and radiolysis effects,” *Nuclear Technology*, vol. 207, no. 2, pp. 217–227, 2021. DOI: 10.1080/00295450.2020.1762456.
- [255] W. D. Luedtke, J. Gao, and U. Landman, “Dielectric nanodroplets: Structure, stability, thermodynamics, shape transitions and electrocrystallization in applied electric fields,” *The Journal of Physical Chemistry C*, vol. 115, no. 42, pp. 20 343–20 358, 2011. DOI: 10.1021/jp206673j.
- [256] J. Bonse, S. Hohm, S. V. Kirner, A. Rosenfeld, and J. Kruger, “Laser-induced periodic surface structures- a scientific evergreen,” *IEEE Journal of Selected Topics in Quantum Electronics*, vol. 23, no. 3, p. 7 581 030, 2017. DOI: 10.1109/JSTQE.2016.2614183.
- [257] W. Pamler and E. E. Marinero, “Transient conductivity studies in tellurium thin films,” *Journal of Applied Physics*, vol. 61, no. 6, pp. 2294–2300, 1987. DOI: 10.1063/1.337939.

- [258] D. Woodbury, R. M. Schwartz, E. Rockafellow, J. K. Wahlstrand, and H. M. Milchberg, "Absolute measurement of laser ionization yield in atmospheric pressure range gases over 14 decades," *Physical Review Letters*, vol. 124, p. 013 201, 1 2020. DOI: 10.1103/PhysRevLett.124.013201.
- [259] X. Li *et al.*, "High-pressure dissociation of selenium and tellurium," *Physical Chemistry Chemical Physics*, vol. 20, pp. 6116–6120, 9 2018. DOI: 10.1039/C7CP08002F.
- [260] C. Hejny and M. I. McMahon, "Complex crystal structures of Te-II and Se-III at high pressure," *Physical Review B*, vol. 70, p. 184 109, 18 2004. DOI: 10.1103/PhysRevB.70.184109.
- [261] H. Hu, X. Wang, and H. Zhai, "High-fluence femtosecond laser ablation of silica glass: Effects of laser-induced pressure," *Journal of Physics D: Applied Physics*, vol. 44, no. 13, 2011. DOI: 10.1088/0022-3727/44/13/135202.
- [262] G. Cheng, Y. Wang, J. D. White, Q. Liu, W. Zhao, and G. Chen, "Demonstration of high-density three-dimensional storage in fused silica by femtosecond laser pulses," *Journal of Applied Physics*, vol. 94, no. 3, pp. 1304–1307, 2003. DOI: 10.1063/1.1589596.
- [263] S. Juodkazis *et al.*, "Multi-megabar pressure and super-dense materials created by laser-induced micro-explosion inside of transparent solid," *AIP Conference Proceedings*, vol. 955, no. 1, pp. 1041–1044, 2007. DOI: 10.1063/1.2832894.
- [264] A. Vailionis, E. G. Gamaly, V. Mizeikis, W. Yang, A. V. Rode, and S. Juodkazis, "Evidence of superdense aluminium synthesized by ultrafast microexplosion," *Nature Communications*, vol. 2, no. 445, pp. 1–6, 2011. DOI: 10.1038/ncomms1449.
- [265] C. Hejny and M. I. McMahon, "Large structural modulations in incommensurate Te-III and Se-IV," *Physical Review Letters*, vol. 91, p. 215 502, 21 2003. DOI: 10.1103/PhysRevLett.91.215502.
- [266] C. Hejny, S. Falconi, L. F. Lundegaard, and M. I. McMahon, "Phase transitions in tellurium at high pressure and temperature," *Physical Review B*, vol. 74, p. 174 119, 17 2006. DOI: 10.1103/PhysRevB.74.174119.
- [267] F. Mauri, O. Zakharov, S. de Gironcoli, S. G. Louie, and M. L. Cohen, "Phonon softening and superconductivity in tellurium under pressure," *Physical Review Letters*, vol. 77, pp. 1151–1154, 6 1996. DOI: 10.1103/PhysRevLett.77.1151.
- [268] A. Nussbaum, "Electrical properties of pure tellurium and tellurium-selenium alloys*," *Physical Review*, vol. 94, no. 2, pp. 337–342, 1954. DOI: 10.1063/1.334563.
- [269] R. W. McKay and W. E. Gravelle, "The hall effect and resistivity of tellurium," *Canadian Journal of Physics*, vol. 39, no. 4, pp. 534–550, 1961. DOI: 10.1139/p61-055.
- [270] A. do Carmo Capiotto *et al.*, "Influence of synthesis temperature and atmosphere on Te⁴⁺ ion formation in lithium tellurite glass," *Ceramics International*, vol. 47, no. 22, pp. 32 195–32 201, 2021. DOI: <https://doi.org/10.1016/j.ceramint.2021.08.112>.

- [271] C. W. Lee, J.-Y. Pyo, H.-S. Park, J. H. Yang, and J. Heo, "Immobilization and bonding scheme of radioactive iodine-129 in silver tellurite glass," *Journal of Nuclear Materials*, vol. 492, pp. 239–243, 2017. DOI: <https://doi.org/10.1016/j.jnucmat.2017.05.024>.
- [272] D. Milanese *et al.*, "Investigation of infrared emission and lifetime in Tm-doped 75TeO₂-20ZnO-5Na₂O (mol%) glasses: Effect of Ho and Yb co-doping," *Journal of Non-Crystalline Solids*, vol. 354, no. 18, pp. 1955–1961, 2008. DOI: <https://doi.org/10.1016/j.jnoncrsol.2007.11.010>.
- [273] N. G. Boetti *et al.*, "Thermal stability and spectroscopic properties of erbium-doped niobic-tungsten-tellurite glasses for laser and amplifier devices," *Journal of Luminescence*, vol. 132, no. 5, pp. 1265–1269, 2012. DOI: <https://doi.org/10.1016/j.jlumin.2011.12.057>.
- [274] X. Feng *et al.*, "Towards water-free tellurite glass fiber for 2-5 μ m nonlinear applications," *Fibers*, vol. 1, no. 3, pp. 70–81, 2013. DOI: [10.3390/fib1030070](https://doi.org/10.3390/fib1030070).
- [275] V. K. Malinovsky and A. P. Sokolov, "The nature of boson peak in Raman scattering in glasses," *Solid State Communications*, vol. 57, no. 9, pp. 757–761, 1986. DOI: [10.1016/0038-1098\(86\)90854-9](https://doi.org/10.1016/0038-1098(86)90854-9).
- [276] H. Shintani and H. Tanaka, "Universal link between the boson peak and transverse phonons in glass," *Nature Materials*, vol. 7, no. 11, pp. 870–877, 2008. DOI: [10.1038/nmat2293](https://doi.org/10.1038/nmat2293).
- [277] M. P. Belançon and G. Simon, "Low frequency Raman study of the Boson peak in a tellurite-tungstate glass over temperature," *Journal of Non-Crystalline Solids*, vol. 481, pp. 295–298, 2018. DOI: [10.1016/j.jnoncrsol.2017.11.002](https://doi.org/10.1016/j.jnoncrsol.2017.11.002).
- [278] J. Schroeder, W. Wu, J. L. Apkarian, M. Lee, L. G. Hwa, and C. T. Moynihan, "Raman scattering and Boson peaks in glasses: Temperature and pressure effects," *Journal of Non-Crystalline Solids*, vol. 349, no. 1-3, pp. 88–97, 2004. DOI: [10.1016/j.jnoncrsol.2004.08.265](https://doi.org/10.1016/j.jnoncrsol.2004.08.265).
- [279] J. Bonse, A. Rosenfeld, and J. Krüger, "On the role of surface plasmon polaritons in the formation of laser-induced periodic surface structures upon irradiation of silicon by femtosecond-laser pulses," *Journal of Applied Physics*, vol. 106, no. 10, p. 104 910, 2009. DOI: [10.1063/1.3261734](https://doi.org/10.1063/1.3261734).
- [280] M. Huang and Z. Xu, "Spontaneous scaling down of femtosecond laser-induced apertures towards the 10-nanometer level: the excitation of quasistatic surface plasmons," *Laser & Photonics Reviews*, vol. 8, no. 4, pp. 633–652, 2014. DOI: [10.1002/lpor.201300212](https://doi.org/10.1002/lpor.201300212).
- [281] K. Sokolowski-Tinten *et al.*, "Short-pulse laser induced transient structure formation and ablation studied with time-resolved coherent XUV-scattering," *AIP Conference Proceedings*, vol. 1278, no. 1, pp. 373–379, 2010. DOI: [10.1063/1.3507123](https://doi.org/10.1063/1.3507123).

- [282] T. J.-Y. Derrien, R. Koter, J. Krüger, S. Höhm, A. Rosenfeld, and J. Bonse, “Plasmonic formation mechanism of periodic 100-nm-structures upon femtosecond laser irradiation of silicon in water,” *Journal of Applied Physics*, vol. 116, no. 7, p. 074 902, 2014. DOI: 10.1063/1.4887808.
- [283] A. M. Bonch-Bruevich, M. N. Libenson, V. S. Makin, and V. V. Trubaev, “Surface electromagnetic waves in optics,” *Optical Engineering*, vol. 31, no. 4, pp. 718–730, 1992. DOI: 10.1117/12.56133.
- [284] X. Y. Yang, H. T. Liu, and P. Lalanne, “Cross conversion between surface plasmon polaritons and quasicylindrical waves,” *Physical Review Letters*, vol. 102, p. 153 903, 15 2009. DOI: 10.1103/PhysRevLett.102.153903.
- [285] J. Canning, M. Lancry, K. Cook, A. Weickman, F. Brisset, and B. Poumellec, “Anatomy of a femtosecond laser processed silica waveguide,” *Optical Materials Express*, vol. 1, no. 5, pp. 998–1008, 2011. DOI: 10.1364/OME.1.000998.
- [286] G. Torun, A. Yadav, K. A. Richardson, and Y. Bellouard, “Ultrafast laser direct-writing of self-organized microstructures in Ge-Sb-S chalcogenide glass,” *Frontiers in Physics*, vol. 10, 2022. DOI: 10.3389/fphy.2022.883319.
- [287] C. Schultz-Sellack, “Diathermansie einer reihe von stoffen für wärme sehr geringer brechbarkeit,” *Annalen der Physik*, vol. 215, no. 1, pp. 182–187, 1870. DOI: <https://doi.org/10.1002/andp.18702150111>.
- [288] C. Lin, C. Rüssel, and S. Dai, “Chalcogenide glass-ceramics: functional design and crystallization mechanism,” *Progress in Materials Science*, vol. 93, pp. 1–44, 2018. DOI: <https://doi.org/10.1016/j.pmatsci.2017.11.001>.
- [289] S. H. Messaddeq, V. K. Tikhomirov, Y. Messaddeq, D. Lezal, and M. S. Li, “Light-induced relief gratings and a mechanism of metastable light-induced expansion in chalcogenide glasses,” *Physical Review B*, vol. 63, p. 224 203, 22 2001. DOI: 10.1103/PhysRevB.63.224203.
- [290] R. Zallen, “Chalcogenide glasses and organic polymers,” in *The Physics of Amorphous Solids*. John Wiley Sons, Ltd, 1998, ch. 3, pp. 86–134. DOI: <https://doi.org/10.1002/9783527617968.ch3>.
- [291] R. A. Loretz, T. J. Loretz, and K. A. Richardson, “Predictive method to assess chalcogenide glass properties: bonding, density and the impact on glass properties,” *Optical Materials Express*, vol. 12, no. 5, pp. 2012–2027, 2022. DOI: 10.1364/OME.455523.
- [292] J. Sanghera and D. Gibson, “5-Optical properties of chalcogenide glasses and fibers,” in *Chalcogenide Glasses*, Woodhead Publishing, 2014, pp. 113–138. DOI: <https://doi.org/10.1533/9780857093561.1.113>.
- [293] C. Nathan, “A solution based approach to the fabrication of novel chalcogenide glass materials and structures,” *PhD dissertation. Clemson University*, 2010. [Online]. Available: https://tigerprints.clemson.edu/all_dissertations/554.

- [294] I. Kotsalas, D. Papadimitriou, C. Raptis, M. Vlcek, and M. Frumar, "Raman study of photostructural changes in amorphous $\text{Ge}_x\text{Sb}_{0.4x}\text{S}_{0.61}$," *Journal of Non-Crystalline Solids*, vol. 226, no. 1, pp. 85–91, 1998. DOI: [https://doi.org/10.1016/S0022-3093\(97\)00493-6](https://doi.org/10.1016/S0022-3093(97)00493-6).
- [295] Schott. "Infrared glasses and materials." (The last access on 28.03.2023). (), [Online]. Available: <https://www.schott.com/en-au/products/ir-materials-p1000261/technical-details>.
- [296] L. Červinka, O. Smotlacha, J. Bergerová, and L. Tichý, "The structure of the glassy Ge-Sb-S system and its connection with the MRO structures of GeS_2 and Sb_2S_3 ," *Journal of Non-Crystalline Solids*, vol. 137-138, pp. 123–126, 1991. DOI: [https://doi.org/10.1016/S0022-3093\(05\)80072-9](https://doi.org/10.1016/S0022-3093(05)80072-9).
- [297] S. Neov *et al.*, "Neutron diffraction study on the medium and short-range order of ternary chalcogenide glasses," *Journal of Materials Science*, vol. 34, no. 15, pp. 3669–3676, 1999. DOI: [10.1023/A:1004699205414](https://doi.org/10.1023/A:1004699205414).
- [298] I. Pethes *et al.*, "Atomic level structure of Ge-Sb-S glasses: Chemical short range order and long Sb-S bonds," *Journal of Alloys and Compounds*, vol. 774, pp. 1009–1016, 2019. DOI: <https://doi.org/10.1016/j.jallcom.2018.09.334>.
- [299] A. V. Kolobov, Y. Saito, P. Fons, and M. Krbal, "Structural metastability in chalcogenide semiconductors: The role of chemical bonding," *physica status solidi (b)*, vol. 257, no. 11, p. 2 000 138, 2020. DOI: <https://doi.org/10.1002/pssb.202000138>.
- [300] V. Nazabal and J.-L. Adam, "(invited)Infrared luminescence of chalcogenide glasses doped with rare earth ions and their potential applications," *Optical Materials: X*, vol. 15, p. 100 168, 2022. DOI: <https://doi.org/10.1016/j.omx.2022.100168>.
- [301] A. Kumar, R. Shukla, A. Kumar, and R. Gupta, "Light induced effects defects in chalcogenide glassy semiconductors: a review," *Infrared Physics Technology*, vol. 102, p. 103 056, 2019. DOI: <https://doi.org/10.1016/j.infrared.2019.103056>.
- [302] T. Anderson *et al.*, "Femtosecond laser photo-response of $\text{Ge}_{23}\text{Sb}_7\text{S}_{70}$ films," *Optics Express*, vol. 16, no. 24, pp. 20 081–20 098, 2008. DOI: [10.1364/OE.16.020081](https://doi.org/10.1364/OE.16.020081).
- [303] S. Geiger *et al.*, "Understanding aging in chalcogenide glass thin films using precision resonant cavity refractometry," *Optical Materials Express*, vol. 9, no. 5, pp. 2252–2263, 2019. DOI: [10.1364/OME.9.002252](https://doi.org/10.1364/OME.9.002252).
- [304] S. Raoux, "Scaling properties of phase change materials," in *Phase Change Materials*. Springer US, 2009, pp. 99–124. DOI: [10.1007/978-0-387-84874-7_6](https://doi.org/10.1007/978-0-387-84874-7_6).
- [305] T. Kavetsky, O. Shpotyuk, I. Kaban, and W. Hoyer, "Radiation-modified structure of $\text{Ge}_{25}\text{Sb}_{15}\text{S}_{60}$ and $\text{Ge}_{35}\text{Sb}_5\text{S}_{60}$ glasses," *The Journal of Chemical Physics*, vol. 128, no. 24, p. 244 514, 2008. DOI: [10.1063/1.2945300](https://doi.org/10.1063/1.2945300).
- [306] L. Calvez, "Chalcogenide glasses and glass-ceramics: transparent materials in the infrared for dual applications," *Comptes Rendus Physique*, vol. 18, no. 5, pp. 314–322, 2017. DOI: <https://doi.org/10.1016/j.crhy.2017.05.003>.

- [307] J.-L. Adam, L. Calvez, J. Trolès, and V. Nazabal, "Chalcogenide glasses for infrared photonics," *International Journal of Applied Glass Science*, vol. 6, no. 3, pp. 287–294, 2015. DOI: <https://doi.org/10.1111/ijag.12136>.
- [308] N. Carlie *et al.*, "Integrated chalcogenide waveguide resonators for mid-IR sensing: leveraging material properties to meet fabrication challenges," *Optics Express*, vol. 18, no. 25, pp. 26 728–26 743, 2010. DOI: 10.1364/OE.18.026728.
- [309] B. J. Eggleton, B. Luther-Davies, and K. Richardson, "Chalcogenide photonics," *Nature Photonics*, vol. 5, no. 3, pp. 141–148, 2011. DOI: <https://doi.org/10.1038/nphoton.2011.309>.
- [310] K. Richardson, D. Krol, and K. Hirao, "Glasses for photonic applications," *International Journal of Applied Glass Science*, vol. 1, no. 1, pp. 74–86, 2010. DOI: <https://doi.org/10.1111/j.2041-1294.2010.00008.x>.
- [311] G. Tao *et al.*, "Infrared fibers," *Advances in Optics and Photonics*, vol. 7, no. 2, pp. 379–458, 2015. DOI: 10.1364/AOP.7.000379.
- [312] L. Li *et al.*, "Integrated flexible chalcogenide glass photonic devices," *Nature Photonics*, vol. 8, no. 8, pp. 643–649, 2014. DOI: 10.1038/nphoton.2014.138.
- [313] S. D. Jackson, "Towards high-power mid-infrared emission from a fibre laser," *Nature Photonics*, vol. 6, no. 7, pp. 423–431, 2012. DOI: 10.1038/nphoton.2012.149.
- [314] I. Kubat and O. Bang, "Multimode supercontinuum generation in chalcogenide glass fibres," *Optics Express*, vol. 24, no. 3, pp. 2513–2526, 2016. DOI: 10.1364/OE.24.002513.
- [315] J. Harbold, F. Ilday, F. Wise, and B. Aitken, "Highly nonlinear Ge-As-Se and Ge-As-S-Se glasses for all-optical switching," *IEEE Photonics Technology Letters*, vol. 14, no. 6, pp. 822–824, 2002. DOI: 10.1109/LPT.2002.1003105.
- [316] J. De Neufville, S. Moss, and S. Ovshinsky, "Photostructural transformations in amorphous As₂Se₃ and As₂S₃ films," *Journal of Non-Crystalline Solids*, vol. 13, no. 2, pp. 191–223, 1974. DOI: [https://doi.org/10.1016/0022-3093\(74\)90091-X](https://doi.org/10.1016/0022-3093(74)90091-X).
- [317] J. S. Berkes, S. W. Ing, and W. J. Hillegas, "Photodecomposition of Amorphous As₂Se₃ and As₂S₃," *Journal of Applied Physics*, vol. 42, no. 12, pp. 4908–4916, 1971. DOI: 10.1063/1.1659873.
- [318] K. Tanaka, "Light-induced anisotropy in amorphous chalcogenides," *Science*, vol. 277, no. 5333, pp. 1786–1787, 1997. DOI: 10.1126/science.277.5333.1786.
- [319] K. Tanaka, "Photo-induced phenomena in chalcogenide glass: comparison with those in oxide glass and polymer," *Journal of Non-Crystalline Solids*, vol. 352, no. 23, pp. 2580–2584, 2006. DOI: <https://doi.org/10.1016/j.jnoncrysol.2006.02.070>.
- [320] K. Tanaka, A. Saitoh, and N. Terakado, "Giant photo-expansion in chalcogenide glass," *Journal of Optoelectronics and Advanced Materials*, vol. 8, no. 6, pp. 2058–2065, 2006. [Online]. Available: <http://hdl.handle.net/2115/18936>.

- [321] L. Calvez, Z. Yang, and P. Lucas, "Reversible giant photocontraction in chalcogenide glass," *Optics Express*, vol. 17, no. 21, pp. 18 581–18 589, 2009. DOI: 10.1364/OE.17.018581.
- [322] N. Long, M. Xia, P. Zhang, Q. Nie, and Y. Xu, "Effect of chemical composition on the structure, optical properties and femtosecond laser ablation performance of Ge-Sb-Se glasses," *Journal of Alloys and Compounds*, vol. 779, pp. 543–549, 2019. DOI: <https://doi.org/10.1016/j.jallcom.2018.11.058>.
- [323] S. H. Messaddeq, A. Dumont, A. Douaud, M. El-Amraoui, and Y. Messaddeq, "Formation of cross-superposed LIPSSs on bulk chalcogenide glasses using fs-laser," *Advanced Optical Technologies*, vol. 7, no. 5, pp. 311–319, 2018. DOI: doi:10.1515/aot-2018-0031.
- [324] M. Zhang *et al.*, "Femtosecond laser induced damage on Ge-As-S chalcogenide glasses," *Optical Materials Express*, vol. 9, no. 2, pp. 555–561, 2019. DOI: 10.1364/OME.9.000555.
- [325] L. Zhu *et al.*, "Optical and thermal stability of Ge-as-Se chalcogenide glasses for femtosecond laser writing," *Optical Materials*, vol. 85, pp. 220–225, 2018. DOI: <https://doi.org/10.1016/j.optmat.2018.08.041>.
- [326] L. Petit *et al.*, "Effect of IR femtosecond laser irradiation on the structure of new sulfoselenide glasses," *Optical Materials*, vol. 29, no. 8, pp. 1075–1083, 2007. DOI: <https://doi.org/10.1016/j.optmat.2006.04.008>.
- [327] M. Gecevičius, M. Beresna, J. Zhang, W. Yang, H. Takebe, and P. G. Kazansky, "Extraordinary anisotropy of ultrafast laser writing in glass," *Optics Express*, vol. 21, no. 4, pp. 3959–3968, 2013. DOI: 10.1364/OE.21.003959.
- [328] Y. Zhang *et al.*, "Raman gain and femtosecond laser induced damage of Ge-As-S chalcogenide glasses," *Optics Express*, vol. 25, no. 8, pp. 8886–8895, 2017. DOI: 10.1364/OE.25.008886.
- [329] L. Pan *et al.*, "Optical properties of Ge-Sb-Se thin films induced by femtosecond laser," *Optics Communications*, vol. 496, p. 127 123, 2021. DOI: <https://doi.org/10.1016/j.optcom.2021.127123>.
- [330] L. Liu *et al.*, "The mutual influence between rare earth element doping and femtosecond laser-induced effects in Ga-As-Sb-S chalcogenide glass," *Ceramics International*, vol. 47, no. 5, pp. 6388–6396, 2021. DOI: <https://doi.org/10.1016/j.ceramint.2020.10.219>.
- [331] C. Xiao *et al.*, "Study on the factors affecting the refractive index change of chalcogenide films induced by femtosecond laser," *Optics Laser Technology*, vol. 120, p. 105 708, 2019. DOI: <https://doi.org/10.1016/j.optlastec.2019.105708>.
- [332] C. D'Amico *et al.*, "Ultrafast laser-induced refractive index changes in Ge₁₅As₁₅S₇₀ chalcogenide glass," *Optical Materials Express*, vol. 6, no. 6, pp. 1914–1928, 2016. DOI: 10.1364/OME.6.001914.
- [333] Y. Hu *et al.*, "Mid-infrared nonlinear optical performances of Ge-Sb-S chalcogenide glasses," *Optical Materials Express*, vol. 11, no. 3, pp. 695–706, 2021. DOI: 10.1364/OME.412731.

- [334] M. Xie *et al.*, “Correlation among Structure, Water Peak Absorption, and Femtosecond Laser Ablation Properties of Ge-Sb-Se Chalcogenide Glasses,” *Journal of Physical Chemistry C*, vol. 122, no. 3, pp. 1681–1687, 2018. DOI: 10.1021/acs.jpcc.7b10894.
- [335] C. You *et al.*, “Mid-infrared femtosecond laser-induced damages in As₂S₃ and As₂Se₃ chalcogenide glasses,” *Scientific Reports*, vol. 7, no. 1, pp. 2–10, 2017. DOI: 10.1038/s41598-017-06592-3.
- [336] G. Dong *et al.*, “Microstructural modification of chalcogenide glasses by femtosecond laser,” *Journal of Non-Crystalline Solids*, vol. 357, no. 11, pp. 2392–2395, 2011. DOI: <https://doi.org/10.1016/j.jnoncrysol.2010.11.074>.
- [337] J. David Musgraves *et al.*, “Effect of replacement of As by Ge and Sb on the photo-response under near infrared femtosecond laser irradiation in As-based sulfide glasses,” *International Journal of Applied Glass Science*, vol. 2, no. 4, pp. 308–320, 2011. DOI: <https://doi.org/10.1111/j.2041-1294.2011.00060.x>.
- [338] W. Liu, Q. Zhang, L. Liu, L. Xu, Y. Xu, and G. Chen, “Enhancement of second-order optical nonlinearity in photo-darkened Ge₂₅Sb₁₀S₆₅ chalcogenide glass by femtosecond laser light,” *Optics Communications*, vol. 282, no. 10, pp. 2081–2084, 2009. DOI: <https://doi.org/10.1016/j.optcom.2009.02.025>.
- [339] J. M. Almeida, K. T. Paula, C. B. Arnold, and C. R. Mendonça, “Sub-wavelength self-organization of chalcogenide glass by direct laser writing,” *Optical Materials*, vol. 84, pp. 259–262, 2018. DOI: <https://doi.org/10.1016/j.optmat.2018.06.068>.
- [340] L. Liu *et al.*, “Femtosecond laser ablation and photo-induced effects of As₄₀S₆₀, Ga_{0.8}As_{39.2}S₆₀ and Ga_{0.8}As_{29.2}Sb₁₀S₆₀ chalcogenide glasses,” *Optical Materials Express*, vol. 9, no. 9, pp. 3582–3593, 2019. DOI: 10.1364/OME.9.003582.
- [341] T. Gretzinger, T. T. Fernandez, S. Gross, A. Arriola, and M. J. Withford, “Boson band mapping: revealing ultrafast laser induced structural modifications in chalcogenide glass,” *Optics Letters*, vol. 45, no. 13, pp. 3369–3372, 2020. DOI: 10.1364/OL.393511.
- [342] W. Ma *et al.*, “Surface damage and threshold determination of Ge-As-Se glasses in femtosecond pulsed laser micromachining,” *Journal of the American Ceramic Society*, vol. 103, no. 1, pp. 94–102, 2020. DOI: <https://doi.org/10.1111/jace.16699>.
- [343] M. Somayaji, C. D’Amico, Y. Wu, J. Troles, and R. Stoian, “Influence of thermal annealing on ultrafast laser-induced local densification in bulk sulfur-based chalcogenide glasses,” *physica status solidi (a)*, vol. 216, no. 3, p. 1 800 568, 2019. DOI: <https://doi.org/10.1002/pssa.201800568>.
- [344] L. Petit *et al.*, “Effect of Ga and Se addition on the “near-surface” photo-response of new Ge-based chalcogenide glasses under IR femtosecond laser exposure,” *Optical Materials*, vol. 31, no. 6, pp. 965–969, 2009. DOI: <https://doi.org/10.1016/j.optmat.2008.11.001>.

- [345] P. Masselin, D. Le Coq, and E. Bychkov, "Refractive index variations induced by femtosecond laser direct writing in the bulk of As_2S_3 glass at high repetition rate," *Optical Materials*, vol. 33, no. 6, pp. 872–876, 2011. DOI: <https://doi.org/10.1016/j.optmat.2011.01.014>.
- [346] Q. Zhang, W. Liu, L. Liu, L. Xu, Y. Xu, and G. Chen, "Large and opposite changes of the third-order optical nonlinearities of chalcogenide glasses by femtosecond and continuous-wave laser irradiation," *Applied Physics Letters*, vol. 91, no. 18, p. 181 917, 2007. DOI: 10.1063/1.2805636.
- [347] M. R. Vázquez *et al.*, "Femtosecond laser inscription of nonlinear photonic circuits in gallium lanthanum sulphide glass," *Journal of Physics: Photonics*, vol. 1, no. 1, p. 015 006, 2018. DOI: 10.1088/2515-7647/aade60.
- [348] H. Wang *et al.*, "In-situ and ex-situ characterization of femtosecond laser-induced ablation on As_2S_3 chalcogenide glasses and advanced grating structures fabrication," *Materials*, vol. 12, no. 1, 2019. DOI: 10.3390/ma12010072.
- [349] Q. Zhang, H. Lin, B. Jia, L. Xu, and M. Gu, "Nanogratings and nanoholes fabricated by direct femtosecond laser writing in chalcogenide glasses," *Optics Express*, vol. 18, no. 7, pp. 6885–6890, 2010. DOI: 10.1364/OE.18.006885.
- [350] X. Yu *et al.*, "In-situ and ex-situ physical scenario of the femtosecond laser-induced periodic surface structures," *Optics Express*, vol. 27, no. 7, pp. 10 087–10 097, 2019. DOI: 10.1364/OE.27.010087.
- [351] X. Yu *et al.*, "Femtosecond laser-induced large area of periodic structures on chalcogenide glass via twice laser direct-writing scanning process," *Optics Laser Technology*, vol. 124, p. 105 977, 2020. DOI: <https://doi.org/10.1016/j.optlastec.2019.105977>.
- [352] S. H. Messaddeq, R. Vallée, P. Soucy, M. Bernier, M. El-Amraoui, and Y. Messaddeq, "Self-organized periodic structures on Ge-S based chalcogenide glass induced by femtosecond laser irradiation," *Optics Express*, vol. 20, no. 28, pp. 29 882–29 889, 2012. DOI: 10.1364/OE.20.029882.
- [353] Y. Zhang *et al.*, "Femtosecond-laser-induced submicron grating periodic structures on As_2S_3 and $\text{As}_{35}\text{Se}_{65}$ glasses," *Optics Laser Technology*, vol. 108, pp. 306–309, 2018. DOI: <https://doi.org/10.1016/j.optlastec.2018.07.002>.
- [354] S. Juodkazis, H. Misawa, O. A. Louchev, and K. Kitamura, "Femtosecond laser ablation of chalcogenide glass: explosive formation of nano-fibres against thermo-capillary growth of micro-spheres," *Nanotechnology*, vol. 17, no. 19, p. 4802, 2006. DOI: 10.1088/0957-4484/17/19/003.
- [355] D. Le Coq, P. Masselin, C. Przygodski, and E. Bychkov, "Morphology of waveguide written by femtosecond laser in As_2S_3 glass," *Journal of Non-Crystalline Solids*, vol. 355, no. 37, pp. 1832–1835, 2009. DOI: <https://doi.org/10.1016/j.jnoncrysol.2009.05.065>.

- [356] M. Hughes, W. Yang, and D. Hewak, "Fabrication and characterization of femtosecond laser written waveguides in chalcogenide glass," *Applied Physics Letters*, vol. 90, no. 13, p. 131 113, 2007. DOI: 10.1063/1.2718486.
- [357] A. Zoubir *et al.*, "Direct femtosecond laser writing of waveguides in As₂S₃ thin films," *Optics Letters*, vol. 29, no. 7, pp. 748–750, 2004. DOI: 10.1364/OL.29.000748.
- [358] H. L. Butcher, D. G. MacLachlan, D. Lee, R. R. Thomson, and D. Weidmann, "Demonstration and characterization of ultrafast laser-inscribed mid-infrared waveguides in chalcogenide glass IG2," *Optics Express*, vol. 26, no. 8, pp. 10 930–10 943, 2018. DOI: 10.1364/OE.26.010930.
- [359] M. A. Hughes, W. Yang, and D. W. Hewak, "Spectral broadening in femtosecond laser written waveguides in chalcogenide glass," *Journal of the Optical Society of America B*, vol. 26, no. 7, pp. 1370–1378, 2009. DOI: 10.1364/JOSAB.26.001370.
- [360] C. Florea, J. Sanghera, and I. Aggarwal, "Direct-write gratings in chalcogenide bulk glasses and fibers using a femtosecond laser," *Optical Materials*, vol. 30, no. 10, pp. 1603–1606, 2008. DOI: <https://doi.org/10.1016/j.optmat.2007.10.006>.
- [361] T. Kohoutek *et al.*, "Highly efficient relief diffraction gratings inscribed in a chalcogenide bulk glass by a femtosecond laser," in *Micro-Optics 2012*, SPIE, vol. 8428, 2012, p. 84281C. DOI: 10.1117/12.921381.
- [362] M. Popescu, A. Velea, S. Miclos, and D. Savastru, "Optics of microlenses created by irradiation of As₂S₃ amorphous chalcogenide films with femtosecond laser pulses," *Philosophical Magazine Letters*, vol. 93, no. 4, pp. 213–220, 2013. DOI: 10.1080/09500839.2012.760058.
- [363] C. D'Amico, G. Martin, J. Troles, G. Cheng, and R. Stoian, "Multiscale laser written photonic structures in bulk chalcogenide glasses for infrared light transport and extraction," *Photonics*, vol. 8, no. 6, 2021. DOI: 10.3390/photonics8060211.
- [364] H. L. Butcher, D. G. MacLachlan, D. Lee, R. R. Thomson, and D. Weidmann, "Ultrafast laser-inscribed mid-infrared evanescent field directional couplers in GeAsSe chalcogenide glass," *OSA Continuum*, vol. 1, no. 1, pp. 221–228, 2018. DOI: 10.1364/OSAC.1.000221.
- [365] D. M. Simanovskii, H. A. Schwettman, H. Lee, and A. J. Welch, "Midinfrared optical breakdown in transparent dielectrics," *Physical Review Letters*, vol. 91, p. 107 601, 10 2003. DOI: 10.1103/PhysRevLett.91.107601.
- [366] T. Q. Jia *et al.*, "Ultraviolet-infrared femtosecond laser-induced damage in fused silica and CaF₂ crystals," *Physical Review B*, vol. 73, p. 054 105, 5 2006. DOI: 10.1103/PhysRevB.73.054105.
- [367] C. B. Schaffer, J. F. García, and E. Mazur, "Bulk heating of transparent materials using a high-repetition-rate femtosecond laser," *Applied Physics A: Materials Science and Processing*, vol. 76, no. 3, pp. 351–354, 2003. DOI: 10.1007/s00339-002-1819-4.

- [368] H. Jain, A. Kovalskiy, and M. Vlcek, "Chalcogenide glass resists for lithography," in *Chalcogenide Glasses*, Woodhead Publishing, 2014, pp. 562–596. DOI: <https://doi.org/10.1533/9780857093561.2.562>.
- [369] J. Orava, T. Wagner, M. Krbal, T. Kohoutek, M. Vlcek, and M. Frumar, "Selective wet-etching of undoped and silver photodoped amorphous thin films of chalcogenide glasses in inorganic alkaline solutions," *Journal of Non-Crystalline Solids*, vol. 352, no. 9, pp. 1637–1640, 2006. DOI: <https://doi.org/10.1016/j.jnoncrysol.2005.09.041>.
- [370] B. J. Riley, S. Sundaram, B. R. Johnson, and L. V. Saraf, "Differential etching of chalcogenides for infrared photonic waveguide structures," *Journal of Non-Crystalline Solids*, vol. 354, no. 10, pp. 813–816, 2008. DOI: <https://doi.org/10.1016/j.jnoncrysol.2007.08.061>.
- [371] J. Lapointe, J.-P. Bérubé, S. Pouliot, and R. Vallée, "Control and enhancement of photo-induced refractive index modifications in fused silica," *OSA Continuum*, vol. 3, no. 10, pp. 2851–2862, 2020. DOI: [10.1364/OSAC.406247](https://doi.org/10.1364/OSAC.406247).
- [372] E. Bricchi, B. G. Klappauf, and P. G. Kazansky, "Form birefringence and negative index change created by femtosecond direct writing in transparent materials," *Optics Letters*, vol. 29, no. 1, pp. 119–121, 2004. DOI: [10.1364/OL.29.000119](https://doi.org/10.1364/OL.29.000119).
- [373] B. McMillen, C. Athanasiou, and Y. Bellouard, "Femtosecond laser direct-write waveplates based on stress-induced birefringence," *Optics Express*, vol. 24, no. 24, pp. 27 239–27 252, 2016. DOI: [10.1364/OE.24.027239](https://doi.org/10.1364/OE.24.027239).
- [374] Y. Wang, M. Lancry, M. Cavillon, and B. Poumellec, "Lifetime prediction of nanogratings inscribed by a femtosecond laser in silica glass," *Optics Letters*, vol. 47, no. 5, pp. 1242–1245, 2022. DOI: [10.1364/OL.449486](https://doi.org/10.1364/OL.449486).
- [375] P. Knotek and L. Tichy, "On photo-expansion and microlens formation in $(\text{GeS}_2)_{0.74}(\text{Sb}_2\text{S}_3)_{0.26}$ chalcogenide glass," *Materials Research Bulletin*, vol. 47, no. 12, pp. 4246–4251, 2012. DOI: <https://doi.org/10.1016/j.materresbull.2012.09.024>.
- [376] N. Bellini *et al.*, "Femtosecond laser fabricated monolithic chip for optical trapping and stretching of single cells," *Optics Express*, vol. 18, no. 5, pp. 4679–4688, 2010. DOI: [10.1364/OE.18.004679](https://doi.org/10.1364/OE.18.004679).
- [377] H. Ma, R. A. Zakoldaev, A. Rudenko, M. M. Sergeev, V. P. Veiko, and T. E. Itina, "Well-controlled femtosecond laser inscription of periodic void structures in porous glass for photonic applications," *Optics Express*, vol. 25, no. 26, pp. 33 261–33 270, 2017. DOI: [10.1364/OE.25.033261](https://doi.org/10.1364/OE.25.033261).
- [378] R. Graf, A. Fernandez, M. Dubov, H. Brueckner, B. Chichkov, and A. Apolonski, "Pearl-chain waveguides written at megahertz repetition rate," *Applied Physics B*, vol. 87, pp. 21–27, 2007. DOI: <https://doi.org/10.1007/s00340-006-2480-y>.

- [379] J. Musgraves *et al.*, “Comparison of the optical, thermal and structural properties of Ge-Sb-S thin films deposited using thermal evaporation and pulsed laser deposition techniques,” *Acta Materialia*, vol. 59, no. 12, pp. 5032–5039, 2011. DOI: <https://doi.org/10.1016/j.actamat.2011.04.060>.
- [380] L. Petit *et al.*, “Compositional dependence of the nonlinear refractive index of new germanium-based chalcogenide glasses,” *Journal of Solid State Chemistry*, vol. 182, no. 10, pp. 2756–2761, 2009. DOI: <https://doi.org/10.1016/j.jssc.2009.07.027>.
- [381] S. K. Pal, N. Mehta, V. Mikla, A. Horvat, V. Minkovich, and A. Dahshan, “Insights into the physical aging in chalcogenide glasses: A case study of a first-generation As₂Se₃ binary glass,” *Coordination Chemistry Reviews*, vol. 442, p. 213 992, 2021. DOI: <https://doi.org/10.1016/j.ccr.2021.213992>.
- [382] A. Kozdras, “Kinetics of light-assisted physical ageing in S-rich arsenic sulphide glasses,” *Bulletin of Materials Science*, vol. 39, pp. 997–1000, 2016. DOI: <https://doi.org/10.1007/s12034-016-1252-5>.
- [383] H. Takebe, H. Maeda, and K. Morinaga, “Compositional variation in the structure of Ge-S glasses,” *Journal of Non-Crystalline Solids*, vol. 291, no. 1, pp. 14–24, 2001. DOI: [https://doi.org/10.1016/S0022-3093\(01\)00820-1](https://doi.org/10.1016/S0022-3093(01)00820-1).
- [384] Z. Černošek, E. Černošková, and L. Beneš, “Raman scattering in GeS₂ glass and its crystalline polymorphs compared,” *Journal of Molecular Structure*, vol. 435, no. 2, pp. 193–198, 1997. DOI: [https://doi.org/10.1016/S0022-2860\(97\)00184-1](https://doi.org/10.1016/S0022-2860(97)00184-1).
- [385] C. Lin *et al.*, “Network Structure in GeS₂-Sb₂S₃ Chalcogenide Glasses: Raman Spectroscopy and Phase Transformation Study,” *The Journal of Physical Chemistry C*, vol. 116, no. 9, pp. 5862–5867, 2012. DOI: [10.1021/jp208614j](https://doi.org/10.1021/jp208614j).
- [386] L. Petit *et al.*, “Effect of the substitution of S for Se on the structure of the glasses in the system Ge_{0.23}Sb_{0.07}S_{0.70x}Se_x,” *Journal of Physics and Chemistry of Solids*, vol. 66, no. 10, pp. 1788–1794, 2005. DOI: <https://doi.org/10.1016/j.jpics.2005.08.090>.
- [387] N. J. Tostanoski, E. J. Heilweil, P. F. Wachtel, J. D. Musgraves, and S. K. Sundaram, “Structure-terahertz property relationship and femtosecond laser irradiation effects in chalcogenide glasses,” *Journal of Non-Crystalline Solids*, vol. 600, p. 122 020, 2023. DOI: <https://doi.org/10.1016/j.jnoncrysol.2022.122020>.
- [388] G. Torun, A. Romashkina, T. Kishi, and Y. Bellouard, “Femtosecond laser direct-write photoconductive patterns on tellurite glass,” 2023, submitted.
- [389] S. Kiyama, S. Matsuo, S. Hashimoto, and Y. Morihira, “Examination of etching agent and etching mechanism on femtosecond laser microfabrication of channels inside vitreous silica substrates,” *The Journal of Physical Chemistry C*, vol. 113, no. 27, pp. 11 560–11 566, 2009. DOI: [10.1021/jp900915r](https://doi.org/10.1021/jp900915r).
- [390] E. V. Shkol’nikov, “Thermodynamics of the dissolution of amorphous and polymorphic TiO₂ modifications in acid and alkaline media,” *Russian Journal of Physical Chemistry A*, vol. 90, pp. 567–571, 2016. DOI: <https://doi.org/10.1134/S0036024416030286>.

- [391] M. Ochoa, P. Roldán-Varona, J. F. Algorri, J. M. López-Higuera, and L. Rodríguez-Cobo, "Polarisation-independent ultrafast laser selective etching processing in fused silica," *Lab Chip*, vol. 23, pp. 1752–1757, 7 2023. DOI: 10.1039/D3LC00052D.
- [392] J. Sunada, K. Oishi, A. Kasai, and T. Kitahara, "Photoconduction in Te thin film after exposure to UV light," *Japanese Journal of Applied Physics*, vol. 21, no. 12, p. 1781, 1982. DOI: 10.1143/JJAP.21.1781.
- [393] K. Oishi, K. Okamoto, and J. Sunada, "Photoconduction on photo-oxidized tellurium thin films," *Thin Solid Films*, vol. 148, no. 1, pp. 29–40, 1987. DOI: [https://doi.org/10.1016/0040-6090\(87\)90118-0](https://doi.org/10.1016/0040-6090(87)90118-0).
- [394] J. Sunada, K. Okamoto, K. Oishi, and S. Shimazu, "UV photo-oxidation of Te films (photon energy dependence)," *Applied Surface Science*, vol. 33-34, no. C, pp. 434–442, 1988. DOI: 10.1016/0169-4332(88)90337-6.
- [395] J. Sunada, Y. Hashimoto, K. Oishi, and K.-i. Fukuchi, "The role of oxygen species in photoconduction of surface oxidized Ge films," *Physics Letters A*, vol. 151, no. 8, pp. 447–451, 1990. DOI: 10.1016/0375-9601(90)90920-J.
- [396] J. Sunada, K. Osada, T. Namekawa, K. Oishi, and K.-i. Fukuchi, "Photoconduction in Te and Te-oxide bilayered film sensitive to UV light," *Physics Letters A*, vol. 146, no. 1-2, pp. 85–88, 1990. DOI: 10.1016/0375-9601(90)90035-M.
- [397] M. Palomba, U. Coscia, G. Carotenuto, S. De Nicola, and G. Ambrosone, "Fabrication and characterizations of films made of Te/TeO₂ nanopowder consolidated by poly(methyl methacrylate)," *Physica Status Solidi (C) Current Topics in Solid State Physics*, vol. 12, no. 12, pp. 1317–1321, 2015. DOI: 10.1002/pssc.201510134.
- [398] D. Tsiulyanu, S. Marian, V. Miron, and H. D. Liess, "High sensitive tellurium based NO₂ gas sensor," *Sensors and Actuators, B: Chemical*, vol. 73, no. 1, pp. 35–39, 2001. DOI: 10.1016/S0925-4005(00)00659-6.
- [399] D. Tsiulyanu, "Gas-sensing features of nanostructured tellurium thin films," *Beilstein Journal of Nanotechnology*, vol. 11, pp. 1010–1018, 2020. DOI: 10.3762/bjnano.11.85.
- [400] F. Arab, M. Mousavi-Kamazani, and M. Salavati-Niasari, "Synthesis, characterization, and optical properties of Te, Te/TeO₂ and TeO₂ nanostructures: Via a one-pot hydrothermal method," *RSC Advances*, vol. 6, no. 75, pp. 71 472–71 480, 2016. DOI: 10.1039/c6ra10770b.
- [401] R. N. Hampton, W. Hong, G. A. Saunders, and R. A. El-Mallawany, "The electrical conductivity of pure and binary TeO₂ glasses," *Journal of Non-Crystalline Solids*, vol. 94, no. 3, pp. 307–314, 1987. DOI: [https://doi.org/10.1016/S0022-3093\(87\)80066-2](https://doi.org/10.1016/S0022-3093(87)80066-2).
- [402] M. Çelikkbilek, "Investigation of glass formation behavior, glass properties and thermochromic behavior of tellurite systems," *Ph.D. Thesis, Istanbul Technical University*, 2013. [Online]. Available: <http://hdl.handle.net/11527/18896>.

- [403] G. Fischer, G. K. White, and S. B. Woods, "Thermal and electrical resistivity of tellurium at low temperatures," *Physical Review*, vol. 106, no. 3, pp. 480–483, 1957. DOI: 10.1103/PhysRev.106.480.
- [404] M. A. Dinno, M. Schwartz, and B. Giammara, "Structural dependence of electrical conductivity of thin tellurium films," *Journal of Applied Physics*, vol. 45, no. 8, pp. 3328–3331, 1974. DOI: 10.1063/1.1663780.
- [405] X. Zhang *et al.*, "Hydrogen-assisted growth of ultrathin Te flakes with giant gate-dependent photoresponse," *Advanced Functional Materials*, vol. 29, no. 49, 2019. DOI: 10.1002/adfm.201906585.
- [406] X. Zhao *et al.*, "Controllable synthesis of high-quality two-dimensional tellurium by a facile chemical vapor transport strategy," *iScience*, vol. 25, no. 1, p. 103 594, 2022. DOI: 10.1016/j.isci.2021.103594.
- [407] U. Coscia *et al.*, "Photoconductivity of tellurium-poly(methyl methacrylate) in the ultraviolet-visible-near infrared range," *Applied Surface Science*, vol. 457, pp. 229–234, 2018. DOI: 10.1016/j.apsusc.2018.06.221.
- [408] Q. Xiao *et al.*, "Facile fabrication of highly uniform tellurium nanorods for self-powered flexible optoelectronics," *Advanced Electronic Materials*, vol. 6, no. 2000240, 2020. DOI: 10.1002/aelm.202000240.
- [409] D. Tsiulyanu and O. Mocreac, "Concentration induced damping of gas sensitivity in ultrathin tellurium films," *Sensors and Actuators, B: Chemical*, vol. 177, pp. 1128–1133, 2013. DOI: 10.1016/j.snb.2012.12.022.
- [410] C. Zhao, L. Hurtado, and A. Javey, "Thermal stability for Te-based devices," *Applied Physics Letters*, vol. 117, no. 19, 2020. DOI: 10.1063/5.0018045.
- [411] V. Selamneni, T. Akshaya, V. Adepu, and P. Sahatiya, "Laser-assisted micropatterned PDMS encapsulation of 1D tellurium nanowires on cellulose paper for highly sensitive strain sensor and its photodetection studies," *Nanotechnology*, vol. 32, no. 45, 2021. DOI: 10.1088/1361-6528/ac19d8.
- [412] M. Peng *et al.*, "Room-temperature blackbody-sensitive and fast infrared photodetectors based on 2D Tellurium/Graphene Van der Waals heterojunction," *ACS Photonics*, vol. 9, pp. 1775–1782, 2022. DOI: 10.1021/acsp Photonics.2c00246.
- [413] Y. Yan *et al.*, "A tellurium short-wave infrared photodetector with fast response and high specific detectivity," *Nanoscale*, vol. 14, pp. 13 187–13 191, 2022. DOI: 10.1039/d2nr02822k.
- [414] Q. Zhao *et al.*, "The role of traps in the photocurrent generation mechanism in thin InSe photodetectors," *Materials Horizons*, vol. 7, pp. 252–262, 2020. DOI: 10.1039/c9mh01020c.
- [415] Q. Zhang *et al.*, "Solution-processed graphene quantum dot deep-UV photodetectors," *ACS Nano*, vol. 9, no. 2, pp. 1561–1570, 2015. DOI: 10.1021/acsnano.5b00437.

- [416] H.-G. Junginger, "Electronic band structure of tellurium," *Solid State Communications*, vol. 5, no. 7, pp. 509–511, 1967. DOI: [https://doi.org/10.1016/0038-1098\(67\)90534-0](https://doi.org/10.1016/0038-1098(67)90534-0).
- [417] M. Razeghi and A. Rogalski, "Semiconductor ultraviolet detectors," *Journal of Applied Physics*, vol. 79, no. 10, pp. 7433–7473, 1996. DOI: 10.1063/1.362677.
- [418] K. Okuyama and Y. Kumagai, "Hall mobility of evaporated tellurium films," *Japanese Journal of Applied Physics*, vol. 12, no. 12, pp. 1884–1889, 1973. DOI: 10.1143/JJAP.12.1884.
- [419] P. Bhaskar, A. W. Achtstein, M. J. Vermeulen, and L. D. Siebbeles, "Charge mobility and recombination mechanisms in tellurium van der waals solid," *Journal of Physical Chemistry C*, vol. 123, pp. 841–847, 2019. DOI: 10.1021/acs.jpcc.8b09665.
- [420] V. Popovych and M. Bester, "Measurements of photoconductive transients in vapor grown CdTe:Cl over wide temperature and dopant concentration ranges," *Journal of Applied Physics*, vol. 112, no. 023705, pp. 1–5, 2012. DOI: <https://doi.org/10.1063/1.4737782>.
- [421] D. Guo *et al.*, "Self-powered ultraviolet photodetector with superhigh photoresponsivity (3.05 A/W) based on the GaN/Sn:Ga₂O₃ pn junction," *ACS Nano*, vol. 12, no. 12, pp. 12 827–12 835, 2018. DOI: 10.1021/acs.nano.8b07997.
- [422] S. Jeon *et al.*, "Gated three-terminal device architecture to eliminate persistent photoconductivity in oxide semiconductor photosensor arrays," *Nature Materials*, vol. 11, no. 4, pp. 301–305, 2012. DOI: 10.1038/nmat3256.
- [423] A. George *et al.*, "Giant persistent photoconductivity in monolayer MoS₂ field-effect transistors," *npj 2D Materials and Applications*, vol. 5, no. 15, 2021. DOI: 10.1038/s41699-020-00182-0.
- [424] E. Arslan, S. Bütün, S. B. Lisesivdin, M. Kasap, S. Ozcelik, and E. Ozbay, "The persistent photoconductivity effect in AlGaN/GaN heterostructures grown on sapphire and SiC substrates," *Journal of Applied Physics*, vol. 103, no. 10, 2008. DOI: 10.1063/1.2921832.
- [425] M. Amani *et al.*, "Solution-synthesized high-mobility tellurium nanoflakes for short-wave infrared photodetectors," *ACS Nano*, vol. 12, no. 7, pp. 7253–7263, 2018. DOI: 10.1021/acs.nano.8b03424.
- [426] Y. Wang, Z. Tang, P. Podsiadlo, Y. Elkasabi, J. Lahann, and N. A. Kotov, "Mirror-like photoconductive layer-by-layer thin films of Te nanowires: The fusion of semiconductor, metal, and insulator properties," *Advanced Materials*, vol. 18, no. 4, pp. 518–522, 2006. DOI: 10.1002/adma.200501465.
- [427] C. Shen *et al.*, "Tellurene Photodetector with High Gain and Wide Bandwidth," *ACS Nano*, vol. 14, pp. 303–310, 2020. DOI: 10.1021/acs.nano.9b04507.
- [428] M. Peng *et al.*, "Blackbody-sensitive room-temperature infrared photodetectors based on low-dimensional tellurium grown by chemical vapor deposition," *Science Advances*, vol. 7, no. 16, pp. 1–12, 2021. DOI: 10.1126/sciadv.abf7358.

- [429] L. Li *et al.*, “Single-crystalline CdS nanobelts for excellent field-emitters and ultrahigh quantum-efficiency photodetectors,” *Advanced Materials*, vol. 22, no. 29, pp. 3161–3165, 2010. DOI: 10.1002/adma.201000144.
- [430] W. Zhao *et al.*, “Single CdS nanorod for high responsivity UV-Visible photodetector,” *Advanced Optical Materials*, vol. 5, no. 12, p. 1700159, 2017. DOI: <https://doi.org/10.1002/adom.201700159>.
- [431] W. Xing *et al.*, “High-throughput fabrication of photoconductors with high detectivity, photosensitivity, and bandwidth,” *ACS Nano*, vol. 6, no. 6, pp. 5627–5634, 2012. DOI: 10.1021/nn301567c.
- [432] K. Hu, H. Chen, M. Jiang, F. Teng, L. Zheng, and X. Fang, “Broadband photoresponse enhancement of a high-performance t-Se microtube photodetector by plasmonic metallic nanoparticles,” *Advanced Functional Materials*, vol. 26, no. 36, pp. 6641–6648, 2016. DOI: 10.1002/adfm.201602408.
- [433] K. Keramatnejad, F. Khorramshahi, S. Khatami, and E. Asl-Soleimani, “Optimizing uv detection properties of n-ZnO nanowire/p-Si heterojunction photodetectors by using a porous substrate,” *Optical and Quantum Electronics*, vol. 47, no. 7, pp. 1739–1749, 2015. DOI: 10.1007/s11082-014-0032-y.
- [434] H. Shang *et al.*, “Optical investigation of chalcogenide glass for on-chip integrated devices,” *Results in Physics*, vol. 28, p. 104552, 2021. DOI: <https://doi.org/10.1016/j.rinp.2021.104552>.
- [435] Y. Yu *et al.*, “Experimental demonstration of linearly polarized 2–10 μm supercontinuum generation in a chalcogenide rib waveguide,” *Optics Letters*, vol. 41, no. 5, pp. 958–961, 2016. DOI: 10.1364/OL.41.000958.
- [436] T. Kohoutek, J. Orava, T. Sawada, and H. Fudouzi, “Inverse opal photonic crystal of chalcogenide glass by solution processing,” *Journal of Colloid and Interface Science*, vol. 353, no. 2, pp. 454–458, 2011. DOI: <https://doi.org/10.1016/j.jcis.2010.10.011>.
- [437] S. Tzadka *et al.*, “Surface plasticizing of chalcogenide glasses: a route for direct nanoimprint with multifunctional antireflective and highly hydrophobic structures,” *Optics Express*, vol. 28, no. 19, pp. 28352–28365, 2020. DOI: 10.1364/OE.400038.
- [438] L. Li, J. Ari, P. A. Deymier, and P. Lucas, “Broadband pyramid antireflective structure on chalcogenide glasses by the hot embossing method for infrared photonics,” *Optical Materials Express*, vol. 12, no. 4, pp. 1638–1647, 2022. DOI: 10.1364/OME.454683.
- [439] T. D. Gupta *et al.*, “Self-assembly of nanostructured glass metasurfaces via templated fluid instabilities,” *Nature Nanotechnology*, vol. 14, pp. 320–327, 2019. DOI: 10.1038/s41565-019-0362-9.
- [440] L. Karam *et al.*, “Spatially microstructured topology of chalcogenide glasses by a combination of the electrothermal process and selective etching for functional infrared media,” *Optical Materials Express*, vol. 12, no. 5, pp. 1920–1931, 2022. DOI: 10.1364/OME.447641.

- [441] H. Deng *et al.*, “Femtosecond laser writing of infrared microlens arrays on chalcogenide glass,” *Optics Laser Technology*, vol. 159, p. 108 953, 2023. DOI: <https://doi.org/10.1016/j.optlastec.2022.108953>.
- [442] J. H. Lee *et al.*, “Thermal properties of ternary Ge-Sb-Se chalcogenide glass for use in molded lens applications,” *Journal of Non-Crystalline Solids*, vol. 431, pp. 41–46, 2016. DOI: <https://doi.org/10.1016/j.jnoncrysol.2015.04.003>.
- [443] B. Temelkuran, S. D. Hart, G. Benoit, J. D. Joannopoulos, and Y. Fink, “Wavelength-scalable hollow optical fibres with large photonic bandgaps for CO₂ laser transmission,” *Nature*, vol. 420, no. 6916, pp. 650–653, 2002. DOI: 10.1038/nature01275.
- [444] J. Carcreff *et al.*, “Investigation on chalcogenide glass additive manufacturing for shaping mid-infrared optical components and microstructured optical fibers,” *Crystals*, vol. 11, no. 3, 2021. DOI: 10.3390/cryst11030228.
- [445] A. Ahmed Simon *et al.*, “Introduction of chalcogenide glasses to additive manufacturing: Nanoparticle ink formulation, inkjet printing, and phase change devices fabrication,” *Scientific Reports*, vol. 11, no. 14311, 2021. DOI: 10.1038/s41598-021-93515-y.
- [446] E. Casamenti *et al.*, “Glass-in-glass infiltration for 3D micro-optical composite components,” *Optics Express*, vol. 30, no. 8, pp. 13 603–13 615, 2022. DOI: 10.1364/OE.451026.
- [447] W. Zhou *et al.*, “Fabrication of microlens array on chalcogenide glass by wet etching-assisted femtosecond laser direct writing,” *Ceramics International*, vol. 48, no. 13, pp. 18 983–18 988, 2022. DOI: <https://doi.org/10.1016/j.ceramint.2022.03.181>.
- [448] C. M. Schwarz *et al.*, “Processing and properties of arsenic trisulfide chalcogenide glasses for direct laser writing of 3D microstructures,” in *Advanced Fabrication Technologies for Micro/Nano Optics and Photonics VII*, vol. 8974, 2014, 89740P. DOI: 10.1117/12.2042809.
- [449] S. Wong *et al.*, “Direct laser writing of three-dimensional photonic crystals with a complete photonic bandgap in chalcogenide glasses,” *Advanced Materials*, vol. 18, no. 3, pp. 265–269, 2006. DOI: <https://doi.org/10.1002/adma.200501973>.
- [450] C. M. Schwarz *et al.*, “Processing and fabrication of micro-structures by multiphoton lithography in germanium-doped arsenic selenide,” *Optical Materials Express*, vol. 8, no. 7, pp. 1902–1915, 2018. DOI: 10.1364/OME.8.001902.
- [451] S. Song, N. Carlie, J. Boudies, L. Petit, K. Richardson, and C. B. Arnold, “Spin-coating of Ge₂₃Sb₇S₇₀ chalcogenide glass thin films,” *Journal of Non-Crystalline Solids*, vol. 355, no. 45, pp. 2272–2278, 2009. DOI: <https://doi.org/10.1016/j.jnoncrysol.2009.07.015>.
- [452] M. Michailov, S. Mamedov, and S. Tsvetarnyi, “Dissolution kinetics of glassy arsenic sulfide in alkali and amine solutions,” *Journal of Non-Crystalline Solids*, vol. 176, no. 2, pp. 258–262, 1994. DOI: [https://doi.org/10.1016/0022-3093\(94\)90085-X](https://doi.org/10.1016/0022-3093(94)90085-X).
- [453] S. Rajesh and Y. Bellouard, “Towards fast femtosecond laser micromachining of fused silica: the effect of deposited energy,” *Optics Express*, vol. 18, no. 20, pp. 21 490–21 497, 2010.

- [454] C. Y. Wang, Z. X. Shen, and B. V. R. Chowdari, "Raman studies of $\text{Ag}_2\text{O}-\text{WO}_3-\text{TeO}_2$ ternary glasses," *Journal of Raman Spectroscopy*, vol. 29, no. 9, pp. 819–823, 1998.
- [455] H. Liu, M. Foley, Q. Lin, and J. Liu, "EDP2XRD: a computer program for converting electron diffraction patterns into X-ray diffraction patterns," *Journal of Applied Crystallography*, vol. 49, no. 2, pp. 636–641, 2016. DOI: 10.1107/S1600576716000613.
- [456] C. Maurel *et al.*, "Processing and characterization of new oxysulfide glasses in the Ge-Ga-As-S-O system," *Journal of Solid State Chemistry*, vol. 181, no. 10, pp. 2869–2876, 2008. DOI: <https://doi.org/10.1016/j.jssc.2008.07.019>.

Curriculum Vitae

Gözden Torun
Born on November 18th, 1993
gozdentorun@gmail.com

Education

2018-2023	Ph.D. in Advanced Manufacturing Institute of Electrical and Micro Engineering - Galatea Laboratory Ecole Polytechnique Fédérale de Lausanne (EPFL), Switzerland
2016-2018	M.Sc. in International Materials Science and Engineering Department of Materials Processing - Kawasaki Laboratory Tohoku University, Japan
2011-2016	B.Sc. in Metallurgical and Materials Engineering Department of Metallurgical and Materials Engineering Middle East Technical university (METU), Turkey

Journal articles

G. Torun, A. Yadav, K. A. Richardson, and Y. Bellouard, *3D microstructuring of chalcogenide glass by femtosecond laser exposure and chemical etching*, submitted (2023).

G. Torun, A. Romashkina, T. Kishi, and Y. Bellouard, *Femtosecond laser direct-write photoconductive patterns on tellurite glass*, submitted (2023).

G. Torun, T. Kishi, D. Pugliese, D. Milanese, and Y. Bellouard, *Formation mechanism of elemental Te produced in tellurite glass systems by femtosecond laser irradiation*, *Advanced Materials*, 2210446 (2023).

E. Casamenti, G. Torun, L. Borasi, M. Lautenbacher, M. Bertrand, J. Faist, A. Mortensen, and Y. Bellouard, *Glass-in-glass infiltration for 3D micro-optical composite components*, *Optics Express* 30 (8), 13603-13615 (2022).

G. Torun, A. Yadav, K. A. Richardson, and Y. Bellouard, *Ultrafast laser direct-writing of self-organized microstructures in Ge-Sb-S chalcogenide glass*, *Frontiers in Physics*, 316 (2022).

G. Torun, T. Kishi, and Y. Bellouard, *Direct-write laser-induced self-organization and metalization beyond the focal volume in tellurite glass*, *Physical Review Materials* 5 (5), 055201 (2021).

Conferences

June 2023 - G. Torun, S. Benketaf, M. Lesik, P. Vlugter, and Y. Bellouard, *On the use of a femtosecond laser micro-processing combined with chemical etching for free-form microstructures in Ultra-low expansion (ULE) glass*, 24th International Symposium on Laser Precision Microfabrication (LPM), Hiroasaki, Japan. (Oral presentation)

June 2023 - G. Torun, M. Lesik, P. Vlugter, and Y. Bellouard, *Femtosecond laser-induced photostructural and photochemical modifications in ultra-low expansion (ULE) glass*, 24th International Symposium on Laser Precision Microfabrication (LPM), Hiroasaki, Japan. (Oral presentation)

January 2023 - G. Torun, A. Romashkina, L. Chautems, T. Kishi, and Y. Bellouard, *Femtosecond direct-write photoconductive tracks on the surface of a tellurite glass*, SPIE Photonics West, San Francisco, USA. (Oral presentation)

November 2022 - G. Torun, K. A. Richardson, and Y. Bellouard, *Advanced manufacturing of chalcogenide glass through femtosecond laser processing: from waveguides to 3D dimensional micro-structures fabrication*, Materials Research Society Fall Meeting (MRS2022 Fall), Boston, USA. (Poster presentation)

September 2022 - G. Torun, A. Romashkina, L. Chautems, T. Kishi, and Y. Bellouard, *Electrical and photo-response properties of femtosecond laser direct-write Te-wires on the surface of tellurite glass*, The 25th Congress of the International Commission for Optics (ICO25), Dresden Germany. (Oral presentation)

June 2022 - G. Torun, E. Casamenti, L. Borasi, M. Lautenbacher, T. Kishi, M. Bertrand, J. Faist, A. Mortensen, and Y. Bellouard, *A laser-based glass-in-glass infiltration process for mid-IR micro-optical components*, 23rd International Symposium on Laser Precision Microfabrication (LPM), Dresden Germany. (Oral presentation)

May 2022 - G. Torun, L. Borasi (co-presenter), E. Casamenti, R. Charvet, C. Dénéreaz, S. Pollonghini, L. Deillon, L.M. Lautenbacher, T. Kishi, M. Bertrand, J. Faist, A. Mortensen, and Y. Bellouard, *Microcasting of metals and glass, an enabling process for micro technologies*, Micronarc Alpine Meeting (MaM), Villars-sur-Ollon, Switzerland. (Oral presentation)

June 2021 - G. Torun, T. Kishi, D. Pugliese, D. Milanese, E. Descrovi, and Y. Bellouard, *Comparative study of femtosecond laser-induced self-organization on the surface of tellurite glasses*,

22nd International Symposium on Laser Precision Microfabrication (LPM), Hirosaki, Japan (Online). (Oral presentation)

December 2021 - G. Torun, T. Kishi, D. Pugliese, D. Milanese, E. Descrovi, and Y. Bellouard, *Investigating femtosecond laser interaction with tellurite glass family*, 14th Pacific Rim Conference on Ceramic and Glass Technology (PACRIM 14) including Glass and Optical Materials Division 2021 Annual Meeting (GOMD 2021), Vancouver Canada (Online). (Oral presentation)

September 2021 - G. Torun, T. Kishi, and Y. Bellouard, *Femtosecond laser machining of tellurite glass: evidence of laser-induced crystallization and self-organization beyond the focal volume*, 15th European Congress and Exhibition on Advanced Materials and Processes (FEMS EUROMAT2021), Graz, Austria (Online). (Oral presentation)

December 2020 - G. Torun, T. Kishi, and Y. Bellouard, *Effect of high repetition rate femtosecond laser exposure on ternary tellurite glass*, Glass Meeting 2020 (GM2020), Tokyo, Japan (Online). (Oral presentation; The best presentation award)

June 2019 - G. Torun, K. Saadi, E. Block, K. A. Richardson, and Y. Bellouard, *Investigating femtosecond laser interaction with $Ge_{23}Sb_7S_{70}$ chalcogenide glass*, 25th International Conference on Glass (ICG), Boston, USA. (Oral presentation)